Observation of $B \to K^0_S \pi^+ \pi^-$ and $B \to K^*(892)^{\pm} \pi^{\mp}$ and Measurement of the Charge Asymmetry in $B \to K^*(892)^{\pm} \pi^{\mp}$

Thesis by

Werner M. Sun

In Partial Fulfillment of the Requirements

for the Degree of

Doctor of Philosophy

California Institute of Technology

Pasadena, California

2003

(Submitted May 19, 2003)

Acknowledgments

I am fortunate to have been encouraged, aided, taught, and befriended by so many individuals during my time as a student. Hitoshi Yamamoto sparked my interest in high-energy physics and introduced me to the joys of conducting experimental research. My advisor, Alan Weinstein, a font of unfailing enthusiasm and boundless knowledge, allowed me to work independently but supplied incisive and consummately perceptive suggestions at just the right times. Frank Würthwein, with whom I worked closely during the first stages of the research in this thesis, has continued to be a source of encouragement, advice, and inspiration. Jon Rosner provided many insightful comments on the last chapter of this thesis. My collaborations with the CLEO Rare B PTA and the CLEO III tracking group were consistently and immensely enjoyable and rewarding, even under the direst circumstances. Chris Jones, Martin Lohner, and Adam Lyon revealed to me the beauties of object-oriented programming. Lawrence Gibbons' guidance of the CLEO III software effort was visionary, and it was a pleasure to work with him. Special thanks are due to Dan Peterson and David Urner for their detailed interest in the Kalman filter. Ed Thorndike and Persis Drell spearheaded the quick search for a $\tilde{b}$ squark that turned into an intensely hectic but satisfying few months. The CLEO Collaboration extended to me great hospitality, and its members, past and present, have shown me the many styles and aspects of being a physicist and have provided me with innumerable role models.

I offer profuse thanks to my fellow Caltech/CLEO graduate students Elliot Lipeles and Anna Shapiro-Bridger, with whom I shared many nights of homework problems and philosophical discussions; to Gregg (and Jana) Thayer for brightening our apartment with utmost jollity; to my voice teacher, Angus Godwin, for his gentle patience; to Rice Majors for broadening my horizons; to the members of the Cornell Chamber Singers, Vox Turturis, and the Cornell Savoyards, especially Kevin Lash, Doug Mathews, Colin Miyamoto, and Amanda Smith, for indulging my musical fantasies; to Daniel Kim, living proof that one can do it all, for keeping me well-oiled with symphony tickets; and to Anna Herforth for her wit, humor, and dulcet oboe tones.

Chief among the debts I owe is the one to my parents for their constant support. To Jeremy Rassen I give heartfelt appreciation for many years of friendship. And finally, my deepest gratitude goes to Rob Costello for enriching my life beyond expression.

Abstract

We report on a search for charmless hadronic B decays to the three-body final states $K^0_S h^\pm \pi^\mp$, $K^\pm h^\mp \pi^0$, and $K^0_S h^\pm \pi^0$ ($h^\pm$ denotes a charged pion or kaon), using 9.12 fb^{-1} of integrated luminosity produced at $\sqrt{s} = 10.58$ GeV and collected with the CLEO detector. We observe the decay $B \to K^0/\bar{K}^0 \pi^+ \pi^-$ with a branching fraction $(50^{+10}_{-9} \pm 7) \times 10^{-6}$ and the decay $B \to K^*(892)^\pm \pi^\mp$ with a branching fraction $(16^{+6}_{-5} \pm 2) \times 10^{-6}$, where the uncertainties are statistical and systematic, respectively. Both branching fractions are averages over CP-conjugate states. We also search for a CP-violating asymmetry in the decay $B \to K^*(892)^\pm \pi^\mp$. We find $\mathcal{A}_{CP}(B \to K^*(892)^\pm \pi^\mp) = 0.26^{+0.33+0.10}_{-0.34-0.08}$, giving an allowed interval of $[-0.31, 0.78]$ at the 90% confidence level. These measurements are used to constrain fundamental parameters of the Standard Model.

Contents

List of Figures

List of Tables

Chapter 1 Introduction

Throughout the millenia, philosophers and scientists have sought to identify and explain the behavior of the building blocks of our material world. This pursuit has engendered many accounts of the origin of matter, from the mythological to the rigorously mathematical. Some ancient cultures, including the Greeks and the Chinese, believed in four fundamental elements: earth, air, fire, and water. Before the fifth century BCE, Greek philosophers debated how these elements transformed into one another or whether one was more fundamental than another. Democritus of Abdera (460?–370? BCE) introduced the notion of atoms, which he saw as tiny, indivisible, eternal particles in constant motion, of which all things were made, including one's soul. Aristotle (384–322 BCE) dismissed these ideas, and the concept of the atom did not resurface until our current scientific age.

By the middle of the nineteenth century, many of the chemical elements familiar to us today were recognized as distinct substances that could be combined to form compound substances with different properties. Each element was composed of a single type of atom. In 1869, Dimitry Mendeleev organized the elements by atomic weight and observed a periodicity in their chemical properties. This periodic structure was not understood until J. J. Thompson's 1897 discovery of the electron and Ernest Rutherford's 1911 elucidation of atomic structure. Rutherford went on to discover the proton in 1918, and his student, James Chadwick, did the same for the neutron in 1932. At the time, electrons, protons, and neutrons were thought to be fundamental constituents of matter.

However, cosmic ray experiments from roughly the same time were yielding a plethora of new particles, such as muons, pions, and kaons, which have the same charge as a proton but different mass. Many attempts were made to explain the spectrum of new particles and their decays. In this pursuit, Wolfgang Pauli proposed a hypothetical particle, the neutrino [1] (1930), and Murray Gell-Mann formulated the quark model [2] (1964). In doing so, they deduced the existence of fundamental particles that had not yet been observed experimentally, and they founded the two main classes of fermions, leptons and quarks, that we recognize and seek to understand today.

These experiments also brought to light the existence of antiparticles, which is one of the deepest consequences of the CPT invariance of relativistic quantum mechanics. Today, we employ a quantum field theory, known as the Standard Model of elementary particle physics, to describe all the known particles and antiparticles. As we shall see, comparision of the properties of particles with those of their antiparticles is a rich area of study that may allow us to glimpse physics beyond the Standard Model.

In addition to the fundamental subatomic particles, physicists have also identified four fundamental forces that act on these particles. In order of decreasing strength at everyday energy scales,

they are the strong nuclear force, the electromagnetic (EM) force, the weak nuclear force, and gravity. While the weak force consists of both charged and neutral currents, EM currents are purely neutral, and the strong force is now understood to have only neutral currents at the fundamental level. The Standard Model provides a description of these three forces. One beautiful feature of the Standard Model is its depiction of the electromagnetic and weak nuclear forces as manifestations of a single electroweak force. It is hoped that this unification can be extended to the strong nuclear force and to gravity. The theory of the strong force, known as quantum chromodynamics (QCD), is a mathematical variant on that of the electroweak force, both of which are based on relativistic quantum mechanics.

The theory of general relativity has accurately predicted and explained gravitational phenomena from terrestrial to astronomical length scales. However, attempts to quantize gravity and incorporate it into the Standard Model have not met with success. Furthermore, it is expected that this grand unification, should it be achieved, would occur at the Planck scale with energies of 10^{28} eV, far above our current experimental reach.

According to the Standard Model, all matter consists of two classes of particles, fermions, which have half-integer spin, and bosons, which have integral spin. There are twelve fundamental fermions, and these are subdivided into two groups, six leptons and six quarks, as shown in Table 1.1. The particles in each of these two groups are arranged in three generations containing two particles each. Each member of a generation possesses characteristics similar to those of corresponding particles in different generations. For instance, the three generations of charged leptons (e, μ, and τ) have identical charge and weak coupling constants. The most salient feature distinguishing the three generations is the mass of the member particles; particles of higher generation number tend to be more massive. With the charged leptons, the muon is about 200 times heavier than the electron, and the tau, in turn, is about 17 times heavier than the muon.

				Forces	Strong	EM (Charge)	Weak	Gravity
BOSONS				Relative Strength	1	10^{-2}	10^{-5}	10^{-39}
				Mediators	g	γ	$W^{\pm}$, Z^0	graviton
		Gen. 1	Gen. 2	Gen. 3				
FERMIONS	Quarks	$\begin{pmatrix} u \\ d \end{pmatrix}$	$\begin{pmatrix} c \\ s \end{pmatrix}$	$\begin{pmatrix} t \\ b \end{pmatrix}$	• •	• $(+\frac{2}{3})$ • $(-\frac{1}{3})$	• •	• •
	Leptons	$\begin{pmatrix} e \\ \nu_e \end{pmatrix}$	$\begin{pmatrix} \mu \\ \nu_\mu \end{pmatrix}$	$\begin{pmatrix} \tau \\ \nu_\tau \end{pmatrix}$		• (-1) (0)	• •	• •

Table 1.1: Standard Model particles and their interactions.

The three generations of quarks comprise three up-type quarks (u, c, t) and three down-type

quarks (d, s, b). All up-type quarks have charge $+\frac{2}{3}e$, where e is the electron charge, and all down-type quarks have charge $-\frac{1}{3}e$. However, the strengths of the weak couplings are not constant across the generations. The weak charged current converts an up-type quark into a down-type quark and vice versa. The two quarks that participate in a weak charged current need not belong to the same generation. For example, a t quark can, in principle, decay to a b, s, or d quark. The coupling constants of the weak charged current are described by the Cabibbo-Kobayashi-Maskawa (CKM) matrix:

$$V_{CKM} = \begin{pmatrix} V_{ud} & V_{us} & V_{ub} \\ V_{cd} & V_{cs} & V_{cb} \\ V_{td} & V_{ts} & V_{tb} \end{pmatrix}. \tag{1.1}$$

In practice, the CKM matrix is nearly diagonal, meaning that the weak charged interaction tends to preserve generation number. Understanding this pattern of quark generation mixing and measuring the elements of the CKM matrix forms a major motivation for many of today's experimental and theoretical programs, including the research presented in this thesis.

The fundamental bosons in the Standard Model act as force mediators. Interactions between particles are understood to be exchanges of intermediate gauge bosons. As shown in Table 1.1, each fundamental force is carried by vector bosons unique to that interaction: the photon (γ) for EM, the $W^{\pm}$ and Z^0 for the weak force, and gluons (g) for the strong force. Although gravity is not included in the Standard Model, it is expected to be mediated by a tensor boson known as the graviton. There also exists a neutral scalar Higgs boson, which is responsible for endowing all the fundamental particles with mass. The precise nature of the Higgs boson is unknown, as it has not yet been observed in the laboratory.

Nearly every Standard Model particle has a corresponding antiparticle, with identical mass as its partner but whose electric charge and all other quantum numbers are reversed in sign. The exceptions are the neutral gauge bosons γ, Z^0, g, and the Higgs boson, which are their own antiparticles. Particles behave identically to their antiparticles in almost all cases. That is, most processes are invariant under CP, the combined operations of charge conjugation and parity inversion. However, in certain situations involving the weak interaction, an inequality can arise between the rates for a process and its CP reflection. This rare phenomenon is known as CP violation, and since its discovery in neutral kaons in 1964 [3], the physics community has sought to clarify its origin. In the current view, CP violation is hypothesized to stem from the complex phase of the CKM matrix, known as γ, and a large amount of experimental and theoretical effort has been and continues to be geared towards either validating or refuting this picture.

The study of the weak interaction in the quark sector is hampered by the fact that free quarks are never observed in the laboratory. Instead, they are bound by the strong interaction to other quarks and antiquarks to form hadrons. The B meson is a hadron consisting of a $\bar{b}$ antiquark bound

to a u or d quark. B mesons decay via the weak decay of the $\bar{b}$, through a quark-level process such as $\bar{b} \to W^+\bar{c}$, where the W^+ is virtual. Hence, B decays are sensitive to CKM matrix elements. Semileptonic decays, $B \to X_{\bar{c},\bar{u}}\ell^+\nu$, where $X_{\bar{c},\bar{u}}$ denotes a hadron containing a $\bar{c}$ or $\bar{u}$ antiquark, are among the most common B decays, with branching fractions of about 10%. These processes allow us to measure the magnitudes of the CKM matrix elements V_{cb} and V_{ub}, but they are not expected to exhibit CP violation.

In contrast, charmless hadronic B decays are far more likely to be sources of CP-violating behavior. Indeed, rate differences between CP conjugate decays in modes such as $B \to K\pi$, $K^*\pi$, or ρK are predicted to be 20%–30% of the CP-averaged rates, and the sizes of these rate differences are related to the CKM phase γ. However, these rare decays pose great challenges. Experimentally, they are difficult to observe, having branching fractions of order 10^{-5} or smaller. Furthermore, the hadron-level strong interactions often obscure the quark-level weak interactions so that extraction of the weak coupling constants from experimental measurements is subject to sizeable theoretical uncertainties.

As will be discussed in Chapter 2, precise measurements of the parameters governing CP violation provides for a rigorous test of the Standard Model. Discrepancies between experiment and theory may point to the existence of physics beyond the Standard Model. Such New Physics is generally anticipated by physicists who are dissatisfied with the need to introduce into the Standard Model a number of free parameters, such as the masses of the fundamental particles, whose values are not predicted by the theory; instead, they must be determined from experiment. Since these parameters are not calculable from first principles, any derivation of their values must lie beyond the Standard Model.

There are other arguments supporting the presence of New Physics, such as the failure of the Standard Model to account for the number of particle generations or the so-called heirarchy problem wherein parameters must be fine-tuned in order to prevent the mass of the Higgs boson from diverging. One additional piece of evidence for New Physics is related to the phenomenon of CP violation. The CKM matrix and its complex phase do not generate enough CP violation to explain the overwhelming dominance of matter over antimatter in today's universe. Indeed, one could consider our very existence as an indication of physics beyond the Standard Model. Therefore, one strategy in the pursuit of New Physics is to search for new sources of CP violation. Such a program can be carried out using the charmless hadronic B decays introduced above, and Chapter 8 of this thesis presents an example of such a search.

Throughout this thesis, measurements are given in natural units, in which $\hbar = c = 1$.

Chapter 2 The Standard Model

For the past quarter of a century, the Standard Model has stood as a remarkably successful description of the interactions of quarks and leptons via the strong nuclear and electroweak forces. Time and again, its predictions have been verified to high precision. This fact, while impressive, has been a source of unease, brought about by the existence in the Standard Model of twenty-five free parameters not determined by the theory. Since these parameters are not calculable from first principles, it is believed that they must have their origin in physics beyond the Standard Model. The discovery of this New Physics through deviations from the Standard Model's predictions is the most common goal behind the theoretical and experimental endeavors in high-energy physics today.

The Standard Model [4] employs a Lagrangian formalism to describe the interactions among the twelve fundamental fermions. These fermions are classified according to the forces to which they are subject. The six leptons engage only in electroweak interactions, while the six quarks also participate in strong interactions. All particles experience gravitational forces which depend on their masses, but since, at the subatomic scale, gravity is more than thirty orders of magnitude weaker than the interactions of the Standard Model, they are usually ignored in high-energy physics. The strength of the EM force experienced by each particle depends on its electric charge. Neutral-current weak interactions depend on the "weak charge", which can be related to the electric charge and to weak isospin in the unified theory. All quarks carry the same color charge, so the strength of the strong interaction is identical for all flavors. The remaining Standard Model interaction, the weak charged current, is the only interaction to exert universal strength for all fermions. Neutrinos, being electrically neutral, are unaffected by the EM force, but they do participate in charged and neutral weak currents.

The particles in each class of fermions are grouped into three generations of weak isospin doublets, as shown in Table 1.1. This table also lists the interactions available to each particle, along with their relative strengths. The masses of the charged fermions increase with generation number. Although the neutrino masses are not yet precisely known, their mass heirarchy is likely to be ill-defined because their weak eigenstates are very different from their mass eigenstates [5]. Within a generation, the mass of a fermion is correlated with the relative strength of its dominant interaction [6].

The particles in each doublet differ in electric charge by $\pm e$, and they are connected by the charged current of the weak interaction. Until recently, the masses of the three flavors of neutrinos were thought to be degenerate and identically zero, an arrangement that would have eliminated inter-generational mixing in the lepton sector. However, the discovery of neutrino flavor oscillations and, hence, of finite neutrino masses has changed that picture. For massive neutrinos, their weak

eigenstates are not, in general, equal to their mass eigenstates. Therefore, the weak charged current can connect any charged lepton to any flavor of neutrino, and a propagating neutrino produced in a weak eigenstate evolves as an oscillating superposition of mass eigenstates, resulting in flavor mixing. Experimentally, no evidence has been found for neutral weak currents that affect a particle's flavor quantum number. Therefore, flavor-changing neutral currents (FCNCs) are forbidden at tree level in the Standard Model.

An analogous situation obtains in the quark sector. Here, the charged weak interaction acts predominantly within a generation. Transitions between generations occur less frequently than those which preserve generation number by an order of magnitude or more. The b quark, with which this thesis is concerned, is less massive than its isospin partner, the t quark, so it can only decay via these suppressed inter-generational transitions. For this reason, rare or anomalous phenomena associated with the weak interaction are more apparent in decays of the b quark than of quarks whose dominant decay channels are not suppressed; the transitions of interest are less likely to be overwhelmed by background from competing processes.

Because of a property of the strong interaction known as color confinement, free quarks are never observed in nature. The strong force is transmitted by the exchange of gluons, which are themselves carriers of color charge. Because gluons can interact with each other, the strength of the strong interaction, unlike that of gravity or the EM force, increases with the distance between color charges and, conversely, decreases with the energy of the exchanged gluon. The particles that we detect in the laboratory are observed to be color singlets. Before we gain access to individual quarks, which are colored, they interact with other quarks or antiquarks that have the appropriate colors and anticolors to form colorless bound states known as hadrons, of which there are two types: mesons (quark-antiquark states) and baryons (three-quark or three-antiquark states). Thus, although we wish to measure the properties of the b quark, we cannot probe them directly. Instead, we study B mesons, which are bound states of a u or d quark and a $\bar{b}$ antiquark. Our view of quark-level weak processes is obscured by the hadron-level strong interactions. These hadronic interactions are complex, non-perturbative, residual, effective manifestations of the fundamental quark-level strong interactions.

These properties of fermions and their interactions are encoded in the Standard Model Lagrangian, which is invariant under local transformations given by the gauge group $\mathrm{SU}(3) \otimes \mathrm{SU}(2) \otimes \mathrm{U}(1)$. This group is the direct product of the symmetry groups for color, weak isospin, and hypercharge, respectively. Each generator of these groups corresponds to a gauge boson that carries the associated force between fundamental fermions. Hence, the strong force is mediated by eight gluons, and the electroweak force by four bosons: W^+, W^-, Z^0, and γ. The Higgs mechanism for electroweak symmetry breaking, whereby all particles acquire their mass, leaves a remnant known as the Higgs boson, which is the only Standard Model particle that has not yet been observed

experimentally.

For all of the Standard Model's successes, there remain several mysteries, mostly concerning the Higgs sector and the origin of mass. The masses of the fundamental fermions and bosons constitute fourteen of the Standard Model's twenty-five free parameters, and their generational structure, while suggestive, defies explanation at the moment. Another unanswered question about the Standard Model concerns the apparent number of particle generations. Measurements of the Z^0 lineshape at LEP indicate that there exist only three flavors of active neutrinos, but the theory does not favor this number over any other. However, the most pressing deficiency of the Standard Model is the so-called heirarchy problem, in which the Higgs boson mass (m_H) suffers from an instability under radiative corrections. The Higgs boson can fluctuate into a pair of virtual t quarks, $W^{\pm}$, Z^0, and γ gauge bosons, or even Higgs bosons themselves, and these one-loop diagrams contribute quadratic divergences to m_H. Direct experimental searches place a lower bound on the Higgs mass of $m_H > 114$ GeV. An upper limit on m_H is given by the triviality bound, which results from demanding a non-zero self-coupling below the scale of New Physics. For a New Physics scale of ~ 10 TeV, the triviality bound is $m_H < 700$ GeV. In order for the Standard Model Higgs to obey both of these constraints, the couplings of the Higgs to these loop particles must be tuned to the unsatisfying level of tens of decimal places citelangacker. Extensions to the Standard Model that eliminate the need for fine-tuning include supersymmetry [5] and Little Higgs [8] models. Such models generally predict the appearance of new particles at the TeV scale.

Current high-energy collider experiments have verified the Standard Model up to $\lesssim 1$ TeV. In the next decade, the LHC at CERN will explore the 1–10 TeV region, and the boundaries of the energy frontier as well as the New Physics reach will be extended considerably. However, it is also possible to discern the effects of novel TeV-scale physics at lower energies, particularly in processes involving loop diagrams, where new particles can appear virtually. Rare decays of B mesons, such as those studied in this thesis, hold promise both in the search for New Physics and in the detailed understanding of the Standard Model's weak sector. One phenomenon in the B system that has attracted special interest in this regard is CP violation.

2.1 Properties of B Mesons

The spectrum of observed b-flavored mesons consists of bound states where the $\bar{b}$ antiquark is paired with a lighter quark. The masses and lifetimes of these mesons are listed in Table 2.1. In addition to the four pseudoscalars, there exists a complementary series of radially excited vector states, most of which are poorly understood. The b quark also forms, in principle, a set of baryons, although only the Λ_b^0 has been definitively seen. There exists evidence for the Ξ_b states, but the Σ_b baryons (uub, udb, ddb) and the Ω_b^- (ssb) are merely hypothetical. In this thesis, we study B^+ and B^0 mesons

and their charge conjugates produced near threshold through the reaction $e^+e^- \to \Upsilon(4S) \to \bar{B}B$ at center-of-mass energy $E_{\rm cm} \simeq 10.6$ GeV. Higher mass bottom hadrons are not produced at these energies.

Particle	Valence Quarks	J^P	Mass (MeV)	Lifetime or Width
B^+	$\bar{b}u$	0^-	5279.0 ± 0.5	$\tau = 1.674 \pm 0.018$ ps
B^0	$\bar{b}d$	0^-	5279.4 ± 0.5	$\tau = 1.542 \pm 0.016$ ps
B^{*+}	$\bar{b}u$	1^-	5325.0 ± 0.6	?
B^{*0}	$\bar{b}d$	1^-		
$B_J^*(5732)$	$\bar{b}u/\bar{b}d$	$?^?$	5698 ± 8	$\Gamma = 128 \pm 18$ MeV
B_s^0	$\bar{b}s$	0^-	5369.6 ± 2.4	$\tau = 1.461 \pm 0.057$ ps
B_s^{*0}	$\bar{b}s$	1^-	5416.6 ± 3.5	?
$B_{sJ}^*(5850)^0$	$\bar{b}s$	$?^?$	5853 ± 15	$\Gamma = 47 \pm 22$ MeV
B_c^+	$\bar{b}c$	0^-	6400 ± 410	$\tau = 0.46^{+0.18}_{-0.16}$ ps
Λ_b^0	udb	$\frac{1}{2}^+$	5624 ± 9	$\tau = 1.229 \pm 0.080$ ps
Ξ_b^0	usb	$\frac{1}{2}^+$	?	$\tau = 1.39^{+0.34}_{-0.28}$ ps
Ξ_b^-	dsb	$\frac{1}{2}^+$		

Table 2.1: Spectra of observed b-flavored mesons and baryons. Charge conjugation is implied.

Bottom hadrons are uniquely well-positioned to probe the generational structure of the quark sector. Because the b quark is lighter than its weak isospin partner, the t quark, it can only decay to quarks of the first and second generations, making it the only quark that decays with appreciable branching fractions to quarks of the two other generations. In contrast, generation-changing decays of the t quark are expected to be overwhelmed by the dominant process, $t \to W^+b$. Thus, B mesons offer us a window into the weak couplings between quarks of the third generation and those of the other two generations, namely, the CKM matrix elements, V_{cb}, V_{ub}, V_{ts}, and V_{td}. In addition, the presence of loop diagrams in several of the decay amplitudes give rare B decays sensitivity to New Physics at mass scales higher than those directly accessible today.

B^0 and B^+ mesons can decay via the weak interaction to leptonic, semileptonic, or hadronic final states. The dominant quark-level transition is the tree-level $\bar{b} \to W^+\bar{c}$ process, shown in Figure 2.1a and 2.1b. If the virtual W^+ materializes as quark-antiquark pair ($q_u\bar{q}_d$, where $q_u = c, u$ and $q_d = s, d$), then the final state is purely hadronic. If, instead, the W^+ decays into a lepton-neutrino pair ($\ell^+\nu$), the result is a semileptonic final state. Tree-level $\bar{b} \to W^+\bar{u}$ transitions proceed via similar Feynman diagrams, but these processes are highly suppressed relative to the dominant $\bar{b} \to W^+\bar{c}$.

Charmless hadronic final states, which are studied in this thesis, can be generated by all six diagrams pictured in Figure 2.1. However, the W-exchange, annihilation, and penguin annihilation

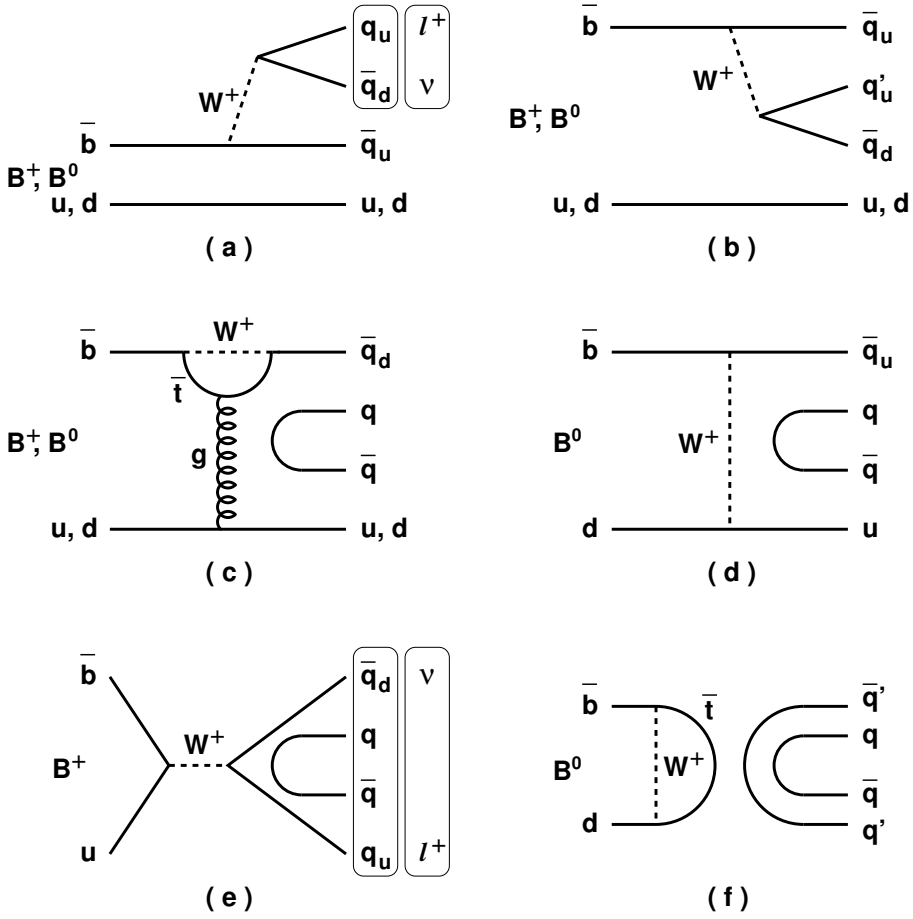

Figure 2.1: Feynman diagrams for B decays: external tree (a), internal color-suppressed tree (b), gluonic penguin (c), W-exchange (d), annihilation (e), and penguin annihilation (f). Up-type quarks are denoted by $q_u = u, c$, down-type quarks by $q_d = d, s$, and light quarks $q = u, d, s$. Vertical boxes indicate correlated variations in particle content.

diagrams (Figures 2.1d–f) are expected to be negligible. The primary contributions to these rare decays come from tree-level $b \to u$ processes and from gluonic penguin diagrams (Figure 2.1c), which result in effective $b \to s$ or $b \to d$ FCNC transitions.

Purely leptonic final states $B^+ \to \ell^+\nu$ occur only through the annihilation diagram (Figure 2.1e), which is suppressed by helicity conservation, by the smallness of $|V_{ub}|^2 \sim \mathcal{O}(10^{-5})$, and by $(f_B/m_B)^2 \sim 10^{-3}$, where f_B is the B meson decay constant, which quantifies the wavefunction overlap of the $\bar{b}$ and u quarks. Because of helicity suppression, the branching fraction $\mathcal{B}(B^+ \to \ell^+\nu)$ is proportional to the mass squared of the charged lepton. Hence, the most common leptonic B decays are expected to be $B^+ \to \tau^+\nu_\tau$ with a predicted branching fraction of $\mathcal{O}(10^{-5})$, compared to $\mathcal{O}(10^{-7})$ and $\mathcal{O}(10^{-12})$ for $B^+ \to \mu^+\nu_\mu$ and $B^+ \to e^+\nu_e$, respectively. None of these leptonic B decays has been observed experimentally.

There is also a class of charmless B decays associated with the electroweak penguin diagrams shown in Figure 2.2. These diagrams are similar to the penguin diagrams in Figure 2.1 except that a photon or Z^0 is radiated instead of a gluon. Electroweak penguins can yield hadronic final states, as well as leptonic or semileptonic ones. However, since the lepton pairs are produced through neutral gauge bosons, they are of the type $\ell^+\ell^-$ and $\nu\bar{\nu}$ instead of $\ell^+\nu$. Other Standard Model processes that give the semileptonic final states $X_{s,d}\ell^+\ell^-$ and $X_{s,d}\nu\bar{\nu}$ are shown in Figures 2.2e and 2.2f.

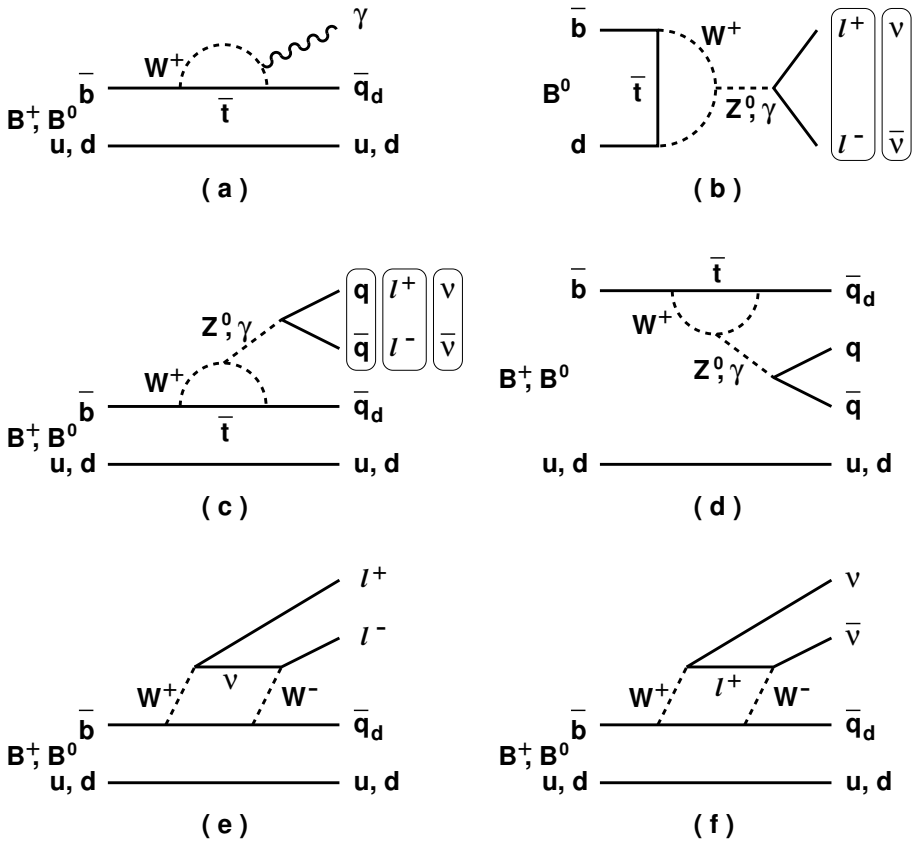

Figure 2.2: Electroweak penguin diagrams for charmless B decays: electromagnetic penguin $B \to X_{s,d}\gamma$ (a), penguin annihilation (b), external penguin (c), internal color-suppressed penguin (d). Also shown are loop diagrams contributing to $B \to X_{s,d}\ell^+\ell^-$ (e) and $B \to X_{s,d}\nu\bar{\nu}$ (f). Up-type quarks are denoted by $q_u = u, c$, down-type quarks by $q_d = d, s$, and light quarks $q = u, d, s$. Vertical boxes indicate correlated variations in particle content.

The electromagnetic penguin in Figure 2.2a radiates a real photon, giving the final state $X_{s,d}\gamma$. The rate for $B \to X_s\gamma$ relative to $B \to X_d\gamma$ is given by the ratio $|V_{ts}/V_{td}|^2 \approx 30$. Because FCNCs are forbidden at tree level in the Standard Model, $B \to X_{s,d}\gamma$ decays can only proceed via loop diagrams, making them particularly sensitive to possible new heavy loop particles. Both the inclusive rate and the photon spectrum are theoretically well-understood, being dominated by perturbative short-distance interactions. Therefore, because $B \to X_{s,d}\gamma$ receives only one, precisely

calculated contribution in the Standard Model, any significant deviation from its predictions can immediately be ascribed to New Physics. The current experimental measurements of the $B \to X_s\gamma$ rate and photon spectrum agree well with expectations. Similar tests of the Standard Model can be performed with $X_{s,d}\ell^+\ell^-$ and $X_{s,d}\nu\bar{\nu}$ decays, although the theoretical uncertainties are somewhat larger.

The dominant decays of B mesons can be described with the spectator model, in which the b quark is treated as a weakly decaying free particle, as in the $\bar{b} \to W^+\bar{q}_u$ tree diagrams of Figures 2.1a and 2.1b. The accompanying spectator quark is incorporated into a final state hadron after the decay of the b has taken place. Corrections to this simple picture arise from QCD effects where gluons are exchanged between the spectator quark and the other final state quarks.

The spectator model provides a qualitative explanation of the B^0 and B^+ lifetimes. For a free $\bar{b}$ quark, the partial width for each W^+ decay channel is

$$\Gamma = \frac{G_F^2 m_b^5}{192\pi^3}|V_{q_u b}|^2 N_c \Phi, \tag{2.1}$$

where m_b is the mass of the b quark and Φ is a phase space suppression factor to account for finite masses of the three final state fermions. N_c is the number of colors in the W^+ decay (3 for $W^+ \to q_u\bar{q}_d$, 1 for $W^+ \to \ell^+\nu$), although it can be converted into a phenomenological parameter to include QCD corrections, giving it a value of approximately 4 for $W^+ \to q_u\bar{q}_d$. Considering the five W^+ final states, $u\bar{d}$, $c\bar{s}$, $e^+\nu_e$, $\mu^+\nu_\mu$, and $\tau^+\nu_\tau$, the total lifetime in the spectator model is found to be 1.58 ps, and the separate inclusive branching fractions are listed in Table 2.2.

Mode	N_c	Φ	$\lvert V_{qb}\rvert$	$\mathcal{B}$
		$q = c$		
$\bar{c}u\bar{d}$	4	0.52	0.038	0.483
$\bar{c}c\bar{s}$	4	0.25	0.038	0.232
$\bar{c}e^+\nu_e$	1	0.52	0.038	0.121
$\bar{c}\mu^+\nu_\mu$	1	0.52	0.038	0.121
$\bar{c}\tau^+\nu_\tau$	1	0.13	0.038	0.030
		$q = u$		
$\bar{u}u\bar{d}$	4	1.00	0.003	0.006
$\bar{u}c\bar{s}$	4	0.52	0.003	0.003
$\bar{u}e^+\nu_e$	1	1.00	0.003	0.001
$\bar{u}\mu^+\nu_\mu$	1	1.00	0.003	0.001
$\bar{u}\tau^+\nu_\tau$	1	0.25	0.003	0.000

Table 2.2: Inclusive B meson branching fractions in the spectator model.

Thus, $b \to c$ transitions constitute nearly 99% of all B decays. The relative scarcity of $b \to u$

transitions is determined by the ratio $|V_{ub}/V_{cb}|^2 \approx 0.008$. Semileptonic decays, $\bar{b} \to \bar{c}\ell^+\nu$ and $\bar{b} \to \bar{u}\ell^+\nu$, constitute about 24% of the total width. These decays are instrumental in measuring the magnitudes of V_{cb} and V_{ub} because they are theoretically manageable; there no strong interactions between the $\ell^+\nu$ pair and the quarks in the final state. The uncertainties related to the hadronization of the c or u quark and the spectator quark are controlled by applying heavy quark effective theory (HQET) [9, 10], which expands QCD around the heavy quark limit, $m_b \to \infty$. In this limit, the b quark inside a B mesons acts as a stationary color source and the spin degrees of freedom of the heavy quark decouple from the dynamics of the system. HQET simplifies the theoretical expressions for inclusive and exclusive semileptonic B decay and relates the hadronic uncertainties to universal, measureable parameters.

All B decays that do not proceed via the dominant $b \to c$ transition are referred to as "rare" processes. These include $b \to u$, $b \to d$, and $b \to s$ transitions to charmless hadronic final states, which are governed by the CKM matrix elements V_{ub}, V_{td}, and V_{ts}, respectively. In general, these decays can be produced through more than one of the amplitudes pictured in Figures 2.1 and 2.2. In order to extract the CKM matrix elements, one must separate the various amplitudes. In addition, non-perturbative long-distance QCD effects loom large in these hadronic final states, and theoretical uncertainties abound. Disentagling these several contributions requires measurements of many modes that are related by symmetries of the strong interaction.

Because of the interference among competing (but suppressed) amplitudes, charmless hadronic B decay rates are sensitive not only to the magnitudes of the weak couplings but to their CP-violating phases as well. This interference is a necessary condition for CP violation, and the CP asymmetries in some of these modes are expected to be as large as 20%–30%. Indeed, the very presence of the rare $b \to u$ transitions is connected to the existence of CP violation; if $|V_{ub}|$ were zero, CP violation would not exist in the Standard Model. Thus, in addition to carrying information about weak quark couplings, non-perturbative strong interactions, and, potentially, New Physics, charmless hadronic B decays provide a testing ground for the Standard Model's description of CP violation.

2.2 CP Violation

In 1956, an experiment studying β-transitions of polarized cobalt nuclei showed that the weak interaction violated parity symmetry maximally [11]. This discovery implied a vector-minus-axial ($V - A$) Lorentz structure for the weak interaction, which acts only on left-handed fermions and right-handed antifermions. The proposed structure was also invariant under the combined operation of charge-conjugation and parity inversion (CP), which was then believed to be a symmetry of the weak interaction. Less than a decade later, in 1964, this assumption was refuted by the observation of a small CP-violating effect in decays of neutral kaons [3].

Among the attempts to reconcile CP violation with the two-generation theory of weak interactions then in existence was the Kobayashi-Maskawa (KM) mechanism [12], which required a hypothetical third family of quarks. With only two families (four quarks), the unitary quark mixing matrix is purely real [13]. Expanding the matrix to three families allows for a non-trivial imaginary phase, which is the sole source of CP violation in the Standard Model. In this form, the quark mixing matrix is called the CKM matrix, which was introduced earlier in Chapter 1. Recent experimental results [14, 15] from the B meson system have provided strong evidence in favor of the KM model. We now know that this CP-violating phase is large and that the rarity of CP violating phenomena stems not from the approximate conservation of CP in nature but rather from the suppression of inter-generational mixing in the weak interaction.

The phenomenon of CP violation is closely linked to the composition of the observable universe, which consists mainly of matter with very little antimatter. If the Big Bang created the two in equal quantities, as is commonly believed, then today's matter-antimatter imbalance must have arisen during the evolution of the universe [16]. The KM model provides a mechanism for generating CP violation, but the magnitude of this effect is not large enough to explain the current baryon-to-photon ratio [17, 18], for which we must turn to physics beyond the Standard Model. In general, these extensions imply the existence of many new CP violating parameters which have no *a priori* reason to be small. However, any viable TeV-scale model must be reconciled with the apparent success of the KM hypothesis at the electroweak scale.

Conversely, measurements of CP-violating Standard Model quantities are uniquely sensitive to New Physics. The simplicity of the KM hypothesis gives it predictive power in a wide range of processes. All forms of CP-violating phenomena in the Standard Model are related to the single imaginary phase in the CKM matrix. Therefore, is it desirable not only to measure this parameter as precisely as possible, but also to measure it in as many processes as possible. Any inconsistency among these various measurements would signal the presence of New Physics.

Ultimately, any complete theory of CP violation must explain not only its presence in the weak interaction but also its absence in the strong interaction. In principle, the Standard Model allows for a CP violating parameter in QCD [19, 20, 21], but measurements of the electric dipole moment of the neutron have constrained it to be less than 10^{-10} [22]. The inability of currently accepted theories to account naturally for this vanishing parameter has led to the so-called strong CP problem.

2.2.1 The CKM Matrix and the Unitarity Triangle

In the Standard Model, the weak eigenstates and mass eigenstates of left-handed quarks are related by the CKM matrix (Equation 1.1) of complex couplings for charged-current weak interactions. For three generations of quarks, this unitary matrix is fully determined by three real parameters, which act like Euler angles, and one CP-violating phase. Experimentally, it has been determined that the

CKM matrix is nearly diagonal, and generation number is nearly conserved. The subdominant transitions between generations are characterized by the parameter $\lambda = |V_{us}| \approx 0.22$, which is the sine of the Cabibbo angle. The strengths of the couplings between the first and second generations, second and third generations, and first and third generations are $\mathcal{O}(\lambda)$, $\mathcal{O}(\lambda^2)$, and $\mathcal{O}(\lambda^3)$, respectively. This heirarchical structure allows the CKM matrix to be expressed in the following approximate form, known as the Wolfenstein parametrization [23]:

$$V_{CKM} = \begin{pmatrix} 1-\frac{1}{2}\lambda^2 & \lambda & A\lambda^3(\rho - i\eta) \\ -\lambda & 1-\frac{1}{2}\lambda^2 & A\lambda^2 \\ A\lambda^3(1-\rho-i\eta) & -A\lambda^2 & 1 \end{pmatrix} + \mathcal{O}(\lambda^4). \tag{2.2}$$

A and λ has been measured to high precision ($\mathcal{O}(1\%)$), but the parameters ρ and η, which together represent the CP-violating phase, are known only to 50% and 15%, respectively [5].

The unitarity of the CKM matrix leads to six orthogonality relations involving pairs of columns or pairs of rows. Each of these relations defines a triangle in the complex plane. These six triangles share a common area, given by the Jarlskog invariant [24, 25], $\frac{1}{2}|\Im(V_{i\alpha}V_{j\beta}V_{i\beta}^*V_{j\alpha}^*)|$ ($i \neq j$, $\alpha \neq \beta$), which is non-zero if CP is violated. In four of the six triangles, the three sides are not of comparable magnitude; one side is shorter than the other two by $\mathcal{O}(\lambda^2)$ or $\mathcal{O}(\lambda^4)$. Of the remaining non-squashed triangles, the one most relevant to B physics is given by

$$V_{ud}V_{ub}^* + V_{cd}V_{cb}^* + V_{td}V_{tb}^* = 0. \tag{2.3}$$

It is depicted in Figure 2.3 and has been dubbed the Unitarity Triangle (UT). The lengths of the sides have been scaled by $V_{cd}V_{cb}^* = A\lambda^3$, which places the apex of the triangle at $(\bar{\rho}, \bar{\eta})$, where $\bar{\rho} = \rho(1-\frac{1}{2}\lambda^2)$ and $\bar{\eta} = \eta(1-\frac{1}{2}\lambda^2)$. This geometric representation of the CKM matrix allows constraints from various sources to be combined conveniently. The most commonly cited goal of B physics today is to overconstrain the UT by measuring its sides and angles in as many different ways as possible. Consistency among the various measurements would support the KM mechanism as the source of CP violation in the Standard Model. In particular, the Standard Model predicts the sum of the UT angles, $\alpha + \beta + \gamma$, to be π, and New Physics can cause this relation to be violated.

Generally speaking, the lengths of the sides are probed by decay rates, and the angles by CP asymmetries. Decay rates are also sensitive to the CKM phase when a process receives contributions from two or more amplitudes of comparable magnitudes but with differing weak phases. The interference between these amplitudes is partially governed by the phases of the weak quark couplings. Such is the case with several of the charmless hadronic B decays studied in the research presented in this thesis.

The length of the left side of the UT is determined by measuring $|V_{cb}|$ with $b \to c\ell^-\nu$ decays and

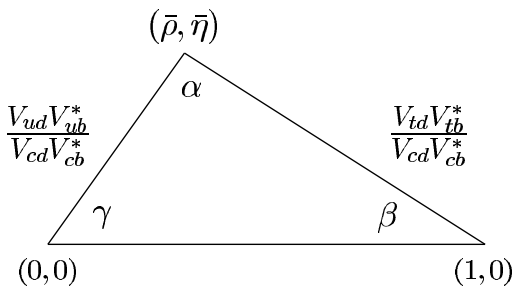

Figure 2.3: The CKM unitarity triangle.

$|V_{ub}|$ with $b \to u\ell^-\nu$ decays. Both quantities are accessible through the decays of B mesons. The experimental uncertainty on the ratio $|V_{ub}/V_{cb}|$ is currently about 20% and is shrinking quickly. The ratio $|V_{ud}/V_{cd}|$ is given to a precision of about 7% by nuclear beta decay and neutrino scattering experiments [5]. For the right side of the UT, the product $|V_{td}V_{tb}^*|$ is extracted from the B^0-$\bar{B}^0$ mixing parameter, which is related to the mass difference of the B^0 mass eigenstates, Δm_d (see Section 2.2.2). The position of the apex is also constrained by the parameter ϵ that quantifies the size of indirect CP violation in the neutral kaon system.

Of the three angles in the unitarity triangle, only $\beta = \arg V_{td}^*$ has been measured to any meaningful precision in a study of time-dependent CP violation in $b \to c\bar{c}s$ transitions where the final state is a CP eigenstate, such as $B \to J/\psi K_S^0$ [14, 15]. This method is experimentally favorable and relatively free from theoretical uncertainty. On the other hand, the angles α and $\gamma = \arg V_{ub}^*$ are not as straightforward to probe. They depend on measurements of rare B decays that receive contributions from more than one quark-level amplitude. In these processes, the penguin loop diagram, shown in Figure 2.1c, plays an important role. At times, it is a necessary ingredient, but at other times, it is a nuisance and a complication. Methods of determining all three angles are discussed in more detail in Section 2.2.2.

Combining the experimental inputs on the lengths of the sides of the UT ($|V_{ub}/V_{cb}|$, B^0-$\bar{B}^0$ mixing, and ϵ) gives the "standard" analysis of the allowed region in the $\bar{\rho}$-$\bar{\eta}$ plane [26]. The current (and also rapidly changing) estimate of this region is shown in Figure 2.4. Overlaid but not included in the fit is the world average $\sin 2\beta = 0.734 \pm 0.054$. The remarkable agreement of the standard fit with the measured $\sin 2\beta$ validates the KM mechanism, suggesting that it is responsible for the bulk of CP violation in flavor changing processes. The constraints on α and γ are still too imprecise to have much bearing on this determination. As an illustration, Figure 2.5 presents an alternate, independent analysis [27, 28] of the allowed $\bar{\rho}$-$\bar{\eta}$ region using the rare $B \to K\pi$ decays, which are sensitive to γ. This analysis makes no reference to B^0-$\bar{B}^0$ mixing or to B_s-$\bar{B}_s$ mixing and is therefore independent of the top quark sector. While the preferred value of γ is slightly larger than that of the

standard fit, there is no conclusive discrepancy to be seen. Future reductions in the experimental and theoretical uncertainties should help to refine this assessment.

The KM hypothesis has successfully survived the first round of experimental scrutiny, and the Standard Model has been shown to provide a viable description of all observed CP-violating phenomena. CKM unitarity continues to be tested by experimental measurements currently in progress, and the hope of uncovering a deviation remains strong. That there must be non-Standard-Model sources of CP violation is almost demanded by the strong CP problem and by cosmological baryogenesis. However, the dominance of the KM mechanism below 1 TeV severely limits the range of possibilities for new CP violating mechanisms above the TeV scale.

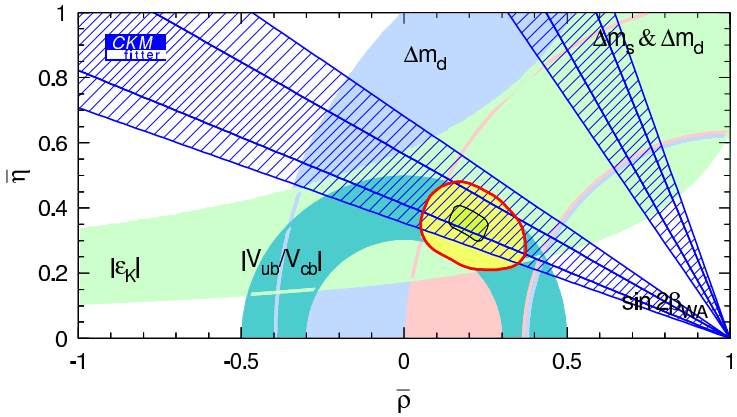

Figure 2.4: Standard constraints on $(\bar{\rho}, \bar{\eta})$ with 95% and 68% confidence level contours [26]. The world average $\sin 2\beta$ is overlaid but not included in the fit.

2.2.2 CP Violation in B Decays

The Standard Model contains three methods of generating CP violation in B decays via the CKM phase. The first of these occurs in the B^0-$\bar{B}^0$ mixing transition ($|\Delta B| = 2$), which proceeds through the diagrams shown in Figure 2.6, and is referred to as "indirect" CP violation. The neutral B mass eigenstates are defined as

$$\begin{aligned} |B_1\rangle &\equiv p|B^0\rangle + q|\bar{B}^0\rangle \\ |B_2\rangle &\equiv p|B^0\rangle - q|\bar{B}^0\rangle. \end{aligned} \tag{2.4}$$

If q and p were not equal, then the mass eigenstates would not be CP eigenstates, and B^0-$\bar{B}^0$ mixing would not conserve CP. In the Standard Model, $|q/p|$ is expected to be close to unity, and the deviation of $\mathcal{O}(10^{-2})$ is usually neglected. The value of $|q/p|$ is accessible through the CP

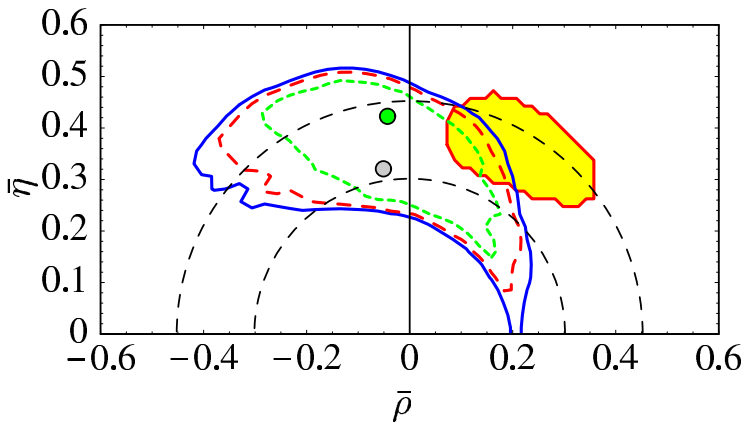

Figure 2.5: The confidence level contours for $(\bar{\rho}, \bar{\eta})$ at 95% (solid), 90% (dashed), and 68% (short-dashed), based on a fit to $B \to K\pi$ and $\pi\pi$ branching fractions in the QCD factorization framework [28]. The two dots represent the best fit for two different sets of hadronic input parameters. The dashed circles centered at the origin are the 95% confidence level contours for the world average $|V_{ub}/V_{cb}|$, which is not included in the fit. The 95% confidence level contour of the standard fit including the world average $\sin 2\beta$ [26] is given by the shaded region.

asymmetry in wrong-sign semileptonic B^0 decays:

$$\frac{\Gamma(\bar{B}^0 \to \ell^+ X) - \Gamma(B^0 \to \ell^- X)}{\Gamma(\bar{B}^0 \to \ell^+ X) + \Gamma(B^0 \to \ell^- X)} = \frac{1 - |q/p|^4}{1 + |q/p|^4}. \tag{2.5}$$

Since this asymmetry is very small in the Standard Model, experimental evidence for a non-zero value may be due to New Physics.

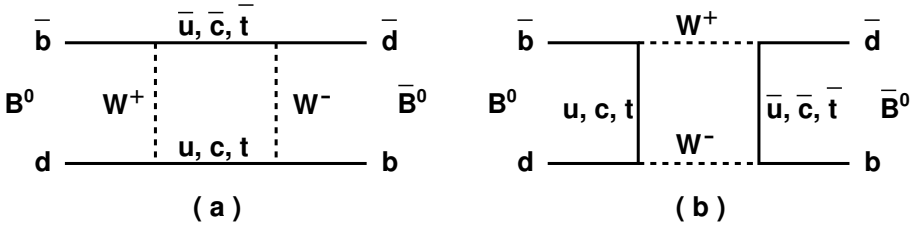

Figure 2.6: Feynman diagrams for B^0-$\bar{B}^0$ mixing.

The other two types of CP violation occur in the interference of two amplitudes with different CP-violating weak phases that contribute to a single process. These contributions also carry, in general, different CP-conserving phases. Hence, the two CP partner amplitudes can be expressed as

$$A(\bar{B} \to \bar{f}) \quad = \quad A_1 + A_2 = |A_1| e^{i(\delta_1 + \phi_1)} + |A_2| e^{i(\delta_2 + \phi_2)} \tag{2.6}$$

$$A(B \to f) \quad = \quad \bar{A}_1 + \bar{A}_2 = |A_1| e^{i(\delta_1 - \phi_1)} + |A_2| e^{i(\delta_2 - \phi_2)},$$

where the A_i are the contributing amplitudes, and ϕ_i and δ_i are their CP-violating and CP-conserving phases, respectively. We have assumed that $|A_i| = |\bar{A}_i|$. Hence, the CP asymmetry is evaluated to be

$$\begin{aligned} \mathcal{A}_{CP} &\equiv \frac{|A(\bar{B} \to \bar{f})|^2 - |A(B \to f)|^2}{|A(\bar{B} \to \bar{f})|^2 + |A(B \to f)|^2} \\ &= \frac{2|A_1||A_2| \sin(\delta_1 - \delta_2) \sin(\phi_1 - \phi_2)}{|A_1|^2 + |A_2|^2 + 2|A_1||A_2| \cos(\delta_1 - \delta_2) \cos(\phi_1 - \phi_2)}. \end{aligned} \tag{2.7}$$

From this expression, it is seen that $\mathcal{A}_{CP}$ vanishes if either $\phi_1 = \phi_2$ or $\delta_1 = \delta_2$. Therefore, the necessary conditions for a non-zero $\mathcal{A}_{CP}$ in a given process are that more than one amplitude contribute to the decay, that each amplitude carry a different CP-conserving phase, and that each amplitude also carry a different CP-violating weak phase.

For B^0 decays to CP eigenstates, f_{CP}, the final state can be reached either directly ($B^0 \to f_{CP}$) or through the mixed state ($B^0 \to \bar{B}^0 \to f_{CP}$). The time evolution of amplitudes for initial states that are pure B^0 or $\bar{B}^0$ at $t = 0$ is given by

$$\begin{aligned} A(B^0(t) \to f_{CP}) &\propto \cos\left(\frac{\Delta m_d t}{2}\right) A + i\frac{q}{p} \sin\left(\frac{\Delta m_d t}{2}\right) \bar{A} \\ A(\bar{B}^0(t) \to f_{CP}) &\propto i\frac{p}{q} \sin\left(\frac{\Delta m_d t}{2}\right) A + \cos\left(\frac{\Delta m_d t}{2}\right) \bar{A}, \end{aligned} \tag{2.8}$$

where $A \equiv A(B^0 \to f_{CP})$, $\bar{A} \equiv A(\bar{B}^0 \to f_{CP})$, and Δm_d is the mass difference between the neutral B mass eigenstates. Thus, the decay amplitude receives two contributions with a CP-violating weak phase difference of $\arg(q\bar{A}/pA)$, with $\arg(q/p) = -2\beta$. The imaginary sine terms arise from the fact that the mixing channel is virtual or "dispersive," whereas the direct channel is "absorptive." As a result, the CP-conserving phase difference between the two contributions is simply $\frac{\pi}{2}$, and $B^0(t) \to f_{CP}$ exhibits a *time-dependent* CP asymmetry:

$$\begin{aligned} \mathcal{A}_{CP}(t) &\equiv \frac{|A(\bar{B}^0(t) \to f_{CP})|^2 - |A(B^0(t) \to f_{CP})|^2}{|A(\bar{B}^0(t) \to f_{CP})|^2 + |A(B^0(t) \to f_{CP})|^2} \\ &= \frac{2\Im(q\bar{A}/pA) \sin(\Delta m_d t) - \left(1 - |q\bar{A}/pA|^2\right) \cos(\Delta m_d t)}{1 + |q\bar{A}/pA|^2}. \end{aligned} \tag{2.9}$$

If $|\bar{A}/A| = |q/p| = 1$, then the above asymmetry simplifies to $\mathcal{A}_{CP}(t) = \Im(q\bar{A}/pA) \sin(\Delta m_d t)$. In the case of $B \to J/\psi K^0_S$, all Standard Model contributions except the $b \to c\bar{c}s$ tree diagram are negligible, so A and $\bar{A}$ have the same magnitude as well as the same weak phase in the Wolfenstein parametrization. Therefore, the time-dependent CP asymmetry in $B \to J/\psi K^0_S$ is proportional to $\sin 2\beta$, although the time-integrated CP asymmetry vanishes. The fact that $A(B^0 \to J/\psi K^0_S)$ is

dominated by a single amplitude allows the details of hadronization to be ignored, since only the ratio $\bar{A}/A$ appears in the above expressions and the strong interaction is assumed to be CP-invariant. This method of determining β is thus practically free from theoretical uncertainty.

In principle, the B decay to the CP eigenstate $\pi^+\pi^-$ can be used to determine α in a manner similar to $B \to J/\psi K^0_S$ for β. However, the situation in $B \to \pi^+\pi^-$ is complicated by the presence of both tree and penguin diagrams with differing weak phases. If we consider only the dominant $b \to u\bar{u}d$ tree contribution, then $\bar{A}/A = e^{-i2\gamma}$, and the time-dependent CP asymmetry probes $\sin 2(\beta+\gamma) = \sin 2\alpha$, where we have used $\alpha+\beta+\gamma = \pi$. However, the $b \to d$ penguin amplitude, whose magnitude is estimated to be one-fifth that of the tree amplitude, cannot be neglected. Since its weak phase is β, $\arg(\bar{A}/A)$ is no longer simply -2γ but instead depends on the magnitude of the penguin amplitude. Furthermore, if the strong phases of the tree and penguin amplitudes differ, then, for reasons given below, $|\bar{A}/A| \neq 1$. The effect of a sizeable penguin amplitude is to shift the measured value of α from its true value. The theoretical uncertainty introduced by this "penguin pollution" can be resolved with an isospin analysis of the three $B \to \pi\pi$ modes [29]. However, this program faces the hurdle of a very small branching fraction for $B \to \pi^0\pi^0$ ($< 4 \times 10^{-6}$), which has not yet been observed.

An alternate method of determining α makes use of the Dalitz plot for $B \to \pi^+\pi^-\pi^0$ [30, 31, 32]. The interference regions between the three $\rho(770)$ resonance bands allow extraction of α (as well as the strong phase between the tree and penguin amplitudes) without the fourfold ambiguity of the $B \to \pi^+\pi^-$ method. However, fierce experimental backgrounds and the possible existence of a virtual intermediate B^* or a three-body non-resonant component may limit the utility of this approach [33, 34].

The angle γ is conventionally regarded as the most difficult angle of the Unitarity Triangle to determine because the B meson does not decay to a CP eigenstate where a time-dependent CP asymmetry measurement would yield γ. However, γ can be probed with the last type of CP violation in the B system, known as "direct" CP violation because it originates in the decay amplitude itself, independent of CP violation in B^0-$\bar{B}^0$ mixing. Direct CP violation is the most common form of CP violation in decays to non-CP-eigenstates, and it is the only allowed form in decays of the charged $B^\pm$ meson. It is not expected in B decays to charm, which are dominated by a single amplitude, but it may appear in charmless hadronic final states, where the interfering amplitudes can be of similar size. Because of CKM unitarity, there are at most two different CP-violating weak phases in any charmless hadronic B decay. If the constituent amplitudes also have different strong phases, then the requisite CP-conserving phase difference is present, and direct CP violation can occur. Unlike with decays to CP eigenstates, direct CP asymmetries can be observed in the time-integrated rates.

In decays with interference between $b \to u\bar{u}s$ tree amplitudes and $b \to s\bar{q}q$ penguin amplitudes, the weak phase difference is γ, and both the CP asymmetry and the CP-averaged branching fraction

(denominator of Equation 2.7) provide a window on the CKM phase. Because of this expected sensitivity, $B \to K\pi$ decays have received much attention recently. These decays are experimentally challenging to detect because of their small branching fractions ($\mathcal{O}(10^{-5})$) and because of difficulty in distinguishing charged pions from charged kaons at high momentum. Current experiments have managed to overcome both of these drawbacks with high-luminosity particle colliders and innovative particle-identification devices. The CP-averaged branching fractions for all four $B \to K\pi$ decays have now been measured to a precision of 10%–20%.

In addition to the two-pseudoscalar (PP) $B \to K\pi$ decays, the pseudoscalar-vector (PV) decays $B \to K^*(892)\pi$ and $B \to \rho(770)K$ can also be used to constrain γ. In particular, the decay $B \to K^*(892)^{\pm}\pi^{\mp}$, whose branching fraction is measured in this thesis, receives only contributions from $b \to u$ tree and $b \to s$ penguin diagrams (see Section 2.5). So, as long as the hadronic uncertainties can be controlled, this decay provides a clean determination of γ. Experimentally, these $B \to PV$ decays are accompanied by higher background levels than the corresponding $B \to PP$ decays caused by the higher final state multiplicity. They are also more difficult to calculate theoretically because of the increased number of independent amplitudes associated with PV modes. It has been suggested that a broader analysis examining the Dalitz plot of $B \to K\pi\pi$ decays, which includes $B \to K^*(892)\pi$ and $\rho(770)K$, may also permit extraction of the strong phases among the various amplitudes contributing to the decay [30, 35, 36, 37, 38, 39].

Other methods of determining γ involve decays, like $B \to D\pi$ [40, 41, 42] or $B \to DK$ [43, 44, 45, 46, 47], where a $b \to c\bar{u}\{d, s\}$ amplitude interferes with a $b \to u\bar{c}\{d, s\}$ amplitude. Such methods are not subject to uncertainties from penguin contributions, but their experimental feasibility is limited either by small decay rates or by small CP asymmetries. A recent proposal [48] involving $B^{\pm} \to D^0 K^{\pm}$, where $D^0 \to K^*(892)^{\pm}K^{\mp}$, makes use of processes with substantial branching fractions and does not require a time-dependent analysis or B flavor tagging, thereby overcoming the statistical limitations of the other $B \to DK$ methods.

In order to extract the weak phase from direct CP violation measurements, one must know both the magnitudes and strong phases of A_1 and A_2 in Equation 2.7. Evaluation of these hadronic matrix elements is a formidable theoretical undertaking since the strong interaction cannot always be treated perturbatively. Below, we discuss two complementary approaches to this problem. The first exploits the approximate flavor symmetry of the u, d and s quarks, employing the SU(3) group to relate the matrix elements of various processes. In this approach, no assumptions are made about the form of the hadronic matrix element. In contrast, the decay rates can be calculated using an effective low-energy Hamiltonian and applying a factorization assumption, which states that the two final state hadrons do not interact with each other. Typically, in these calculations, the electroweak and perturbative QCD contributions are directly evaluated, while the non-perturbative contributions are parametrized as form factors and decay constants and are taken from other independent sources.

2.3 SU(3) Flavor Symmetry

One approach to determining the strong interaction amplitudes in two-body charmless hadronic B decays is to invoke SU(3) flavor symmetry [49, 50]. Under this assumption, the u, d, and s quarks transform as a triplet under the strong interaction, while the c, b, and t quarks are all flavor singlets. SU(3) symmetry results in relations among the various amplitudes contributing to these decays, but the absolute sizes of these amplitudes are not predicted; they must be estimated experimentally or by other means. Nevertheless, the simplicity of the SU(3) relations gives rise to a number of powerful constraints on the CKM parameters. SU(3) symmetry is broken by the large mass of the s quark compared to the u and d quarks, and corrections to the SU(3) predictions occur at the $m_{u,d}/m_s$ level. While SU(3) is not an exact symmetry of the strong interaction, deviations caused by symmetry breaking are generally eclipsed by the precision of current experimental measurements.

The quark-level process for charmless hadronic B decays, $\bar{b} \to \bar{q}_1 q_2 \bar{q}_3$, connects a singlet with three triplets under SU(3). Therefore, the transition amplitude transforms as $\bar{\mathbf{3}} \otimes \mathbf{3} \otimes \bar{\mathbf{3}} = \bar{\mathbf{3}} \oplus \bar{\mathbf{3}} \oplus \mathbf{6} \oplus \overline{\mathbf{15}}$. Adding the triplet light spectator quark in the B meson leads to the following representations for the meson-level process:

$$\begin{aligned} \bar{\mathbf{3}} \otimes \mathbf{3} &= \mathbf{1} \oplus \mathbf{8}_1 \\ \mathbf{6} \otimes \mathbf{3} &= \mathbf{8}_2 \oplus \mathbf{10} \\ \overline{\mathbf{15}} \otimes \mathbf{3} &= \mathbf{8}_3 \oplus \overline{\mathbf{10}} \oplus \mathbf{27}. \end{aligned} \tag{2.10}$$

For B decays to two mesons, the final state consists of two SU(3) octets, which form the multiplets

$$\mathbf{8} \otimes \mathbf{8} = \mathbf{27} \oplus \mathbf{10} \oplus \overline{\mathbf{10}} \oplus \mathbf{8}_S \oplus \mathbf{8}_A \oplus \mathbf{1}, \tag{2.11}$$

where the subscripts S and A denote multiplets symmetrized and antisymmetrized under exchange of the two final state mesons. When the daughter mesons are both pseudoscalars ($B \to PP$), they exist in an S-wave state because of angular momentum conservation. Bose symmetry requires that we only consider the symmetric product

$$(\mathbf{8} \otimes \mathbf{8})_S = \mathbf{27} \oplus \mathbf{8}_S \oplus \mathbf{1}. \tag{2.12}$$

Each final state multiplet in Equation 2.12 that matches a multiplet in Equation 2.10 corresponds to an independent transition amplitude. Therefore, $B \to PP$ decays are characterized by one singlet, three octet, and one **27**-plet amplitude. Separate amplitudes apply to strangeness-preserving ($\Delta I = \frac{1}{2}$ or $\frac{3}{2}$) and strangeness-changing ($\Delta I = 0$ or 1) transitions. For $B \to PV$ decays, there is no symmetry requirement because the two final state particles belong to different meson octets, so

all six $\mathbf{8} \otimes \mathbf{8}$ multiplets in Equation 2.11 are permitted, leading to ten independent amplitudes.

It is convenient to adopt an equivalent graphical representation of these SU(3) amplitudes using a set of quark topologies corresponding to the Feynman diagrams shown in Figure 2.1. These quark topologies are labeled T (external color-favored tree), C (internal color-suppressed tree), P (gluonic penguin), E (W-exchange), A (annihilation), and PA (penguin annihilation). The so-called "charming penguin" topologies [51, 52], which take the form $\bar{b} \to \bar{c}c\{\bar{s}, \bar{d}\}$, and which can rescatter into a charmless final state, are not included in this decomposition. We adopt a notation in which amplitudes for $|\Delta S| = 1$ transitions are primed, while those for $\Delta S = 0$ transitions are unprimed. For $B \to PP$ decays, the six diagrams form an overcomplete representation of the five independent amplitudes, and the two representations are related as follows:

$$\begin{aligned}
\mathbf{1} &= 2\sqrt{3}\left[PA + \frac{2}{3}(E+P) - \frac{1}{12}C + \frac{1}{4}T\right] \\
\mathbf{8}_1 &= -\sqrt{\frac{5}{3}}\left[P + \frac{3}{8}(T+A) - \frac{1}{8}(C+E)\right] \\
\mathbf{8}_2 &= \frac{\sqrt{5}}{4}(C + A - T - E) \\
\mathbf{8}_3 &= -\frac{1}{8\sqrt{3}}[T + C + 5(A+E)] \\
\mathbf{27} &= -\frac{1}{2\sqrt{3}}(T+C),
\end{aligned} \tag{2.13}$$

with analogous relations for the $|\Delta S| = 1$ transitions. Each independent amplitude carries its own strong phase. For flavor singlet mesons, there exists an additional penguin contribution, denoted S.

For $B \to PV$ decays, the spectator quark can be absorbed by either the vector or the pseudoscalar, so the number of diagrams doubles, as does the number of SU(3) multiplet amplitudes. A subscript P or V on the T, C, and P amplitudes indicates whether the spectator quark hadronizes into the pseudoscalar or vector meson, respectively. For E, A, and PA, the subscript stands for the meson that incorporates the outgoing quark q_2 in $\bar{b}q_1 \to q_2\bar{q}_3$.

Higher order contributions from electroweak penguins, pictured in Figures 2.2c and 2.2d, do not add SU(3) amplitudes because no new flavor topologies are introduced [53]. However, since the coupling of the photon or Z^0 depends on flavor of the pair-produced quarks, electroweak penguins violate isospin symmetry, and the strength of the $b \to q\bar{u}u$ transition relative to the $b \to q\bar{d}d$ and $b \to q\bar{s}s$ transitions is altered. The effects of the color-favored and color-suppressed electroweak penguin amplitudes (denoted P_{EW} and P_{EW}^C, respectively) are incorporated by modifying the existing amplitudes as follows:

$$\begin{aligned}
t &\equiv T + P_{EW}^C & c &\equiv C + P_{EW} \\
p &\equiv P - \tfrac{1}{3}P_{EW}^C & s &\equiv S - \tfrac{1}{3}P_{EW} \\
a &\equiv A & e + pa &\equiv E + PA.
\end{aligned} \tag{2.14}$$

In the tree diagrams, the b quark emits a virtual W^-, which subsequently decays into a $\bar{u}s$ or $\bar{u}d$ quark pair. These two quarks can hadronize either together in a final state meson (external emission), as in Figure 2.1a, or separately in different mesons (internal emission), as in Figure 2.1b. Internal emission is suppressed by the need to match the color content of the quarks from the W^- with that of the spectator and u quarks so that the resulting mesons are color singlets. Experimental measurements of the suppression factor place the value around 0.2. The discrepancy with the naive expectation of $\frac{1}{3}$ (given by the number of colors) is not fully understood but it is possibly related to the details of hadronization. For both tree topologies, the strangeness-changing transition is suppressed relative to the strangeness-preserving one by a factor $|V_{us}/V_{ud}| \approx \lambda = 0.22$.

The gluonic penguin (Figure 2.1c) is a loop process that results in an effective flavor-changing neutral current, which is forbidden at tree level in the Standard Model. Any up-type quark can appear in the loop, but the t quark component is believed to be by far the dominant contribution because of the GIM suppression of the u and c contributions (the cancellation is exact if $m_u = m_c$) and because m_t is much larger than m_u and m_c. Therefore, the CKM vertex factors associated with penguins are $V_{tb}V_{ts}^*$ and $V_{tb}V_{td}^*$ for $b \to s$ and $b \to d$ transitions, respectively. In order to conserve energy and momentum, a virtual gluon is emitted, and its vertices contribute a factor of α_s. Because the gluon is not a color singlet, the quarks it produces are hadronized internally rather than externally, but without color-suppression.

The remaining three diagrams in Figure 2.1, W-exchange (d), annihilation (e), and penguin annihilation (f), are expected to be much smaller than the tree and penguin diagrams. The W-exchange and annihilation diagrams are related by crossing symmetry. Both are helicity-suppressed by the $V - A$ structure of the weak interaction. The annihilation diagram is also suppressed by the overlap of the b and $\bar{u}$ wavefuctions, characterized by the B meson decay constant, f_B. The penguin annihilation diagram is both helicity- and OZI-suppressed, in addition to being f_B-suppressed. Most calculations ignore these three contributions, although the smallness of annihilation diagrams has been questioned in recent literature.

Electroweak penguins involve the emission of a virtual photon or Z^0 that produces a pair of quarks in a color singlet state that can be hadronized either internally (color-suppressed) or externally (color-allowed). Electroweak penguins carry the same CKM factors as gluonic penguins. However, the quarks couple more weakly to the photon and Z^0 than to the gluon. Since the coupling to the Z^0 is expected to dominate, electroweak penguin amplitudes are reduced relative to gluonic penguins by a factor of approximately $\alpha_2/\alpha_s \approx \frac{1}{30}/0.2 \approx \frac{1}{6}$, where both couplings are evaluated at m_b.

Table 2.3 organizes the SU(3) amplitudes by their size relative to the dominant amplitude in $\Delta S = 0$ and $|\Delta S| = 1$ transitions separately. In this context, the parameter $\lambda = 0.22$ does not necessarily refer to the CKM parameter. For instance, the color-suppression factor of C relative to T is roughly λ. Also, $|P_{EW}/P| \approx \lambda$ because of the ratio of coupling constants. Finally, the factor

$f_B/m_B \approx 0.05 \approx \lambda^2$ characterizes $|E/T|$, $|A/T|$, and $|PA/P|$. The order-of-magnitude estimates that produce this heirarchy do not include dynamical considerations relating to hadronization or to the helicity configuration of the final state. Fully incorporating these effects can alter the picture presented above and represents the bulk of the current theoretical activity in calculating these amplitudes directly.

	$\Delta S = 0$		$\lvert\Delta S\rvert = 1$	
$\mathcal{O}(1)$	T	t	P'	p'
$\mathcal{O}(\lambda)$	C, P	c, p	T', P'_{EW}	t', c', s'
$\mathcal{O}(\lambda^2)$	E, A, P_{EW}	e, a, s	C', PA', $P^{C'}_{EW}$	pa'
$\mathcal{O}(\lambda^3)$	PA, P^C_{EW}	pa	E', A', PA'_{EW}	e', a'

Table 2.3: Heirarchy of SU(3) amplitudes.

In $|\Delta S| = 1$ transitions, the vertex factors of the tree diagrams are $\mathcal{O}(\lambda^4)$ while those of the $b \to s$ penguin are $\mathcal{O}(\lambda^2 \alpha_s) \sim \mathcal{O}(\lambda^3)$. Therefore, strangeness-changing decays should be dominated by the penguin amplitude. This qualitative observation is borne out by the measured $B \to K\pi$ branching fractions, which far exceed expectations from the tree diagrams alone.

The situation is reversed for $\Delta S = 0$ decays. The tree and penguin diagrams are of the same order in CKM factors, but the penguin is further suppressed by α_s. Therefore, tree contributions dominate the strangeness-preserving decays. However, the $b \to d$ penguin cannot be ignored, as demonstrated in the above discussion of $B \to \pi^+\pi^-$.

SU(3) symmetry is broken by the mass difference between the s and d quarks [54]. In T' diagrams, the strange meson in the final state is coupled directly to the weak current. Therefore, the magnitude of SU(3)-breaking is characterized by the ratio of decay constants $(f_K - f_\pi)/f_\pi \approx 0.2$. SU(3)-breaking effects in P' and C' diagrams can be incorporated as form factor corrections, while those in E', A', and PA' diagrams are governed by the difference in the pair production amplitudes for $s\bar{s}$ and $u\bar{u}$ or $d\bar{d}$. The size of the corrections in non-T' diagrams is not well-understood, but it is usually assumed that they are of the same order as in T' diagrams. The SU(3)-breaking diagrams may also have different strong phases than their unbroken counterparts. For instance, T'/T is given by f_K/f_π and an unknown phase. Such unpredictable phase differences can affect both branching fractions and CP asymmetries, thereby potentially clouding the extraction of the CKM parameters within the SU(3) framework.

A promising application of the SU(3) decomposition is to constrain γ with $|\Delta S| = 1$ decays. There exist various methods of deriving information on γ, most of which involving taking ratios of branching fractions or constructing amplitude triangles or quadrangles, the sides of which can be determined from branching fraction measurements [55, 56, 57, 58, 59]. Both the $K\pi$ (PP)

modes and the $K^*(892)\pi$ or $\rho(770)K$ (PV) modes can be used, although, in general, the PP modes provide greater power because of the smaller number of independent amplitudes. With twice the number of amplitudes, the PV analyses introduce more unknown parameters, and the system is often underdetermined without making simplifying assumptions. Therefore, methods using $B \to PV$ decays often have greater statistical and theoretical uncertainties than methods using $B \to PP$ decays. Nevertheless, it is important to compare γ determined from $B \to K\pi$ with that from $B \to K^*(892)\pi$ and $B \to \rho(770)K$. In Chapter 8, we present one such constraint on γ using various $B \to PV$ branching fractions.

2.4 Effective Low-Energy Hamiltonian

The quark-level Feynman diagrams in Figures 2.1 and 2.2 serve as useful tools for visualizing and classifying the various flavor topologies that give rise to rare B decays. However, these diagrams do not depict the meson-level QCD interactions involved in hadronization of the quark pairs and possible final state interactions (FSI). Absolute rate predictions for these processes including strong effects are calculated not by evaluating these Feynman diagrams directly, but rather by means of an operator product expansion [60].

Charmless hadronic B decays contain three distinct energy scales: the weak scale, $m_W \sim 80$ GeV; the scale of energy released in the decay, $m_b \sim 5$ GeV; and the scale at which the strong interaction becomes non-perturbative, $\Lambda_{QCD} \sim 200$ MeV. Processes with characteristic energies below the masses of the $W^{\pm}$, Z^0, and t can be described by an effective Hamiltonian obtained by integrating out these heavy degrees of freedom. For two-body hadronic B decays, performing this integration results in point-like interactions, as shown in Figure 2.7, and the Hamiltonian becomes a product of local four-quark operators. To account for the $W^{\pm}$, Z^0, and t, which no longer appear explicitly in the theory, their propagators are replaced by effective coupling constants (Wilson coefficients), and the running masses of the remaining particles in the theory are modified. Thus, the physics at the weak scale is separated from the physics at m_b and Λ_{QCD}. The effective theory reproduces the full theory up to corrections of order m_b/m_W.

In general, hadronic matrix elements of this effective Hamiltonian are impractical to compute. However, the Hamiltonian can be reorganized with the operator product expansion. A time-ordered product of local operators can be expressed as an expansion in local operators that depend on position x:

$$T(O_a(x)O_b(0)) = \sum_k c_{abk}(x)O_k(0). \tag{2.15}$$

The momentum-space version of the operator product expansion is given by the Fourier transform

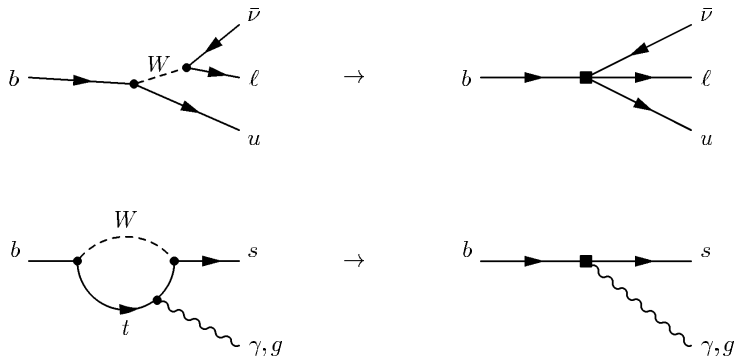

Figure 2.7: Integrating out the heavy degrees of freedom.

of Equation 2.15:

$$\int e^{iqx} T(O_a(x) O_b(0)) d^4x = \sum_k c_{abk}(q) O_k(0). \tag{2.16}$$

Matrix elements of the left-hand sides of Equations 2.15 and 2.16 are completely equivalent to those of the right-hand sides, and the Wilson coefficients c_{abk} are independent of the matrix elements, provided the momenta of the external states are much smaller than $1/x$. In this kinematic region, the QCD coupling constant is small because of asymptotic freedom, and the c_{abk} can be computed perturbatively.

The effective Hamiltonian for $|\Delta S| = 1$ charmless hadronic B decays consists of an expansion in ten local four-fermion operators, denoted $O_1, \ldots, O_{10}$:

$$\mathcal{H}_{\text{eff}} = \frac{G_F}{\sqrt{2}} \left[\sum_{q=u,c} V_{qb} V_{qs}^* (c_1 O_1^q + c_2 O_2^q) - V_{tb} V_{ts}^* \sum_{i=3}^{10} c_i O_i \right] + \text{Hermitian conjugate.} \tag{2.17}$$

The operators O_i consist of two currents of the form $J_1^\mu J_{2\mu} = (\bar{q}_1 q_2)_{V\pm A} (\bar{q}_3 q_4)_{V\pm A} \equiv [\bar{q}_1 \gamma_\mu (1 \pm \gamma_5) q_2][\bar{q}_3 \gamma^\mu (1 \pm \gamma_5) q_4]$:

$$\begin{array}{ll}
O_1^u = (\bar{b}_i u_i)_{V-A} (\bar{u}_j s_j)_{V-A} & O_1^c = (\bar{b}_i c_i)_{V-A} (\bar{c}_j s_j)_{V-A} \\
O_2^u = (\bar{b}_i u_j)_{V-A} (\bar{u}_j s_i)_{V-A} & O_2^c = (\bar{b}_i c_j)_{V-A} (\bar{c}_j s_i)_{V-A} \\
O_3 = (\bar{b}_i s_i)_{V-A} \sum_q (\bar{q}_j q_j)_{V-A} & O_4 = (\bar{b}_i s_j)_{V-A} \sum_q (\bar{q}_j q_i)_{V-A} \\
O_5 = (\bar{b}_i s_i)_{V-A} \sum_q (\bar{q}_j q_j)_{V+A} & O_6 = (\bar{b}_i s_j)_{V-A} \sum_q (\bar{q}_j q_i)_{V+A} \\
O_7 = \frac{3}{2} (\bar{b}_i s_i)_{V-A} \sum_q e_q (\bar{q}_j q_j)_{V+A} & O_8 = \frac{3}{2} (\bar{b}_i s_j)_{V-A} \sum_q e_q (\bar{q}_j q_i)_{V+A} \\
O_9 = \frac{3}{2} (\bar{b}_i s_i)_{V-A} \sum_q e_q (\bar{q}_j q_j)_{V-A} & O_{10} = \frac{3}{2} (\bar{b}_i s_j)_{V-A} \sum_q e_q (\bar{q}_j q_i)_{V-A},
\end{array} \tag{2.18}$$

where the subscripts i and j on the quark fields are SU(3) color indices, the sums are over quark

flavors $q = u, d, s, c$, and e_q is the electric charge of the quark q. The first two operators are tree operators, with O_1 corresponding to the dominant W-emission contribution ($c_1 = 1 + \mathcal{O}(\alpha_s)$) and O_2 representing the QCD correction ($c_2 = 0 + \mathcal{O}(\alpha_s)$). The operators $O_3, \ldots, 0_6$ arise from the gluonic penguin diagrams, which contribute at order α_s, and $O_7, \ldots, O_{10}$ are the electroweak penguins. One obtains the $\Delta S = 0$ Hamiltonian by replacing the s quark fields not appearing in the sums with d quark fields.

In practice, the Wilson coefficients $c_i(\mu)$ are calculated at the energy scale $\mu \sim m_W$, and the couplings of the effective theory are matched to those of the full theory. The couplings and coefficients are then evolved to $\mu \sim m_b$ using renormalization group equations. The renormalization procedure guarantees that that matrix elements of the Hamiltonian, which correspond to observable quantities, are independent of the renormalization scale μ. The μ-dependence of the Wilson coefficients is compensated by that of the operators order by order in α_s.

However, truncation of the perturbative series for the $c_i(\mu)$ at the weak scale induces a μ-dependence that becomes more severe the farther the Hamiltonian is evolved. This unknown dependence on the renormalization scale, as well as on the appropriate value of m_b itself, usually dominates the theoretical uncertainty. One method of addressing this uncertainty is to extract the scale-dependence of the operators and absorb this dependence into a redefinition of the Wilson coefficients so that the resultant effective coefficients c_i^{eff} are scale-independent. However, extraction of the scale-dependence of the O_i is plagued by infrared divergences, which are regulated by introducing an infrared cutoff and a gauge parameter. Therefore, the scale-dependence of the c_i is replaced by the gauge-dependence of the c_i^{eff}.

Determination of these coefficients varies according to the renormalization scheme and the value of m_b used in the calculations. Typical values for the coefficients at next-to-leading order in α_s, taken from Reference [65], are

$$\begin{aligned}
c_1^{\text{eff}} &= 1.149 & c_2^{\text{eff}} &= -0.325 \\
c_3^{\text{eff}} &= 0.0211 + 0.0045i & c_4^{\text{eff}} &= -0.0450 - 0.0136i \\
c_5^{\text{eff}} &= 0.0134 + 0.0045i & c_6^{\text{eff}} &= -0.0560 - 0.0136i \\
c_7^{\text{eff}} &= -(0.0276 + 0.0369i)\alpha & c_8^{\text{eff}} &= 0.054\alpha \\
c_9^{\text{eff}} &= -(1.318 + 0.0369i)\alpha & c_{10}^{\text{eff}} &= 0.263\alpha.
\end{aligned} \tag{2.19}$$

Since the strong coupling constant does not depend on quark flavor, these c_i^{eff} hold for all B decays. Contributions from O_7 and O_8 are usually ignored because of the smallness of their corresponding Wilson coefficients. Were it not for the CKM factors, charmless hadronic B decays would be overwhelmingly dominated by the tree operators. The ratio of c_2^{eff} to c_1^{eff} gives an estimate of the color-suppression of internal tree diagrams relative to external tree diagrams.

2.4.1 Factorization

The operator product expansion filters the short-distance perturbative physics at the weak scale into the Wilson coefficients that describe the quark-level process. The long-distance non-perturbative physics, characterized by the scale Λ_{QCD}, that governs the meson-level dynamics of hadronization is obtained by calculating the matrix elements of the local four-fermion operators: $\langle M_1 M_2|O_i|B\rangle$, where $|B\rangle$ represents the B meson and $|M_1 M_2\rangle$ the two-body final state of the decay.

For inclusive final states, the hadronic matrix element can be approximated by the matrix element for free quarks, $\langle\{d,s\}|O_i|b\rangle$, which is easily computed. However, for exclusive final states, $\langle M_1 M_2|O_i|B\rangle$ is difficult to compute from first principles. Because of quark confinement, these matrix elements cannot be treated in perturbation theory. Use of the full theory is made by numerical techniques like lattice QCD [61], which, so far, have successfully been applied only to semileptonic decays (where only one current participates in the strong interaction) or under the quenched approximation (neglect of quark pair production and annihilation in the vacuum). However, rapid progress is being made in performing unquenched calculations and in extending the technique to more complicated hadronic systems.

In the meantime, analytical calculations of the hadronic matrix elements are performed usually relying on some form of the factorization *ansatz* [62, 63, 64, 65]. This approximation is based on the postulate that the matrix elements can be expressed as a product of hadronic currents:

$$\langle M_1 M_2|O_i|B\rangle = \langle M_1 M_2|J_1^\mu J_{2\mu}|B\rangle \approx \langle M_1|J_1^\mu|B\rangle\langle M_2|J_{2\mu}|0\rangle. \tag{2.20}$$

The factorized currents are then parametrized in terms of decay constants and form factors, which depend on the quarks' four-momenta. These phenomenological inputs can be taken from lattice calculations and QCD sum rules [66, 67, 68], or they can be derived from data under various model assumptions.

The application of factorization is justified by the color transparency [69] of the outgoing mesons; energetic quarks in a color-singlet state decouple from soft gluons. Mesons can be viewed as small color dipoles that are opaque to high energy gluons, since these short-wavelength probes can resolve the two halves of the dipole. However, these dipoles are transparent to long-wavelength, low energy gluons, and they act as apparent color singlets. Another intuitive argument is that after hadronization, the quarks are dressed as mesons that move away from each other so quickly ($E_M \sim m_B/2$) that they are not given a chance to interact. Therefore, long-distance non-perturbative final state interactions can be neglected. Short-distance QCD effects, which are crucial in predicting CP asymmetries, can be included perturbatively.

The combinations of effective Wilson coefficients that appear in the decay amplitudes are given

by the quantities a_i, defined as follows:

$$a_i \equiv \begin{cases} c_i^{\rm eff} + \frac{1}{N_c} c_{i+1}^{\rm eff}, \ i = 1,3,5,7,9 \\ c_i^{\rm eff} + \frac{1}{N_c} c_{i-1}^{\rm eff}, \ i = 2,4,6,8,10 \end{cases} , \tag{2.21}$$

where N_c is the number of colors. Deviations from factorization are incorporated by converting N_c into a phenomenological parameter, $N_c^{\rm eff}$. This substitution is made only when N_c appears in the a_i. This approach accounts for the finite energies of the B decay products and for the fact that the matrix elements of the octet-octet currents are discarded since they, unlike the singlet-singlet matrix elements, are not directly measured experimentally. Also, factorization is expected to work best with decays dominated by external W-emission. The use of factorization for color-suppressed internal W-emission has been shown to be invalid in $B \to D\pi$ and $B \to J/\psi K^*(892)$ decays [64, 70, 71], and the same is expected to be true for penguin amplitudes. It is unclear whether a single parameter $N_c^{\rm eff}$ is sufficient to describe non-factorizable effects in all ten operators. In principle, $N_c^{\rm eff}$ can be extracted from experimental data. However, the fact that $N_c^{\rm eff}$ is process-dependent limits the predictive power of the factorization assumption. The formalism sketched above has come to be known as "naive" factorization (NF).

Recently, there have emerged two new approaches for incorporating hard-scattering QCD effects into NF by factorizing the strong physics at the scales m_b and Λ_{QCD}. As with the operator product expansion, these methods are exact up to corrections suppressed by the inverse of the heavy scale, $\mathcal{O}(\Lambda_{QCD}/m_b)$. The QCD factorization approach (QCDF) [72, 27] applies methods from the heavy quark expansion and NF to separate the perturbative radiative corrections, represented by hard-scattering kernels, $T^{I,II}$, from the non-perturbative portion, parametrized by form factors, $F^{B\to M}$, and by light-cone meson distribution amplitudes (wavefunctions), Φ_M. Schematically, the matrix element for a B decay to mesons M_1 and M_2 assumes the following form:

$$\langle M_1 M_2 | O_i | B \rangle = F^{B\to M_1}(0) \cdot T_i^I(\mu) \otimes \Phi_{M_2} + \Phi_B \otimes T_i^{II}(\mu) \otimes \Phi_{M_1} \otimes \Phi_{M_2} \tag{2.22}$$

$$= \langle M_1 | J_1^\mu | B \rangle \langle M_2 | J_{2\mu} | 0 \rangle \cdot \left[1 + \mathcal{O}(\alpha_s) + \mathcal{O}\left(\frac{\Lambda_{QCD}}{m_b} \right) \right], \tag{2.23}$$

where M_1 is the meson that absorbs the spectator quark. The T_i^I are running coupling constants that include hard gluon exchanges between mesons not involving the spectator quark. At lowest order, the T_i^I term in Equation 2.22 reproduces the NF result. The T_i^{II} represent hard gluon interactions with the spectator quark and only appear at order α_s. The $\mathcal{O}(\alpha_s)$ terms are the non-factorizable radiative corrections to NF, and they can be computed systematically. The theoretical uncertainty in QCDF stems from the power corrections ($\mathcal{O}(\Lambda_{QCD}/m_b)$ terms) and the neglected annihilation contributions. While it is not yet fully understood how to estimate the size of the power corrections, some of the tools being considered are QCD sum rules [73] and soft-colinear

effective theory [74, 75, 76, 77]. It has been suggested that charming penguin operators [78] or the intrinsic charm content of the B meson [79] may also represent non-factorizable corrections of similar size to the power corrections.

The second technique for calculating interactions between final state mesons is known as the perturbative hard-scattering (PQCD) approach [80, 81, 82]. In PQCD, the form factors, $F^{B\to M}$, are assumed to be perturbatively calculable. Sudakov effects are invoked to suppress the kinematic region where the spectator quark is soft. Therefore, all exchanged gluons are hard, and the form factors formally do not contribute at leading order, but only at $\mathcal{O}(\alpha_s)$. In other words, PQCD differs from QCDF in that all the perturbative corrections are treated in the presence of the spectator quark, *i.e.*, all the scattering kernels are of the type T^{II}. One result of this procedure is that annihilation topologies and other non-factorizable corrections are included on the same footing as the factorizable terms.

Under NF, there exist very small CP asymmetries because the form factors and decay constants are purely real, and the effective Wilson coefficients are almost purely real. Therefore, sizeable CP asymmetries only arise from non-factorizable effects. QCDF predicts that, in the heavy quark limit, strong phases enter only at $\mathcal{O}(\alpha_s)$, so CP asymmetries in charmless hadronic B decays should be small ($\sim 5\%$). In contrast, the annihilation contributions in PQCD generate significant strong phases, and the predicted CP asymmetries can be as large as 15%–30%. Furthermore, the CP asymmetries in the two approaches tend to have opposite signs.

Both QCDF and PQCD have achieved some degree of success in explaining the branching fractions in $B \to PP$ decays (see Section 2.5), although the size of the theoretical and experimental uncertainties precludes any definitive statement about the validity of either approach. In the future, precise measurements of CP asymmetries in charmless hadronic B decays should be able to distinguish between these two methods.

2.5 Theoretical Predictions

The research described in this thesis focuses on rare charmless three-body B decays of the type $B \to K\pi\pi$ and $B \to \bar{K}K\pi$. Among the contributions to these three-pseudoscalar final states are quasi-two-body decays with intermediate vector resonances, $B \to K^*(892)\pi$ and $B \to \rho(770)K$. The primary goal of our analysis is to search for these $B \to PV$ decays, but non-resonant production of the three-body final states must also be understood in order to extract the $B \to PV$ branching fractions accurately. There may also be contributions from high-mass scalar, vector, and tensor resonances with sizeable branching fractions to $\pi\pi$ or $K\pi$, such as $f_0(980)$, $f_2(1270)$, $f_4(2050)$, $K^*(1410)$, $K_0^*(1430)$, $K_2^*(1430)$, $K^*(1680)$, $K_3^*(1780)$, and $K_4^*(2045)$. Because of the large intrinsic width of these resonances (> 100 MeV), decays through these intermediate states are nearly indistinguishable

from non-resonant decays except that the amplitude and phase across the Dalitz plot is not strictly constant.

The quark topologies contributing to these rare B decays are perhaps most easily viewed in the SU(3) framework. Tables 2.4 and 2.5 give the amplitude decomposition for a selection of $B \to PP$ and $B \to PV$ decays. Contributions of order λ^2 and smaller have been omitted unless they are dominant. Modes that can provide information on the UT angle γ are $|\Delta S| = 1$ transitions with interfering tree and penguin amplitudes. Of the $B \to PV$ processes that have been observed, $B^0 \to K^*(892)^+\pi^-$ stands out as being particularly sensitive. All that is required to determine γ is knowledge of the ratio of tree to penguin amplitudes, $|t'_P/p'_P|$, as well as their relative strong phase. One method of estimating this amplitude ratio is given in Chapter 8.

Mode	Amplitudes	Observed
	$\Delta S = 0$	
$\pi^+\pi^-$	$-(t+p)$	•
$\pi^+\pi^0$	$-\frac{1}{\sqrt{2}}(t+c)$	•
$\pi^0\pi^0$	$\frac{1}{\sqrt{2}}(p-c)$	
K^+K^-	$-(e+pa)$	
$K^+\bar{K}^0$	p	
$K^0\bar{K}^0$	$p+pa$	
	$\lvert\Delta S\rvert = 1$	
$K^+\pi^-$	$-(p'+t')$	•
$K^0\pi^0$	$\frac{1}{\sqrt{2}}(p'-c')$	•
$K^+\pi^0$	$-\frac{1}{\sqrt{2}}(p'+t'+c')$	•
$K^0\pi^+$	p'	•

Table 2.4: SU(3) amplitude decomposition to $\mathcal{O}(\lambda)$ for $\{B^0, B^+\} \to PP$ modes.

Before discussing the experimental details of the searches, we give in Tables 2.6 and 2.7 some branching fraction predictions, for the decays under consideration in the context of the factorization frameworks introduced above. In almost all cases, the preferred branching fractions are 10^{-5} or smaller. At these levels, the current generation of experiments has begun to observe some $B \to PV$ decays, and hopefully, many more will soon follow. Because of the high uncertainty endemic to calculations of these processes, a full picture of charmless hadronic B decays with the ability to determine γ and to test the various theoretical models will require the precise measurement of an ensemble of both $B \to PP$ and $B \to PV$ modes.

Non-resonant three-body decays have received much less theoretical attention than $B \to PV$ decays because they suffer from greater hadronic uncertainties. The approach usually taken is to combine heavy quark effective theory with chiral perturbation theory [97, 98, 99]. However,

Mode	Amplitudes	Observed
	$\Delta S = 0$	
$\rho(770)^+\pi^-$	$-(t_P + p_P)$	•
$\rho(770)^-\pi^+$	$-(t_V + p_V)$	•
$\rho(770)^0\pi^0$	$-\frac{1}{2}(c_P + c_V - p_P - p_V)$	
$\rho(770)^+\pi^0$	$-\frac{1}{\sqrt{2}}(t_P + c_V + p_P - p_V)$	
$\rho(770)^0\pi^+$	$-\frac{1}{\sqrt{2}}(t_V + c_P + p_V - p_P)$	•
$K^*(892)^+K^-$	$-(e_V + pa_P + pa_V)$	
$K^*(892)^-K^+$	$-(e_P + pa_P + pa_V)$	
$K^*(892)^0\bar{K}^0$	p_V	
$\bar{K}^*(892)^0K^0$	p_P	
$K^*(892)^+\bar{K}^0$	p_V	
$\bar{K}^*(892)^0K^+$	p_P	
$\phi(1020)\pi^0$	$\frac{1}{\sqrt{2}}s_P$	
$\phi(1020)\pi^+$	s_P	
	$\lvert\Delta S\rvert = 1$	
$\rho(770)^-K^+$	$-(t'_V + p'_V)$	
$\rho(770)^0K^0$	$\frac{1}{\sqrt{2}}(p'_V - c'_P)$	
$\rho(770)^+K^0$	p'_V	
$\rho(770)^0K^+$	$-\frac{1}{\sqrt{2}}(t'_V + c'_P + p'_V)$	
$K^*(892)^+\pi^-$	$-(p'_P + t'_P)$	• (this thesis)
$K^*(892)^0\pi^0$	$\frac{1}{\sqrt{2}}(p'_P - c'_V)$	
$K^*(892)^+\pi^0$	$-\frac{1}{\sqrt{2}}(t'_P + c'_V + p'_P)$	
$K^*(892)^0\pi^+$	p'_P	•
$\phi(1020)K^0$	$p'_P + s'_P$	•
$\phi(1020)K^+$	$p'_P + s'_P$	•

Table 2.5: SU(3) amplitude decomposition to $\mathcal{O}(\lambda)$ for $\{B^0, B^+\} \to PV$ modes.

the chiral symmetry breaking scale is $\Lambda_\chi \sim 830$ MeV, so chiral perturbation theory is applicable in only a portion of the kinematically allowed region. Prediction of the total non-resonant rate using this approach requires some *ad hoc* limits on the use of chiral perturbation theory, and one estimate [100] places the branching fraction for $B \to K^0\pi^+\pi^-$ at 5×10^{-6}. Another possibility explored recently is to extend PQCD factorization to three-body non-resonant decays by introducing two-meson distribution amplitudes [101].

CP asymmetries in rare B decays constitute another set of observables sensitive to the differences between theoretical models (as well as to γ). The currently measured asymmetries for $B \to PP$ modes are shown in Table 2.8. A reduction of the uncertainties on these measurements by about an order of magnitude would provide for an interesting comparision with the theoretical predictions.

Mode	NF	QCDF	PQCD	Experiment
		$\Delta S = 0$		
$\pi^+\pi^-$	$[9, 15]$	4.8	7.0	4.7 ± 0.5
$\pi^+\pi^0$	$[3, 8]$	5.4	3.7	5.8 ± 1.0
$\pi^0\pi^0$	$[0.1, 0.8]$	1.0	0.3	2.0 ± 0.7
K^+K^-		0.05	0.06	< 1.9
$K^+\bar{K}^0$	$[0.8, 1.5]$		1.4	< 2.4
$K^0\bar{K}^0$	$[0.8, 1.4]$		1.4	< 17
		$\lvert\Delta S\rvert = 1$		
$K^+\pi^-$	$[14, 21]$	19.0	15.5	18.5 ± 1.0
$K^0\pi^0$	$[5, 9]$	8.2	8.6	10.1 ± 1.5
$K^+\pi^0$	$[9, 15]$	11.4	9.1	12.6 ± 1.3
$K^0\pi^+$	$[14, 26]$	20.1	16.4	17.9 ± 1.7

Table 2.6: Branching fraction predictions [64, 86, 87] for $\{B^0, B^+\} \to PP$ modes, in units of 10^{-6}. Experimental measurements [5, 89, 90, 91, 92, 93, 94, 95, 96] are CP-averaged.

In the $B \to PV$ modes, CP asymmetries are beginning to be measured, and the analysis in this thesis contributes to this effort. We list the available measurements in Table 2.9. This table also compares the theoretically expected ranges for CP asymmetries in these modes using the QCDF and PQCD approaches. In particular, $B \to K^*(892)\pi$ decays may prove to be a fertile testing ground for these two models. QCDF and PQCD predict the branching fractions for $B \to K^*(892)\pi$ to be similar, but their CP asymmetries are quite different. Measuring these asymmetries requires much greater statistical power than measuring CP-averaged branching fractions, so it may be some time before a comprehensive, detailed understanding of charmless hadronic B decays is reached.

SU(3) symmetry also leads to a number of relations among CP-violating rate differences among B^0, B^+, and B_s mesons [102, 103]. Below, we give the relations involving $B \to PP$ decays to $\pi\pi$, $K\pi$, and $\bar{K}K$ final states and their $B \to PV$ analogues. We define $\Delta(\bar{B} \to M_1M_2) \equiv \Gamma(\bar{B} \to M_1M_2) - \Gamma(B \to \bar{M}_1\bar{M}_2)$. SU(3)-breaking effects are estimated by ratios of the decay constants and form factors used in the factorization approximation. We have also assumed that annihilation topologies are negilgible. The smallness of these contributions can be assessed with the branching fractions for $B^+ \to \bar{K}^0K^+$, $B^0 \to K^*(892)^\pm K^\mp$, and $B_s \to \pi^+\pi^-$, $\pi^0\pi^0$, $\rho(770)^\pm\pi^\mp$, $\rho(770)^0\pi^0$, or $\omega\pi^0$.

$$\begin{aligned} \Delta(B^- \to K^-K^0) &= \Delta(\bar{B}^0 \to K^0\bar{K}^0) \\ &= -\left[\frac{F_0^{B\to\pi}(m_K^2)}{F_0^{B\to K}(m_K^2)}\right]^2 \Delta(B^- \to \bar{K}^0\pi^-) \end{aligned} \tag{2.24}$$

	Mode	SU(3)	NF	QCDF	PQCD	Experiment
			$\Delta S = 0$			
	$\rho(770)^+\pi^-$	$[6, 30]$	$[21, 34]$	$[21, 23]$		25.4 ± 4.2
	$\rho(770)^-\pi^+$	$[15, 32]$	$[6, 9]$	10		
	$\rho(770)^0\pi^0$		$[0.07, 1.7]$	0.1		< 5.5
	$\rho(770)^+\pi^0$	$[4, 15]$	$[11, 16]$	$[12, 14]$		< 43
	$\rho(770)^0\pi^+$	$[8, 17]$	$[1, 7]$	8.9		10 ± 4
•	$K^*(892)^\pm K^\mp$			0.02		< 12.5
	$K^*(892)^0\bar{K}^0$		$[4, 20] \times 10^{-4}$	$[0.03, 0.06]$		
	$\bar{K}^*(892)^0 K^0$		$[0.3, 0.6]$	$[0.2, 0.3]$		
•	$\bar{K}^*(892)^0 K^+$		$[0.3, 0.7]$	$[0.2, 0.3]$		< 5.0
	$K^*(892)^+\bar{K}^0$		$[5, 20] \times 10^{-4}$	$[0.04, 0.06]$		
	$\phi(1020)\pi^0$		$[0.002, 0.2]$	$[6, 8] \times 10^{-4}$		< 5
	$\phi(1020)\pi^+$		$[0.005, 0.4]$	$[12, 17] \times 10^{-4}$		< 1.4
			$\lvert\Delta S\rvert = 1$			
•	$K^*(892)^+\pi^-$	$[7, 17]$	$[6, 8]$	11	9.1	$16.5^{+4.1}_{-3.9}$
•	$K^*(892)^0\pi^0$	$[1, 2]$	$[2, 4]$	$[0.7, 0.9]$	2.8	< 3.3
•	$K^*(892)^+\pi^0$	$[4, 7]$	$[4, 7]$	$[2, 4]$	3.2	< 26
•	$K^*(892)^0\pi^+$	$[5, 12]$	$[6, 12]$	10	10.0	$12.6^{+2.4}_{-2.5}$
	$\rho(770)^-K^+$	$[6, 10]$	$[0.4, 0.6]$	12		< 32
•	$\rho(770)^0K^0$	$[6, 14]$	$[0.5, 0.7]$	1.2		< 21
•	$\rho(770)^+K^0$	$[5, 12]$	$[0.01, 0.03]$	$[0.6, 0.8]$		< 52
	$\rho(770)^0K^+$	$[1, 2]$	$[0.5, 0.7]$	$[0.4, 0.6]$		< 12
	$\phi(1020)K^0$		$[0.4, 18]$	8.4	9.6	8.2 ± 1.1
	$\phi(1020)K^+$		$[0.5, 18]$	8.9	10.2	8.7 ± 1.6

Table 2.7: Branching fraction predictions [83, 84, 64, 85, 86, 87, 88] for $\{B^0, B^+\} \to PV$ modes, in units of 10^{-6}. Experimental measurements from Reference [5] are CP-averaged and are supplemented by contributions from this thesis (marked by bullets).

$$\Delta(\bar{B}^0 \to \pi^+\pi^-) = -\left[\frac{f_\pi F_0^{B\to\pi}(m_\pi^2)}{f_K F_0^{B\to\pi}(m_K^2)}\right]^2 \Delta(\bar{B}^0 \to K^-\pi^+) \tag{2.25}$$

$$\Delta(\bar{B}^0 \to \bar{K}^0\pi^0) = \left[\frac{f_K F_0^{B\to\pi}(m_K^2)}{f_\pi F_0^{B\to\pi}(m_\pi^2)}\right]^2 \Delta(\bar{B}^0 \to \pi^0\pi^0) \tag{2.26}$$

$$\begin{aligned}\Delta(B^- \to K^*(892)^0K^-) &= \Delta(\bar{B}^0 \to K^*(892)^0\bar{K}^0) \\ &= -\left[\frac{F_1^{B\to K}(m_{K^*}^2)}{F_1^{B\to\pi}(m_{K^*}^2)}\right]^2 \Delta(B^- \to \bar{K}^*(892)^0\pi^-)\end{aligned} \tag{2.27}$$

$$\begin{aligned}\Delta(B^- \to K^*(892)^-K^0) &= \Delta(\bar{B}^0 \to \bar{K}^*(892)^0K^0) \\ &= -\left[\frac{A_0^{B\to K^*}(m_K^2)}{A_0^{B\to\rho}(m_K^2)}\right]^2 \Delta(B^- \to \rho(770)^-\bar{K}^0)\end{aligned} \tag{2.28}$$

$$\Delta(\bar{B}^0 \to \rho(770)^+ K^-) = -\left[\frac{f_K A_0^{B\to\rho}(m_K^2)}{f_\pi A_0^{B\to\rho}(m_\pi^2)}\right]^2 \Delta(\bar{B}^0 \to \rho(770)^+ \pi^-) \quad (2.29)$$

$$\Delta(\bar{B}^0 \to K^*(892)^- \pi^+) = -\left[\frac{f_{K^*} F_1^{B\to\pi}(m_{K^*}^2)}{f_\rho F_1^{B\to\pi}(m_\rho^2)}\right]^2 \Delta(\bar{B}^0 \to \rho(770)^- \pi^+) \quad (2.30)$$

The ratios of form factors, as calculated from lattice QCD or light cone sum rules, are all consistent with unity [64] with possible deviations at the 20% level. The decay constants are extracted from experimental measurements and are known to 1%–3%. The relevant ratios are given by $f_\pi/f_K \approx 0.82$ and $f_\rho/f_{K^*} \approx 0.98$. We also consider the sum of Equations 2.29 and 2.30:

$$\begin{aligned}\Delta(\bar{B}^0 \to \rho(770)^+ \pi^-) + \Delta(\bar{B}^0 \to \rho(770)^- \pi^+) = -\Bigg\{ &\left[\frac{f_\pi A_0^{B\to\rho}(m_\pi^2)}{f_K A_0^{B\to\rho}(m_K^2)}\right]^2 \Delta(\bar{B}^0 \to \rho(770)^+ K^-) \\ &+ \left[\frac{f_\rho F_1^{B\to\pi}(m_\rho^2)}{f_{K^*} F_1^{B\to\pi}(m_{K^*}^2)}\right]^2 \Delta(\bar{B}^0 \to K^*(892)^- \pi^+) \Bigg\}. \quad (2.31)\end{aligned}$$

An evaluation of Equations 2.29–2.31 using currently available measurements is presented in Chapter 8.

The current availability of a variety of calculational techniques may be important in the presence of New Physics. These techniques are not all based on the same assumptions, and their uncertainties have separate origins, so it is conceivable that non-Standard-Model contributions would modify each of their predictions differently. Thus, the presence of New Physics might be discerned with rare B decays in several ways. First, the various experimental measurements may not yield an internally consistent value of γ within a single calculational framework. Second, the various frameworks may agree on a value of γ that differs from that of the standard CKM fit of Figure 2.4. Finally, different frameworks may arrive at different values of γ. In this last case, if we assume these methods are all valid, then investigating the successes and failures of each model might shed some light on the nature of possible New Physics.

Mode	QCDF	PQCD	Experiment
	$\Delta S = 0$		
$\pi^+\pi^-$	$[16, 30]$	$[-18, 6]$	42 ± 22
$\pi^+\pi^0$	0	0	13 ± 21
	$\lvert\Delta S\rvert = 1$		
$K^+\pi^-$	$[-22, -13]$	$[-4, 14]$	-9 ± 4
$K^+\pi^0$	$[-17, -10]$	$[-2, 16]$	-10 ± 7
$K^0\pi^+$	$[-2, -1]$	$[0, 2]$	4 ± 8

Table 2.8: $\mathcal{A}_{CP} \equiv [\mathcal{B}(\bar{B} \to \bar{f}) - \mathcal{B}(B \to f)]/[\mathcal{B}(\bar{B} \to \bar{f}) + \mathcal{B}(B \to f)]$ predictions [27, 87] for $B \to PP$ modes with experimental measurements [89, 91, 93, 95], in percent.

Mode	QCDF	PQCD	Experiment
	$\Delta S = 0$		
$\rho(770)^+\pi^-$	$[-13, 20]$		-11 ± 18
$\rho(770)^-\pi^+$	$[-32, 26]$		-82 ± 35
$\rho(770)^0\pi^0$	$[-29, 19]$		
$\rho(770)^+\pi^0$	$[-12, -3]$		
$\rho(770)^0\pi^+$	$[3, 14]$		
$K^*(892)^\pm K^\mp$	$[-25, 17]$		
$K^*(892)^0\bar{K}^0$	$[-12, -9]$		
$\bar{K}^*(892)^0K^0$	$[20, 23]$		
$\bar{K}^*(892)^0K^+$	$[-32, -21]$		
$K^*(892)^+\bar{K}^0$	$[-9, 9]$		
$\phi(1020)\pi^0$	1		
$\phi(1020)\pi^+$	0		
	$\lvert\Delta S\rvert = 1$		
$K^*(892)^+\pi^-$	$[14, 47]$	-19	26^{+34}_{-35} (this thesis)
$K^*(892)^0\pi^0$	$[-12, -9]$	-10	
$K^*(892)^+\pi^0$	$[15, 36]$	-44	
$K^*(892)^0\pi^-$	$[1, 2]$	-4	
$\rho(770)^+K^-$	$[-54, 3]$		19 ± 18
$\rho(770)^0K^0$	$[24, 27]$		
$\rho(770)^+K^0$	$[-0.4, 0.4]$		
$\rho(770)^0K^+$	$[-79, 3]$		
$\phi(1020)K^0$	34		
$\phi(1020)K^+$	1		

Table 2.9: $\mathcal{A}_{CP} \equiv [\mathcal{B}(\bar{B} \to \bar{f}) - \mathcal{B}(B \to f)]/[\mathcal{B}(\bar{B} \to \bar{f}) + \mathcal{B}(B \to f)]$ predictions [85, 88] for $B \to PV$ modes with experimental measurements [104, 105], in percent.

Chapter 3 The CLEO Experiment

3.1 The Cornell Electron Storage Ring

The discovery of the J/ψ resonance in 1974 [106, 107] prompted experimental efforts around the world to search for new resonances with even higher mass. Among these endeavors was the addition of the Cornell Electron Storage Ring (CESR) to the Cornell Synchrotron, located on the Cornell University campus in Ithaca, New York. At the time of CESR's inception in 1979, the $\Upsilon(1S)$ and $\Upsilon(2S)$ resonances had already discovered [108] and identified as $b\bar{b}$ bound states. These resonances, with masses near 10 GeV, fall neatly in the energy range of 9–16 GeV for which CESR was designed, and the experiments located at CESR have been at the forefront of the study of the b quark.

CESR is a symmetric e^+e^- collider that has been operating in the center-of-mass energy range of 9.4–11.2 GeV for more than two decades. From 1980–1990, collisions at two points along the ring provided data for the CLEO and CUSB detectors. In 1990, CESR moved to single interaction region running for the CLEO detector only. CESR also delivers x-rays from synchrotron radiation to the Cornell High Energy Synchrotron Source (CHESS) facility.

Figure 3.1 shows a schematic diagram of the CESR facility. Electrons are obtained from a heated filament in a voltage potential and are placed in a 30 m linear accelerator (linac). At the end of the linac, the electrons have an energy of 300 MeV, and they are injected into the synchrotron, where they are brought to an energy of around 5 GeV. After reaching their final energy, the electrons are transferred to the storage ring, where they remain until annihilating with the positrons in the interaction region or colliding with the walls of CESR.

At the midpoint of the linac, accelerated electrons at 140 MeV strike a tungsten target to produce a shower of particles containing positrons as well as electrons, x-rays, and protons. The positrons are captured and steered with magnets and are accelerated to 150 MeV in the remainder of the linac. From there, they are injected into the synchrotron and then into CESR, circulating in the opposite direction as the electrons.

CESR has a circumference of 768 m and lies 12 m below Cornell's Alumni Fields. For the data analyzed in this thesis, CESR maintained beam energies at or near 5.29 GeV. While circulating in CESR, the electrons and positrons lose energy at the rate of 1.2 MeV per turn. This energy loss is caused by synchrotron radiation, which is enhanced by the wiggler magnets placed in the beam orbit to provide additional radiation for CHESS. This lost energy is restored by two RF regions with five-cell cavities operating at 500 MHz. These accelerating cavities shape the beams into discrete bunches of particles. Initially, CESR ran with one bunch for each particle type. Over the years, the

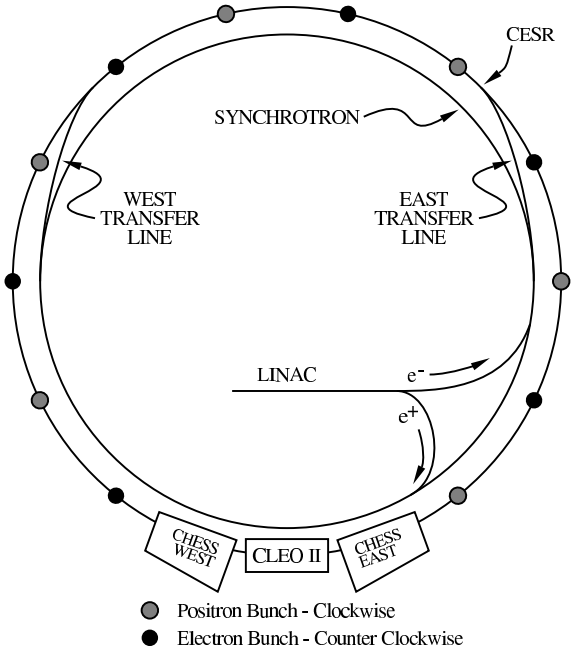

Figure 3.1: Schematic diagram of the CESR facility.

number of bunches in each beam was increased and the trajectories of the particles were adjusted to avoid parasitic collisions at points other than the interaction region. By 1999, when the latest data analyzed in this thesis were collected, CESR was running with twenty-seven bunches in each beam, organized into nine trains of three bunches each.

The rate of collisions is given by the interaction cross section multiplied by the luminosity, $\mathcal{L}$, which is defined as follows:

$$\mathcal{L} \equiv \frac{f N_B n_1 n_2}{4\pi\sigma_x\sigma_y}, \tag{3.1}$$

where f is the frequency with which a given bunch passes the interaction region, N_B is the number of bunches in each beam, n_1 and n_2 are the number of particles in the electron and positron bunches, and σ_x and σ_y characterize the transverse beam profiles in the horizontal and vertical directions. At CESR, the transverse bunch dimensions are typically $\sigma_x \approx 300$ μm and $\sigma_y \approx 6$ μm, and the length of the bunch parallel to the beam is $\sigma_z \approx 2$ cm. With approximately 10^{11} particles per bunch and a transit frequency of 3.9×10^5 Hz, the peak luminosity achieved by CESR was 8.5×10^{32} cm^{-2}s^{-1}.

The hadronic cross section in CESR's operating energy range is shown in Figure 3.2. Most of the data analyzed in this thesis were produced at a center-of-mass energy of $\sqrt{s} = 10.58$ GeV, on the peak of the $\Upsilon(4S)$ resonance. This energy is 20 MeV above the threshold for pair production of B mesons, and the $\Upsilon(4S)$ decays exclusively to B^+B^- or $B^0\bar{B}^0$. The process $e^+e^- \to \Upsilon(4S) \to B\bar{B}$ accounts for 1.07 nb of the hadronic cross section at $\sqrt{s} = 10.58$ GeV. The remaining 3.4 nb corresponds

to $e^+e^- \rightarrow q\bar{q}$ events, where $q = u, d, s, c$. This component of the total cross section known as the continuum, and, typically, it dominates the background in the study of rare B decays on the $\Upsilon(4S)$. To better understand this continuum background, one-third of the luminosity was produced at $\sqrt{s} = 10.52$ GeV, 35 MeV below the $B\bar{B}$ treshold. This off-resonance data is used extensively in this thesis to study the properties of the continuum background without making use of Monte Carlo simulated data.

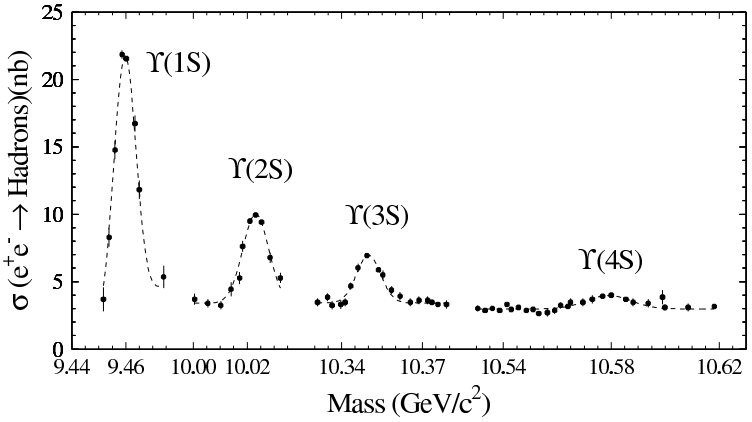

Figure 3.2: Hadronic cross section in the region of the Υ resonances.

3.2 The CLEO II Detector

The CLEO II detector [109] is situated at CESR's south interaction region, where it records the passage of particles produced in the e^+e^- collisions. CLEO II was designed to detect both neutral and charged particles with high efficiency and to measure their energies and momenta with excellent resolution. A schematic diagram of CLEO II appears in Figure 3.3. Like many cylindrical general purpose particle detectors, it possesses tracking chambers that detect charged particles, an electromagnetic calorimeter for photon and electron identification, and time-of-flight scintillator counters that identify charged particles and participate in the trigger. These systems reside in a 1.5 T solenoidal magnetic field, and muon chambers are embedded in the return yoke of the magnet. CLEO II boasts high-precision tracking and photon energy measurements, as well as a high hermeticity, covering 94% of the solid angle. Below, we describe each of the subsystems in more detail.

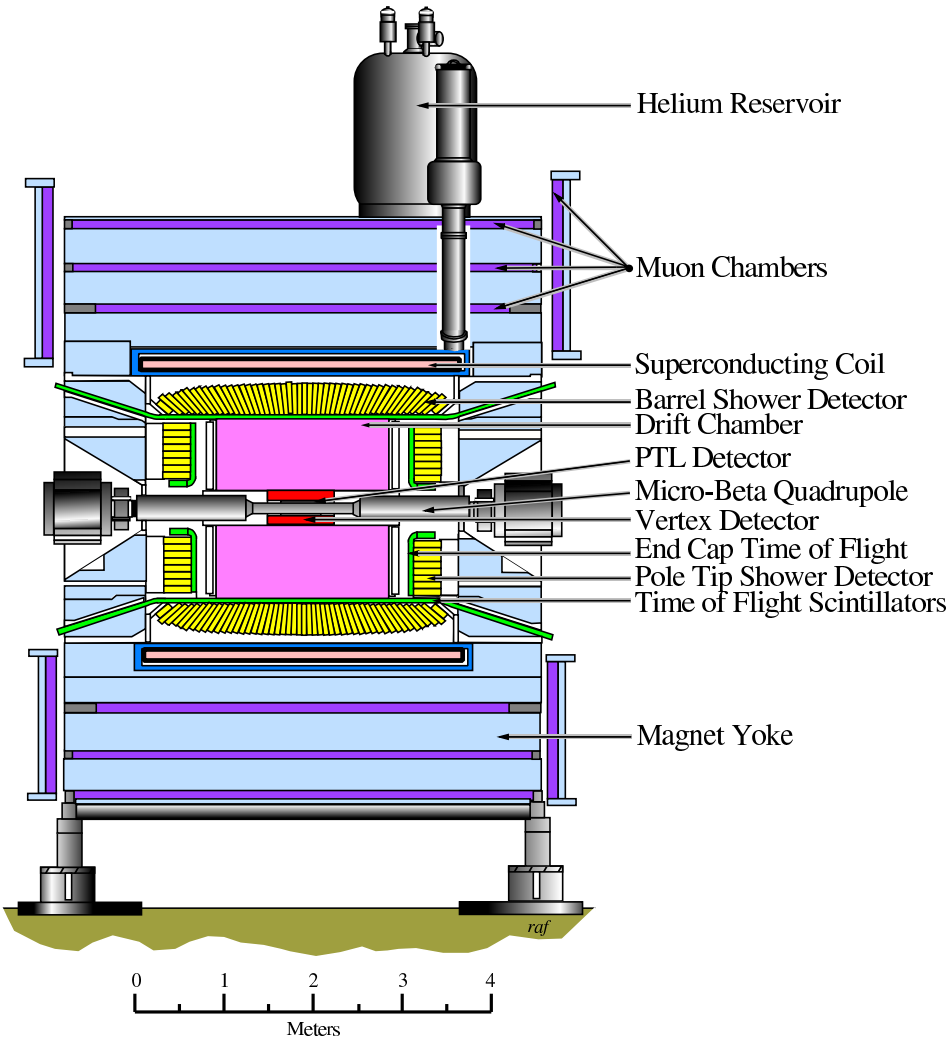

Figure 3.3: Schematic diagram of the CLEO II detector.

3.2.1 Charged Particle Tracking

Tracking of charged particles is accomplished by three concentric devices immediately surrounding the beam line: the precision tracking layer (PTL), the vertex detector (VD), and the main drift chamber (DR). All three devices operate in a gas mixture of 50% argon and 50% ethane (C_2H_6). When charged particles traverse these detectors, they ionize the gas. Wires held at a positive voltage collect the electrons from the avalanche initiated by the primary ionization electrons. The helical trajectories of the particles are reconstructed from the spatial distribution of the ionization. Furthermore, the amount of ionizaton along the path is a measure of energy lost by the particle (dE/dx), which can help determine its mass.

The tracking device closest to the beamline is the PTL, which consists of six layers of straw tubes.

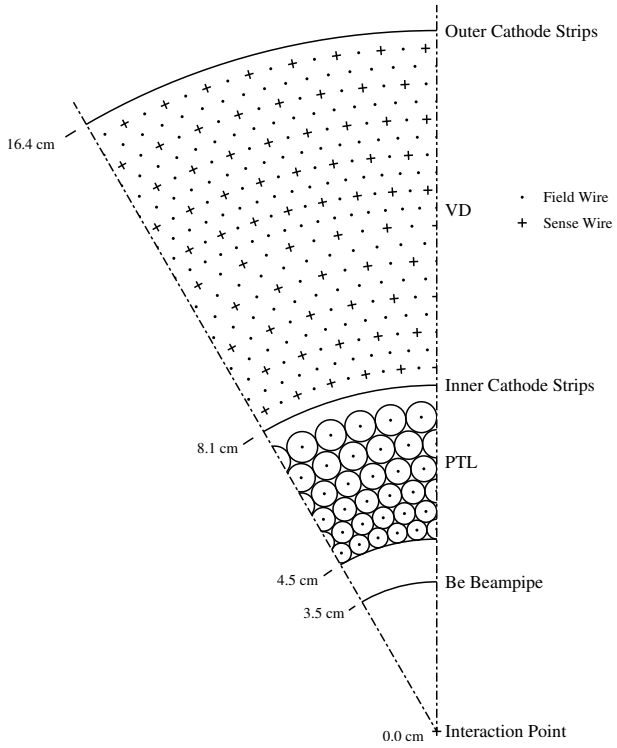

Figure 3.4: Schematic diagram of the PTL and VD.

In each layer, there are 64 gold-plated tungsten axial wires, each surrounded by an aluminized mylar tube, which shapes the electric field. These cells are arranged with half-cell staggering between adjacent layers, as shown in Figure 3.4, to provide local resolution of the drift distance sign ambiguity. The PTL has an inner radius of 4.5 cm, an outer radius of 7.7 cm, and the wires have a half-length of 25.0 cm. It provides precise transverse position measurements near the IP with a resolution of 90 μm in the r-ϕ plane. No longitudinal (z) information is obtained from the PTL. Its material constitutes 0.35% radiation lengths in the transverse direction. It was installed in 1989 and replaced in 1995 by a three-layer silicon vertex detector (See Section 3.4).

Just beyond the PTL, between the radii of 8.1 cm and 16.6 cm, lies the VD, which contributes 1.2% radiation lengths of material. It was installed in 1984 and provides ten layers of measurements from 800 nickel-chromium sense wires with 20 μm diameter and 35.0 cm half-length. The sense wires, along with the 2272 aluminum field wires, are arranged in hexagonal cells, as shown in Figure 3.4. As in the PTL, the wires of the VD are all axial, but the finite resistivity of nickel-chromium permits charge division measurements, hence providing z information. Additional z measurements are made by the inner and outer cathode surfaces, which are constructed from longitudinally segmented aluminized Mylar and detect the image charges of the ionization avalanche at the first and last layers. The position resolutions of the VD are 150 μm in r-ϕ and 750 μm in z.

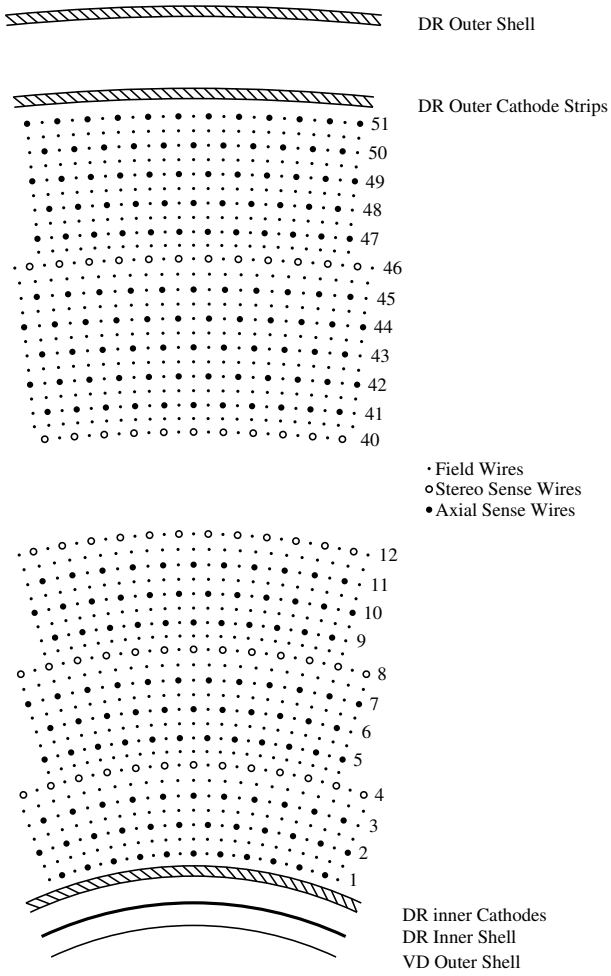

Figure 3.5: Layout of the DR wires.

The DR, installed in 1986, covers radii 17.8–94.7 cm, has a half-length of 96.2 cm, and, with 51 measurement layers, provides the bulk of the tracking measurements for particles with transverse momentum $p_t > 100$ MeV. The 12240 gold-plated tungsten sense wires and 36240 aluminum field wires are organized in rectangular half-staggered cells that have roughly uniform size over the volume of the chamber. Forty of the 51 layers are populated by axial sense wires, which make only r-ϕ measurements. The remaining eleven layers, occurring at regular intervals among the axial layers, have sense wires tilted at a small angle (1.9°–3.5°, depending on radius) with respect to the z axis. Because of this stereo angle, these layers are capable of measuring the z position of the track. As with the VD, the inner and outer cathode surfaces are instrumented with segmented aluminum for further longitudinal sensitivity. The amount of material seen by a track at normal incidence is 0.4% radiation lengths from the gas and wires and 3.5% radiation lengths from the inner and outer shells and cathodes. The DR has achieved r-ϕ resolutions of 110 μm for axial wires and 130 μm for stereo

wires as well as z resolutions of 3 cm for stereo wires and 1 mm for the cathodes.

Tracks are reconstructed from hits in the PTL, VD, and DR by means of a pattern recognition algorithm. These hits are then fitted to a helical trajectory to extract the position and momentum vectors of the particle at the IP. The fitter makes use of a Kalman filter [110] to account dynamically for deviations of the trajectory from a perfect helix. These deviations arise during flight and include both deterministic and random perturbations caused by energy loss and multiple Coulomb scattering in the material of the detector. The resultant error matrix for the track parameters correctly describes the uncertainties on a track-by-track basis. The detectors are calibrated and aligned using bhabha and $e^+e^- \to \mu^+\mu^-$ events.

The combined momentum resolution of all three tracking devices is

$$\left(\frac{\sigma_{p_t}}{p_t}\right)^2 = (0.0017 p_t)^2 + (0.0050)^2, \tag{3.2}$$

where the p_t is given in GeV. The first term in the above equation reflects the intrinsic resolution of the tracking devices in measuring the track curvature. The second term, which dominates the resolution up to momenta of about 3 GeV, arises from multiple Coulomb scattering. The resolutions of the azimuth angle ϕ and the polar angle θ, measured at high momentum ($\sim$ 5 GeV), are $\sigma_\phi = 1$ mrad and $\sigma_\theta = 4$ mrad.

For tracks with $|\cos\theta| < 0.71$ and $p_t > 250$ MeV, the track detection efficiency is about 95% and is independent of momentum. Tracks outside of this kinematic region suffer inefficiencies from geometric effects. The diameter of curvature of a track is given by $d = 2p_t/0.3B$, where d is given in meters, p_t in GeV, and B is the magnetic field in tesla. Since the outermost tracking layer is 95 cm from the interaction point (IP), tracks with d smaller than this distance, *i.e.*, with $p_t < 225$ MeV, will curl back on themselves before passing through all the measurement layers. These tracks are also more likely to undergo hard scatters or to lose all of their energy in the detector material. Therefore, the detection efficiency in this regime is significantly degraded, as illustrated by Figure 3.6, and the tracking resolution worsens. A reduction in the number of measurements also occurs for tracks with $|\cos\theta| > 0.71$, which exit the detector through the endcap.

Each B meson decay produces, on average, five charged tracks [111], from which one can form a primary vertex with a resolution in the r-ϕ plane of 180 μm. Since the B mesons at CLEO are produced at $\sqrt{s} = 10.58$ GeV, with a momentum of 300 MeV, they typically travel only 25 μm before decaying. Therefore, B meson decay vertices are nearly impossible to distinguish from the IP. However, longer-lived particles, such as K^0_S and Λ, have flight distances of a few centimeters, so these secondary vertices are easily identified by their separation from the beamspot.

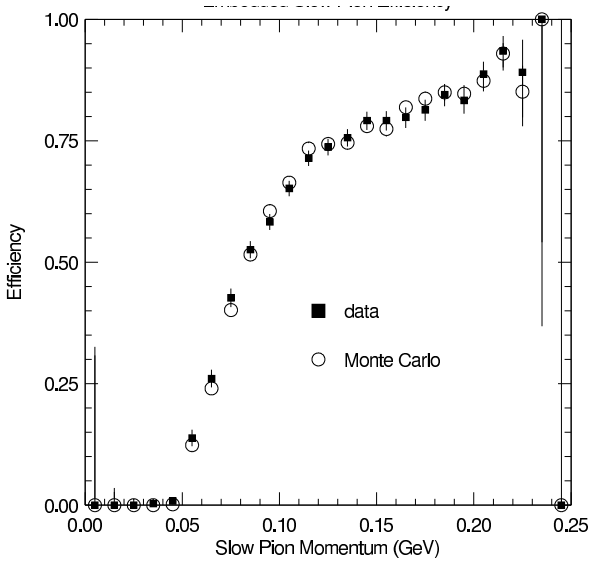

Figure 3.6: Track detection efficiency versus momentum.

3.2.2 Time of Flight

The time-of-flight (TOF) system was designed to provide fast trigger information and particle identification for tracks with momentum less than 1 GeV. Located just outside the DR, the barrel TOF system consists of 64 plastic scintillator counters that have dimensions 5 cm by 10 cm by 2.8 m. These scintillators are arranged longitudinally in a single layer around the DR cylinder. Both ends of the counters are coupled to two-meter-long lucite light guides, which carry the scintillation photons to photomultiplier tubes (PMTs) situated outside the solenoidal magnetic field. The PMTs capture the incident photons and amplify the signal, whose time and pulse height are then recorded.

The barrel TOF system extends over the angular region $|\cos\theta| < 0.81$. Most of the remaining solid angle, $0.81 < |\cos\theta| < 0.97$, is covered by the endcap TOF system, consisting of 28 wedges of plastic scintillator mounted on each endcap. PMTs are attached directly to the scintillator and are oriented parallel to the beam line to minimize the effect of the solenoidal magnetic field. Both the barrel and endcap TOF counters amount to 12% radiation lengths.

The TOF system has achieved a timing resolution of 154 ps for pions in the barrel, which allows separation of 1 GeV kaons and pions at the level of two standard deviations (σ). The K/π separation decreases with momentum, and the TOF has limited value for particle identification of tracks with momentum greater than 1 GeV.

3.2.3 Crystal Calorimeter

Photons are detected by the electromagnetic calorimeter (CC), which is located outside the TOF system, with an inner radius of 1.02 m and an outer radius of 1.3 m. The CC comprises 7800 thallium-doped CsI crystals, 6144 in the barrel and 828 in each endcap, which cover 95% of the solid angle. The transverse dimensions of approximately 5 cm square and the depth of 30 cm (equivalent to 16 radiation lengths) were chosen to balance the competing needs for high granularity and resolution and low cost of assembly and readout.

The barrel calorimeter provides coverage for $|\cos\theta| < 0.85$, and its crystals are arranged such that photons originating at the IP strike the crystal faces at nearly normal incidence. The endcap calorimeter overlaps slightly with the barrel calorimenter, covering $0.81 < |\cos\theta| < 0.97$, and its crystals are all parallel to the z axis. To detect photons from electromagnetic showers in the crystals, four photodiodes, each with an active area of 1 cm^2, are attached to a lucite window at the end of each crystal.

The reconstruction software forms shower clusters from groups of adjacent crystals with energies above threshold, where only one local maximum occurs. A shower's energy and position are calculated from its N most energetic crystals, where N depends on the shower energy and increases logarithmically from 4 at 25 MeV to 17 for 4 GeV and higher. The absolute energy normalization is calibrated using radiative bhabha events, π^0 decays, and $e^+e^- \to \gamma\gamma\gamma$ events and is known to $\pm 1\%$ at 25 MeV, $\pm 0.5\%$ at 100 MeV, and $\pm 0.2\%$ at 5 GeV.

The performance of the CC varies with polar angle because of the distribution of material in front of the crystals. Particles traveling from the IP see substantially less material in the barrel than in the endcap or the barrel-endcap overlap region. In this thesis, we use photons with $|\cos\theta| < 0.95$. Table 3.1 gives the parametrizations for the photon energy and angular resolutions for the barrel and endcap regions. The resolution is dominated by calibration uncertainty and electronic noise for low shower energies and by insufficient crystal depth to fully contain the shower at high energies.

	Barrel	Endcap
$\frac{\sigma_E}{E}$ (%)	$\frac{0.35}{E^{0.75}} + 1.9 - 0.1E$	$\frac{0.26}{E} + 2.5$
σ_ϕ (mrad)	$\frac{2.8}{\sqrt{E}} + 1.9$	$\frac{3.7}{\sqrt{E}} + 7.3$
σ_θ (mrad)	$0.8\sigma_\phi \sin\theta$	$\frac{1.4}{\sqrt{E}} + 5.6$

Table 3.1: Energy and angular resolutions for the CC for photon energies in GeV.

In this thesis, the CC is used primarily for two purposes. The first is to reconstruct $\pi^0 \to \gamma\gamma$ decays. The resolution on the π^0 invariant mass is about 5 MeV. To improve the momentum and angular π^0 resolution, two-photon candidates are kinematically constrained to the known π^0 mass.

In addition, the CC used to reject charged tracks positively identified as electrons, which, unlike other stable charged particles, deposit nearly all of their energy in the CC. Therefore, they can be identified by the ratio of momentum in the tracking chambers to associated energy in the CC.

3.2.4 Muon Chambers

The muon detection system consists of three sets of plastic proportional chambers embedded in the iron return yoke of the solenoid at depths of 36, 72, and 108 cm, corresponding to 3, 5, and 7 nuclear interaction lengths at normal incidence from the IP. Three layers of counters in each set provide redundancy and increase the geometrical acceptance. These barrel counters identify muons with $|\cos\theta| < 0.71$. The angular region $0.71 < |\cos\theta| < 0.87$ is covered by a single set (three layers) of counters on each endcap.

The proportional chambers are 8.3 cm wide, 1 cm thick, and 5 m long. Each counter contains eight anode wires separated by graphite-coated plastic walls that act as cathodes. External copper strips of the same width as the counters are mounted perpendicular to the anode wires and detect the image charge induced on the cathode. The intrinsic resolution of the copper strips is 5.3 cm in the z direction. For the anodes, the eight wires in each counter are ganged together, giving an intrinsic resolution of $8.3/\sqrt{12} = 2.4$ cm in the r-ϕ direction.

Tracks reconstructed in the central detector are extrapolated into the muon chambers, accounting for dE/dx energy loss. Muon chamber hits are then matched to the track by the distance between the measured and projected hit positions. The spatial resolutions for the anodes are 3.7, 4.6, and 5.7 cm for the units at 3, 5, and 7 interaction lengths, respectively, and 7.2 cm for the endcap units. The corresponding resolutions for the cathode strips are 5.5, 7.0, 7.5, and 9.0 cm.

Muons are not used in the current analysis. Instead, we reject tracks that are consistent with being muons by requiring the track candidate to penetrate fewer than seven interaction lengths or to register no hits in one of the preceeding units.

3.2.5 Trigger and Data Acquisition

The CLEO II and II.V trigger [113] consists of three levels of progressively restrictive event selection in hardware and one level in software after the detector has been read out. The CLEO detector is gated with every beam crossing, at which time, the L0 trigger is evaluated using hits in the TOF and CC and crude track segments in the VD. The L0 trigger requires 400 ns and reduces the event rate by about two orders of magnitude. A successful L0 trigger disables data taking, which is resumed no later than 2.0 ms after the L0 trigger, depending on the decisions of the L1 and L2 triggers.

The L1 trigger, which takes 2.2 μs, incorporates DR hits and performs additional tracking calculations, including determining the charges of the tracks. The L2 trigger takes 40 μs and discriminates

against beam-wall and beam-gas interactions as well as cosmic rays with the help of more sophisticated tracking.

Events satisfying the L2 trigger are read out by the data acquisition system [114], which uses a parallel readout system and VME-based CPUs for processing the raw data and shipping them to the host computer. Analog signals above threshold are digitized by the front end crates, and the output is placed in a 32-event buffer. The detector is reenabled when the front end crates have emptied their buffers. The detector readout takes 2 ms and incurs the bulk of the dead time during data taking. The data in the event buffers is sparsified by VME CPU boards, which takes 16 ms, thus constraining the maximum trigger rate to 50 Hz. The event builder CPU assembles the sparsified data and sends it to the host computer.

The physics cross section at the $\Upsilon(4S)$ has the following contributions: 4.5 nb from hadrons, 0.91 nb from τ-pairs, 15 nb from prescaled bhabhas, and 2 nb from μ-pairs and two-photon events. The trigger efficiency for physics events is better than 99%. At the peak CLEO II.V luminosity of 8.5×10^{32} cm^{-1} s^{-1}, these events contribute about 20 Hz to the trigger rate. The remainder of the rate of 50 Hz is dominated by beam-wall, beam-gas, and cosmic ray backgrounds. Most of these background events are rejected by the L3 software trigger, which runs on the host computer. L3 rejects 45% of the L2 triggers while maintaining an efficiency for hadronic events above 99%. Physics events with low multiplicity, like one-prong τ or two-photon events, suffer a small efficiency loss of 0.5%. Events passing the L3 trigger are written to disk and eventually to archival tape storage.

3.3 Charged Particle Identification

There are five species of charged particles with lifetimes long enough that they decay outside of the CLEO detector: electrons, muons, pions, kaons, and protons. Of these, electrons and muons are easy to identify using the CC and muon chambers. To separate the remaining three types, we rely on a determination of the particle's velocity. Since the momentum of the particle is known from its curvature in the tracking devices, a velocity measurement determines the mass.

Particle velocity can be obtained from two devices in CLEO: the TOF and the DR. The TOF measures the flight time of the particle, which, when combined with its path length in the tracking chambers, gives its velocity. However, a large percentage of tracks from low-multiplicity B decays, such as those searched for in this thesis, have momentum greater than 1 GeV. The TOF provides meager K/π separation at these momenta, so it is not used for particle identification in the current analysis.

In the DR, the pulse height of the hits measures the amount of ionization energy loss (dE/dx) undergone by the particle, which is a function of the particle's velocity. Figure 3.7 shows the dE/dx as a function of momentum for pions and kaons. Both the theoretical expectation and the

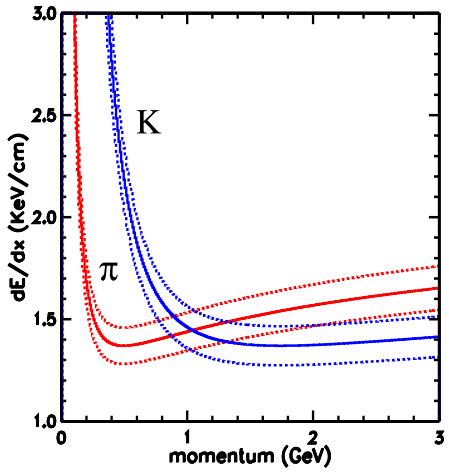

Figure 3.7: dE/dx as a function of momentum for charged pions and kaons. The solid curves represent the expected energy loss and the dotted curves the experimental resolution ($\pm 1\sigma$).

experimental resolution are displayed. In the vicinity of 1 GeV, no discrimination of pions from kaons is possible, but the separation increases with momentum to about 1.7σ at 2.6 GeV.

For each track, only the hits with pulse height smaller than the median pulse height are used in the dE/dx determination so that sensitivity to the Landau tail on the high side is reduced. Instead of the raw dE/dx value, we make use of a normalized dE/dx constructed by taking the difference the measured dE/dx and the expectation for a given particle hypothesis and dividing by the experimental resolution. These normalized dE/dx values are denoted $\sigma^{\pi}_{dE/dx}$ for the pion hypothesis and $\sigma^{K}_{dE/dx}$ for the kaon hypothesis. Figure 3.8 shows the $\sigma^{K}_{dE/dx}$ distributions for charged pions and kaons at 2.6 GeV under the kaon hypothesis.

The dE/dx calculation is calibrated with charged particles of known identity. Such samples are obtained from $K^0_S \to \pi^+\pi^-$ decays and $D \to K^{\pm}\pi^{\mp}$ decays. The D daughter tracks are identified either kinematically by selecting asymmetric decays where exchanging the daughter track mass assignments would shift the D mass by more than 7σ from the known mass or by reconstructing $D^{*\pm} \to D^0/\bar{D}^0\pi^{\pm}$ and using the charge of the primary pion to determine the flavors of the D daughters.

3.4 The CLEO II.V Detector

In 1995, the PTL was replaced with a three-layer double-sided silicon strip detector (SVX) [115], pictured in Figure 3.9. The SVX covers 92% of the solid angle and corresponds to 1.4% radiation lengths for a normally incident track. It was designed for high-precision impact parameter measurement to permit the resolution of secondary D and τ decay vertices from the primary vertex at the

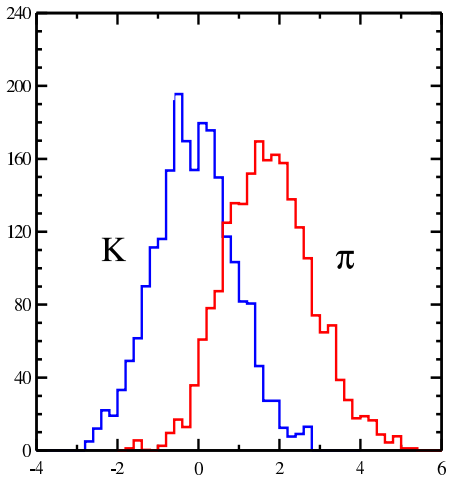

Figure 3.8: Normalized dE/dx under the kaon hypothesis, $\sigma^K_{dE/dx}$ for charged pions and kaons at 2.6 GeV.

IP. The radii of the beampipe and of the first layer of the SVX (2.0 and 2.35 cm, respectively) are minimized for optimal impact parameter resolution.

Each of the 96 wafers in the SVX has double-sided readout, so measurements in both the r-ϕ and z directions are made. Because the SVX is an important source of longitudinal information, the z-measurement side of each wafer is mounted facing the beam pipe to minimize the effect of multiple scattering in the wafer material on z resolution. The pitch of the silicon strips on the z sides is about 100 μm, and each one is read out. On the r-ϕ sides, the strips have a pitch of about 28 μm, which is one-fourth of the readout pitch. The entire SVX contains 26208 readout channels.

The ratio of signal to noise (S/N) affects the efficiency, occupancy, and resolution of the detector. Measurements taken for colliding beam data find a S/N of 9–13, which is slightly lower than the design specifications. The occupancy of the detector is typically 5%, of which less than 2% results from physics; the rest is dominated by electronic and beam-related noise.

Figure 3.10 shows the intrinsic resolution of the SVX as a function of the track's angle of incidence on the silicon wafer. At normal incidence, the achieved resolutions are 19 μm and 29 μm for the r-ϕ and z measurements, respectively. On the r-ϕ side, the resolution improves with track inclination because the signal grows as $1/\sin\theta$. However, since the signal charge also spreads in z as the inclination increases, the resolution worsens as $1/\cos\theta$ on the z side.

The installation of the SVX was accompanied by a change in the gas in which the DR operated. The argon-ethane gas mixture was replaced by 60% helium and 40% propane (C_2H_6). Helium-propane yields a slower drift velocity for the ionization electrons within 3 mm of the sense wire (half a cell width). However, the smaller Lorentz angle of helium-propane regulates the behavior of electrons near the edge of the cell, giving shorter drift times at long drift distances. Thus, the use

of helium-propane raises the single hit efficiency and brings the overall spatial resolution from 172 μm to 150 μm [116]. Although helium-propane provides fewer primary ions than argon-ethane, the dE/dx resolution is not degraded because the improved efficiency and spatial precision result in a 20% increase in the number of contributing measurements. Indeed, the K/π separation at 2.6 GeV increases from 1.7σ for CLEO II to 2.0σ for CLEO II.V.

Roughly two-thirds of the data analyzed in this thesis were collected with the CLEO II.V detector. We do not make explicit use of the vertexing abilities of the SVX. However, the CLEO II.V data show a 20% improvement in tracking resolution (due to both the SVX and the DR gas modification) and increased K/π separation, both of which improve the experimental sensitivity to charmless hadronic B decays.

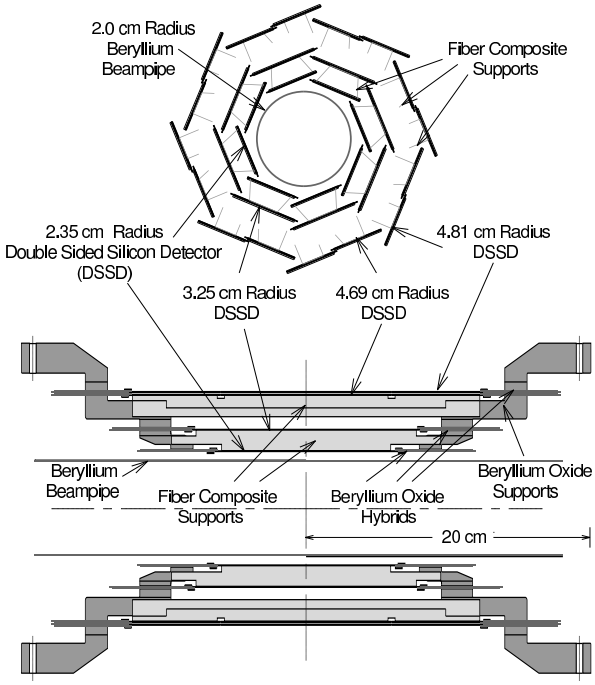

Figure 3.9: Front and side views of the CLEO II.V SVX detector.

3.5 Monte Carlo Simulation

In addition to the data collected with the CLEO detector, we also use Monte Carlo (MC) simulated data to study the response of the detector to the decays we hope to observe. The simulation occurs in two steps. First, a program known as QQ generates the physical processes of interest, including $e^+e^- \to q\bar{q}$ and the production and decay of B mesons. The output of QQ consists of the four-momenta for all the particles in a particular decay chain. These four-momenta are

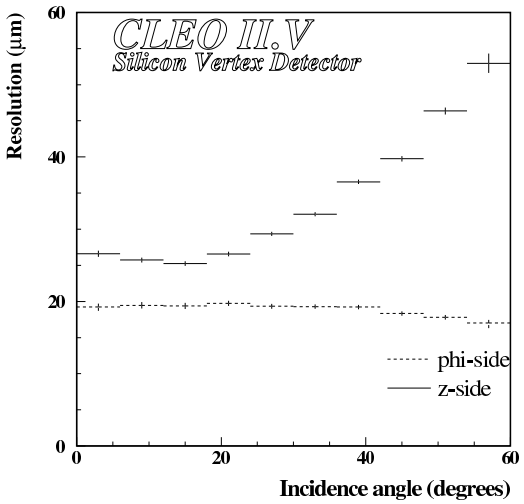

Figure 3.10: Resolution of the CLEO II.V SVX as a function of incidence angle.

given to a GEANT-based [112] package, called CLEOG, that simulates the detector response to the particles generated in QQ. CLEOG makes use of a detailed description of the material in the detector to simulate processes like bremsstrahlung, multiple Coulomb scattering, photon conversions, and hadronic interactions. It also handles the decays of relatively long-lived particles such as charged pions and kaons and K^0_Ss, which tend to decay in the active volume of the detector, rather than in the vacuum of the beampipe. The electronic response generated by CLEOG, which includes noise hits, can be processed with the standard offline reconstruction software.

We measure detection efficiencies and crossfeed among signal modes with MC simulated signal events. To study backgrounds from other B decays, we also make use of a MC sample consisting of exclusive $b \to c$ transitions with relative branching fractions taken from the PDG summary [5]. The sizes of the $b \to c$ MC samples correspond to at least 3.4 times the luminosity collected with CLEO II and CLEO II.V.

Chapter 4 Event Selection

We search for B decays with the following final state topologies: $K^0_S h^\pm \pi^\mp$, $K^\pm h^\mp \pi^0$, and $K^0_S h^\pm \pi^0$, where $h^\pm$ denotes a charged pion or kaon. We study these three-body decays "inclusively" by disregarding the possible resonant substructure. We also analyze the Dalitz plots of these decays to search for exclusive quasi-two-body or three-body non-resonant (NR) decays. Finally, we extend the Dalitz plot analysis to measure the CP asymmetry in $B \to K^*(892)^\pm \pi^\mp$. All of these analyses are performed using a maximum likelihood technique.

The possible intermediate resonances we consider are those with sizeable branching fractions to $K\pi$ or $\pi\pi$: $K^*(892)$, $K^*_0(1430)$, $\rho(770)$, and $f_0(980)$. Figure 4.1 shows the momentum distributions for the three final state particles in $B \to K^0_S \pi^+ \pi^-$ for NR decay and two representative intermediate resonances. The other three-body final states possess similar spectra, as shown in Figures 4.4 and 4.5. NR decays populate the Dalitz plot uniformly, and the momentum distributions exhibit no structure within the kinematic limits. The quasi-two-body decay $B \to K^*_0(1430)^\pm \pi^\mp$ with $K^*_0(1430)^\pm \to K^\pm \pi^\mp$ produces a monoenergetic pion at 2.6 GeV, whose momentum is smeared by detector resolution. Since the pseudoscalar B decays to two spin-0 particles, the $K^*_0(1430)^\pm$ daughters emerge isotropically, and their spectra are relatively flat over the kinematically allowed region. On the other hand, in the vector-pseudoscalar decay $B \to K^*(892)^\pm \pi^\mp$, the vector $K^*(892)^\pm$ is transversely polarized because of helicity conservation. Therefore, the $K^*(892)^\pm$ daughters emerge preferentially along the $K^*(892)^\pm$ flight direction in the B rest frame, giving rise to their bimodal momentum distributions. In the Dalitz analysis, we exploit these differences in helicity structure to differentiate various decay modes with identical final state particles.

The data used for this analysis comprises 13.48 fb^{-1} produced at or near the $\Upsilon(4S)$. Roughly one-third of this luminosity was collected with the CLEO II detector; the remainder was collected with CLEO II.V. The 9.12 fb^{-1} produced on the $\Upsilon(4S)$ is referred to as the on-resonance data sample, and it corresponds to 9.66×10^6 $B\bar{B}$ pairs (3.32×10^6 CLEO II and 6.34×10^6 CLEO II.V). The 4.36 fb^{-1} produced at $\sqrt{s} = 10.52$ GeV is referred to as the off-resonance data, 2.75 fb^{-1} of which was collected with CLEO II.V. The entire data sample was recorded between November 1990 and February 1999.

In Section 4.1, we describe the general event properties used to select candidate events. We also present the requirements that reject poorly reconstructed charged tracks and calorimeter showers and that provide cleanly identified $K^0_S \to \pi^+\pi^-$ and $\pi^0 \to \gamma\gamma$ decays. In Section 4.2, the kinematic properties of the B decay candidate are used to distinguish signal decays from continuum background. We reserve discussion of the maximum likelihood technique for Chapter 5.

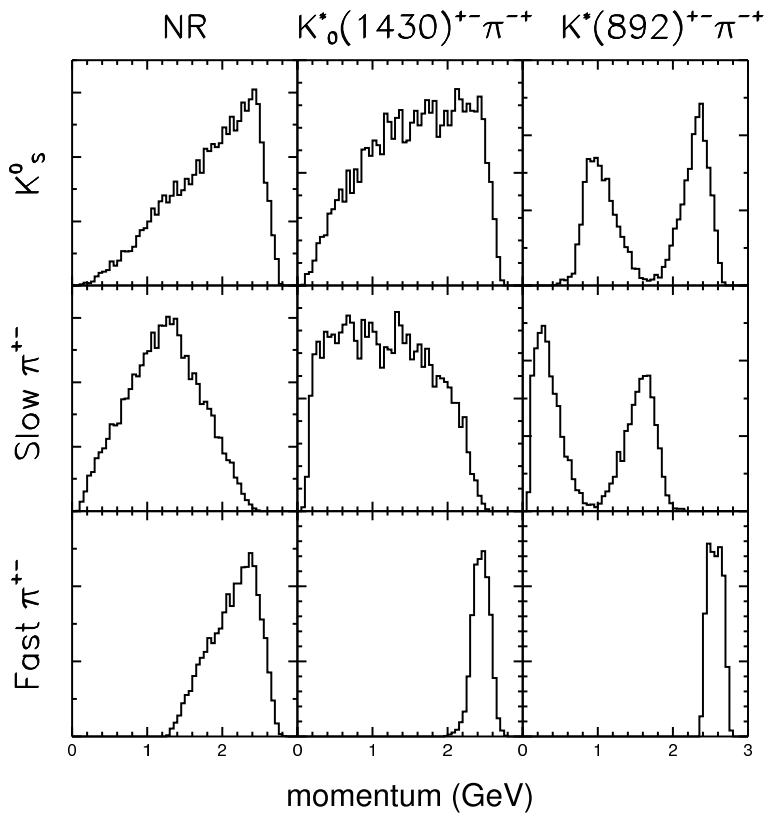

Figure 4.1: Momentum spectra obtained from MC for the final state particles in $B \to K^0_S\pi^+\pi^-$: K^0_S (top row), the slower $\pi^\pm$ (middle row), and the faster $\pi^\pm$ (bottom row). The three-body decays are modeled as NR decay (left column), $B \to K^*_0(1430)^\pm\pi^\mp$ (middle column), and $B \to K^*(892)^\pm\pi^\mp$ (right column).

4.1 General Event Properties

Hadronic events are selected by requiring that three charged tracks originate near the IP and that the total visible energy from tracks and calorimeter showers be greater than 15% of the center-of-mass energy $\sqrt{s}$. These criteria remove tau-pair and two-photon events, as well as beam-wall, beam-gas, and cosmic ray backgrounds.

4.1.1 Track Reconstruction

Fitted tracks are given to a post-processing package that detects two main types of tracking pathologies: spurious tracks formed from unused hits along a real track and particles that curl up inside the DR (because of insufficient momentum to reach its outer wall) which are then identified as two separate tracks. Only tracks that survive this filter are given further consideration, and we discard events with fewer than five such tracks.

Additional requirements are placed on the quality of the track fit. Tracks that are inconsistent

with coming from a secondary vertex must point back to the IP. Also, the number of hits assigned to the track must exceed 30% of the number of hits expected, given the track's trajectory through the detector. The above criteria are imposed on all tracks in the event, not just those forming the B candidate, because non-candidate tracks participate in background suppression, as discussed in Section 4.2.

Primary tracks in the B candidate must pass even more stringent cuts. They must have momentum greater than 100 MeV and $|\cos\theta| < 0.90$ to ensure that they are measured with sufficient precision and that they are well-modeled by the MC simulation. Particles that are positively identified as electrons or muons are not allowed in the B candidate. Muon identification is described in Section 3.2.4. Electron identification is accomplished by a combination of E/p, dE/dx, TOF information, the distribution of energy in the CC crystals, and the distance between the track and the associated shower.

As discussed in Section 3.3, charged pions and kaons are statistically separated by dE/dx. At momenta above 1 GeV, this separation degrades to less than 3σ, and dE/dx provides weak discrimination between the two particle hypotheses. We label tracks with ambiguous particle ID by $h^\pm$ to denote a $\pi^\pm$ or $K^\pm$. In the $K^0_S h^\pm \pi^\mp$ and $K^\pm h^\mp \pi^0$ topologies, the $h^\pm$ is chosen to be the faster of the two tracks in the candidate, and it typically has momentum greater than 1 GeV. The other, slower, track in the candidate must have dE/dx that agrees with its particle ID assignment, with $\left|\sigma^{K/\pi}_{dE/dx}\right| < 3$ for the appropriate particle hypothesis. In the $K^0_S h^\pm \pi^0$ topology, the $h^\pm$ is the only track in the candidate and may have momentum between 0.1 and 2.4 GeV. For the $h^\pm$, we require $|\cos\theta| < 0.85$ and $-5 < \sigma^\pi_{dE/dx} < 3$. The latter cut eliminates badly-behaved tails in the $\sigma^\pi_{dE/dx}$ distribution while maintining high efficiency for both pions and kaons.

This selection procedure introduces slight inefficiencies for signal decays with two misidentified tracks, *i.e.*, $K^0_S K^\pm \pi^\mp$ decays where $p_K < p_\pi$ and $K^\pm \pi^\mp \pi^0$ decays where $p_\pi < p_K$. In principle, a loss of efficiency also occurs in all three topologies when $h^\pm = K^\pm$ and the track's momentum is low enough so that $\sigma^\pi_{dE/dx} < -5$. In practice, however, this second inefficiency is unnoticeable. Table 4.1 gives the efficiencies of the dE/dx cuts in all three topologies for the pion and kaon $h^\pm$ hypotheses, measured with simulated NR signal events. In all cases, these selection requirements amount to a relative inefficiency of less than 7%. The effect is larger in $K^\pm h^\mp \pi^0$ than in $K^0_S h^\pm \pi^\mp$ because, as discussed below, we only accept π^0 candidates with momentum above 1 GeV. This requirement reduces the average momentum of the other final state particles, making misidentification of both tracks in the candidate more likely. The cumulative efficiency for all track quality requirements is about 98% per track for momenta above 1 GeV. Below 1 GeV, the efficiency decreases steadily to about 92% at 300 MeV.

Topology	$\epsilon^{\pi}_{dE/dx}$	$\epsilon^{K}_{dE/dx}$	$2\left\lvert\frac{\epsilon^{\pi}-\epsilon^{K}}{\epsilon^{\pi}+\epsilon^{K}}\right\rvert_{dE/dx}$
$K^0_S h^{\pm}\pi^{\mp}$	98.9 ± 0.1	95.7 ± 0.4	3.3 ± 0.4
$K^{\pm} h^{\mp}\pi^0$	90.8 ± 0.3	96.7 ± 0.3	6.3 ± 0.4
$K^0_S h^{\pm}\pi^0$	99.4 ± 0.1	99.6 ± 0.2	0.2 ± 0.2

Table 4.1: Efficiencies, in percent, for the dE/dx selection requirements under the pion and kaon hypotheses for $h^{\pm}$, measured using simulated NR signal decays. Also given are the relative inefficiencies for the two particle hypotheses.

4.1.2 K^0_S Reconstruction

K^0_S decays are reconstructed from the $\pi^+\pi^-$ final state, which occurs with a branching fraction of 0.686 ± 0.003 [5]. The K^0_S reconstruction software considers pairs of oppositely charged tracks with good fit quality that overlap in r-ϕ or that have an r-ϕ miss distance of less than 2 mm. These tracks are transported to the estimated vertex position, taking energy loss in the detector material into account, and are fitted with a vertex constraint. Dipion candidates with an invariant mass within 10 MeV (about 2.5σ) of the known K^0_S mass are accepted for this analysis. To reduce the combinatoric background, we also place requirements on the significance of the vertex flight distance, the K^0_S and daughter pion impact parameters to the IP, and the ratio of the number of hits on the daughter tracks to the number expected. The efficiency of these requirements is greater than 90% at all K^0_S momenta, and the resultant signal-to-background ratio is around 10. The width of the K^0_S mass peak increases roughly linearly with momentum from 3 MeV for $p_{K^0_S}$ below 500 MeV to 4 MeV for $p_{K^0_S}$ above 2.5 GeV. Figure 4.2 shows the invariant mass distribution for K^0_S candidates in all the $B \to K^0_S h^{\pm}\pi^{\mp}$ candidates from on-resonance data accepted for this analysis.

The effects of the selection criteria for K^0_S candidates are studied by fitting the $\pi^+\pi^-$ invariant mass peaks to a bifurcated Gaussian (a Gaussian with different widths above and below the peak) and a second-order polynomial background. The signal (S) and background (B) yields thus obtained are used to form a figure of merit, $S^2/(S+B)$, and the cut positions are chosen to maximize this quantity.

4.1.3 Photon and π^0 Reconstruction

Photons reconstructed in the CC are combined in pairs to form $\pi^0 \to \gamma\gamma$ candidates. At least one of the photons must have $|\cos\theta| < 0.71$. Both photons must not be associated with charged tracks and must satisfy a minimum distance requirement between the shower centroid and the nearest track. The spatial distribution of energy within a shower distinguishes photons from hadrons, and both π^0 daughters must have energy profiles consistent with being photons. In order to suppress the combinatoric background from real photons, the energy of the less energetic photon in a π^0 candidate

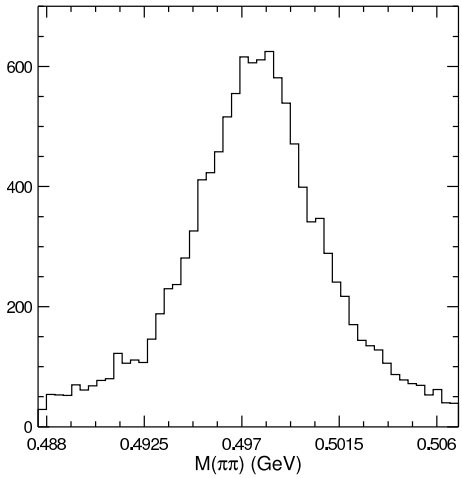

Figure 4.2: Invariant mass distribution for K^0_S candidates forming $B \to K^0_S h^\pm \pi^\mp$ candidates in on-resonance data.

must lie above a cutoff given by a quadratic function of the π^0 momentum. The above requirements are chosen by optimizing $S^2/(S+B)$ in the $\gamma\gamma$ invariant mass distributions. The efficiency of these requirements rises linearly with π^0 momentum from 90% at 100 MeV to nearly 100% at 3 GeV. Photon pairs with invariant mass between 115 MeV and 155 MeV ($\pm 3\sigma$) are kinematically fitted to the known π^0 mass to improve the π^0 energy and momentum resolution.

Prior to the mass constraint, the π^0 mass resolution is about 5.3 MeV for $p_{\gamma\gamma} < 1$ GeV and about 6.6 MeV for $p_{\gamma\gamma} > 1$ GeV. The unconstrained diphoton invariant mass distributions for these two momentum regions are shown in Figure 4.3. Because of the severity of the combinatoric background at low momentum, we discard π^0 candidates with momenta less than 1 GeV. The loss in signal efficiency balances the gain in background reduction so that the sensitivity to rare B decays is essentially unchanged. Figures 4.4 and 4.5 show the momentum spectra for the final state particles in various exclusive modes belonging to the $K^\pm h^\mp \pi^0$ and $K^0_S h^\pm \pi^0$ topologies. The effect of the π^0 momentum requirement is also displayed.

CC showers that do not form π^0 candidates and that are not associated with charged tracks participate in continuum suppression, as detailed in Section 4.2. These showers must have $|\cos\theta| < 0.95$ and an energy between 50 MeV and 5 GeV. Stale showers due to bhabhas from earlier beam crossings are removed by rejecting back-to-back shower pairs with a combined energy above 6 GeV.

4.2 Background Suppression

The primary background in this analysis comes from continuum $e^+e^- \to q\bar{q}$ events, where $q = u, d, s, c$. These events are distinguished from signal events by means of kinematic constraints on the

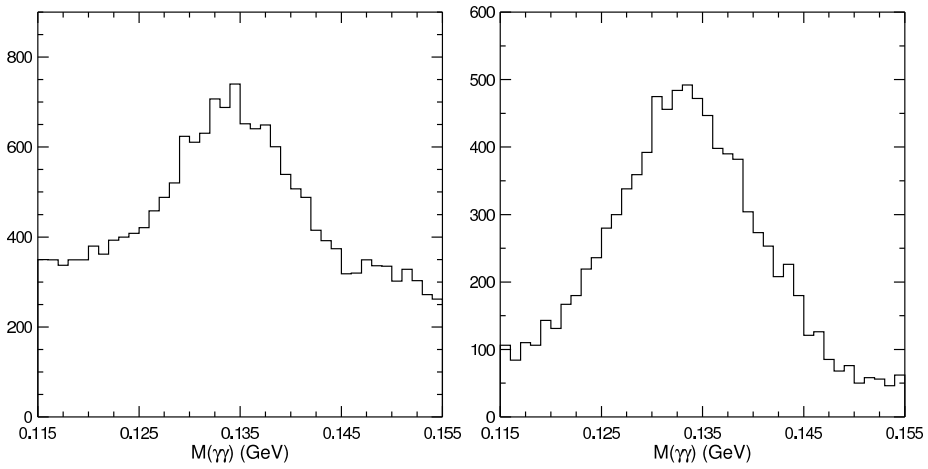

Figure 4.3: Invariant mass distribution for π^0 candidates with momentum less than 1 GeV (left) and greater than 1 GeV (right) forming $B \to K^0_S h^\pm \pi^0$ candidates in on-resonance data.

B candidate and by the spatial distribution of all the decay products in the event. The kinematic constraints also discriminate against combinatoric background and other non-signal B decay modes. Various $B \to D\pi$ or $B \to J/\psi$ modes have final states identical to those for which we search. These exclusive $b \to c$ transitions are vetoed by rejecting narrow bands in the Dalitz plots.

4.2.1 Kinematic Constraints

In identifying B decays, the two most powerful kinematic variables are the ones that express energy and momentum conservation. Because the $B\bar{B}$ pairs are produced with the B mesons nearly at rest, the summed energy of the B decay daughters is equal to the beam energy. We define the energy difference ΔE to be

$$\Delta E \equiv E_1 + E_2 + E_3 - E_{\rm beam} \tag{4.1}$$

where E_1, E_2, and E_3 are the energies of the B candidate daughters. For signal decays, the width of the ΔE distribution is dominated by the detector resolution. Final states with a K^0_S and two charged tracks have a ΔE uncertainty of about 20 MeV for CLEO II and 15 MeV for CLEO II.V. A π^0 in the final state degrades this resolution by approximately a factor of two. ΔE is always calculated assuming the $h^\pm$ is a pion. Therefore, the ΔE distribution for pions is centered at zero, while that for kaons is shifted by at least -40 MeV.

The complementary variable expressing momentum conservation is the beam-constrained mass of the B, m_B. This variable is defined to be the invariant mass of the B candidate, with the

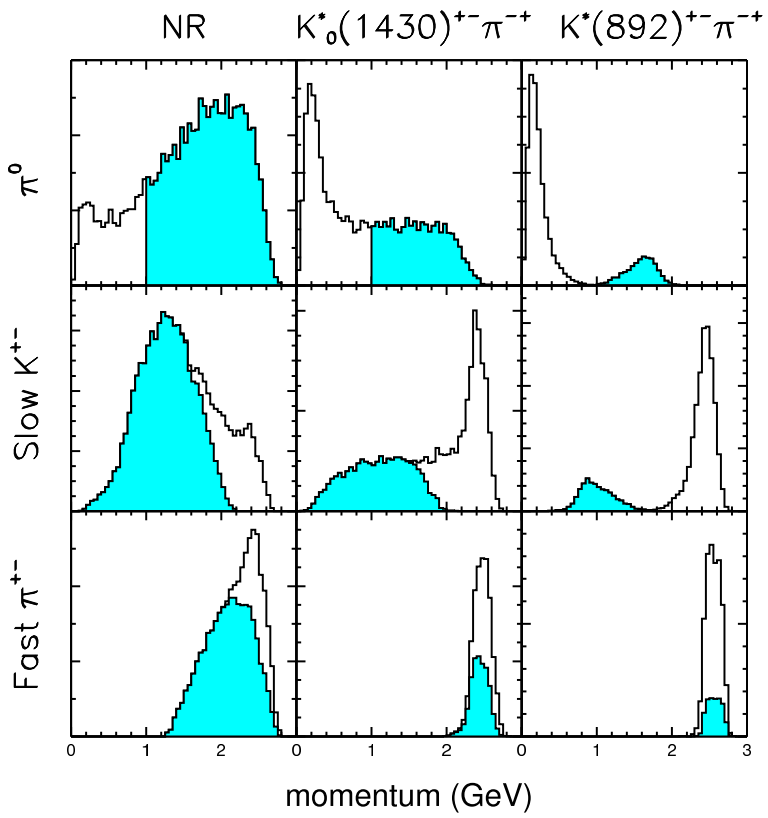

Figure 4.4: Momentum spectra obtained from MC for the final state particles in $B \to K^{\pm}\pi^{\mp}\pi^0$: π^0 (top row), the slow $K^{\pm}$ (middle row), and the fast $\pi^{\pm}$ (bottom row). The three-body decays are modeled as NR decay (left column), $B \to K_0^*(1430)^{\pm}\pi^{\mp}$ (middle column), and $B \to K^*(892)^{\pm}\pi^{\mp}$ (right column). The shaded regions are retained by the $p_{\pi^0} > 1$ GeV requirement.

reconstructed energy replaced by the beam energy:

$$m_B \equiv \sqrt{E_{\rm beam}^2 - \mathbf{p}_B^2}, \tag{4.2}$$

where $\mathbf{p}_B$ is the momentum of the B candidate. Performing this substitution improves the resolution of m_B by one order of magnitude, to about 2.7 MeV. This width is dominated by the spread in the beam energy.

Figure 4.6 shows a typical two-dimensional m_B-ΔE signal distribution, using $B \to K^*(892)^{\pm}\pi^{\mp}$ MC. Apart from the peak in the signal region, demarcated by the horizontal and vertical lines at $\pm 3\sigma$, there is also a combinatoric background covering the plane that accounts for roughly 30% of the events. Projecting the two-dimensional distribution onto one variable while applying a 3σ requirement on the other variable results in the one-dimensional distributions in Figure 4.7. The peaks in both variables are parametrized by bifurcated Gaussians. The combinatoric tails are not included in the parametrization. The m_B width does not change from CLEO II to CLEO II.V, but

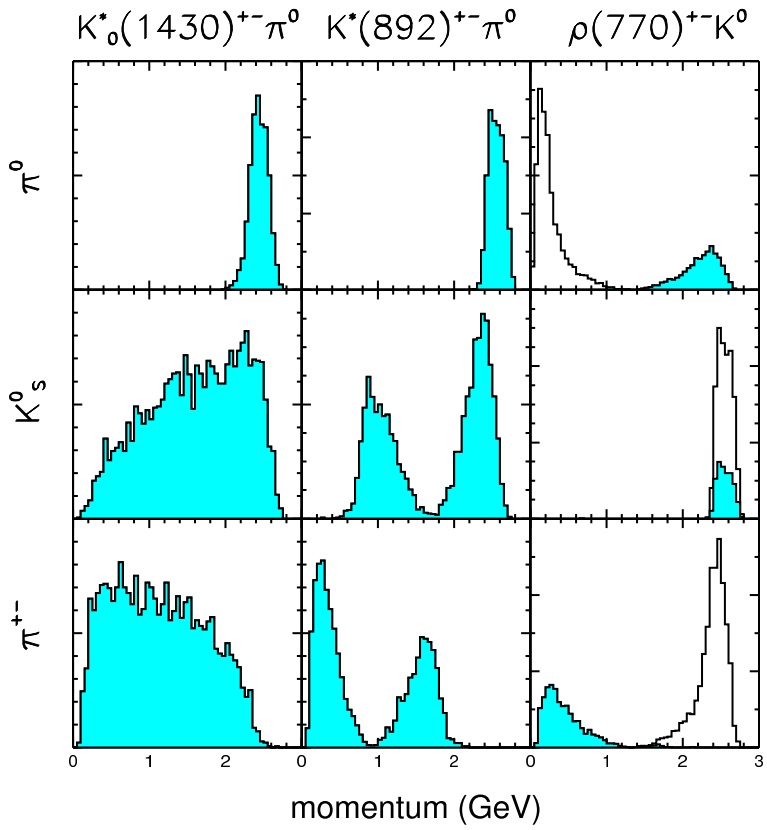

Figure 4.5: Momentum spectra obtained from MC for the final state particles in $B \to K^0_S \pi^\pm \pi^0$: π^0 (top row), K^0_S (middle row), and $\pi^\pm$ (bottom row). The three-body decays are modeled as $B \to K^*_0(1430)^\pm \pi^0$ (left column), $B \to K^*(892)^\pm \pi^0$ (middle column), and $B \to \rho(770)^\pm K^0_S$ (right column). The shaded regions are retained by the $p_{\pi^0} > 1$ GeV requirement. The distributions for NR decay, $B \to K^*_0(1430)^0 \pi^\mp$, and $B \to K^*(892)^0 \pi^\mp$ are similar to those in Figure 4.4.

the ΔE width decreases by about 23%.

Figure 4.8 shows the continuum m_B and ΔE distributions obtained from off-resonance data. CLEO II and CLEO II.V are observed to have similar distributions. The continuum ΔE distribution is parametrized by a first-order polynomial. For the continuum m_B distribution, we use an empirically determined shape, known as the Argus function [117]:

$$A(m_B) \propto m_B \sqrt{1 - \left(\frac{m_B}{E_{\rm beam}}\right)^2}\, e^{\alpha \left[1 - \left(\frac{m_B}{E_{\rm beam}}\right)^2\right]}. \tag{4.3}$$

In our analysis, we accept B candidates with m_B between 5.2 and 5.3 GeV and with $|\Delta E|$ less than 300 MeV for $K^\pm h^\mp \pi^0$ and $K^0_S h^\pm \pi^0$ and 200 MeV for $K^0_S h^\pm \pi^\mp$. This region includes the signal region and a high-statistics sideband for background normalization.

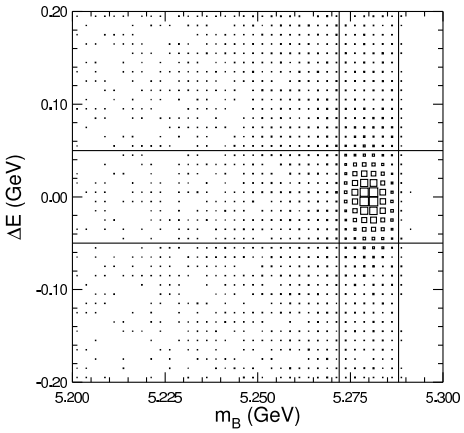

Figure 4.6: Two-dimensional signal m_B-ΔE distribution obtained from $B \to K^*(892)^{\pm}(K^0_S\pi^{\pm})\pi^{\mp}$ MC. The horizontal and vertical lines demarcate 3σ regions around the peak in each variable.

4.2.2 Event Topology

Because B mesons produced through the $\Upsilon(4S)$ are nearly at rest in the center-of-mass frame, the directions of the daughters from the two B mesons are uncorrelated, and they follow an isotropic spatial distribution. On the other hand, the particles generated in continuum $e^+e^- \to q\bar{q}$ events are collimated around the boost direction of the two initial quarks. Examples of these two types of events are shown in Figure 4.9.

The sphericity of a collection of N particles in an event is defined to be

$$S \equiv \frac{3}{2}\left(\frac{\sum_{i=1}^{N}|\mathbf{p_t}^i|}{\sum_{i=1}^{N}|\mathbf{p}^i|}\right), \tag{4.4}$$

where the index i labels the particles in the collection, the $\mathbf{p}^i$ are momentum vectors, and the $\mathbf{p_t}^i$ are the components of the $\mathbf{p}^i$ transverse to a given axis. The sphericity axis of the collection is the axis that minimizes S.

A variable that highlights the difference between the event topologies of $B\bar{B}$ and continuum events is the angle between the sphericity axis of the B candidate and that of the remaining particles in the event, denoted by $\theta_{\rm sph}$. In continuum events, the two-jet structure causes these two axes to be correlated, so the $|\cos\theta_{\rm sph}|$ peaks strongly at 1. In contrast, the isotropic nature of $B\bar{B}$ events makes the two sphericity axes uncorrelated, and such events are flat in $|\cos\theta_{\rm sph}|$. Figure 4.10 shows representative distributions of $|\cos\theta_{\rm sph}|$ for the two types of events. In our analysis, we accept candidates with $|\cos\theta_{\rm sph}| < 0.8$, thus rejecting 83% of the continuum background while retaining roughly 83% of signal B decays.

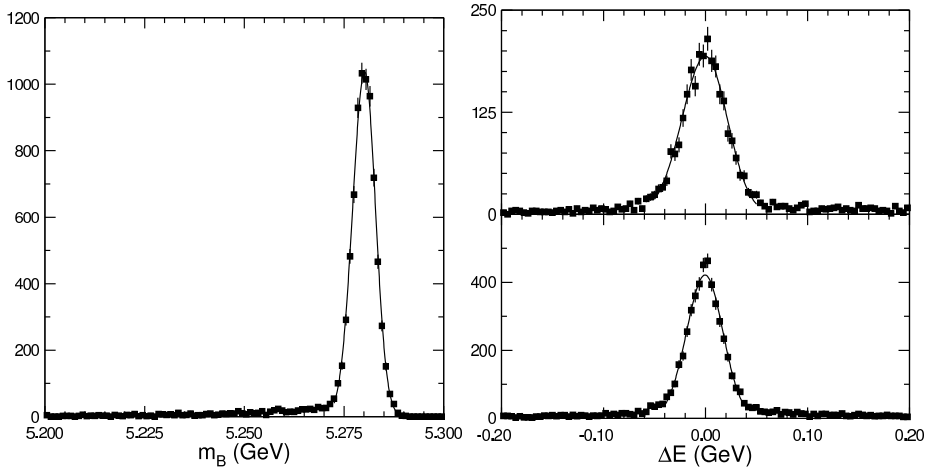

Figure 4.7: Signal distributions for m_B (left) and ΔE in CLEO II (right top) and CLEO II.V (right bottom), obtained from $B \to K^*(892)^{\pm}(K^0_S\pi^{\pm})\pi^{\mp}$ MC. In plotting m_B, a 3σ cut on ΔE was applied, and vice versa.

4.2.3 Fisher Discriminant

The variable $\cos\theta_{\rm sph}$ provides a powerful discriminator between $B\bar{B}$ and continuum events, but even more information can be extracted from a more fine-grained examination of the event topology. We make use of a virtual calorimeter, which divides the event into nine 10° angular bins around the sphericity axis of the B candidate, as shown in Figure 4.11. We sum the magnitudes of the momenta for all the charged and neutral particles in each angular bin. These particles must pass the loose selection criteria described in Section 4.1.

In addition to the nine momentum sums, we use two additional variables. The first of these is the ratio of second to zeroth Fox-Wolfram moments [118], which provides a global characterization of the event topology. The second is the angle between the sphericity axis of the B candidate and the z (beam) axis, denoted by $\theta_{\rm cand}$. Because of angular momentum conservation, continuum events distribute themselves according to $1+\cos^2\theta_{\rm cand}$ while signal B decays are flat in $\cos\theta_{\rm cand}$.

Each of the above eleven variables weakly distinguishes $B\bar{B}$ signal from continuum background. The cumulative power of these variables is harnessed by combining them in a multivariate linear discriminant, known as a Fisher discriminant ($\mathcal{F}$):

$$\mathcal{F} \equiv \sum_{i=1}^{11} \alpha_i x_i. \tag{4.5}$$

x_i denotes the input variables, and the coefficients α_i are chosen to maximize the separation between

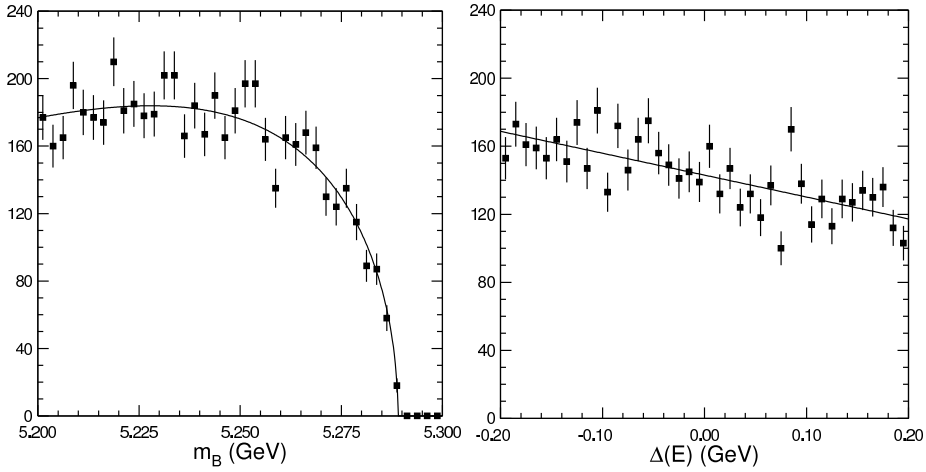

Figure 4.8: Continuum distributions for m_B (left) and ΔE (right) in the $K^0_S h^\pm \pi^\mp$ topology, obtained from off-resonance data.

signal and continuum:

$$\alpha_i = \sum_{j=1}^{11} (V_{ij}^{\rm cont} + V_{ij}^{\rm sig})^{-1} (\mu_i^{\rm cont} - \mu_i^{\rm sig}), \tag{4.6}$$

where $V_{ij}^{\rm cont}$ and $V_{ij}^{\rm sig}$ are the covariance matrix elements in the input variables for continuum and signal, respectively, and the μ_i are the mean values of the input variables. In the case of uncorrelated variables ($V_{ij} = 0$ for $i \neq j$), the coefficients become

$$\alpha_i = \frac{\mu_i^{\rm cont} - \mu_i^{\rm sig}}{(\sigma_i^{\rm cont})^2 + (\sigma_i^{\rm bkg})^2}. \tag{4.7}$$

Thus, the Fisher discriminant gives greatest weight to those variables with large separation and small variance.

The optimal coefficients were determined from off-resonance data and signal MC events and were found to be independent of B decay mode. Figure 4.12 shows the $\mathcal{F}$ distribution for off-resonance events selected for the $K^0_S h^\pm \pi^\mp$ topology and NR $B \to K^0_S \pi^+ \pi^-$ signal MC events. The Fisher discriminant provides separation of signal from continuum at the level of around 1σ.

4.2.4 Exclusive $b \to c$ Vetos

Figure 4.13 shows the Dalitz plots of the three topologies for off-resonance and $b \to c$ MC events that pass all selection criteria in a 3σ region in m_B and ΔE. The phase space scaling discussed in Section 5.3.1 is not applied in this Figure. The two-particle invariant masses are all calculated under the pion hypothesis for $h^\pm$. In the $K^0_S h^\pm \pi^\mp$ and $K^\pm h^\mp \pi^0$ topologies, each candidate contains two possibilities for $m_{K^0_S \pi^\pm}$ or $m_{\pi^\pm \pi^0}$. We choose the two-particle combination with the lower invariant

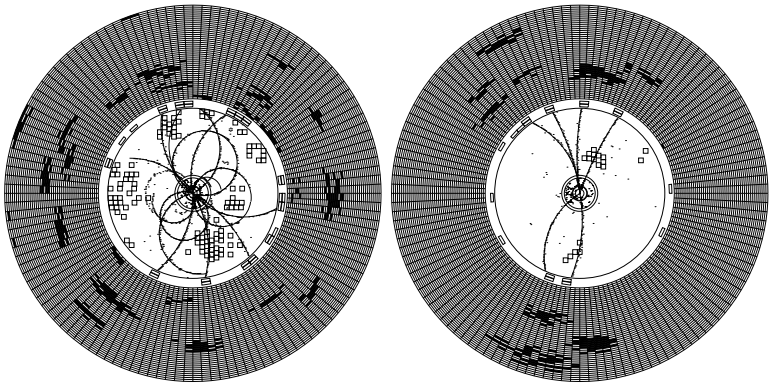

Figure 4.9: Comparison of event topologies for $B\bar{B}$ (left) and continuum (right) events. Tracks in the VD, PT, and DR are shown, along with hits in the TOF and barrel and endcap CC. The barrel CC is shown in the outermost region of each event, with the z coordinate mapped to radial distance from the IP.

mass so that the tracks forming the intermediate resonances are positively identified (according to the dE/dx selection criteria). For this reason, the Dalitz plots for these two topologies are "folded", with $m^2_{K^0_S\pi^\pm}$ and $m^2_{\pi^\pm\pi^0}$ each covering half the range it normally would. In the $K^\pm h^\mp\pi^0$ and $K^0_S h^\pm\pi^0$ topologies, the ranges of $m^2_{K^\pm\pi^\mp}$ and $m^2_{K^0_S\pi^\pm}$ are limited by the π^0 momentum cut.

The background from continuum events is most severe near the edges of the Dalitz plots, which is also where most of the intermediate resonances lie. In addition, several exclusive $b \to c$ decays enter this analysis with high rate. These processes have similar or identical final state particles as our much rarer signals and appear as horizontal or vertical bands in the Dalitz plot. To prevent these decays from overwhelming our potential signal, we impose the following vetos:

$K^0_S h^\pm\pi^\mp$:

- $|m_{K^0_S\pi^\pm} - 1.8693\ \text{GeV}| > 30$ MeV to reject $B \to D^\pm\pi^\mp$, $D^\pm \to K^0_S\pi^\mp$.
- $|m_{\pi^+\pi^-} - 3.1000\ \text{GeV}| > 50$ MeV to reject $B \to \psi K^0_S$, where $\psi \to \pi^+\pi^-$ or $\psi \to \mu^+\mu^-$ and the muons are not rejected by the muon veto.

$K^\pm h^\mp\pi^0$:

- $|m_{K^\pm\pi^\mp} - 1.8645\ \text{GeV}| > 30$ MeV for both $K\pi$ mass assignments to reject $B \to D^0\pi^0$, $D^0 \to K^+\pi^-$ and the charge conjugate decay.
- $|m_{\pi^+\pi^-} - 3.1000\ \text{GeV}| > 25$ MeV to reject $B \to \psi\pi^0$, where $\psi \to \pi^+\pi^-$ or $\psi \to \mu^+\mu^-$ and the muons are not rejected by the muon veto. This cut is looser than for $K^0_S h^\pm\pi^\mp$ because $B \to \psi\pi^0$ occurs much less frequently than $B \to \psi K^0_S$.

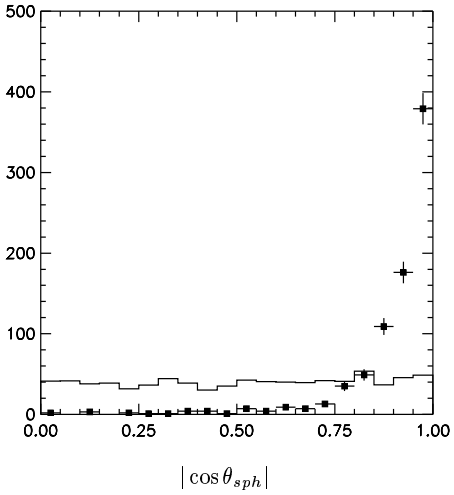

Figure 4.10: Distributions of $|\cos\theta_{\rm sph}|$ for signal (solid histogram) and continuum (points) events.

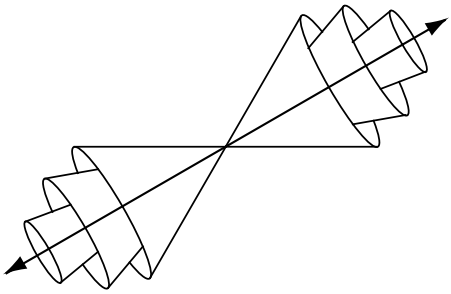

Figure 4.11: Illustration of the virtual calorimeter. Only three of the nine angular bins are shown.

- $|m_{\pi^\pm\pi^0} - 1.8693\ \text{GeV}| > 50$ MeV to reject $B \to D^\pm\pi^\mp$, $D^\pm \to \pi^\pm\pi^0$. No veto is necessary for $D^\pm \to K^\pm\pi^0$ since it is doubly Cabbibo-suppressed and, hence, occurs with low rate.

$K^0_S h^\pm\pi^0$:

- $|m_{K^0_S\pi^\pm} - 1.8693\ \text{GeV}| > 15$ MeV to reject $B \to D^\pm\rho(770)^\mp$ where a slow $\pi^\mp$ from the $\rho(770)^\mp$ is lost. These events accumulate at low values of ΔE (outside the signal region), so they do not appear in Figure 4.13.

- $|m_{K^0_S\pi^0} - 1.8600\ \text{GeV}| > 60$ MeV to reject $B \to D^0\pi^\pm$, $D^0 \to K^0_S\pi^0$ and the charge conjugate decay.

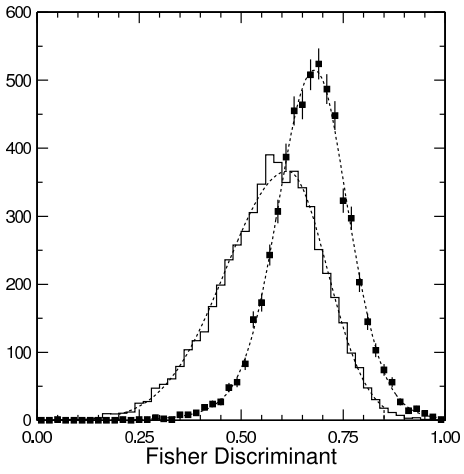

Figure 4.12: $\mathcal{F}$ for off-resonance events selected for the $K^0_S h^\pm \pi^\mp$ topology (points) and NR signal $B \to K^0_S \pi^+ \pi^-$ MC (solid histogram). The signal distribution has been scaled to the same area as the continuum distribution. The dotted lines show the parametrizations used for the maximum likelihood fit, as discussed in Section 5.2.3.

4.3 Multiple Combinations

The three-body signal topologies we consider include a final state particle with momentum typically below 1 GeV. Combinatoric background from fragmentation pions or from the decay of the other B in the event also populates this low-momentum region. Therefore, it is common to find multiple B candidates in each event. Signal decays produce an average of 1.4 candidates per event. However, the vast majority of these extraneous combinations lie outside the signal regions; typically there are only 1.03 candidates per signal event in a 3σ m_B-ΔE region. Therefore, the maximum likelihood fitter (see Chapter 5) will correctly identify the combinatoric background as such. In this analysis, we include all candidates with equal weight.

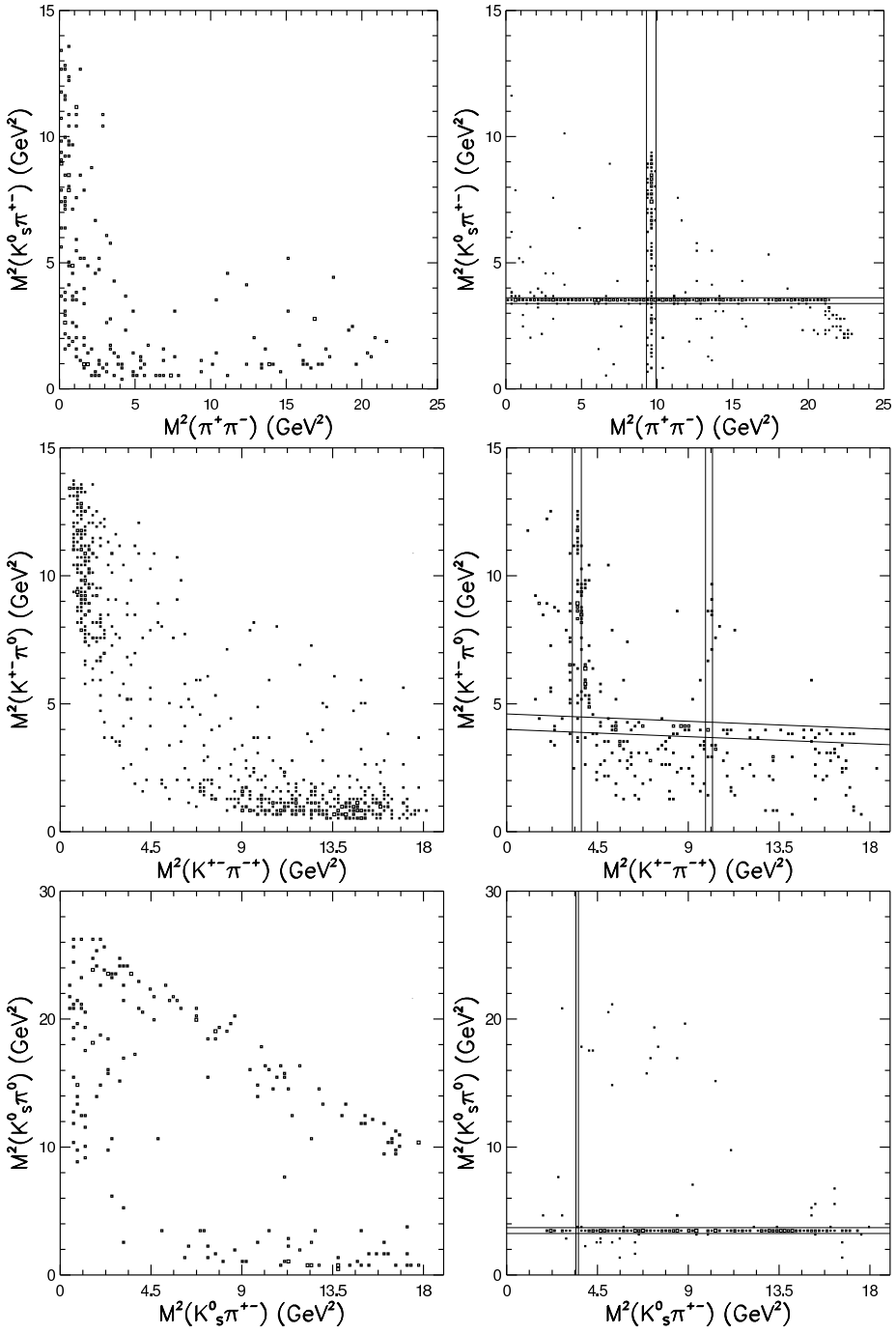

Figure 4.13: Dalitz plots of $B \to K^0_S h^\pm \pi^\mp$ (top), $K^\pm h^\mp \pi^0$ (middle), and $K^0_S h^\pm \pi^0$ (bottom) for off-resonance data (left) and $b \to c$ MC events (right) in a 3σ m_B-ΔE signal region passing all selection criteria except the D and ψ vetos. The horizontal and vertical lines demarcate the vetoed regions of the Dalitz plots.

Chapter 5 Maximum Likelihood Fit

An unbinned maximum likelihood fit is used to extract signal yields from the input sample. In the $K^0_S h^\pm \pi^\mp$, $K^\pm h^\mp \pi^0$, and $K^0_S h^\pm \pi^0$ topologies, the $h^\pm$ refers to the faster of the two tracks, which typically has momentum above 1 GeV. Because dE/dx provides limited separation of pions and kaons at these momenta, we make use of the dE/dx information for the $h^\pm$ in the likelihood fit, rather than imposing a tight selection requirement. The other input variables to the three-body inclusive fits are m_B, ΔE, $\mathcal{F}$, and $\cos\theta_B$, where θ_B is the angle between the flight direction of the reconstructed B and the z-axis. Each of these variables is discussed in Section 5.2. We fit simultaneously for contributions from $h^\pm = \pi^\pm$ and $h^\pm = K^\pm$. At high momentum, these two particle hypotheses are statistically separated by their dE/dx and by ΔE, each of which provides discrimination at the 1.7σ level for CLEO II and the 2.0σ level for CLEO II.V. For the Dalitz plot fits, we also include the two Dalitz plot variables as inputs.

In the maximum likelihood fits, we allow for three types of contributions: signal B decays, generic $b \to c$ background, and continuum background. The probability for an event to be consistent with a given component is the product of the probability distribution function (PDF) values for each of the input variables (neglecting correlations). The likelihood for each event is the sum of probabilities over the allowed components, with relative weights determined by maximizing the total likelihood of the sample, which is given by the following expression:

$$\mathcal{L} = \prod_{i=1}^{\#\text{events}} \left[\sum_{j=1}^{\#\text{components}} \left(f_j \prod_{k=1}^{\#\text{variables}} \mathcal{P}_{ijk} \right) \right]. \tag{5.1}$$

The $\mathcal{P}_{ijk}$ are the per event PDF values, and the f_j are the free parameters optimized by the fit and constrained to sum to unity. Since the PDFs are normalized to unit integral over the fit domain, the f_j can be interpreted as component fractions. The parameters of the dE/dx PDFs are measured from $D \to K^\pm \pi^\mp$ decays in data. For all other variables, the signal and $b \to c$ PDFs are determined from high-statistics Monte Carlo samples, and the continuum PDFs are determined from off-resonance data.

5.1 Correlations Among Variables

As given above, the joint probability for each event to belong to given component, $\prod_{k=1}^{\#\text{variables}} \mathcal{P}_{ijk}$, is calculated assuming the input variables are independent quantities. However, it is known that the detector resolution varies by 10%–20% according to the momenta of the final state particles.

The m_B and ΔE resolutions for signal are worse for symmetric decays than for asymmetric ones. A smaller variation in the resolution is caused by the level of combinatoric background, which increases with decreasing particle momentum (especially for π^0s). $\mathcal{F}$ also depends on the kinematics of the B candidate because it takes a global event shape parameter as one of its inputs.

The impact of correlations among the input variables is reduced by determining the m_B, ΔE, $\mathcal{F}$, and $\cos\theta_B$ PDFs as a function of the event location in the Dalitz plot, for twelve coarse bins in the $m^2_{K\pi}$-$m^2_{\pi\pi}$ plane for $K^0_S h^\pm \pi^\mp$ and ten bins for $K^\pm h^\mp \pi^0$ and $K^0_S h^\pm \pi^0$. These regions are shown in Figures 5.8–5.10. The use of these Dalitz-dependent PDFs results in shifts in signal yield of approximately 15% compared to the Dalitz-independent fits. The effect of any remaining correlations in the PDFs is assesed with a MC study, and we assign a systematic error accordingly (see Chapter 7).

5.2 Three-Body Inclusive Fits

We perform one inclusive fit for each topology, $K^0_S h^\pm \pi^\mp$, $K^\pm h^\mp \pi^0$, and $K^0_S h^\pm \pi^0$, allowing for six components, pion and kaon hypotheses for $h^\pm$ for each of the following: signal, continuum background, and background from $b \to c$ decays. The same PDF parameters are used for CLEO II and II.V except for signal ΔE and the dE/dx variables because both of these have improved resolution in CLEO II.V.

Figure 5.1 shows a schematic table of PDF shapes, omitting the variables and components that describe K/π separation (except ΔE). As described below, the dE/dx PDFs are simply bifurcated Gaussians, and their parametrizations do not vary with type of component.

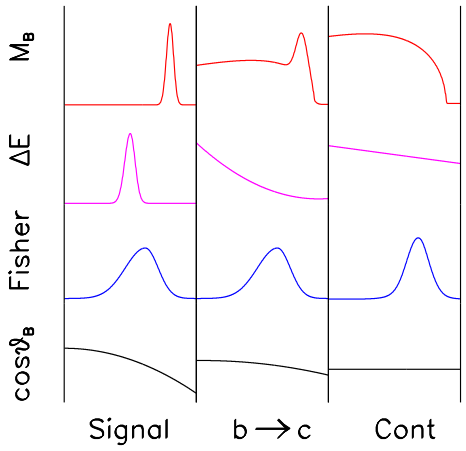

Figure 5.1: PDF shapes for three-body inclusive fits.

The combinatoric background in signal decays creates long tails in the m_B and ΔE distributions,

which are visible in Figure 4.7. Modeling these tails in the PDFs introduces a bias that allows backgrounds to be identified as signal: the fit assumes these two variables to be uncorrelated, but in reality, the tails in the two variables coincide; events in the m_B tail do not peak in ΔE and vice versa. To avoid describing these two variables by a two-dimensional PDF, we truncate the tails of these distributions, and, to measure the signal PDFs, the domain is restricted to a 3σ region around the m_B and ΔE peaks. Thus, the combinatoric background from signal events is not classified as signal, resulting in a fit efficiency of 60%–90%, depending on mode.

Having given a general description of the PDFs and how they are determined, we discuss the notable features of each of the input variables in turn.

5.2.1 Beam-Constrained Mass

The parametrizations of the m_B PDFs for signal and continuum were given in Section 4.2.1. All signal modes in a given topology share a common m_B PDF.

For generic $b \to c$ decays, the m_B distribution consists of a combination of an Argus function and a Gaussian peak at the B mass, as illustrated in Figure 5.1. The peak is caused by candidates with $\Delta E < -40$ MeV and $1.4 < m_{K^0_S\pi^\pm} < 2.2$ GeV, as shown in Figure 5.2. The MC generator-level information for events in this region reveals that about 75% result from $B \to D\pi$, where $D^\pm \to K^0_S K^\pm$ (and the $K^\pm$ is reconstructed as a $\pi^\pm$) or where $D \to K\rho(770)$, $K^*(892)\pi$, or $K\mu\nu$, and a pion or neutrino is lost. The remaining candidates in this region are random combinations but always in the presence of a $B \to D^{(*)}h^\pm$ decay.

In order to incorporate our knowledge of this correlation into the fit, the parametrization of the m_B PDF is allowed to vary with ΔE. For $\Delta E < -40$ MeV, the PDF is represented by an Argus function plus a Gaussian peak. For $\Delta E > -40$ MeV, the Gaussian is removed, and the PDF is renormalized to unit area. The measurement of the PDFs in bins across the Dalitz plot accounts for the dependence of the peak size on $m_{K\pi}$.

5.2.2 ΔE

The ΔE PDFs for the signal components are parametrized by bifurcated Gaussians. For the $K^*\pi^\pm$ modes, ΔE is evaluated assuming the $h^\pm$ is a $\pi^\pm$, so the Gaussian is centered at zero. Since the $h^\pm$ in these decays is monoenergetic, the ΔE PDFs for the $K^*K^\pm$ modes are taken to be identical to those for $K^*\pi^\pm$, except shifted by -45.2 MeV. The CLEO II.V detector benefits from an improvement in tracking resolution over CLEO II, resulting in ΔE resolutions that differ by about 23%. Therefore, the signal PDFs for the different datasets use the corresponding ΔE widths, as measured from signal MC. The variation of the ΔE widths among the signal modes in a given topology is negligible, and we apply a common ΔE PDF. For NR decays, where the $h^\pm$ is not monoenergetic, we ignore the

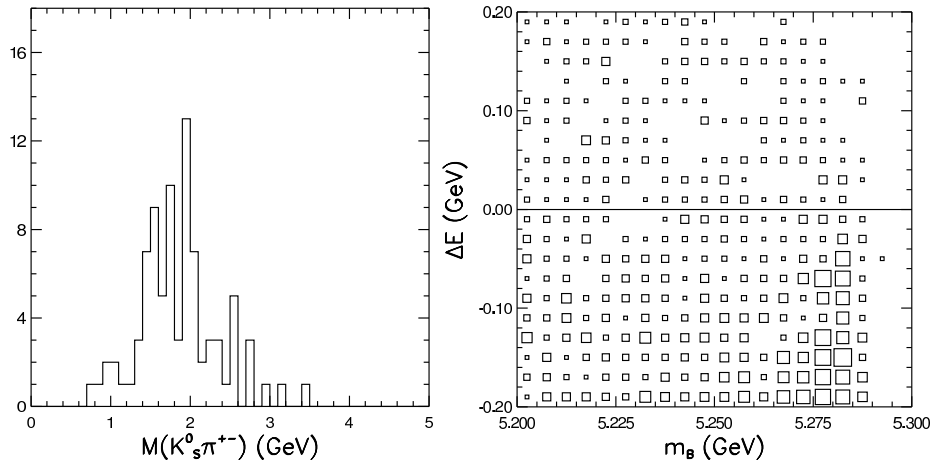

Figure 5.2: $m_{K^0_S\pi^\pm}$ distribution for $b \to c$ MC events in the $K^0_S\pi^+\pi^-$ m_B-ΔE signal region (left). m_B vs. ΔE for $b \to c$ MC events with $1.4 < m_{K^0_S\pi^\pm} < 2.2$ GeV (right).

slight broadening of ΔE for $h^\pm = K^\pm$,

The continuum ΔE distribution is described by a first-order polynomial, and that for $b \to c$ decays by a second-order polynomial. In both cases, the same PDFs are used for CLEO II and CLEO II.V.

5.2.3 Fisher Discriminant

All signal and $b \to c$ components in a given topology share the same $\mathcal{F}$ PDF, which is parameterized by a bifurcated Gaussian. For the continuum $\mathcal{F}$ PDF, care is taken in describing the tails on the low side. If the continuum likelihoods at low values of $\mathcal{F}$ are underestimated, then the significance of an excess in this region can be artificially enhanced. The functional form for the continuum PDF is chosen to be the sum of a Gaussian, a bifurcated Gaussian, and a Breit-Wigner, based on a high-statistics sample from off-resonance data of B candidates in the $h^\pm h^\mp h^\pm$ or $h^\pm h^\mp \pi^0$ topologies. Examples of signal and continuum PDFs along with their parametrizations are shown in Figure 4.12.

5.2.4 B Flight Direction

We define θ_B to be the angle between the flight direction of the reconstructed B and the z-axis. Angular momentum conservation results in different distributions for $\cos\theta_B$ in $B\bar{B}$ and continuum decays. Since B mesons from $\Upsilon(4S)$ decays are produced in a P-wave with $L_z = \pm 1$, they have a preferred flight direction, exhibiting a $1-\cos^2\theta_B$ dependence. On the other hand, the flight direction of misreconstructed B candidates is random, so candidates from continuum are flat in $\cos\theta_B$. The distribution for $b \to c$ decays is a mixture of those for signal and continuum candidates, as shown

in Figure 5.3.

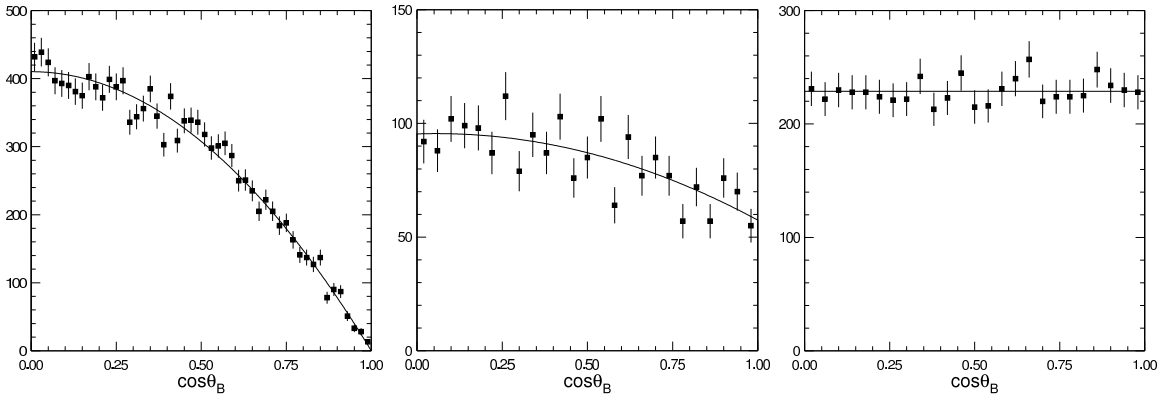

Figure 5.3: Distributions of $\cos\theta_B$ for non-resonant $B \to K^0_S\pi^+\pi^-$ MC events (left), $b \to c$ MC events (center), and continuum events (right) in the $K^0_S h^\pm \pi^\mp$ topology.

5.2.5 *dE/dx*

The PDFs for the normalized dE/dx variables, $\sigma^\pi_{dE/dx}$ and $\sigma^K_{dE/dx}$, are the same for signal, $b \to c$ decays, and continuum components. However, the improved K/π separation in the CLEO II.V data (2.0σ) over CLEO II (1.7σ) reduces the crossfeed between the particle hypotheses. Furthermore, the shapes are sufficiently different between CLEO II and II.V to warrant the use of separate PDFs for the two datasets. We only consider $\sigma^\pi_{dE/dx}$ for $h^\pm = \pi^\pm$ and $\sigma^K_{dE/dx}$ for $h^\pm = K^\pm$. The PDFs are modeled as bifurcated Gaussians, and their parameters are determined separately for CLEO II and II.V as well as for positive and negative charges, using charged daughters of D^*-tagged D^0 decays with momenta between 2.3 and 2.9 GeV. The results of these measurements are reproduced in Table 5.1.

Particle	Mean	σ_{left}	σ_{right}
CLEO II π^+	-0.09 ± 0.09	0.91 ± 0.06	1.16 ± 0.07
CLEO II π^-	-0.15 ± 0.08	0.86 ± 0.05	1.21 ± 0.07
CLEO II.V π^+	-0.02 ± 0.08	0.90 ± 0.05	1.06 ± 0.06
CLEO II.V π^-	-0.00 ± 0.08	0.91 ± 0.05	1.04 ± 0.05
CLEO II K^+	-0.11 ± 0.07	0.96 ± 0.06	1.13 ± 0.06
CLEO II K^-	-0.07 ± 0.08	0.94 ± 0.05	1.13 ± 0.06
CLEO II.V K^+	-0.05 ± 0.08	0.86 ± 0.05	1.03 ± 0.05
CLEO II.V K^-	-0.06 ± 0.07	0.89 ± 0.05	1.08 ± 0.05

Table 5.1: Parameters of the bifurcated-Gaussian dE/dx PDFs for CLEO II and CLEO II.V.

5.2.6 Double Particle Misidentification

For the two NR modes $K^0_S K^\pm \pi^\mp$ and $K^\pm \pi^\mp \pi^0$, the ΔE distribution acquires a tail on one side, and the $\sigma^{K/\pi}_{dE/dx}$ distribution of the high-momentum $h^\pm$ is centered halfway between the pion and kaon hypotheses (see Figures 5.4 and 5.5). This broadening of both distributions is correlated and is caused by misidentifying both tracks in the signal decay. For $B \to K^0_S K^\pm \pi^\mp$ events in the fit domain, one of the tracks often has momentum around 2.6 GeV, and the other between 0.5 and 1.5 GeV so that $m_{K^0_S \pi^\pm}$ or $m_{K^\pm \pi^0}$ lies between 0.7 and 1.8 GeV. Kaons and pions are indistinguishable by their dE/dx around 1 GeV, so the 3σ requirement on the slower track accepts both kaons and pions. When the slower track is misidentified, the faster one is as well. The two misidentifications shift ΔE in opposite directions, but the size of the shift is larger for the slower track. Therefore, the one-sided tail in ΔE coincides with the portion of the $\sigma^{K/\pi}_{dE/dx}$ distribution shifted from zero. This correlated broadening does not exist for the partner modes, $K^0_S \pi^+ \pi^-$ and $K^+ K^- \pi^0$, because it is impossible to misidentify a *signal* decay in the same way.

It was found that modeling this ΔE-$\sigma^{K/\pi}_{dE/dx}$ correlation in the fitter resulted in large positive biases for the NR component in question. The effect is akin to including the combinatoric tails in the m_B and ΔE PDFs; these broadened PDFs allow background events to be classified as signal more easily. To prevent this bias, we truncate the tails in the ΔE PDFs for these two components, and the $\sigma^{K/\pi}_{dE/dx}$ PDFs take the standard form given in Section 5.2.5. For this reason, the fit efficiencies for $K^0_S K^\pm \pi^\mp$ and $K^\pm \pi^\mp \pi^0$ are 30%–50% lower than for $K^0_S \pi^+ \pi^-$ and $K^+ K^- \pi^0$. Any residual bias in the form of crossfeed between components is measured using the technique described in Section 5.2.8.

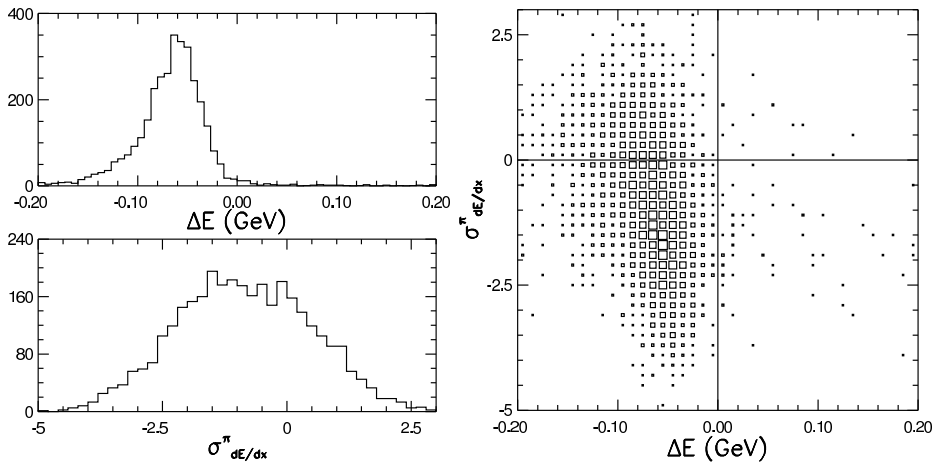

Figure 5.4: Distributions of ΔE and $\sigma^\pi_{dE/dx}$ of the $h^\pm$ in $B \to K^0_S K^\pm \pi^\mp$. On the left are projections of the two-dimensional $\sigma^\pi_{dE/dx}$ vs. ΔE histogram.

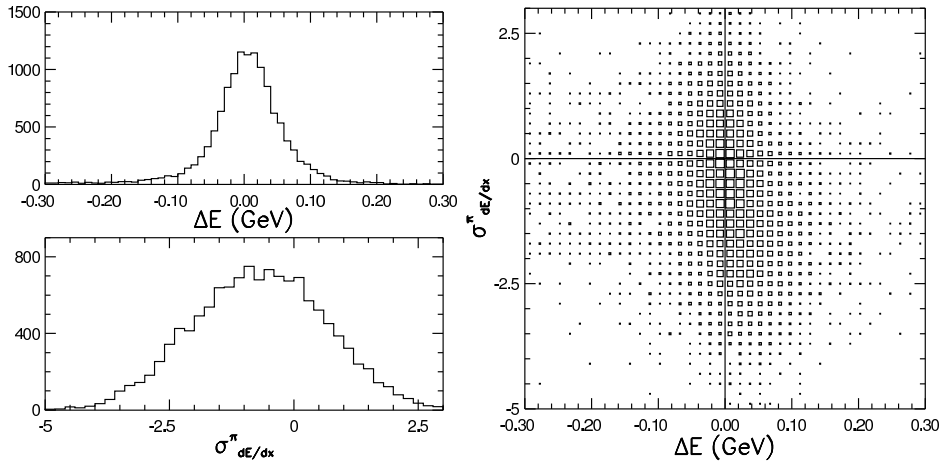

Figure 5.5: Distributions of ΔE and $\sigma^{\pi}_{dE/dx}$ of the $h^{\pm}$ in $B \to K^{\pm}\pi^{\mp}\pi^0$. On the left are projections of the two-dimensional $\sigma^{\pi}_{dE/dx}$ vs. ΔE histogram.

5.2.7 Fitter Performance

We have verified that our maximum likelihood fitter provides an unbiased and efficient estimate of the fraction of signal events in a given sample. This study was performed by generating random events according to the measured PDFs for each variable (hereafter referred to as "toy" Monte Carlo). Then, this sample was fitted as one would a real data sample. We form an ensemble of such experiments, where the number of generated signal events is allowed to undergo Poisson fluctuations around a given mean. The performance of the fitter is evaluated by subtracting the number of signal events from the nominal value and then dividing by the yield uncertainty, giving a figure of merit known as the pull. For an unbiased efficient estimator, the pull distribution should be a unit Gaussian centered at zero. Figure 5.6 shows the results of generating an ensemble of experiments similar in composition to the inclusive $K^0_S h^{\pm}\pi^{\mp}$ on-resonance fit. We obtain similar results in other ensembles of experiments containing different signal components and different ratios of signal to background events.

5.2.8 Efficiency Measurement

For each mode where we observe no yield, *i.e.*, the three $\bar{K}K\pi$ modes, we measure the selection and fit efficiencies for three assumptions of resonant substructure: $K^*(892)K^{\pm}$, $K^*_0(1430)K^{\pm}$, and NR $\bar{K}K\pi$. The fit efficiency is measured from a single fit of all the available MC for each (non-)resonant mode with the off-resonance data. We then use the lowest combined efficiency among these three to establish conservative branching fraction upper limits. In the $K^0_S h^{\pm}\pi^{\mp}$ topology, we find, from MC studies, no crossfeed between $K^0_S\pi^+\pi^-$ and $K^0_S K^{\pm}\pi^{\mp}$. In the other two topologies,

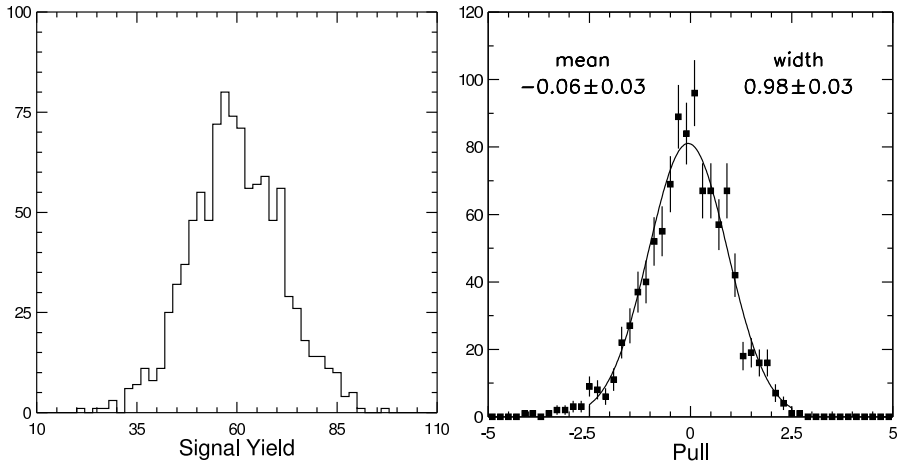

Figure 5.6: Number of signal events returned by the fitter (left) and its pull distribution (right) for toy Monte Carlo. The average number of generated signal events is 60.

there is measurable crossfeed between $K\pi\pi$ and $\bar{K}K\pi$, but the $\bar{K}K\pi$ yields are identically zero, so no crossfeed occurs in practice.

We employ a different procedure for modes with non-zero yields, *i.e.*, the three $K\pi\pi$ modes. Both the selection and fit efficiencies for these three-body final states vary with the momenta of the final state particles; low momentum particles experience reduced detection efficiency and higher combinatoric background. The size of the variation can be as large as a factor of five in either direction. We reduce the model dependence of our branching fractions by measuring the efficiencies in bins across the Dalitz plot. These efficiency histograms are smoothed according to the algorithm described in Section 5.3.1, and a correction is applied to each entry in the fit.

Since NR MC events uniformly populate the available phase space at generator level, we take the Dalitz plot of simulated NR events entering the fit to be the numerator of the selection efficiency. The denominator is the integral of phase space in each Dalitz plot bin, scaled to the number of generated MC events.

The fit efficiency is measured in the presence of background to mimic the situation in real data as closely as possible. We construct an ensemble of experiments that combine toy MC for the $b \to c$ and continuum components and fully-simulated MC for the signal components. The high-statistics pools of signal MC consist of mixtures of resonant and NR decays. For each of the 1000 experiments in the ensemble, we randomly draw 80, 60, or 30 events for $K^0_S\pi^+\pi^-$, $K^\pm\pi^\mp\pi^0$, or $K^0_S\pi^\pm\pi^0$, respectively, and embed these in enough toy continuum and $b \to c$ MC to match the fit sample size with on-resonance data. We record the Dalitz plot coordinates of the embedded signal events to form the denominator of the fit efficiency histogram. For the numerator, we identify the events labeled as signal by the fit by weighting each event (embedded signal or toy background) by

its signal probability:

$$\mathcal{P}_{\rm sig} \equiv \frac{f_{\rm sig}\mathcal{L}_{\rm sig}}{\sum_{i=1}^{\#\ \rm components} f_i\mathcal{L}_i}, \tag{5.2}$$

where the f_i are the component fractions optimized by the fit. The sum of all weights is the signal yield reported by the fit, and Dalitz plot of these weighted events is the fit efficiency numerator.

Examples of the numerators and denominators for the fit and selection efficiencies are shown in Figure 5.7. To correct the on-resonance yields, the signal probability of each event is divided by the product of selection and fit efficiencies from the smoothed histograms. The efficiencies listed in Table 6.1 are averages over the signal events. Because the signal events do not carry uniform weight, the products of the average selection and fit efficiencies do not equal the average total efficiencies. Using the above ensembles of MC experiments, we find no evidence for crossfeed between the $K\pi\pi$ and $\bar{K}K\pi$ signal components in the $K^0_S h^\pm\pi^\mp$ topology. In the other two topologies, where no significant signals are observed, we ignore the crossfeed of 5%–10% to establish conservative upper limits.

5.3 Dalitz Plot Fit

While it is possible to detect strong signals when one ignores the resonant substructure in the three-body final state, it is difficult to interpret these signals theoretically. More useful than these inclusive measurements are observations of NR transitions, or better yet, quasi-two-body decays with an intermediate resonance. We search for these exclusive decays by adding the two Dalitz plot variables as inputs to the fit, described by a two-dimensional PDF. We neglect interference among these various processes, and the implications of this simplification are discussed in Section 7.2.1.

The charmless resonances we choose to reconstruct are ones with mass below the D mass and with sizeable branching fractions to $K\pi$ or $\pi\pi$, namely the vectors $\rho(770)$ and $K^*(892)$, and the scalars $f_0(980)$ and $K^*_0(1430)$. We omit $\Delta S = 0$ transitions unless there is K/π ambiguity in a high momentum track. The signal modes considered for each topology are given in Table 5.2. We do not include the mode $B \to \rho(770)^\mp K^\pm$ in the $K^\pm h^\mp\pi^0$ topology because of low efficiency. In signal decays, the daughter $\pi^\mp$ of the $\rho(770)^\mp$ has lower momentum than the primary $K^\pm$, so it must pass a $\left|\sigma^K_{dE/dx}\right| < 3$ cut, according to our selection criteria. Because we also require $p_{\pi^0} > 1$ GeV, the momenta of the $\pi^\mp$ candidates lie below 1 GeV, with the spectrum peaking at 600 MeV. At these momenta, the $\pi^\mp$ tends to fail the $\sigma^K_{dE/dx}$ requirement, resulting in a selection efficiency of only 2%.

Figures 5.8–5.10 show the Dalitz plots for all the components in the three topologies. Modes with K/π ambiguity use the same Dalitz PDF for $h^\pm = \pi^\pm$ as for $h^\pm = K^\pm$. The two-particle invariant masses are all calculated under the pion hypothesis for $h^\pm$.

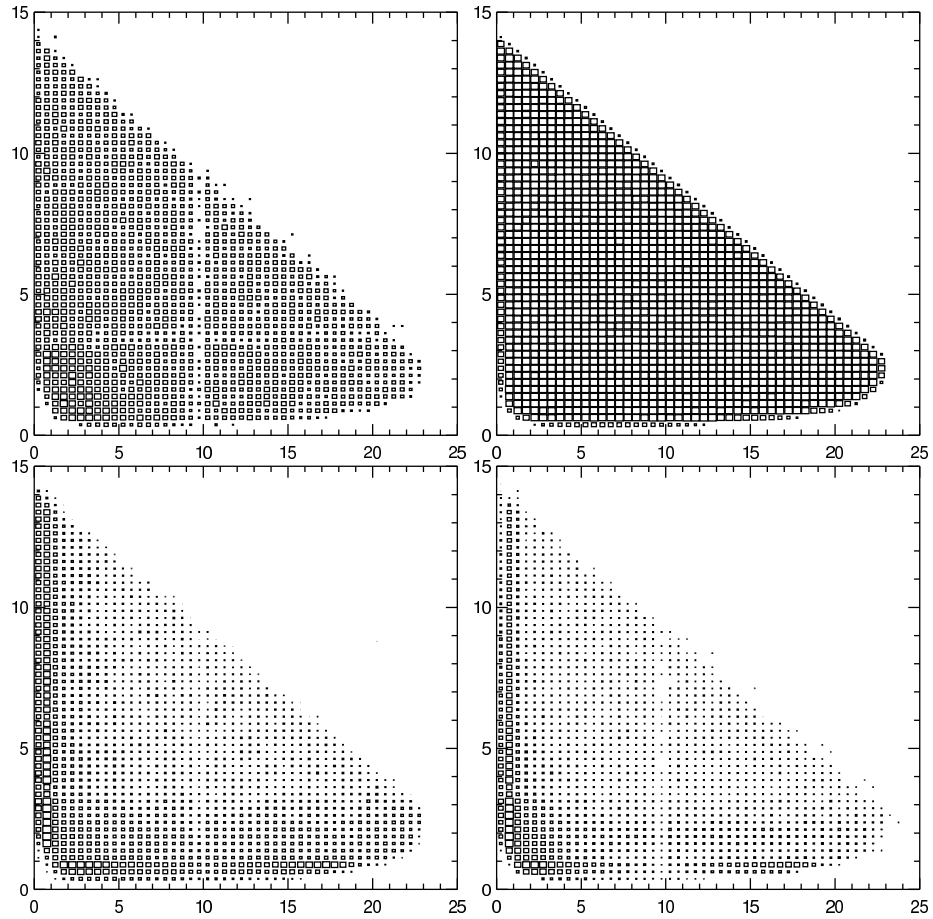

Figure 5.7: $B \to K^0_S\pi^+\pi^-$ Dalitz plots ($m^2_{K^0_S\pi^\pm}$ vs. $m^2_{\pi^+\pi^-}$ in GeV^2) forming the numerators (left) and denominators (right) of the selection (top) and fit (bottom) efficiencies.

5.3.1 Dalitz Plot PDF

Unlike the PDFs used in the inclusive fit, which are smooth functions of the input variables, the Dalitz plot PDF is represented by a two-dimensional histogram. At leading order, the value of the PDF at a given point is the contents of the bin containing that point ($N_{\rm bin}$), normalized by the sum over all bins ($N_{\rm total}$) and by the bin width (w) in each dimension: $\mathcal{P}_{\rm Dalitz} = N_{\rm bin}/(N_{\rm total} w_x w_y)$. To reduce the loss of information caused by binning the PDF, we introduce a first order correction that smooths the histogram. Figure 5.11 shows a data point (X) that lands in the (i,j)-th bin. We construct a box around the data point (shaded) with the same dimensions as the histogram bins. This box overlaps with the bin containing the data point and with three adjacent bins. To calculate the PDF value, we average the contents of these four bins, each weighted by the area of the overlap

$K^0_S h^\pm \pi^\mp$	$K^\pm h^\mp \pi^0$	$K^0_S h^\pm \pi^0$
$K^*(892)^+(K^0_S\pi^+)\pi^-$	$K^*(892)^+(K^+\pi^0)\pi^-$	$K^*(892)^0(K^0_S\pi^0)\pi^+$
$K^*(892)^+(K^0_S\pi^+)K^-$	$K^*(892)^+(K^+\pi^0)K^-$	$\bar{K}^*(892)^0(K^0_S\pi^0)K^+$
$K^*_0(1430)^+(K^0_S\pi^+)\pi^-$	$K^*_0(1430)^+(K^+\pi^0)\pi^-$	$K^*_0(1430)^0(K^0_S\pi^0)\pi^+$
$K^*_0(1430)^+(K^0_S\pi^+)K^-$	$K^*_0(1430)^+(K^+\pi^0)K^-$	$\bar{K}^*_0(1430)^0(K^0_S\pi^0)K^+$
$\rho(770)^0(\pi^+\pi^-)K^0$	$K^*(892)^0(K^+\pi^-)\pi^0$	$K^*(892)^+(K^0_S\pi^+)\pi^0$
$f_0(980)(\pi^+\pi^-)K^0$	$K^*_0(1430)^0(K^+\pi^-)\pi^0$	$K^*_0(1430)^+(K^0_S\pi^+)\pi^0$
$K^0\pi^+\pi^-$ NR	$K^+\pi^-\pi^0$ NR	$\rho(770)^+(\pi^+\pi^0)K^0$
$\bar{K}^0K^+\pi^-$ NR	$K^+K^-\pi^0$ NR	$K^0\pi^+\pi^0$ NR
		$\bar{K}^0K^+\pi^0$ NR

Table 5.2: Modes considered for Dalitz plot fits. Charge conjugation is implied.

in each bin:

$$\mathcal{P}_{\text{Dalitz}} = \frac{[N_{i,j}(w_x - \Delta x) + N_{i-1,j}\Delta x]\,(w_y - \Delta y) + [N_{i,j+1}(w_x - \Delta x) + N_{i-1,j+1}\Delta x]\,\Delta y}{N_{\text{total}} w_x w_y}. \quad (5.3)$$

When the box around the data point crosses over the histogram boundary, we remove the terms in Equation 5.3 corresponding to the non-existent bins and reweight the remaining bins appropriately. This procedure is equivalent to performing a first order Taylor expansion in two dimensions.

The $b \to c$ and continuum Dalitz PDFs suffer from limited statistics which are spread across the full range of the Dalitz plot. As a result, the sparsely populated regions of these histograms contain many bins with zero entries, when in reality, the probability is small but finite. Therefore, we add an additional step to the smoothing procedure for these two PDFs, as well as for the NR PDF. If the average of the four bins (the numerator in Equation 5.3) is less than 10, then the area around the data point is expanded to 9 bins (3×3), then to 25 (5×5) bins, and so forth, until at least 10 events are included in the sum (which gives a 3σ measurement of the probability density). This sum is then corrected for the area of the expanded box around the data point. Area expansion is not invoked for the resonant two-body PDFs because it effectively creates long tails extending into regions of the Dalitz plot far from the resonances. Such tails would bias the fit, enhancing the yield for these signal modes.

The choice of bin size for the Dalitz PDFs is driven by the amount of MC available. Since we have sufficient statistics for the signal components, the binning can be made (almost) arbitrarily fine, and we choose it so that the most populous bins contain 30–40 events, giving typical bin widths of 0.05–0.15 GeV^2. For the NR, $b \to c$, and continuum PDFs, the bins are not allowed to straddle the boundary of the physical region. Otherwise, the probability density in these bins would be underestimated. Because the resonances we consider also occupy the edge of the Dalitz plot, events

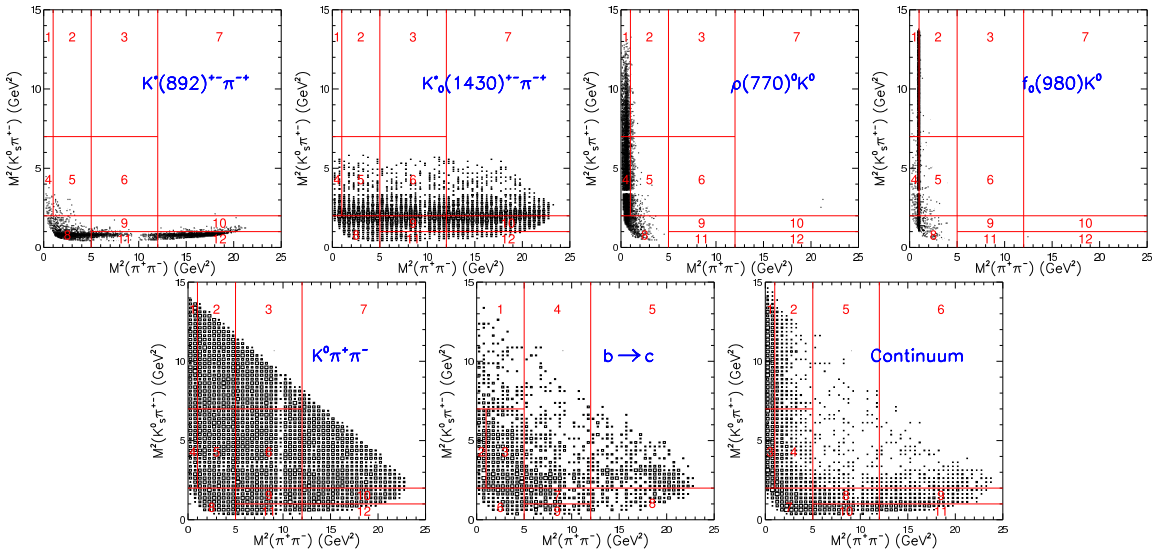

Figure 5.8: Dalitz PDFs for the $K^0_S h^\pm \pi^\mp$ topology. The twelve large bins are the ones used to measure all the other PDFs.

falling in these edge bins would have an artificially enhanced signal to background probability ratio, leading to a biased fit. This problem is overcome by reducing the bin size past a threshold determined by the masses of the final state particles. The bin sizes chosen for the NR, $b \to c$, and continuum PDFs in the three topologies are

- $K^0 h^+ \pi^-$: 0.50 GeV^2 $(m^2_{\pi^+\pi^-}) \times 0.25$ GeV^2 $(m^2_{K^0_S\pi^-})$
- $K^+ h^- \pi^0$: 0.50 GeV^2 $(m^2_{K^+\pi^-}) \times 0.50$ GeV^2 $(m^2_{K^+\pi^0})$
- $K^0_S h^+ \pi^-$: 0.37 GeV^2 $(m^2_{K^0_S\pi^-}) \times 0.40$ GeV^2 $(m^2_{K^0_S\pi^0})$.

In this regime, bin size variations cause shifts in yield of about 15%. This effect is included in the systematic errors.

One additional issue pertains to the $K^0_S h^\pm \pi^0$ topology. The boundaries of the physical region on the horizontal and vertical edges of the Dalitz plot are fixed by the masses of the final state particles. However, the distance of the diagonal boundary from the origin is determined by the invariant mass of the three-body system. In this analysis, we accept B candidates with a large range of invariant mass (not beam-constrained mass): 4.85–5.55 GeV. So, while the continuum and $b \to c$ Dalitz plots have dense bands along the horizontal and vertical edges, their diagonal bands are smeared by the B candidate's invariant mass. As a result, the continuum and $b \to c$ Dalitz probabilities for events in the diagonal band are reduced by as much as an order of magnitude, thereby biasing the fit towards large signal yields.

In principle, there is information in this spread; candidates with large invariant mass will be far

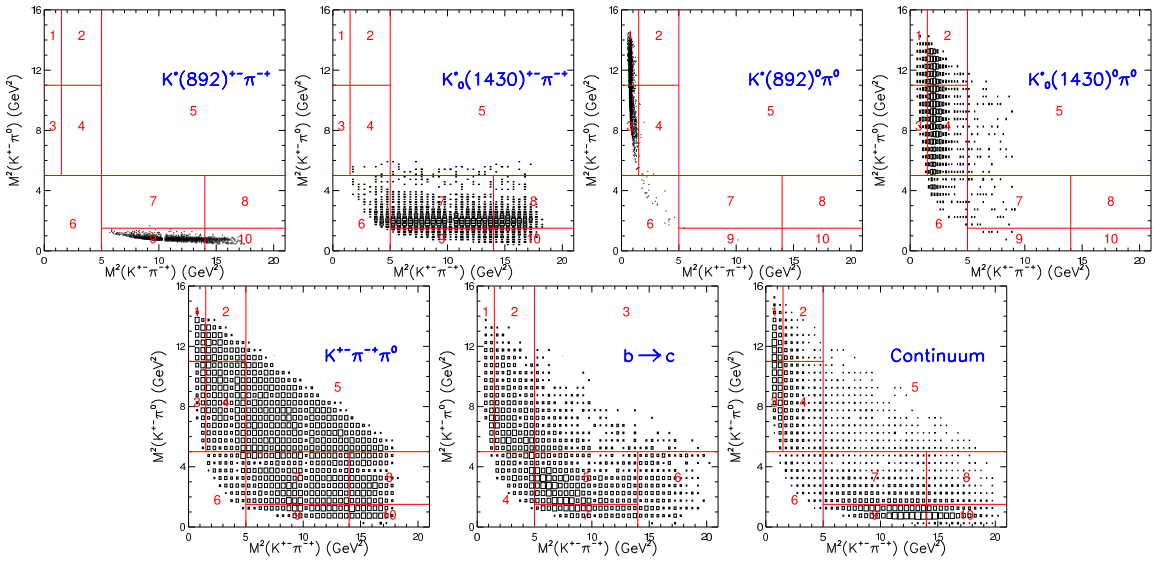

Figure 5.9: Dalitz PDFs for the $K^{\pm}h^{\mp}\pi^0$ topology. The ten large bins are the ones used to measure all the other PDFs.

from the origin. This correlation could be introduced into the fit by measuring the Dalitz PDF as a function of B invariant mass. However, there is insufficient off-resonance data and $b \to c$ MC to permit these measurements. Instead, we eliminate this correlation by scaling the Dalitz variables for all candidates to a uniform invariant mass. For the decay $B \to abc$, the two-body invariant mass m_{ab} is scaled as follows:

$$m_{ab}^2 \to [m_{ab}^2 - (m_a + m_b)^2]\frac{(m'_B - m'_c)^2 - (m'_a + m'_b)^2}{(m_B - m_c)^2 - (m_a + m_b)^2} + (m'_a + m'_b)^2. \tag{5.4}$$

The primed masses are the known masses taken from Reference [5]. For tracks and π^0s, the primed and unprimed masses are identical (the π^0 four-momentum used to form the B candidate has a mass constraint imposed). Figure 5.12 shows the off-resonance Dalitz plot before and after the scaling. This transformation effectively unifies the size of the available phase space for all candidates and creates a dense diagonal edge in the Dalitz plot. The other two topologies, $K^0_S h^{\pm}\pi^{\mp}$ and $K^{\pm}h^{\mp}\pi^0$, do not require phase space scaling because we do not consider any resonances that lie on the diagonal of the Dalitz plot.

5.3.2 Fit Efficiencies

The fit efficiency matrix is again measured with fully simulated signal MC embedded in toy continuum and $b \to c$ background MC, as described in Section 5.2.8, but with different signal pools. A simple implementation of this method would use one ensemble of fits for each of the n signal

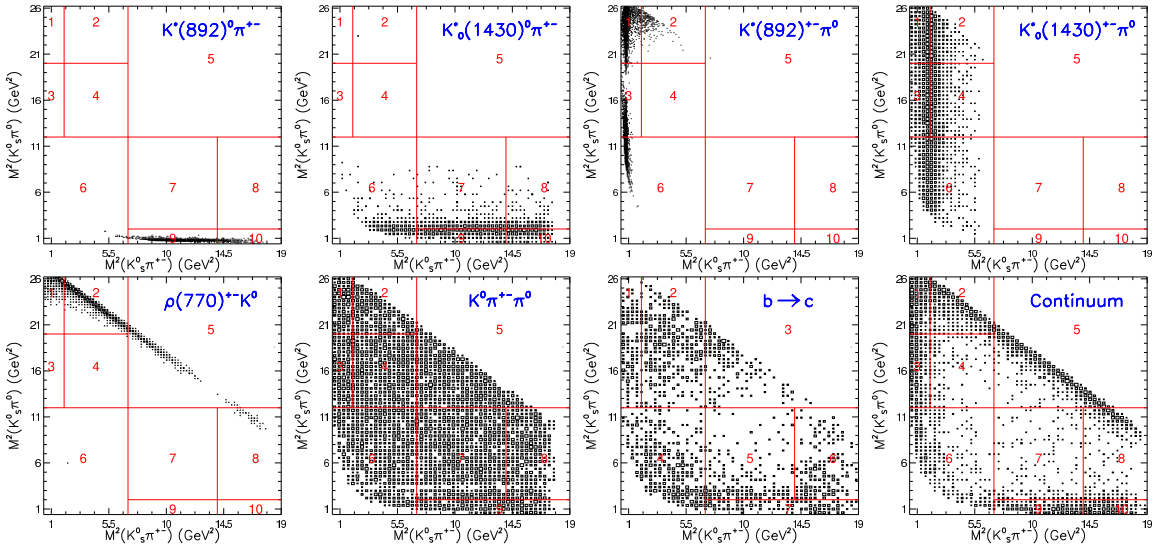

Figure 5.10: Dalitz PDFs for the $K^0_S h^\pm \pi^0$ topology. The ten large bins are the ones used to measure all the other PDFs.

components, with each signal pool containing a single species of signal MC. However, the presence of other signal components affects both the efficiency and the crossfeed. In the Dalitz fits of on-resonance data, we find that the inclusive three-body yields are distributed among the signal components. Therefore, a more accurate measurement of the fit efficiency matrix would be obtained from mixtures of different signal species, instead of pure signal pools of one type. Using n mixtures of varying compositions, we construct two $n \times n$ matrices, one for the true average yields ($\mathbf{A}$), and one for the measured average yields ($\mathbf{M}$) of each signal component. Each ensemble of fits for a given signal pool provides measurements for one column of $\mathbf{A}$ and one column of $\mathbf{M}$. Each of the n signal pools contains MC for all the signal components except one. Therefore, all the diagonal elements of $\mathbf{A}$ are zero. To obtain the efficiency matrix $\mathbf{T}$, we note that $\mathbf{A}$ and $\mathbf{M}$ satisfy the following relation: $\mathbf{TA} = \mathbf{M}$. Hence, we can solve for $\mathbf{T}$ by inverting $\mathbf{A}$: $\mathbf{T} = \mathbf{MA}^{-1}$. The resultant efficiency matrices are shown in Tables 5.3–5.5.

As a simplification, all matrix elements in Tables 5.3, 5.4, and 5.5 that are consistent ($< 3\sigma$)

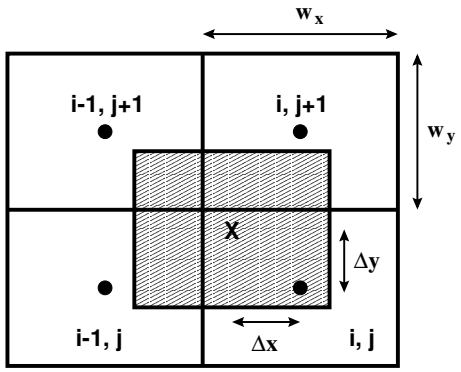

Figure 5.11: Illustration of the Dalitz PDF smoothing algorithm.

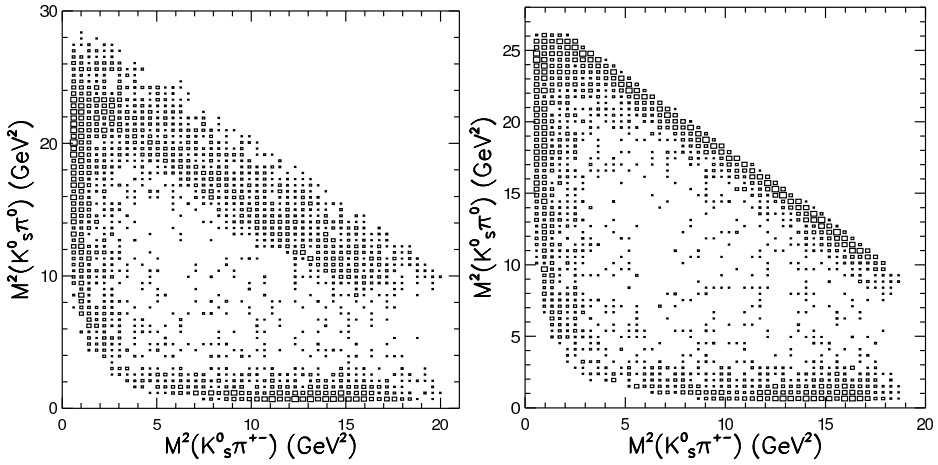

Figure 5.12: $K^0_S h^\pm \pi^0$ off-resonance Dalitz plot without (left) and with (right) phase space scaling.

with zero and with absolute value less than 7.5% are set to zero, resulting in the following matrices:

$$\mathbf{T}_{K^0_S h^\pm \pi^\mp} = \begin{pmatrix} 0.684 & 0 & 0 & 0 & 0 & 0 & 0 & 0 \\ 0 & 0.554 & 0 & 0 & 0 & 0 & 0 & 0 \\ 0 & 0 & 0.724 & 0 & 0 & 0 & 0 & 0 \\ 0 & 0 & 0 & 0.529 & 0 & 0 & 0 & 0.102 \\ 0 & 0 & 0 & 0 & 0.509 & 0 & 0 & 0 \\ 0 & 0 & 0 & 0 & 0 & 0.582 & 0 & 0 \\ 0 & 0 & 0 & 0 & 0 & 0 & 0.749 & 0 \\ 0 & 0 & 0 & 0.085 & 0 & 0 & 0 & 0.289 \end{pmatrix} \tag{5.5}$$

$\mathbf{T}_{K^0_S h^\pm \pi^\mp}$	$K^*(892)^\pm\pi^\mp$	$K^*(892)^\pm K^\mp$	$K^*_0(1430)^\pm\pi^\mp$	$K^*_0(1430)^\pm K^\mp$
$K^*(892)^\pm\pi^\mp$	68.42 ± 0.35	8.87 ± 3.82	-0.32 ± 0.45	4.28 ± 3.66
$K^*(892)^\pm K^\mp$	1.98 ± 0.37	55.43 ± 1.38	0.90 ± 0.25	2.26 ± 2.07
$K^*_0(1430)^\pm\pi^\mp$	-0.73 ± 1.14	-0.88 ± 6.46	72.38 ± 0.43	16.52 ± 6.00
$K^*_0(1430)^\pm K^\mp$	1.02 ± 0.54	1.48 ± 2.92	1.86 ± 0.33	52.91 ± 2.02
$\rho(770)^0 K^0_S$	0.75 ± 0.58	0.78 ± 3.20	0.52 ± 0.37	-1.01 ± 3.09
$f_0(980)K^0_S$	0.38 ± 0.42	2.98 ± 2.15	0.56 ± 0.25	4.25 ± 2.05
$K^0_S\pi^+\pi^-$ NR	-0.44 ± 1.24	1.75 ± 6.65	2.27 ± 0.70	-6.88 ± 6.31
$K^0_S K^\pm\pi^\mp$ NR	-0.17 ± 0.44	-0.64 ± 2.31	0.21 ± 0.29	8.52 ± 2.02

	$\rho(770)^0 K^0_S$	$f_0(980)K^0_S$	$K^0_S\pi^+\pi^-$ NR	$K^0_S K^\pm\pi^\mp$ NR
$K^*(892)^\pm\pi^\mp$	-0.38 ± 1.45	0.10 ± 2.91	1.01 ± 0.31	1.65 ± 3.87
$K^*(892)^\pm K^\mp$	1.68 ± 0.80	0.21 ± 1.67	0.13 ± 0.18	0.53 ± 2.18
$K^*_0(1430)^\pm\pi^\mp$	2.18 ± 2.35	3.12 ± 4.91	2.65 ± 0.43	4.23 ± 6.49
$K^*_0(1430)^\pm K^\mp$	0.61 ± 1.08	1.62 ± 2.28	0.74 ± 0.24	10.19 ± 2.87
$\rho(770)^0 K^0_S$	50.87 ± 0.66	3.49 ± 2.37	1.04 ± 0.25	4.30 ± 3.23
$f_0(980)K^0_S$	1.40 ± 0.82	58.24 ± 0.98	0.58 ± 0.17	-1.61 ± 2.28
$K^0_S\pi^+\pi^-$ NR	-0.31 ± 2.54	2.42 ± 5.09	74.89 ± 0.27	2.55 ± 6.52
$K^0_S K^\pm\pi^\mp$ NR	0.88 ± 0.89	0.33 ± 1.74	1.55 ± 0.17	28.86 ± 1.72

Table 5.3: Fit efficiency matrix for the $K^0_S h^\pm\pi^\mp$ Dalitz fit (reconstructed $\downarrow$ generated $\rightarrow$) with elements given in percent.

$$\mathbf{T}_{K^\pm h^\mp \pi^0} = \begin{pmatrix} 0.734 & 0 & 0 & 0 & 0 & 0 & 0 & 0 \\ 0.294 & 1.005 & 0 & 0 & 0 & 0 & 0 & 0 \\ 0 & 0 & 0.643 & 0 & 0 & 0 & 0 & 0 \\ 0 & 0 & 0 & 0.740 & 0 & 0 & 0 & 0.092 \\ 0 & 0 & 0 & 0 & 0.795 & 0 & 0 & 0 \\ 0 & 0 & 0 & 0 & 0 & 0.689 & 0 & 0 \\ 0 & 0 & 0 & 0 & 0 & 0 & 0.365 & 0 \\ 0 & 0 & 0 & 0 & 0 & 0 & 0.333 & 0.689 \end{pmatrix} \tag{5.6}$$

$\mathbf{T}_{K^\pm h^\mp \pi^0}$	$K^*(892)^\pm\pi^\mp$	$K^*(892)^\pm K^\mp$	$K_0^*(1430)^\pm\pi^\mp$	$K_0^*(1430)^\pm K^\mp$
$K^*(892)^\pm\pi^\mp$	73.39 ± 2.72	-4.06 ± 4.38	1.15 ± 4.21	3.71 ± 4.44
$K^*(892)^\pm K^\mp$	29.36 ± 4.03	100.52 ± 2.96	0.68 ± 4.27	-2.77 ± 4.34
$K_0^*(1430)^\pm\pi^\mp$	-3.78 ± 6.36	5.89 ± 6.46	64.28 ± 4.81	7.04 ± 6.41
$K_0^*(1430)^\pm K^\mp$	3.80 ± 5.94	0.80 ± 6.17	16.42 ± 5.53	73.97 ± 4.56
$K/\bar{K}^*(892)^0\pi^0$	3.81 ± 4.14	2.30 ± 4.41	3.54 ± 4.08	3.62 ± 4.43
$K/\bar{K}_0^*(1430)^0\pi^0$	6.09 ± 8.57	3.06 ± 8.74	8.86 ± 8.59	0.75 ± 8.84
$K^\pm\pi^\mp\pi^0$ NR	10.39 ± 8.49	5.53 ± 9.06	21.70 ± 8.10	-15.01 ± 9.17
$K^+K^-\pi^0$ NR	-14.65 ± 9.24	-0.29 ± 9.72	-14.54 ± 9.01	20.33 ± 9.67

	$K/\bar{K}^*(892)^0\pi^0$	$K/\bar{K}_0^*(1430)^0\pi^0$	$K^\pm\pi^\mp\pi^0$ NR	$K^+K^-\pi^0$ NR
$K^*(892)^\pm\pi^\mp$	-0.16 ± 4.32	1.65 ± 0.59	1.96 ± 0.70	3.91 ± 2.05
$K^*(892)^\pm K^\mp$	3.53 ± 4.08	0.94 ± 0.58	0.24 ± 0.74	0.33 ± 2.12
$K_0^*(1430)^\pm\pi^\mp$	1.35 ± 6.23	2.80 ± 0.85	6.95 ± 0.97	3.46 ± 2.92
$K_0^*(1430)^\pm K^\mp$	10.03 ± 5.63	-0.01 ± 0.85	2.22 ± 0.99	9.20 ± 2.70
$K/\bar{K}^*(892)^0\pi^0$	79.50 ± 2.73	1.62 ± 0.56	1.92 ± 0.69	1.25 ± 1.97
$K/\bar{K}_0^*(1430)^0\pi^0$	0.26 ± 8.21	68.86 ± 0.73	6.62 ± 1.35	-3.84 ± 4.17
$K^\pm\pi^\mp\pi^0$ NR	11.53 ± 8.03	-1.41 ± 1.19	36.47 ± 0.83	1.38 ± 4.06
$K^+K^-\pi^0$ NR	-11.14 ± 9.13	6.82 ± 1.25	33.31 ± 1.26	68.91 ± 4.04

Table 5.4: Fit efficiency matrices for the $K^\pm h^\mp \pi^0$ Dalitz fit (reconstructed $\downarrow$ generated $\rightarrow$) with elements given in percent.

$$\mathbf{T}_{K_S^0 h^\pm \pi^0} = \begin{pmatrix} 0.906 & 0.101 & 0 & 0 & 0 & 0 & 0 & 0 & 0 \\ 0 & 0.832 & 0 & 0 & 0 & 0 & 0 & 0 & 0 \\ 0 & 0 & 0.837 & 0 & 0 & 0 & 0 & 0 & 0 \\ 0 & 0 & 0 & 0.717 & 0 & 0 & 0 & 0 & 0.086 \\ 0 & 0 & 0 & 0 & 0.551 & 0 & 0 & 0 & 0 \\ 0 & 0 & 0 & 0 & 0 & 0.554 & 0 & 0 & 0 \\ 0 & 0 & 0 & 0 & 0 & 0 & 0.433 & 0 & 0 \\ 0 & 0 & 0 & 0 & 0 & 0 & 0 & 0.515 & 0 \\ 0 & 0 & 0 & 0 & 0 & 0 & 0 & 0 & 0.393 \end{pmatrix} \quad (5.7)$$

The inverses of the simplified efficiency matrices, given in Equations 5.8–5.10, are used to deconvolute

$\mathbf{T}_{K^0_S h^\pm \pi^0}$	$K/\bar{K}^*(892)^0\pi^\pm$	$\bar{K}/K^*(892)^0K^\pm$	$K/\bar{K}^*_0(1430)^0\pi^\pm$
$K/\bar{K}^*(892)^0\pi^\pm$	90.55 ± 0.73	10.07 ± 3.03	0.61 ± 1.34
$\bar{K}/K^*(892)^0K^\pm$	5.98 ± 0.91	83.16 ± 1.15	0.08 ± 0.92
$K/\bar{K}^*_0(1430)^0\pi^\pm$	0.06 ± 1.99	-1.42 ± 4.46	83.73 ± 1.10
$\bar{K}/K^*_0(1430)^0K^\pm$	1.73 ± 1.34	3.26 ± 2.84	5.59 ± 1.11
$K^*(892)^\pm\pi^0$	-0.94 ± 2.09	1.38 ± 4.59	-2.06 ± 1.87
$K^*_0(1430)^\pm\pi^0$	0.96 ± 2.56	-3.33 ± 5.72	3.75 ± 2.28
$\rho(770)^\pm K^0_S$	1.95 ± 2.24	-0.85 ± 4.69	1.99 ± 1.98
$K^0_S\pi^\pm\pi^0$ NR	-0.13 ± 3.14	14.11 ± 6.91	3.21 ± 2.69
$K^0_S K^\pm\pi^0$ NR	-1.89 ± 1.73	1.71 ± 3.55	-0.63 ± 1.54

	$\bar{K}/K^*_0(1430)^0K^\pm$	$K^*(892)^\pm\pi^0$	$K^*_0(1430)^\pm\pi^0$
$K/\bar{K}^*(892)^0\pi^\pm$	1.99 ± 2.68	0.18 ± 0.33	0.09 ± 0.43
$\bar{K}/K^*(892)^0K^\pm$	-0.89 ± 1.83	0.26 ± 0.22	0.23 ± 0.30
$K/\bar{K}^*_0(1430)^0\pi^\pm$	4.99 ± 3.48	0.82 ± 0.45	0.55 ± 0.57
$\bar{K}/K^*_0(1430)^0K^\pm$	71.71 ± 1.45	-0.06 ± 0.30	-0.22 ± 0.39
$K^*(892)^\pm\pi^0$	5.19 ± 3.69	55.07 ± 0.23	1.36 ± 0.60
$K^*_0(1430)^\pm\pi^0$	2.49 ± 4.78	-0.35 ± 0.57	55.42 ± 0.42
$\rho(770)^\pm K^0_S$	3.46 ± 3.83	0.11 ± 0.46	1.86 ± 0.62
$K^0_S\pi^\pm\pi^0$ NR	4.15 ± 5.48	-1.28 ± 0.72	0.22 ± 0.89
$K^0_S K^\pm\pi^0$ NR	7.55 ± 2.85	0.05 ± 0.38	0.02 ± 0.48

	$\rho(770)^\pm K^0_S$	$K^0_S\pi^\pm\pi^0$ NR	$K^0_S K^\pm\pi^0$ NR
$K/K^*(892)^0\pi^\pm$	0.46 ± 0.50	0.42 ± 0.35	0.50 ± 1.84
$\bar{K}/K^*(892)^0K^\pm$	-0.25 ± 0.36	0.24 ± 0.24	0.13 ± 1.23
$K/\bar{K}^*_0(1430)^0\pi^\pm$	1.72 ± 0.66	3.79 ± 0.43	-0.11 ± 2.43
$\bar{K}/K^*_0(1430)^0K^\pm$	0.24 ± 0.46	-0.37 ± 0.33	8.56 ± 1.54
$K^*(892)^\pm\pi^0$	0.26 ± 0.69	1.12 ± 0.49	1.23 ± 2.52
$K^*_0(1430)^\pm\pi^0$	0.24 ± 0.88	4.48 ± 0.56	2.79 ± 3.25
$\rho(770)^\pm K^0_S$	43.32 ± 0.41	2.02 ± 0.50	-0.02 ± 2.50
$K^0_S\pi^\pm\pi^0$ NR	-1.56 ± 1.04	51.53 ± 0.33	6.07 ± 3.82
$K^0_S K^\pm\pi^0$ NR	-0.47 ± 0.58	4.76 ± 0.32	39.30 ± 1.39

Table 5.5: Fit efficiency matrix for the $K^0_S h^\pm\pi^0$ Dalitz fit (reconstructed $\downarrow$ generated $\rightarrow$) with elements given in percent.

the raw fitted yields.

$$\mathbf{T}^{-1}_{K^0_S h^\pm \pi^\mp} = \begin{pmatrix} 1.462 & 0 & 0 & 0 & 0 & 0 & 0 & 0 \\ 0 & 1.804 & 0 & 0 & 0 & 0 & 0 & 0 \\ 0 & 0 & 1.382 & 0 & 0 & 0 & 0 & 0 \\ 0 & 0 & 0 & 2.004 & 0 & 0 & 0 & -0.708 \\ 0 & 0 & 0 & 0 & 1.966 & 0 & 0 & 0 \\ 0 & 0 & 0 & 0 & 0 & 1.717 & 0 & 0 \\ 0 & 0 & 0 & 0 & 0 & 0 & 1.335 & 0 \\ 0 & 0 & 0 & -0.592 & 0 & 0 & 0 & 3.675 \end{pmatrix} \tag{5.8}$$

$$\mathbf{T}^{-1}_{K^{\pm}h^{\mp}\pi^0} = \begin{pmatrix} 1.362 & 0 & 0 & 0 & 0 & 0 & 0 & 0 \\ -0.398 & 0.995 & 0 & 0 & 0 & 0 & 0 & 0 \\ 0 & 0 & 1.556 & 0 & 0 & 0 & 0 & 0 \\ 0 & 0 & 0 & 1.352 & 0 & 0 & 0.165 & -0.181 \\ 0 & 0 & 0 & 0 & 1.258 & 0 & 0 & 0 \\ 0 & 0 & 0 & 0 & 0 & 1.452 & 0 & 0 \\ 0 & 0 & 0 & 0 & 0 & 0 & 2.742 & 0 \\ 0 & 0 & 0 & 0 & 0 & 0 & -1.325 & 1.451 \end{pmatrix} \tag{5.9}$$

$$\mathbf{T}^{-1}_{K^0_S h^{\pm}\pi^0} = \begin{pmatrix} 1.104 & -0.134 & 0 & 0 & 0 & 0 & 0 & 0 & 0 \\ 0 & 1.202 & 0 & 0 & 0 & 0 & 0 & 0 & 0 \\ 0 & 0 & 1.194 & 0 & 0 & 0 & 0 & 0 & 0 \\ 0 & 0 & 0 & 1.394 & 0 & 0 & 0 & 0 & -0.304 \\ 0 & 0 & 0 & 0 & 1.816 & 0 & 0 & 0 & 0 \\ 0 & 0 & 0 & 0 & 0 & 1.804 & 0 & 0 & 0 \\ 0 & 0 & 0 & 0 & 0 & 0 & 2.308 & 0 & 0 \\ 0 & 0 & 0 & 0 & 0 & 0 & 0 & 1.941 & 0 \\ 0 & 0 & 0 & 0 & 0 & 0 & 0 & 0 & 2.545 \end{pmatrix} \tag{5.10}$$

5.3.3 Simultaneous Fit of $K^0_S h^{\pm}\pi^{\mp}$ and $K^{\pm}h^{\mp}\pi^0$

As will be shown in Section 6.2, the Dalitz fits of the $K^0_S h^{\pm}\pi^{\mp}$ and $K^{\pm}h^{\mp}\pi^0$ topologies give consistent branching fractions for the four modes $K^*(892)^{\pm}h^{\mp}$ and $K^*_0(1430)^{\pm}h^{\mp}$. The two measurements of each mode could be combined by adding the one-dimensional likelihood contours for each submode, but any correlations among the components would be ignored in the process. To make full use of the available information, we fit the two topologies simultaneously while constraining each of the four branching fractions to be equal in the two $K^{*\pm}$ submodes. To apply this constraint, the selection efficiencies for each mode and the fit efficiency matrix for each topology must be made available to the fitter. Every time the sample likelihood is computed, the fitter solves for the $K^*(892)^{\pm}h^{\mp}$ and $K^*_0(1430)^{\pm}h^{\mp}$ fractions in the $K^{\pm}h^{\mp}\pi^0$ topology based on the same fractions in the $K^0_S h^{\pm}\pi^{\mp}$ topology. The calculation begins by equating the efficiency-corrected yields for $K^*(892)^{\pm}h^{\mp}$ and $K^*_0(1430)^{\pm}h^{\mp}$:

$$N^A \begin{pmatrix} g^A_1/\epsilon^A_1 \\ g^A_2/\epsilon^A_2 \\ g^A_3/\epsilon^A_3 \\ g^A_4/\epsilon^A_4 \end{pmatrix} = N^B \begin{pmatrix} g^B_1/\epsilon^B_1 \\ g^B_2/\epsilon^B_2 \\ g^B_3/\epsilon^B_3 \\ g^B_4/\epsilon^B_4 \end{pmatrix}. \tag{5.11}$$

The superscripts A and B refer to the two topologies, the subscripts 1–4 refer to the four $K^*(892)^{\pm}h^{\mp}$ and $K_0^*(1430)^{\pm}h^{\mp}$ components, ϵ denotes a selection efficiency, and the N^i are the numbers of events in the fit. The g_j are the fit-efficiency-corrected component fractions: $g_j = \sum_{i=1}^{K} T_{ji}^{-1} f_i$, where $\mathbf{T}$ is the fit efficiency matrix, f_i are the raw component fractions, and K is the number of signal components in a given topology. Solving for f_1^B, f_2^B, f_3^B, and f_4^B, we obtain the following system of linear equations:

$$\begin{pmatrix} f_1^B \\ f_2^B \\ f_3^B \\ f_4^B \end{pmatrix} = \mathbf{E}^{-1} \left[\frac{N^A}{N^B} \begin{pmatrix} g_1^A/\epsilon_1^A \\ g_2^A/\epsilon_2^A \\ g_3^A/\epsilon_3^A \\ g_4^A/\epsilon_4^A \end{pmatrix} - \begin{pmatrix} \frac{1}{\epsilon_1^B} \sum_{i=5}^{K^B} (T^B)_{1i}^{-1} f_i^B \\ \frac{1}{\epsilon_2^B} \sum_{i=5}^{K^B} (T^B)_{2i}^{-1} f_i^B \\ \frac{1}{\epsilon_3^B} \sum_{i=5}^{K^B} (T^B)_{3i}^{-1} f_i^B \\ \frac{1}{\epsilon_4^B} \sum_{i=5}^{K^B} (T^B)_{4i}^{-1} f_i^B \end{pmatrix} \right], \tag{5.12}$$

where the matrix $\mathbf{E}$ is given by

$$\mathbf{E} = \begin{pmatrix} (T^B)_{11}^{-1}/\epsilon_1^B & (T^B)_{12}^{-1}/\epsilon_1^B & (T^B)_{13}^{-1}/\epsilon_1^B & (T^B)_{14}^{-1}/\epsilon_1^B \\ (T^B)_{21}^{-1}/\epsilon_2^B & (T^B)_{22}^{-1}/\epsilon_2^B & (T^B)_{23}^{-1}/\epsilon_2^B & (T^B)_{24}^{-1}/\epsilon_2^B \\ (T^B)_{31}^{-1}/\epsilon_3^B & (T^B)_{32}^{-1}/\epsilon_3^B & (T^B)_{33}^{-1}/\epsilon_3^B & (T^B)_{34}^{-1}/\epsilon_3^B \\ (T^B)_{41}^{-1}/\epsilon_4^B & (T^B)_{42}^{-1}/\epsilon_4^B & (T^B)_{43}^{-1}/\epsilon_4^B & (T^B)_{44}^{-1}/\epsilon_4^B \end{pmatrix}. \tag{5.13}$$

In the absence of crossfeed ($(T^i)_{jk}^{-1} = 0$ for $j \neq k$), the above equations reduce to

$$\frac{f_j^B (T^B)_{jj}^{-1} N^B}{\epsilon_j^B} = \frac{f_j^A (T^A)_{jj}^{-1} N^A}{\epsilon_j^A} \tag{5.14}$$

as expected. Substituting these expressions into the likelihood reduces the combined number of free parameters in the two topologies from 22 to 18.

5.4 *CP* Asymmetry Fit

The results of the simultaneous fit of the $K_S^0 h^{\pm}\pi^{\mp}$ and $K^{\pm}h^{\mp}\pi^0$ topologies, given in Section 6.2.1, show a statistically significant yield in $B \to K^*(892)^{\pm}\pi^{\mp}$. In this Section, we present an extension of the above Dalitz fits that allows us to measure the charge asymmetry in $B \to K^*(892)^{\pm}\pi^{\mp}$. The charge state of a $B \to K^*(892)^{\pm}\pi^{\mp}$ decay in either of the two topologies is determined by the charge of $h^{\pm}$, the faster of the two tracks in the candidate. We define the charge asymmetry, $\mathcal{A}_{+-}$, to be

$$\mathcal{A}_{+-} \equiv \frac{\mathcal{B}(B \to h^+) - \mathcal{B}(B \to h^-)}{\mathcal{B}(B \to h^+) + \mathcal{B}(B \to h^-)}. \tag{5.15}$$

Similarly, for a B decay to a final state f, the CP asymmetry, $\mathcal{A}_{CP}$, is defined to be

$$\mathcal{A}_{CP} \equiv \frac{\mathcal{B}(\bar{B} \to \bar{f}) - \mathcal{B}(B \to f)}{\mathcal{B}(\bar{B} \to \bar{f}) + \mathcal{B}(B \to f)}. \tag{5.16}$$

In $B \to K^*(892)^{\pm}\pi^{\mp}$ decays, the primary pion and the $K^*(892)^{\pm}$ daughter track have very different momenta, so it is nearly impossible to confuse the two charge states. In signal MC events falling in a 3σ m_B-ΔE window, we find no misclassified events, and we limit the crossfeed probability to be less than 8.9×10^{-5}, according to the MC sample size. Thus, for $B \to K^*(892)^{\pm}\pi^{\mp}$, the charge asymmetry is essentially the same as the CP asymmetry.

To determine $\mathcal{A}_{+-}$ from the maximum likelihood fit, we fit for both sets of charge conjugate final states at once. In principle, each signal or background component should have an associated charge asymmetry, thus doubling the number of free parameters in the fit. However, in each topology, we find the charge asymmetries in the two background $b \to c$ components and the two continuum components (one each for $h^{\pm} = \pi^{\pm}$ and $h^{\pm} = K^{\pm}$) to be consistent with those of the entire fit sample (0.010 ± 0.009 for $K^0_S h^{\pm}\pi^{\mp}$ and 0.006 ± 0.006 for $K^{\pm}h^{\mp}\pi^0$). Therefore, we fix these four asymmetries to those of the fit sample and add free parameters only for the asymmetries in the signal modes. The consequences of this simplification are investigated in Section 7.

Each candidate enters the fit only once and is given a unique charge assignment. In $|\Delta S| = 1$ transitions, $\bar{B}^0$ decays are associated with h^+ and B^0 decays with h^-. Nonetheless, slight correlations between the two charge states can occur in the fit because the asymmetries of the background components are fixed.

In each topology, we fit for eight resonant and NR signal modes. Four of these ($\rho(770)^0 K^0_S$, $f_0(980)K^0_S$, $K^0_S\pi^+\pi^-$ NR, and $K^+K^-\pi^0$ NR) are CP eigenstates. In these modes, $\mathcal{A}_{+-}$ measures not the CP asymmetry between B^0 and $\bar{B}^0$ decays, which would require tagging the flavor of the other B in the event, but the momentum asymmetry between h^+ and h^-. Absent correlations between flavor and momentum, these asymmetries are, in principle, zero, but we allow them to float in the fit to remain sensitive to novel effects. We explore the effect of constraining these asymmetries in Section 7.

The three modes, $K^*(892)^{\pm}K^{\mp}$, $K^*_0(1430)^{\pm}K^{\mp}$, and $K^0_S K^{\pm}\pi^{\mp}$ NR, are not CP eigenstates, but they can still be reached from both B^0 and $\bar{B}^0$ initial states. Therefore, a charge asymmetry in these $\Delta S = 0$ transitions would not necessarily imply a difference between B^0 and $\bar{B}^0$ decay rates; it might also be generated by a difference between, for example, $\frac{\Gamma(B^0 \to K^*(892)^+ K^-)}{\Gamma(B^0 \to K^*(892)^- K^+)}$ and $\frac{\Gamma(\bar{B}^0 \to K^*(892)^- K^+)}{\Gamma(\bar{B}^0 \to K^*(892)^+ K^-)}$. Furthermore, even if there is a CP asymmetry between the B^0 and $\bar{B}^0$ rates, the charge asymmetry will be zero if both of the above ratios are unity.

We begin by fitting the two topologies, $B \to K^0_S h^{\pm}\pi^{\mp}$ and $B \to K^{\pm}h^{\mp}\pi^0$ separately. Depending

on the charge of the $h^{\pm}$, each event in the fit is assigned a likelihood, $\mathcal{L}^{+}$ or $\mathcal{L}^{-}$, which is given by

$$\mathcal{L}^{\pm} = \sum_{i=1}^{11} \frac{1 \pm \mathcal{A}^{i}_{+-}}{2} f_i \mathcal{P}_i + \frac{1 \pm \mathcal{A}^{12}_{+-}}{2} \left(1 - \frac{N}{N^{\pm}} \sum_{i=1}^{11} \frac{1 \pm \mathcal{A}^{i}_{+-}}{2} f_i \right) \mathcal{P}_{12}, \tag{5.17}$$

where the index i labels the components in the fit, with $i = 1, \ldots, 8$ referring to the eight signal components and $i = 9, \ldots, 12$ to the four background components. N is the total number of events in the fit, and $N^{\pm}$ is the number of events with the corresponding charge of $h^{\pm}$. $\mathcal{P}_i$ is the probability for each event to belong to component i, and the f_i are the component fractions summed over the two charge states. Since the $\mathcal{A}^{i}_{+-}$ for the background components are fixed to $(N^{+} - N^{-})/N$, the above likelihood becomes

$$\mathcal{L}^{\pm} = \sum_{i=1}^{8} \frac{1 \pm \mathcal{A}^{i}_{+-}}{2} f_i \mathcal{P}_i + \frac{N^{\pm}}{N} \sum_{i=9}^{11} f_i \mathcal{P}_i + \left(\frac{N^{\pm}}{N} - \sum_{i=1}^{8} \frac{1 \pm \mathcal{A}^{i}_{+-}}{2} f_i - \frac{N^{\pm}}{N} \sum_{i=9}^{11} f_i \right) \mathcal{P}_{12}. \tag{5.18}$$

The nineteen free parameters in the fit of each topology are f_i and $\mathcal{A}^{i}_{+-}$.

We also determine the charge asymmetries from a simultaneous fit to both the $K^0_S h^{\pm} \pi^{\mp}$ and $K^{\pm} h^{\mp} \pi^0$ topologies by expanding the analogous fit from Section 5.3.3. The four modes, $K^*(892)^{\pm} h^{\mp}$ and $K^*_0(1430)^{\pm} h^{\mp}$, are common to both topologies, and we constrain each of them to have equal charge-averaged branching fractions and $\mathcal{A}_{+-}$ values in the two topologies, giving the fit thirty free parameters.

In calculating the sample likelihoods, the constraints on the $K^*(892)^{\pm} h^{\mp}$ and $K^*_0(1430)^{\pm} h^{\mp}$ branching fractions are applied by solving for the yields in the $K^{\pm} h^{\mp} \pi^0$ topology based on the same yields in the $K^0_S h^{\pm} \pi^{\mp}$ topology. To do so, we use the same efficiency matrices and selection efficiencies for both the h^{+} and h^{-} samples. However, the yields in the two charge states are deconvoluted separately.

Chapter 6 Fit Results

6.1 Inclusive Fit Results

We show the maximum likelihood fit results for on-resonance data in Table 6.1 and for off-resonance data in Table 6.2. The on-resonance continuum yields agree with the off-resonance yields scaled by $\mathcal{L}_{\rm on}\sigma_{\rm on}/\mathcal{L}_{\rm off}\sigma_{\rm off} = 2.071$. In Table 6.1, the efficiencies for the $K\pi\pi$ modes are averages over the signal events, and the daughter branching fractions are included in the selection efficiencies. The branching fractions for the signal processes are calculated using $\epsilon_{\rm tot}$. The significances of the raw yields are statistical; no systematic effects have been included.

Mode	On-res. Yield	$\epsilon_{\rm sel}$ (%)	$\epsilon_{\rm fit}$ (%)	$\epsilon_{\rm tot}$ (%)	$\mathcal{B} \times 10^6$
$K^0\pi^+\pi^-$	$60.2^{+11.5}_{-10.6}(8.1\sigma)$	14.0	77.5	12.4	50^{+10}_{-9}
$\bar{K}^0K^+\pi^-$	$2.4^{+7.1}_{-7.2}(0.4\sigma)$	12.2	65.7	8.0	< 19
$b \to c$, $h = \pi$	505^{+62}_{-61}				
$b \to c$, $h = K$	$32.8^{+46.2}_{-26.2}$				
Continuum, $h = \pi$	$(6.33 \pm 0.01) \times 10^3$				
Continuum, $h = K$	4.96×10^3				
$K^+\pi^-\pi^0$	$43.0^{+14.5}_{-13.5}(3.7\sigma)$	25.2	82.5	19.4	23^{+8}_{-7} (< 34)
$K^+K^-\pi^0$	$0^{+11.5}$	15.0	92.9	13.9	< 16
$b \to c$, $h = \pi$	468^{+89}_{-87}				
$b \to c$, $h = K$	260^{+75}_{-71}				
Continuum, $h = \pi$	$(1.76 \pm 0.01) \times 10^4$				
Continuum, $h = K$	1.02×10^4				
$K^0\pi^+\pi^0$	$20.3^{+10.1}_{-8.8}(2.7\sigma)$	10.0	54.7	6.8	31^{+15}_{-14} (< 53)
$\bar{K}^0K^+\pi^0$	$0^{+1.8}$	4.2	88.1	3.7	< 20
$b \to c$, $h = \pi$	547^{+54}_{-53}				
$b \to c$, $h = K$	$0^{+7.2}$				
Continuum, $h = \pi$	$(7.44^{+0.07}_{-0.08}) \times 10^3$				
Continuum, $h = K$	1.33×10^3				

Table 6.1: Three-body inclusive fit results for on-resonance data. No systematic effects have been included. Yields are sums and branching fractions are averages over charge conjugate modes.

The only mode with a statistically significant yield is $K^0_S\pi^+\pi^-$. Figure 6.1 shows the Dalitz plot of the N most signal-like events in the three modes with non-zero yields N, selected with a

Mode	$K^0_S h^\pm \pi^\mp$	$K^\pm h^\mp \pi^0$	$K^0_S h^\pm \pi^0$
Signal $h = \pi$	$0^{+1.7}$	$5.9^{+9.2}_{-6.3} (0.8\sigma)$	$0^{+2.4}$
Signal $h = K$	$0^{+1.2}$	$0^{+1.6}$	$0^{+1.0}$
$b \to c$, $h = \pi$	$0^{+11.8}$	$0^{+11.0}$	$0^{+7.6}$
$b \to c$, $h = K$	$0^{+9.5}$	$0^{+13.2}$	$0^{+5.0}$
Continuum, $h = \pi$	$(3.16 \pm 0.06) \times 10^3$	$(8.26 \pm 0.09) \times 10^3$	$(3.65 \pm 0.04) \times 10^3$
Continuum, $h = K$	2.56×10^3	4.92×10^3	0.62×10^3

Table 6.2: Three-body inclusive fit results for off-resonance data.

requirement on the signal to background likelihood ratio,

$$\mathcal{R}_{\rm sig} \equiv \frac{\mathcal{L}_{\rm sig}}{\mathcal{L}_{\rm sig} + \sum_{i \neq {\rm sig}}^{\#{\rm components}} f_i \mathcal{L}_i}. \tag{6.1}$$

The NR Dalitz plot is overlaid to indicate the physically allowed region. The signal events tend to congregate near the edges of the Dalitz plot, thus hinting at possible resonant substructure.

Figure 6.2 shows the Dalitz plot projections for the signal events, along with the distributions of off-resonance and generic $b \to c$ events satisfying the same $\mathcal{R}_{\rm sig}$ requirement, normalized to the on-resonance luminosity. Also overlaid are the expected signal distributions, assuming the signal consists of NR decays. For $K^0_S \pi^+ \pi^-$, we also project $m_{\pi^+\pi^-}$ for events with $m_{K^0_S \pi^\pm}$ within 3Γ of the $K^*(892)^\pm$ mass. Clearly, the data disagree with the NR assumption, especially in the $K^0_S \pi^+ \pi^-$ mode, which exhibits an excess of events around the $K^*(892)^\pm$ mass.

6.2 Dalitz Fit Results

The results of the Dalitz fits to the three topologies are shown in Tables 6.3–6.5. The on-resonance yields are corrected by the fit efficiency matrix $\mathbf{T}$ to give the yields in the third column. Dividing these corrected yields by the selection efficiency and by the number of $B\bar{B}$ pairs in the sample, $N_{B\bar{B}} = 9.66 \times 10^6$, we obtain the branching fractions in the last column. For the branching fraction upper limits, we apply only the diagonal elements of the fit efficiency matrices to arrive at conservative estimates. The only significant signal observed is for $K^*(892)^\pm \pi^\mp$ in the $K^0_S h^\pm \pi^\mp$ topology. The same mode in the $K^\pm h^\mp \pi^0$ topology exhibits a much weaker signal but with a consistent branching fraction. In no other mode do we observe a statistically significant yield. Tables 6.6 and 6.7 list the fitted yields in off-resonance data. None of the signal modes have yields significantly different from zero, and the non-zero yields are included the systematic uncertainties.

The projections of the fit onto the two-particle invariant masses shown in Figure 6.3 are identical to those in Figure 6.1 except that the fit predictions contain the resonant contributions measured

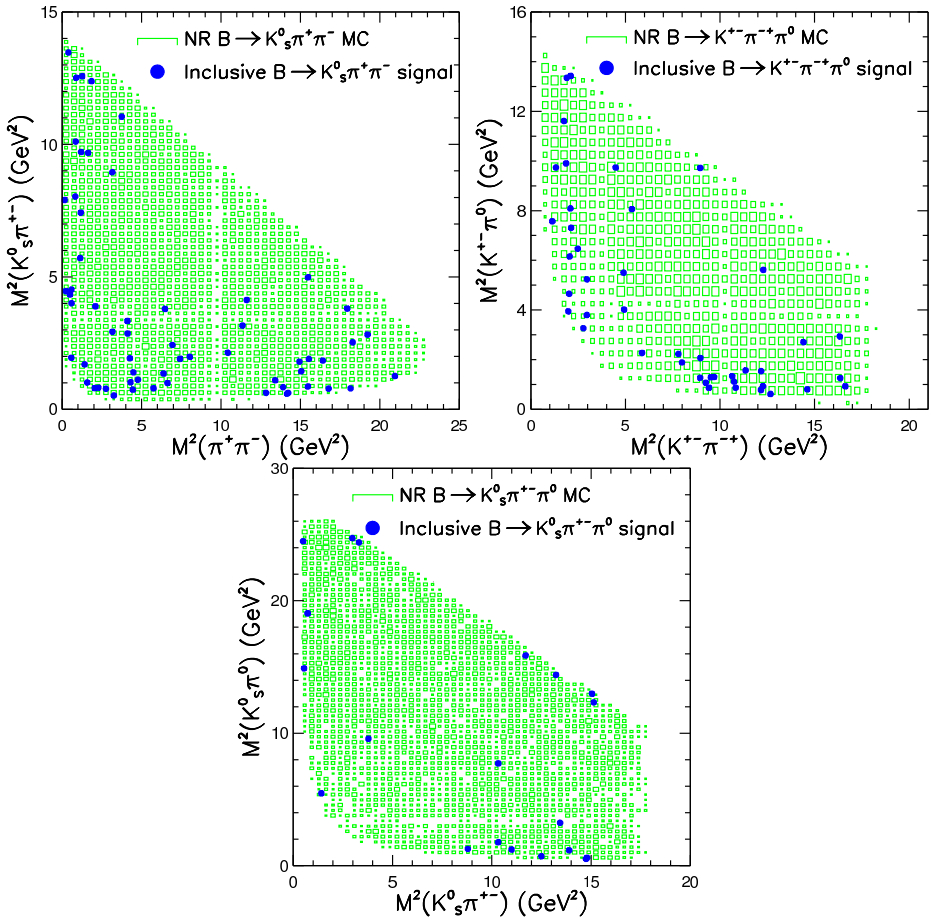

Figure 6.1: Dalitz plots for signal events in $B \to K^0_S\pi^+\pi^-$ (top left), $K^\pm\pi^\mp\pi^0$ (top right), and $K^0\pi^\pm\pi^0$ (bottom), along with Dalitz plot for signal NR decays. Events are selected with a cut on the signal to background likelihood ratio.

from the Dalitz fit, rather than assuming the signal yield is entirely NR. The agreement between the fit prediction and the data in the $K^*(892)$ mass regions is qualitatively better for the Dalitz fits (Figure 6.3) than for the inclusive fits (Figure 6.1). Also, for $K^0_S\pi^+\pi^-$, the $m_{\pi^+\pi^-}$ projection in the $K^*(892)^\pm$ mass region agrees with the vector helicity structure.

We define the helicity angle for $B \to K^*(892)^\pm(K^0_S\pi^\pm)\pi^\mp$, $\theta_{\rm hel}$, to be the angle between the $K^*(892)^\pm$ daughter $\pi^\pm$ direction in the $K^*(892)^\pm$ rest frame and the $K^*(892)^\pm$ direction in the B rest frame. Figure 6.4 shows the distribution of $\cos\theta_{\rm hel}$ in the region $0.75 < m_{K^0_S\pi^\pm} < 1.05$ GeV after subtracting all contributions except $B \to K^*(892)^\pm\pi^\mp$, which are estimated from data collected below the $B\bar{B}$ production threshold and from Monte Carlo simulation. The data are consistent with the $\cos^2\theta_{\rm hel}$ dependence expected for a pseudoscalar-vector B decay and reflected in the overlaid fit projection.

Most of the theoretical work on three-body charmless hadronic B decays has focused, so far, on

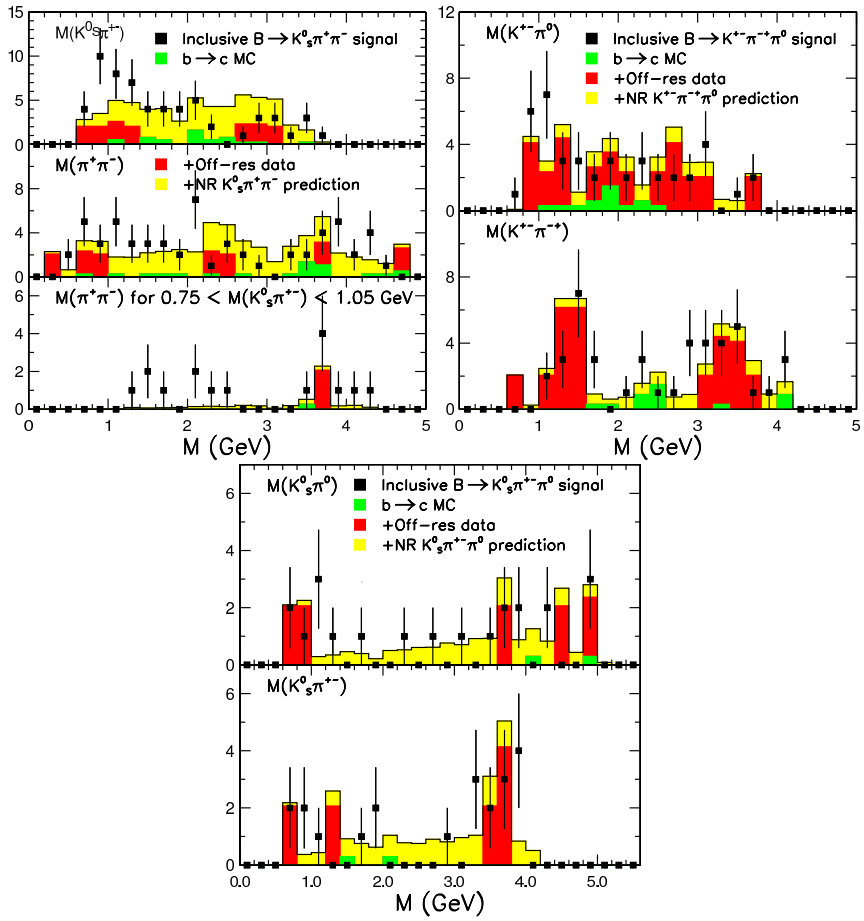

Figure 6.2: Submass projections for signal events in $B \to K^0_S\pi^+\pi^-$ (top left), $K^\pm\pi^\mp\pi^0$ (top right), and $K^0\pi^\pm\pi^0$ (bottom), along with inclusive fit predictions, assuming NR decays. Events are selected with a cut on the signal to background likelihood ratio.

quasi-two-body decays via low-mass intermediate resonances. The results of the Dalitz fits suggest that a complete description of these final states would require fully understanding the contributions from higher-mass resonances as well as from NR decays, which are beginning to attract the attention of theorists. Table 6.8 shows the results of a fit for the fraction of the inclusive $K^0_S\pi^+\pi^-$ yield in each exclusive mode. $K^*(892)^\pm\pi^\mp$ only accounts for 20% of the $K^0_S\pi^+\pi^-$ yield, and this fraction is found to be 7.4σ from unity. Although they are of lower significance, the fractional yields of $K^*_0(1430)^\pm\pi^\mp$ and NR $K^0_S\pi^+\pi^-$ exceed that of $K^*(892)^\pm\pi^\mp$, thus suggesting the presence of contributions that have not been modeled in this exclusive fit. Nevertheless, the $B \to K^*(892)^\pm\pi^\mp$ signal is shown to be stable against variations in these two components in Section 6.3. Future higher-statistics analyses of this topology should probe the exact nature of these broad components.

Mode	On-res. Yield	T-corr. Yield	$\epsilon_{\rm sel}$ (%)	$\mathcal{B} \times 10^6$
$K^*(892)^+\pi^-$	$12.0^{+5.1}_{-4.3}(4.0\sigma)$	$17.5^{+7.5}_{-6.2}$	11.9	15^{+6}_{-5}
$K^*(892)^+K^-$	$1.6^{+2.8}_{-1.8}(0.9\sigma)$	$3.0^{+5.0}_{-3.2}$	11.2	3^{+5}_{-3} (<11)
$K_0^*(1430)^+\pi^-$	$16.2^{+8.1}_{-7.2}(2.6\sigma)$	$22.4^{+11.2}_{-9.9}$	9.5	24^{+12}_{-11} (<42)
$K_0^*(1430)^+K^-$	$0^{+2.3}$	$0^{+5.3}$	8.9	<14
$\rho(770)^0K^0$	$6.9^{+5.1}_{-3.9}(2.3\sigma)$	$13.6^{+10.0}_{-7.7}$	21.0	7^{+5}_{-4} (<14)
$f_0(980)K^0$	$2.6^{+3.1}_{-2.1}(1.4\sigma)$	$4.5^{+5.3}_{-3.6}$	9.8	5^{+6}_{-4} (<14)
$K^0\pi^+\pi^-$ NR	$21.8^{+9.5}_{-8.3}(3.2\sigma)$	$29.0^{+12.8}_{-11.0}$	13.9	22^{+10}_{-8} (<35)
$\bar{K}^0K^+\pi^-$ NR	$0^{+3.7}$	$0^{+13.7}$	12.2	<24
$b\to c$, $h=\pi$	458^{+45}_{-44}			
$b\to c$, $h=K$	$23.9^{+27.0}_{-24.6}$			
Continuum, $h=\pi$	$(6.36\pm0.09)\times10^3$			
Continuum, $h=K$	4.99×10^3			

Table 6.3: Dalitz fit results for $K^0_Sh^\pm\pi^\mp$. Yields are sums and branching fractions are averages over charge conjugate modes.

6.2.1 Simultaneous Fit Results for $K^0_Sh^\pm\pi^\mp$ and $K^\pm h^\mp\pi^0$

The results of the simultaneous fit of the $K^0_Sh^\pm\pi^\mp$ and $K^\pm h^\mp\pi^0$ topologies are shown in Table 6.9. As required by the constraints on the $K^*(892)^\pm h^\mp$ and $K_0^*(1430)^\pm h^\mp$ branching fractions, their values in the two topologies are identical. For $B\to K^*(892)^\pm\pi^\mp$, we find a combined significance of 4.6σ in both submodes, and we claim an observation of this mode based on this fit. The resultant branching fraction is $\mathcal{B}(B\to K^*(892)^\pm\pi^\mp) = (16^{+6}_{-5})\times10^{-6}$. This simultaneous fit is considered the standard fit for branching fraction measurements in the modes covered by these two topologies. The results for off-resonance data are given in Table 6.10.

6.3 Verification of Fit Results

To verify the results of the maximum likelihood fits, we perform three types of studies: counting analyses with restrictive requirements on the variables used in the fit, goodness of fit tests comparing the fit results with expectations, and tests of signal stability under variation of the conditions of the fit.

6.3.1 Counting Analysis

Corroborating evidence for the observed maximum likelihood signals in the inclusive mode $B\to K^0_S\pi^+\pi^-$ and the exclusive mode $B\to K^*(892)^\pm\pi^\mp$ is found in a counting analysis searching for the same decays. We choose our cuts to maximize sensitivity. That is, we adopt the cuts that result

Mode	On-res. Yield	**T**-corr. Yield	$\epsilon_{\rm sel}$ (%)	$\mathcal{B} \times 10^6$
$K^*(892)^+\pi^-$	$7.2^{+5.7}_{-4.3}(2.1\sigma)$	$9.8^{+7.8}_{-5.8}$	5.3	19^{+15}_{-11} (<43)
$K^*(892)^+K^-$	$4.2^{+5.7}_{-4.4}(1.0\sigma)$	$1.4^{+6.1}_{-4.7}$	5.0	3^{+13}_{-10} (<28)
$K_0^*(1430)^+\pi^-$	$2.8^{+9.2}_{-8.2}(0.3\sigma)$	$4.3^{+14.3}_{-12.7}$	6.3	7^{+23}_{-21} (<46)
$K_0^*(1430)^+K^-$	$0^{+3.4}$	$1.0^{+5.3}_{-2.3}$	6.1	2^{+9}_{-4} (<25)
$K^*(892)^0\pi^0$	$0^{+3.7}$	$0^{+4.7}$	12.9	<10
$K_0^*(1430)^0\pi^0$	$15.9^{+8.1}_{-6.9}(2.8\sigma)$	$23.2^{+11.7}_{-10.0}$	16.9	14^{+7}_{-6} (<25)
$K^+\pi^-\pi^0$ NR	$13.8^{+11.6}_{-9.2}(1.6\sigma)$	$37.8^{+31.8}_{-25.2}$	23.0	17^{+14}_{-11} (<16)
$K^+K^-\pi^0$ NR	$7.2^{+10.3}_{-9.2}(0.8\sigma)$	$0^{+21.4}$	23.5	<15
$b\to c$, $h=\pi$	917^{+77}_{-76}			
$b\to c$, $h=K$	512^{+64}_{-62}			
Continuum, $h=\pi$	$(1.72\pm0.01)\times10^4$			
Continuum, $h=K$	9.91×10^3			

Table 6.4: Dalitz fit results for $K^\pm h^\mp\pi^0$. Yields are sums and branching fractions are averages over charge conjugate modes.

in the smallest branching fraction, $\mathcal{B}_{4\sigma}$, where we would expect to observe an excess inconsistent with background fluctuation at the 4σ level ($S/\sqrt{B} > 4$). In practice, we define a 3σ signal region in m_B (±8 MeV) and ΔE (±50 MeV) and require $\left|\sigma^\pi_{dE/dx}\right| < 3$ for all the tracks in the final state as well as $|\cos\theta_{\rm sph}| < 0.8$. We also apply the D and ψ vetos from Section 4.2.4. Then, for a series of values of assumed branching fraction, we determine the cuts that maximize S^2/B. The variables considered for $B\to K^0_S\pi^+\pi^-$ are $\mathcal{F}$ and $\cos\theta_B$. For $K^*(892)^\pm\pi^\mp$, we also cut on m_{K^*} and $\cos\theta_{\rm hel}$. The expected background is determined from off-resonance data and $b\to c$ MC and the expected signal from signal MC. This optimization is performed independently for each variable, but the entire process is iterated to account for correlations among the variables.

Once the optimal requirements have been established, they are applied to the on-resonance data. We define the grand sideband (GSB) to be $5.20 < m_B < 5.27$ GeV and $|\Delta E| < 200$ MeV. The population of the GSB is projected into the signal region to estimate the background due to continuum and combinatoric $b\to c$. The scale factor between the GSB and the signal region is the product of the m_B and ΔE scale factors. For the ΔE dimension, this factor is simply the ratio of the ΔE window sizes because the background is linear in this variable and both windows are centered at zero. For the m_B dimension, we combine off-resonance data and $b\to c$ MC, normalized to a 3:1 ratio (the ratio of cross sections), and fit the m_B distribution to an Argus shape. The m_B scale factor is calculated by integrating the appropriate portions of this curve. For $b\to c$ MC, we require $|\Delta E| > 0$ MeV to prevent peaking around the m_B signal region from the sources described in Section 5.2.1. The size of the $b\to c$ peaks in the signal region are estimated separately from events with $|\Delta E| < 50$ MeV and are included as an additional background contribution.

Mode	On-res. Yield	**T**-corr. Yield	$\epsilon_{\rm sel}$ (%)	$\mathcal{B} \times 10^6$
$K^*(892)^0\pi^+$	$6.6^{+3.7}_{-2.9}(3.2\sigma)$	$7.2^{+4.1}_{-3.2}$	1.5	49^{+28}_{-22} (<93)
$\bar{K}^*(892)^0K^+$	$0.8^{+3.0}_{-2.4}(0.5\sigma)$	$0.9^{+3.6}_{-2.9}$	1.4	7^{+26}_{-21} (<50)
$K_0^*(1430)^0\pi^+$	$0.9^{+3.8}_{-2.8}(0.3\sigma)$	$1.0^{+4.6}_{-3.3}$	1.8	6^{+26}_{-19} (<55)
$\bar{K}_0^*(1430)^0K^+$	$0^{+1.9}$	$0^{+2.7}$	1.7	<52
$K^*(892)^+\pi^0$	$6.4^{+5.7}_{-4.6}(1.5\sigma)$	$11.6^{+10.3}_{-8.3}$	12.1	10^{+9}_{-7} (<23)
$K_0^*(1430)^+\pi^0$	$3.2^{+4.5}_{-2.8}(1.2\sigma)$	$5.7^{+8.2}_{-5.1}$	9.7	6^{+9}_{-5} (<22)
$\rho(770)^+K^0$	$10.3^{+6.8}_{-5.6}(2.2\sigma)$	$23.8^{+15.6}_{-12.9}$	12.7	20^{+13}_{-11} (<39)
$K^0\pi^+\pi^0$ NR	$0^{+2.7}$	$0^{+5.2}$	8.9	<18
$\bar{K}^0K^+\pi^0$ NR	$0^{+1.5}$	$0^{+3.9}$	7.5	<20
$b\to c$, $h=\pi$	322^{+41}_{-40}			
$b\to c$, $h=K$	157^{+32}_{-31}			
Continuum, $h=\pi$	$(7.66\pm0.06)\times10^3$			
Continuum, $h=K$	1.17×10^3			

Table 6.5: Dalitz fit results for $K^0_S h^\pm\pi^0$. Yields are sums and branching fractions are averages over charge conjugate modes.

For inclusive $B\to K^0/\bar{K}^0\pi^+\pi^-$, the optimized cuts are $\mathcal{F}<0.6$ and $|\cos\theta_B|<0.8$, with $\mathcal{B}_{4\sigma}=28.7\times10^{-6}$. The resultant signal efficiency is 6.4%, including daughter branching fractions, and assuming only phase space decay. We observe 95 events in the signal box with an expected background of 59.3 ± 2.0 events. The excess of 35.7 ± 10.0 events is 3.6σ from zero and is inconsistent with being a background fluctuation at the 4.6σ level. Using the efficiency given above, the branching fraction is $(57\pm16)\times10^{-6}$. If, instead, we correct the background-subtracted Dalitz plot of events in the signal box, using the procedure of Section 5.2.8 (but without the histogram smoothing), we obtain a model-independent branching fraction of $(64\pm18)\times10^{-6}$. Both branching fractions are consistent with the likelihood fit result. Figure 6.5 shows the m_B-ΔE plane for this analysis, as well as the projections onto the two variables (with a cut on the variable not being plotted).

For $B\to K^*(892)^\pm\pi^\mp$, we only consider the $K^*(892)^\pm\to K^0_S\pi^\pm$ submode. The optimized requirements are $\mathcal{F}<0.55$, $|\Delta m_{K^*}|<50$ MeV, and $|\cos\theta_{\rm hel}|>0.25$, which gives $\mathcal{B}_{4\sigma}=5.0\times10^{-6}$ and a signal efficiency of 3.0%. The optimization procedure favors no cut on $\cos\theta_B$. We observe 6 events in the signal box with an expected background of 2.0 ± 0.3 events. The excess of 4.0 ± 2.5 events is only 1.6σ from zero, but it is 2.8σ from being a background fluctuation. The branching fraction of $(14\pm8)\times10^{-6}$ agrees well with the likelihood fit result. Figure 6.6 graphically displays the results of this counting analysis.

$K^0_S h^\pm \pi^\mp$		$K^\pm h^\mp \pi^0$	
Mode	Off-res. Yield	Mode	Off-res. Yield
$K^*(892)^\pm \pi^\mp$	$0^{+0.8}$	$K^*(892)^\pm \pi^\mp$	$2.6^{+5.1}_{-3.9}(0.7\sigma)$
$K^*(892)^\pm K^\mp$	$0^{+0.7}$	$K^*(892)^\pm K^\mp$	$0^{+2.7}$
$K^*_0(1430)^\pm \pi^\mp$	$0^{+2.4}$	$K^*_0(1430)^\pm \pi^\mp$	$4.7^{+5.6}_{-4.1}(1.2\sigma)$
$K^*_0(1430)^\pm K^\mp$	$0.8^{+2.7}_{-1.7}(0.4\sigma)$	$K^*_0(1430)^\pm K^\mp$	$0^{+1.0}$
$\rho(770)^0 K^0_S$	$0^{+1.9}$	$K/\bar{K}^*(892)^0 \pi^0$	$2.8^{+4.3}_{-3.2}(0.9\sigma)$
$f_0(980) K^0_S$	$0^{+2.0}$	$K/\bar{K}^*_0(1430)^0 \pi^0$	$7.9^{+5.6}_{-4.6}(1.9\sigma)$
$K^0_S \pi^+ \pi^-$ NR	$0^{+1.0}$	$K^\pm \pi^\mp \pi^0$ NR	$0^{+3.3}$
$K^0_S K^\pm \pi^\mp$ NR	$0^{+1.2}$	$K^+ K^- \pi^0$ NR	$0^{+1.4}$
$b \to c$, $h = \pi$	$0^{+2.9}$	$b \to c$, $h = \pi$	$0^{+15.4}$
$b \to c$, $h = K$	$0^{+4.6}$	$b \to c$, $h = K$	$0^{+26.5}$
Continuum, $h = \pi$	$(3.16 \pm 0.06) \times 10^3$	Continuum, π	$(8.24 \pm 0.09) \times 10^3$
Continuum, $h = K$	2.56×10^3	Continuum, K	4.91×10^3

Table 6.6: Fitted yields for independent Dalitz fits to the $K^0_S h^\pm \pi^\mp$ and $K^\pm h^\mp \pi^0$ topologies for off-resonance data.

6.3.2 Goodness of Fit

To evaluate the quality of the likelihood fit, we perform a series of comparisons between data and MC, where the signal and background composition of the latter is given by the results of the fit. Discrepancies between data and MC can have various origins: neglect of correlations among the input variables, extra sources of background, or PDFs which do not accurately represent the data. Any of these pathologies can bias the fit results, and we find no evidence of them in any of our fits.

Projection Plots

To illustrate the fit results in the various variables used in the fit, we apply background suppression requirements that visually enhance the signals. The variable used for this selection is the ratio $\mathcal{R}_{\rm sig}$, defined in Section 6.1 and computed without the variable being plotted. Thus, the criterion used to select the events is independent of the plotted quantity. The cut on $\mathcal{R}_{\rm sig}$ is chosen to maximize S^2/B in the m_B-ΔE signal region, and this optimization is performed separately for each variable and each mode. Figure 6.7 shows the m_B and ΔE projections for the two modes where we claim an observation. Overlaid on the histograms are predictions from the fit. The dotted curves are the sum of the continuum and $b \to c$ PDFs normalized to the fitted yields and scaled by the efficiencies of the likelihood ratio cut. The solid curves include an extra contribution from the relevant signal PDF. In all four plots, the size of the excess agrees well with the fit prediction.

Mode	Off-res. Yield
$K/\bar{K}^*(892)^0\pi^\pm$	$1.7^{+2.1}_{-1.3}(1.4\sigma)$
$\bar{K}/K^*(892)^0K^\pm$	$0^{+1.3}$
$K/\bar{K}_0^*(1430)^0\pi^\pm$	$0^{+1.8}$
$\bar{K}/K_0^*(1430)^0K^\pm$	$0^{+1.7}$
$K^*(892)^\pm\pi^0$	$0^{+0.9}$
$K_0^*(1430)^\pm\pi^0$	$0^{+1.2}$
$\rho(770)^\pm K_S^0$	$0^{+1.1}$
$K_S^0\pi^\pm\pi^0$ NR	$0^{+1.0}$
$K_S^0K^\pm\pi^0$ NR	$0^{+1.3}$
$b\to c$, $h=\pi$	$0^{+2.4}$
$b\to c$, $h=K$	$0^{+15.6}$
Continuum, $h=\pi$	$(3.65\pm0.04)\times10^3$
Continuum, $h=K$	619

Table 6.7: $K_S^0h^\pm\pi^0$ Dalitz fit results for off-resonance data.

Mode	Fractional On-res. Yield
$K^*(892)^\pm\pi^\mp$	$0.20^{+0.08}_{-0.07}$
$K_0^*(1430)^\pm\pi^\mp$	$0.27^{+0.12}_{-0.12}$
$\rho(770)^0K_S^0$	$0.12^{+0.08}_{-0.06}$
$f_0(980)K_S^0$	$0.04^{+0.05}_{-0.04}$
$K_S^0\pi^+\pi^-$ NR	0.37

Table 6.8: Fractional fit results for $B\to K_S^0\pi^+\pi^-$. The total yield is $59.4^{+10.9}_{-10.0}$ events.

Likelihood Ratio

In addition to observing excesses in the variables used in the fit, we also examine the likelihoods for each event. Figure 6.8 shows the distributions of $\mathcal{R}_{\rm sig}$ for inclusive $B\to K_S^0\pi^+\pi^-$ and $B\to K^*(892)^\pm(K_S^0\pi^\pm)\pi^\mp$ in the $K_S^0h^\pm\pi^\mp$ topology. The distribution for data is compared to the expected distributions for signal and background. The normalizations of the signal contributions are determined by the fit results. Discrepancies in the shape of the distribution or the size of the excess can arise from inaccurate PDFs or neglected sources of background. In both fits, we observe good agreement in shape and number.

Optimized Likelihoods

We also gauge the goodness of fit by comparing the expected distribution of optimized likelihoods, obtained from toy MC, with the value from the fit of on-resonance data. To reduce the contamination

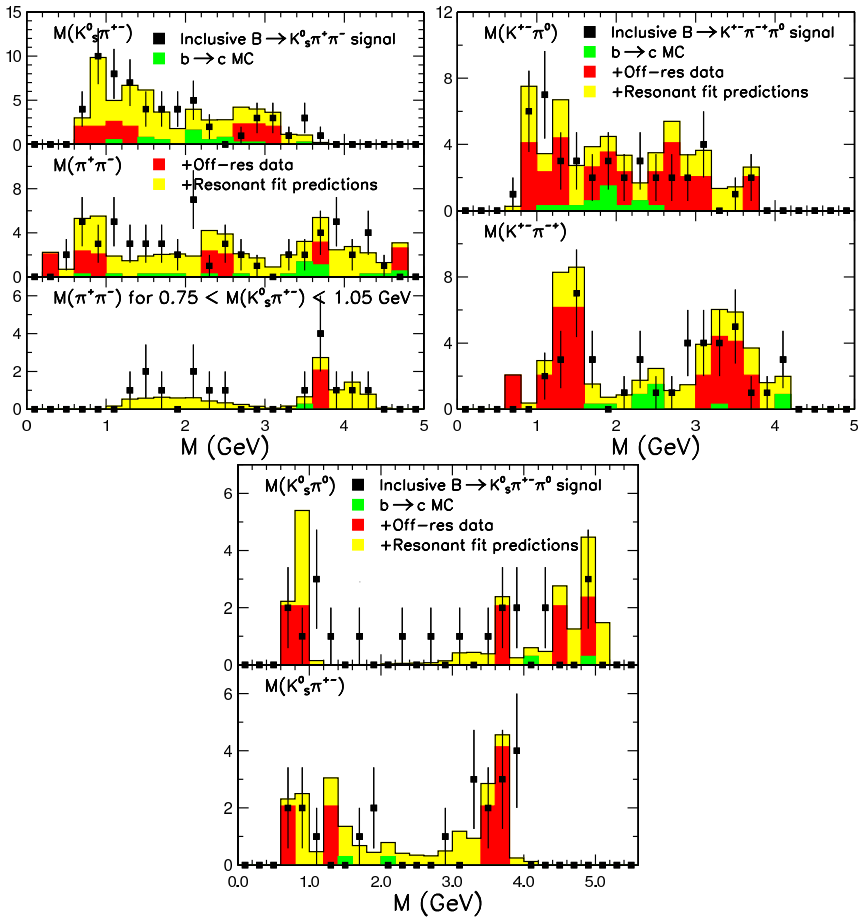

Figure 6.3: Submass projections for the signal events in $B \to K^0_S\pi^+\pi^-$ (top left), $K^\pm\pi^\mp\pi^0$ (top right), and $K^0_S\pi^\pm\pi^0$ (bottom), along with Dalitz fit predictions. Events are selected with a cut on the signal to background likelihood ratio.

from background contributions, we consider only events in a 3σ m_B-ΔE signal region instead of using the full fit domain. We define the normalized sample likelihood to be

$$\bar{\chi}^2 \equiv -\frac{2}{N}\sum_{i=1}^{N} \ln \mathcal{L}^i_{\rm max}, \tag{6.2}$$

where the index i labels the N events in the signal region, and the $\mathcal{L}^i_{\rm max}$ are the event likelihoods evaluated with the optimized component fractions returned by the fit.

In the limit of Gaussian PDFs, $\bar{\chi}^2$ behaves like a figure of merit for a least-squares fit (with an aribtrary offset). Hence, a poor fit would result in a nominal $\bar{\chi}^2$ that lies in the high tail of the expected distribution. On the other hand, if the correlations among the fit variables are not modeled correctly, then the number of degrees of freedom in the fit is effectively overestimated, and the nominal $\bar{\chi}^2$ would lie in the low tail. Since $\bar{\chi}^2$ is obtained by summing the individual log-

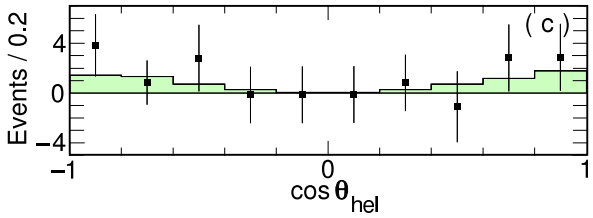

Figure 6.4: $\cos\theta_{\rm hel}$ projection for $B \to K^*(892)^{\pm}(K^0_S\pi^{\pm})\pi^{\mp}$. Shown are the data distribution (points) in the region $0.75 < m_{K^0_S\pi^{\pm}} < 1.05$ GeV with all non-$K^*(892)^{\pm}\pi^{\mp}$ contributions subtracted and the fit prediction for $B \to K^*(892)^{\pm}\pi^{\mp}$ (histogram). The background has been suppressed with a cut on the ratio of signal and background likelihoods computed without the Dalitz plot variables.

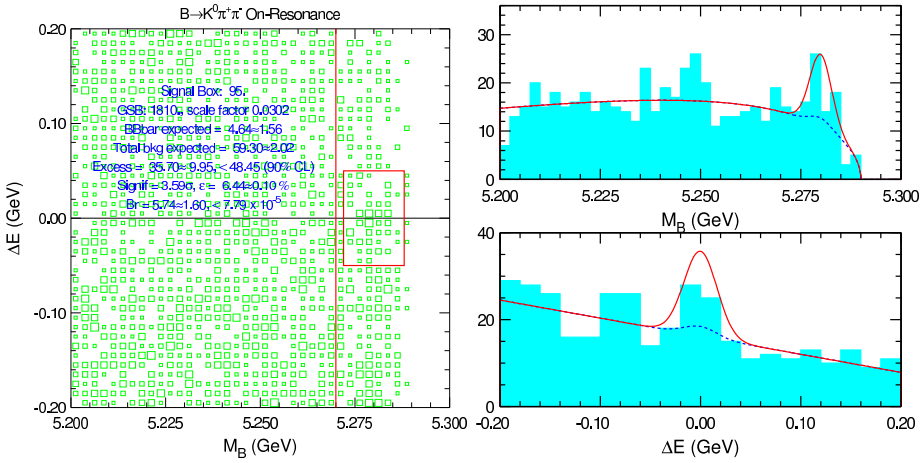

Figure 6.5: Counting analysis results for inclusive $B \to K^0_S\pi^+\pi^-$: the two-dimensional grand sideband and signal region in the m_B-ΔE plane (left) and the one-dimensional projections of m_B for events in the ΔE signal region (left top) and ΔE for events in the m_B signal region (left bottom).

likelihoods for each event, a reasonable value of $\bar{\chi}^2$ can arise by accident; being a global quantity, $\bar{\chi}^2$ is relatively insensitive to variations in the distribution of the individual log-likelihoods. Therefore, we also compare the event distributions of optimized likelihoods in the signal region between data and toy MC.

Figure 6.9 shows the expected distributions for $\bar{\chi}^2$. These distributions are measured using ensembles of toy MC experiments with generated component fractions taken from the on-resonance data fit. The dashed vertical lines in Figure 6.9 show the $\bar{\chi}^2$ values for data, and these agree well with expectations in both fits with significant signals, the inclusive and Dalitz fits of the $K^0_S h^{\pm}\pi^{\mp}$ topology. We define the confidence level to be the fraction of the expected $\bar{\chi}^2$ distribution that lies above the data value. Figure 6.9 also shows the event distributions of $-2\ln\mathcal{L}^i_{\rm max}$ for events in the signal region. Here, the confidence level is that returned by a fit of the data distribution to the expected distribution. For both the inclusive and Dalitz $K^0_S h^{\pm}\pi^{\mp}$ fits, the comparisons between MC

Mode	On-res. Yield	**T**-corr. Yield	$\epsilon_{\rm sel}$ (%)	$\mathcal{B} \times 10^6$
		$K^0_S h^\pm \pi^\mp$		
$K^*(892)^+\pi^-$	$12.6^{+4.6}_{-3.9}(4.6\sigma)$	$18.5^{+6.7}_{-5.8}$	11.9	16^{+6}_{-5}
$K^*(892)^+K^-$	$1.7^{+2.6}_{-1.8}(0.9\sigma)$	$3.1^{+4.7}_{-3.3}$	11.2	3^{+4}_{-3} (<11)
$K^*_0(1430)^+\pi^-$	$14.0^{+7.0}_{-6.3}(2.5\sigma)$	$19.4^{+9.6}_{-8.7}$	9.5	21^{+11}_{-9} (<36)
$K^*_0(1430)^+K^-$	$0^{+1.5}$	$0^{+4.4}$	8.9	<10
$\rho(770)^0K^0$	$6.9^{+5.1}_{-3.9}(2.3\sigma)$	$13.6^{+10.0}_{-7.7}$	21.0	7^{+5}_{-4} (<14)
$f_0(980)K^0$	$2.6^{+3.1}_{-2.1}(1.4\sigma)$	$4.5^{+5.3}_{-3.6}$	9.8	5^{+6}_{-4} (<14)
$K^0\pi^+\pi^-$ NR	$22.8^{+9.5}_{-8.3}(3.4\sigma)$	$30.5^{+12.7}_{-11.1}$	13.9	23^{+9}_{-8} (<35)
$\bar{K}^0K^+\pi^-$ NR	$0^{+4.6}$	$0^{+17.04}$	12.2	<24
		$K^\pm h^\mp \pi^0$		
$K^*(892)^+\pi^-$	$6.1^{+2.2}_{-1.9}$	$8.3^{+3.0}_{-2.6}$	5.3	16^{+6}_{-5}
$K^*(892)^+K^-$	$3.8^{+2.1}_{-1.5}$	$1.4^{+2.2}_{-1.7}$	5.0	3^{+5}_{-4} (<11)
$K^*_0(1430)^+\pi^-$	$8.3^{+4.1}_{-3.7}$	$12.8^{+6.4}_{-5.8}$	6.3	21^{+11}_{-9} (<36)
$K^*_0(1430)^+K^-$	$0^{+1.4}$	$0^{+3.1}$	6.1	<10
$K^*(892)^0\pi^0$	$0^{+3.7}$	$0^{+4.7}$	12.9	<10
$K^*_0(1430)^0\pi^0$	$15.8^{+8.1}_{-6.9}(2.8\sigma)$	$23.0^{+11.7}_{-10.0}$	16.9	14^{+7}_{-6} (<25)
$K^+\pi^-\pi^0$ NR	$14.4^{+10.5}_{-9.0}(1.7\sigma)$	$39.5^{+28.9}_{-24.7}$	23.0	18^{+13}_{-11} (<16)
$K^+K^-\pi^0$ NR	$5.3^{+10.0}_{-9.1}(0.7\sigma)$	$0^{+19.7}$	23.5	<15

Table 6.9: Results of simultaneous fit to the $K^0_S h^\pm \pi^\mp$ and $K^\pm h^\mp \pi^0$ topologies for on-resonance data. Yields are sums and branching fractions are averages over charge conjugate modes.

and data give reasonable confidence levels.

6.3.3 Signal Stability

The stability of the two significant signals is probed by varying the PDFs, the events entering the fit, and the number of free parameters in the fit.

PDF Variation

To assess the sensitivity of the signals to uncertainties in the PDF parameters, we record the response of the fitted yields to extreme PDF variations. To do so, we coherently shift the PDF parameters of m_B, ΔE, and $\mathcal{F}$ for all components by one unit of statistical uncertainty in the direction that minimizes the signal. We repeat the procedure using the reverse variations to maximize the signal. To simplify the procedure, we use the PDFs averaged over the Dalitz plot, so the fit results with unmodified PDFs differ from the standard fit results. Table 6.11 shows the results for the inclusive and Dalitz fits. We find that the $B \to K^0_S\pi^+\pi^-$ yield varies by $\pm 8\%$, and the significance changes by $\pm 0.3\sigma$. The $B \to K^*(892)^\pm(K^0_S\pi^\pm)\pi^\mp$ yield varies by $\pm 7\%$ and its significance by $\pm 0.2\sigma$. Clearly,

$K^0_S h^\pm \pi^\mp$		$K^\pm h^\mp \pi^0$	
Mode	Off-res. Yield	Mode	Off-res. Yield
$K^*(892)^\pm \pi^\mp$	$0^{+0.8}$	$K^*(892)^\pm \pi^\mp$	$0^{+1.8}$
$K^*(892)^\pm K^\mp$	$0^{+0.6}$	$K^*(892)^\pm K^\mp$	$0^{+2.3}$
$K^*_0(1430)^\pm \pi^\mp$	$0.8^{+3.2}_{-2.6}(0.4\sigma)$	$K^*_0(1430)^\pm \pi^\mp$	$0.5^{+1.9}_{-1.5}(0.4\sigma)$
$K^*_0(1430)^\pm K^\mp$	$0^{+2.2}$	$K^*_0(1430)^\pm K^\mp$	$0^{+0.8}$
$\rho(770)^0 K^0_S$	$0^{+2.3}$	$K/\bar{K}^*(892)^0 \pi^0$	$2.8^{+4.3}_{-3.2}(0.9\sigma)$
$f_0(980) K^0_S$	$0.3^{+1.9}_{-1.4}(0.3\sigma)$	$K/\bar{K}^*_0(1430)^0 \pi^0$	$7.9^{+5.7}_{-4.7}(1.9\sigma)$
$K^0_S \pi^+ \pi^-$ NR	$0^{+1.0}$	$K^\pm \pi^\mp \pi^0$ NR	$0.3^{+6.3}_{-0.3}(0.2\sigma)$
$K^0_S K^\pm \pi^\mp$ NR	$0^{+2.2}$	$K^+ K^- \pi^0$ NR	$0^{+1.3}$

Table 6.10: Results of simultaneous fit to the $K^0_S h^\pm \pi^\mp$ and $K^\pm h^\mp \pi^0$ topologies for off-resonance data.

both signals are robust under PDF variation.

Resonance Variation

An additional test of the robustness under PDF variation of the $B \to K^*(892)^\pm (K^0_S \pi^\pm)\pi^\mp$ signal is to vary the resonant components included in the Dalitz fit. We replace the $K^*_0(1430)^\pm$ scalar resonance with the vector $K^*(1410)^\pm$. Figure 6.10 compares the Dalitz PDFs for the two resonances.

The results of the two fits are shown in Table 6.12. The $B \to K^*(892)^\pm \pi^\mp$ yield undergoes a 1.6% change. The use of the $K^*(1410)^\pm$ is somewhat unrealistic, as its branching fraction to $K\pi$ is only 6.6%. This exercise primarily probes the model dependence of our results, and it demonstrates that the $B \to K^*(892)^\pm \pi^\mp$ yield is relatively insensitive to the precise nature of the broad components.

Removal of Events

We remove the two most signal-like events from the inclusive and Dalitz fits to the $K^0_S h^\pm \pi^\mp$ topology to verify that the observed signals are not caused by extremely unlikely events with unusually high weight. These events are identified via the likelihood ratio $\mathcal{R}_{\rm sig}$. There is no overlap between the two best $B \to K^0_S \pi^+ \pi^-$ events and the two best $B \to K^*(892)^\pm (K^0_S \pi^\pm)\pi^\mp$ events. We find that these four events are each assigned a weight of 1.8–1.9 events by the fitter, so they are not solely responsible for the signal yield. Table 6.13 shows the drop in yield and significance as each succesive event is removed.

Removal of Fit Components

Another test of stability is to vary the number of broad scalar components allowed in the fit by constraining the yields for the $K^*_0(1430)$ or the NR components to zero. Table 6.14 shows that

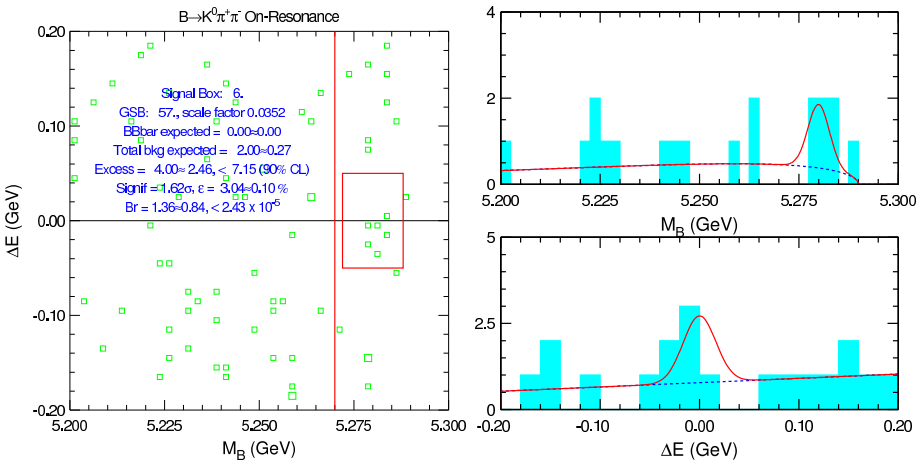

Figure 6.6: Counting analysis results for $B \to K^*(892)^{\pm}\pi^{\mp}$: the two-dimensional grand sideband and signal region in the m_B-ΔE plane (left) and the one-dimensional projections of m_B for events in the ΔE signal region (left top) and ΔE for events in the m_B signal region (left bottom).

fixing one of these two components transfers its yield to the other, suggesting a large correlation between the two. The two $B \to K^*(892)^{\pm}\pi^{\mp}$ yields in both $K^*(892)^{\pm}$ submodes, however, remain roughly constant in these fits. It is only when both components are fixed to zero that the $B \to K^*(892)^{\pm}\pi^{\mp}$ components experience an increase in yield and significance. Such fits, however, are unjustified, as the combined significance of the $K_0^*(1430)$ and NR components is 6.4σ and 4.2σ for the $K_S^0 h^{\pm}\pi^{\mp}$ and $K^{\pm}h^{\mp}\pi^0$ topologies, respectively. The fit demands the presence of a broad scalar component to describe properly the inclusive $B \to K_S^0\pi^+\pi^-$ signal, the bulk of which is not $B \to K^*(892)^{\pm}(K_S^0\pi^{\pm})\pi^{\mp}$.

6.4 Dalitz Fit Results with Charge Asymmetries

Tables 6.15 and 6.16 show the $\mathcal{A}_{+-}$ fit results for the two topologies containing $B \to K^*(892)^{\pm}\pi^{\mp}$. The signal yields and significances do not deviate significantly from those of the charge-summed fits in Section 6.2, where we assumed $\mathcal{A}_{+-} = 0$ in all modes. Some excursions are expected since the sums of the component fractions in the two charge states are not constrained to the $\mathcal{A}_{+-} = 0$ result; the yields for each charge of $h^{\pm}$ are allowed to fluctuate (essentially) independently. In all signal modes, the fitted charge asymmetry is consistent with zero. To assure convergence of the fit, the charge asymmetries for components with yields less than 0.1 events are fixed to zero. Performing a weighted average of the $B \to K^*(892)^{\pm}\pi^{\mp}$ asymmetries from the two topologies gives $\mathcal{A}_{+-}(B \to K^*(892)^{\pm}\pi^{\mp}) = 0.32^{+0.34}_{-0.35}$. Table 6.17 shows the results of the simultaneous fit with charge asymmetries to the $K_S^0 h^{\pm}\pi^{\mp}$ and $K^{\pm}h^{\mp}\pi^0$ topologies, where we find $\mathcal{A}_{+-}(B \to K^*(892)^{\pm}\pi^{\mp}) = 0.26^{+0.33}_{-0.34}$. We henceforth consider this simultaneous fit to be the stan-

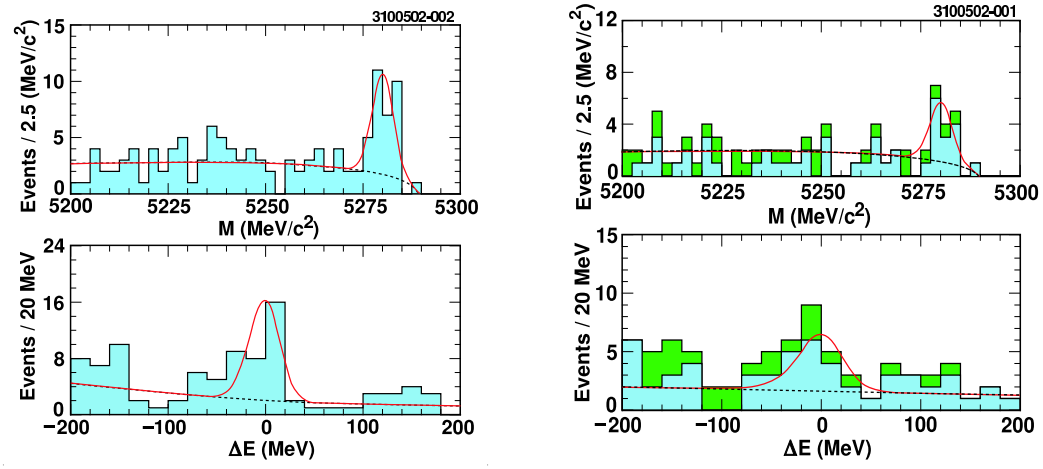

Figure 6.7: m_B and ΔE projections for $B \to K^0_S\pi^+\pi^-$ (left) and $B \to K^*(892)^\pm\pi^\mp$ (right), which includes the two $K^*(892)^\pm$ submodes, $K^*(892)^\pm \to K^0_S\pi^\pm$ (lower histogram) and $K^*(892)^\pm \to K^\pm\pi^0$ (upper histogram). The dashed and solid lines show the fit predictions for background and the sum of signal and background, respectively.

dard fit for the CP asymmetry in $B \to K^*(892)^\pm\pi^\mp$.

We determine the sample likelihood as a function of $\mathcal{A}_{+-}(B \to K^*(892)^\pm\pi^\mp)$ by refitting with the asymmetry fixed to a series of values in the physical region $[-1, 1]$. Recording the likelihood from each fit gives the curve shown in Figure 6.11, which has been arbitrarily normalized. The likelihood function is well-described by a bifurcated Gaussian, and we construct a symmetric allowed interval by integrating this function in the physical region. Each of the excluded regions contains 5% of the integrated area, and, at the 90% confidence level, we find $\mathcal{A}_{+-}(B \to K^*(892)^\pm\pi^\mp) \in [-0.30, 0.75]$ based on the statistical errors only. In Section 7, we inflate this interval to account for systematic effects.

6.5 Sources of Bias in $\mathcal{A}_{+-}$

Investigations of charge- and strangeness-correlated systematic effects in high-momentum tracks and $K^*(892)^\pm$ decays in CLEO were performed using kinematically identified pions and kaons from D decays [95, 119]. These studies found negligible asymmetries in the selection criteria, momentum measurement, and dE/dx measurement. The yield asymmetries for charged pions and kaons was limited to 0.2% for tracks between 2 and 3 GeV and to 0.5% for pions and 1.5% for kaons below 2 GeV. Asymmetries in the dE/dx measurement were limited to 1.0%. It was also found that crossfeed between the $K^0_S\pi^\pm$ and $K^\pm\pi^0$ submodes was negligible. Below, we consider additional sources of bias in the charge asymmetry measurement for $B \to K^*(892)^\pm\pi^\mp$, the only two-body mode with a significant signal.

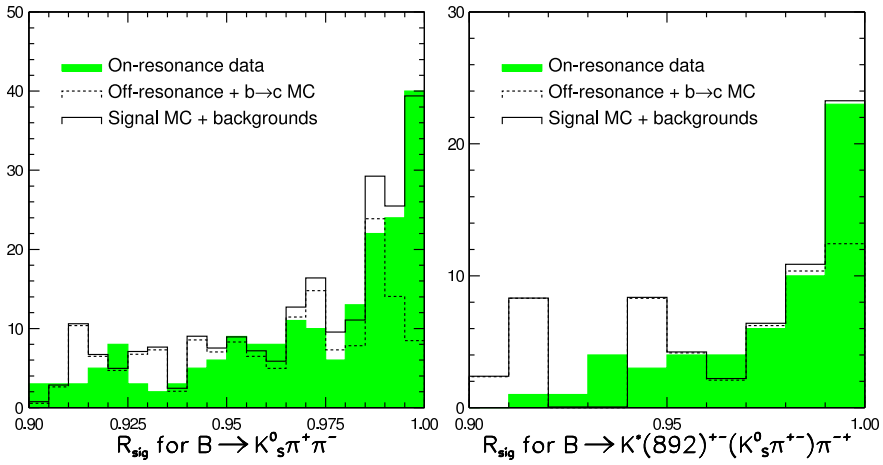

Figure 6.8: Likelihood ratio distributions for inclusive $B \to K^0_S\pi^+\pi^-$ (left) and $B \to K^*(892)^\pm\pi^\mp$ with $K^*(892)^\pm \to K^0_S\pi^\pm$ (right). The data distributions are shown as solid histograms, and the expected distributions for background (dashed) and background plus signal (solid) are overlaid.

Since the fitter uses the same Dalitz plot PDF for both charge states, we check the $K^*(892)^+$ and $K^*(892)^-$ lineshapes for possible charge asymmetries. We examine $K^0_S h^+h^-$ and $\pi^0 h^+h^-$ candidates in both on- and off-resonance data that pass all the fit selection criteria except the $b \to c$ vetos and the dE/dx requirements. In particular, the mass and momentum cuts on the π^0 candidates are retained. For both $K^*(892)^\pm \to K^0_S\pi^\pm$ and $K^*(892)^\pm \to K^\pm\pi^0$, we accept three-body candidates with $|\Delta E| < 300$ MeV and $m_B > 5.17$ GeV. Each three-body candidate contains a $K^*(892)^+$ candidate and a $K^*(892)^-$ candidate. We consider $K^*(892)^\pm$ candidates with invariant mass between 0.7 and 1.1 GeV and require the $K^*(892)^\pm$ daughter track to satisfy $\left|\sigma^\pi_{dE/dx}\right| < 2$ or $\left|\sigma^K_{dE/dx}\right| < 2$. No cuts are placed on the dE/dx of the other track. Figure 6.12 compares the $K^*(892)^+$ and $K^*(892)^-$ lineshapes in the two decay modes. No significant difference is seen. We fit these distributions to a second-order polynomial background and a signal Breit-Wigner with width fixed to the known value [5]. The charge asymmetries in the areas and means of the Breit-Wigner are shown in Table 6.18. We use the sign convention $\mathcal{A} = [K^*(892)^- - K^*(892)^+]/[K^*(892)^- + K^*(892)^+]$. In no case is the asymmetry observed to be different from zero. Because of the limited statistical power of this study, we rely on the work in the two previously published papers mentioned above to establish systematic uncertainties associated with detector bias.

Bias in $\mathcal{A}_{+-}$ may arise from the event selection and the maximum likelihood fit. In Table 6.19, we compare selection and fit efficiencies for MC samples of $\bar{B}^0 \to K^*(892)^+\pi^-$ and $B^0 \to K^*(892)^-\pi^+$. The fit efficiencies are measured by fitting all the available MC with the off-resonance data. We find no evidence for differences in overall efficiency between the two charge states, and we limit the uncertainty on $\mathcal{A}_{+-}$ to less than 2%.

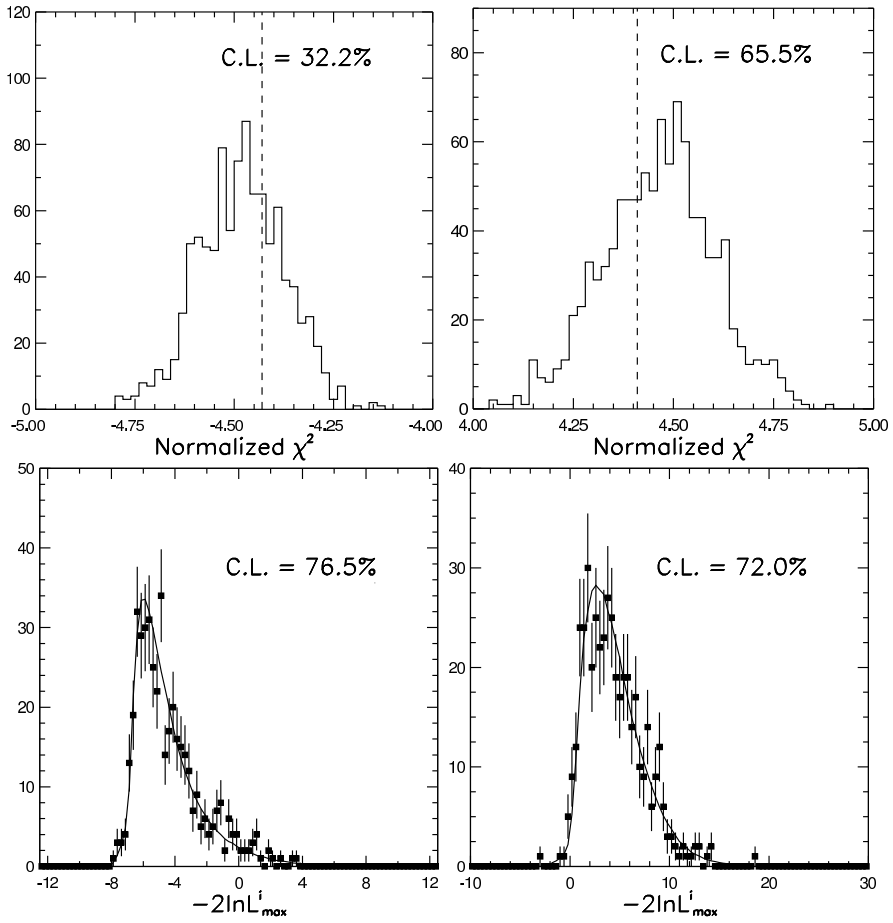

Figure 6.9: Expected distributions (solid histograms) of $\bar{\chi}^2$ (top) and per event $-2\ln\mathcal{L}^i_{\rm max}$ (bottom) in the signal region for the $K^0_S h^\pm\pi^\mp$ inclusive (left) and Dalitz (right) fits. The $\bar{\chi}^2$ values and $-2\ln\mathcal{L}^i_{\rm max}$ distributions for on-resonance data are given by the dashed vertical lines and the square points, respectively.

Another possible source of bias in $\mathcal{A}_{+-}$ for $B \to K^*(892)^\pm\pi^\mp$ is the presence of crossfeed from other signal B decays. In the independent fits of the two topologies, the $\mathcal{A}_{+-}$ values for the signal modes are determined from the raw yields, without being deconvoluted by the efficiency matrices. Ideally, the signal yields in the two charge states would be deconvoluted separately, and $\mathcal{A}_{+-}$ would be determined from the resultant yields. However, in both topologies, the efficiency matrices confirm the lack of crossfeed between $K^*(892)^\pm\pi^\mp$ and the other signal components, so calculating $\mathcal{A}_{+-}$ from the raw yields is a valid procedure. In the simultaneous fit to the two topologies, the efficiency matrices are effectively taken into account, and the above caveat does not apply.

There may also exist crossfeed between one charge state of one mode and the opposite charge state of a different mode. We neglect this effect in the fit, and we estimate its size with a MC study using ensembles of fits to simulated samples. We compare the $\mathcal{A}_{+-}(B \to K^*(892)^\pm\pi^\mp)$ averages of two

Mode	Unmodified PDFs	Extreme Down	Extreme Up
$K^0_S\pi^\pm\pi^\mp$	$65.2^{+11.9}_{-11.1}(8.5\sigma)$	$60.0^{+11.6}_{-10.6}(8.1\sigma)$	$70.4^{+12.3}_{-11.4}(8.8\sigma)$
$K^0_S K^\pm\pi^\mp$	$0^{+6.8}$	$0^{+6.4}$	$0^{+6.0}$
$K^\pm\pi^\mp\pi^0$	$46.5^{+16.3}_{-15.7}(3.4\sigma)$	$37.4^{+15.0}_{-14.5}(3.0\sigma)$	$57.6^{+17.6}_{-16.8}(3.9\sigma)$
$K^+K^-\pi^0$	$0^{+15.2}$	$0^{+14.7}$	$0^{+15.2}$
$K^0_S\pi^\pm\pi^0$	$18.7^{+10.3}_{-9.0}(2.4\sigma)$	$13.1^{+9.3}_{-7.8}(1.9\sigma)$	$25.1^{+11.2}_{-10.0}(2.9\sigma)$
$K^0_S K^\pm\pi^0$	$0^{+2.5}$	$0^{+2.2}$	$0^{+3.0}$
$K^*(892)^\pm(K^0_S\pi^\pm)\pi^\mp$	$14.1^{+5.5}_{-4.6}(4.6\sigma)$	$13.2^{+5.3}_{-4.4}(4.4\sigma)$	$15.1^{+5.6}_{-4.8}(4.8\sigma)$
$K^*(892)^\pm(K^0_S\pi^\pm)K^\mp$	$1.8^{+2.8}_{-1.6}(1.0\sigma)$	$1.7^{+2.7}_{-1.7}(1.0\sigma)$	$1.9^{+2.9}_{-1.8}(1.0\sigma)$
$K^*_0(1430)^\pm(K^0_S\pi^\pm)\pi^\mp$	$17.1^{+8.1}_{-7.2}(2.7\sigma)$	$16.3^{+7.9}_{-7.0}(2.7\sigma)$	$18.1^{+8.3}_{-7.4}(2.8\sigma)$
$K^*_0(1430)^\pm(K^0_S\pi^\pm)K^\mp$	$0^{+2.1}$	$0^{+1.8}$	$0^{+2.3}$
$\rho(770)^0K^0_S$	$9.5^{+5.7}_{-4.6}(2.8\sigma)$	$8.3^{+5.4}_{-4.3}(2.6\sigma)$	$10.9^{+5.9}_{-4.9}(3.0\sigma)$
$f_0(980)K^0_S$	$2.4^{+3.1}_{-2.0}(1.3\sigma)$	$2.2^{+3.0}_{-1.9}(1.2\sigma)$	$2.6^{+3.2}_{-2.1}(1.3\sigma)$
$K^0_S\pi^+\pi^-$ NR	$18.0^{+9.3}_{-7.9}(2.7\sigma)$	$16.6^{+9.0}_{-7.6}(2.6\sigma)$	$19.4^{+9.5}_{-8.1}(2.9\sigma)$
$K^0_S K^\pm\pi^\mp$ NR	$0^{+2.5}$	$0^{+2.4}$	$0^{+2.7}$
$K^*(892)^\pm(K^\pm\pi^0)\pi^\mp$	$10.2^{+6.9}_{-5.4}(2.4\sigma)$	$8.4^{+6.4}_{-5.0}(2.1\sigma)$	$12.4^{+7.4}_{-6.0}(2.7\sigma)$
$K^*(892)^\pm(K^\pm\pi^0)K^\mp$	$7.4^{+6.5}_{-5.2}(1.6\sigma)$	$6.3^{+6.3}_{-4.9}(1.3\sigma)$	$9.0^{+6.8}_{-5.6}(1.8\sigma)$
$K^*_0(1430)^\pm(K^\pm\pi^0)\pi^\mp$	$0^{+7.9}$	$0^{+5.6}$	$2.2^{+9.5}_{-8.0}(0.3\sigma)$
$K^*_0(1430)^\pm(K^\pm\pi^0)K^\mp$	$0^{+2.6}$	$0^{+2.4}$	$0^{+2.8}$
$K/\bar{K}^*(892)^0\pi^0$	$5.8^{+7.4}_{-6.2}(0.9\sigma)$	$2.2^{+6.9}_{-5.6}(0.4\sigma)$	$10.2^{+7.9}_{-6.7}(1.6\sigma)$
$K/\bar{K}^*_0(1430)^0\pi^0$	$14.5^{+8.3}_{-7.0}(2.4\sigma)$	$12.7^{+7.9}_{-6.6}(2.2\sigma)$	$16.8^{+8.8}_{-7.5}(2.7\sigma)$
$K^\pm\pi^\mp\pi^0$ NR	$14.4^{+11.0}_{-9.6}(1.6\sigma)$	$12.2^{+10.4}_{-9.1}(1.4\sigma)$	$16.4^{+11.8}_{-11.4}(1.7\sigma)$
$K^+K^-\pi^0$ NR	$2.2^{+10.3}_{-10.8}(0.3\sigma)$	$1.2^{+10.0}_{-21.7}(0.2\sigma)$	$2.9^{+10.7}_{-9.6}(0.3\sigma)$
$K/\bar{K}^*(892)^0\pi^\pm$	$8.9^{+4.4}_{-3.5}(3.7\sigma)$	$8.1^{+4.2}_{-3.4}(3.5\sigma)$	$9.5^{+4.6}_{-3.7}(3.9\sigma)$
$\bar{K}/K^*(892)^0K^\pm$	$2.3^{+3.2}_{-2.1}(1.1\sigma)$	$2.0^{+3.1}_{-2.0}(1.0\sigma)$	$2.5^{+3.3}_{-2.2}(1.2\sigma)$
$K/\bar{K}^*_0(1430)^0\pi^\pm$	$0.5^{+4.1}_{-5.6}(0.2\sigma)$	$0^{+3.2}$	$1.5^{+4.3}_{-3.3}(0.4\sigma)$
$\bar{K}/K^*_0(1430)^0K^\pm$	$0.3^{+4.9}_{-2.3}(0.1\sigma)$	$0^{+4.2}$	$1.7^{+5.1}_{-4.0}(0.4\sigma)$
$K^*(892)^\pm\pi^0$	$1.7^{+4.5}_{-3.3}(0.5\sigma)$	$0.7^{+4.1}_{-6.2}(0.2\sigma)$	$3.3^{+4.9}_{-3.7}(0.9\sigma)$
$K^*_0(1430)^\pm\pi^0$	$3.6^{+4.7}_{-3.1}(1.3\sigma)$	$2.7^{+4.2}_{-2.6}(1.1\sigma)$	$4.6^{+5.1}_{-3.5}(1.5\sigma)$
$\rho(770)^\pm K^0_S$	$7.0^{+6.3}_{-5.0}(1.6\sigma)$	$4.4^{+5.6}_{-3.9}(1.2\sigma)$	$10.2^{+6.8}_{-5.7}(2.1\sigma)$
$K^0_S\pi^\pm\pi^0$ NR	$0^{+2.5}$	$0^{+2.0}$	$0^{+2.5}$
$K^0_S K^\pm\pi^0$ NR	$0^{+1.7}$	$0^{+1.5}$	$0^{+1.8}$

Table 6.11: Fit results using Dalitz-plot-averaged PDFs with extreme variations.

ensembles with different sample compositions. In the first ensemble, signal MC for $B \to K^*(892)^\pm\pi^\mp$ is embedded in toy MC for the four background components. In the second sample, we replace the $B \to K^*(892)^\pm\pi^\mp$ MC with signal MC for all eight signal components, where the proportions of MC in each signal mode mimics the results of the fits to on-resonance data. The two final state topologies are treated independently. The $B \to K^*(892)^\pm\pi^\mp$ MC sample contains roughly equal amounts of each charge state, and the MC for the CP eigenstates are explicitly generated with $\mathcal{A}_{+-} = 0$. For all other signal modes, $\mathcal{A}_{+-} = -1$ in the MC. The fitted charge asymmetries in on-resonance data are scattered throughout the physical region, so we overestimate the effect of crossfeed between modes by using a common extreme value for the generated asymmetries.

Figure 6.13 shows the distributions of $\mathcal{A}_{+-}(B \to K^*(892)^\pm\pi^\mp)$ from the two ensembles in

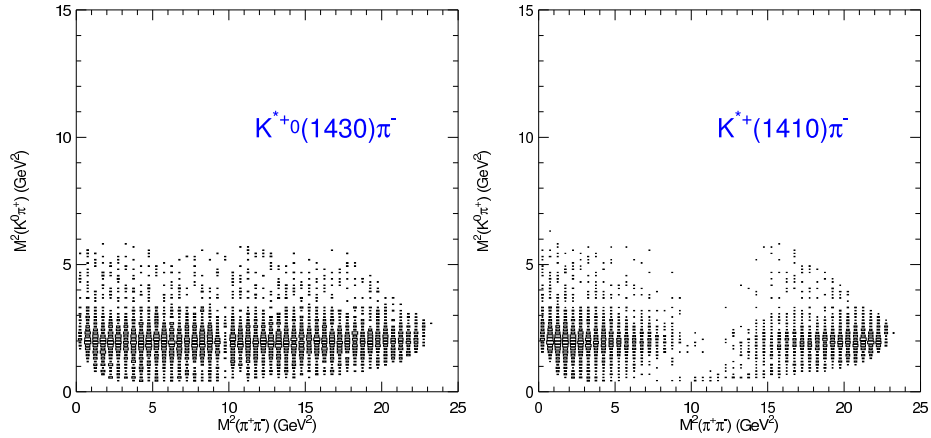

Figure 6.10: Dalitz PDFs for $B \to K_0^*(1430)^\pm h^\mp$ (left) and $B \to K^*(1410)^\pm h^\mp$ (right).

Mode	$K_X^{*\pm} = K_0^*(1430)^\pm$	$K_X^{*\pm} = K^*(1410)^\pm$
$K^*(892)^\pm\pi^\mp$	$12.0^{+5.1}_{-4.3}(4.0\sigma)$	$12.2^{+5.1}_{-4.3}(4.1\sigma)$
$K^*(892)^\pm K^\mp$	$1.6^{+2.8}_{-1.8}(0.9\sigma)$	$1.6^{+2.8}_{-1.8}(0.8\sigma)$
$K_X^{*\pm}\pi^\mp$	$16.2^{+8.1}_{-7.2}(2.6\sigma)$	$8.0^{+7.9}_{-7.0}(1.1\sigma)$
$K_X^{*\pm}K^\mp$	$0^{+2.3}$	$1.2^{+3.4}_{-2.1}(0.5\sigma)$
$\rho(770)^0 K_S^0$	$6.9^{+5.1}_{-3.9}(2.3\sigma)$	$6.5^{+5.0}_{-3.8}(2.2\sigma)$
$f_0(980)K_S^0$	$2.6^{+3.1}_{-2.1}(1.4\sigma)$	$2.4^{+3.1}_{-2.1}(1.2\sigma)$
$K_S^0\pi^+\pi^-$ NR	$21.8^{+9.5}_{-8.3}(3.2\sigma)$	$29.5^{+10.1}_{-8.9}(4.4\sigma)$
$K_S^0 K^\pm\pi^\mp$ NR	$0^{+3.7}$	$0^{+3.4}$

Table 6.12: $K_S^0 h^\pm\pi^\mp$ Dalitz fit results with $K_0^*(1430)^\pm$ and $K^*(1410)^\pm$.

each topology. In neither topology is there evidence for bias away from the true asymmetries of 0.002 for $K_S^0 h^\pm\pi^\mp$ and 0.010 for $K^\pm h^\mp\pi^0$. Also, within each topology, the difference between the average $\mathcal{A}_{+-}(B \to K^*(892)^\pm\pi^\mp)$ values in the two ensembles does not deviate significantly from zero. Nonetheless, the shifts of $\delta\mathcal{A}_{+-}(B \to K^*(892)^\pm\pi^\mp) = 0.03 \pm 0.06$ for $K_S^0 h^\pm\pi^\mp$ and $\delta\mathcal{A}_{+-}(B \to K^*(892)^\pm\pi^\mp) = 0.04 \pm 0.09$ for $K^\pm h^\mp\pi^0$ are included in the systematic uncertainty.

Finally, we consider charge asymmetries in the four background components, which we have assumed in the fit to be those of the entire samples. We make a simplified determination of $\mathcal{A}_{+-}(B \to K^*(892)^\pm\pi^\mp)$ by fitting for the yields of each charge state separately and propagating the bifurcated-Gaussian errors on the resultant branching fractions by MC simulation. Unlike the direct fits for charge asymmetries, we form $\mathcal{A}_{+-}$ values for modes with no yield. In these simultaneous fits to the $K_S^0 h^\pm\pi^\mp$ and $K^\pm h^\mp\pi^0$ topologies, the $\mathcal{A}_{+-}$ values for the background components are effectively allowed to float. This method does not account for the (possible) non-Gaussian shapes of the likelihood functions, and it ignores the (potential) correlations between the

Mode	Standard Fit	Remove One	Remove Two
	$K^0_S h^\pm\pi^\mp$ Inclusive Fit		
$K^0_S\pi^+\pi^-$	$60.2^{+11.5}_{-10.6}(8.1\sigma)$	$58.3^{+11.5}_{-10.6}(7.8\sigma)$	$56.4^{+11.4}_{-10.5}(7.5\sigma)$
$K^0_S K^\pm\pi^\mp$	$2.4^{+7.1}_{-7.2}(0.4\sigma)$	$2.4^{+7.1}_{-6.7}(0.4\sigma)$	$2.5^{+7.1}_{-7.0}(0.4\sigma)$
	$K^0_S h^\pm\pi^\mp$ Dalitz Fit		
$K^*(892)^\pm\pi^\mp$	$12.0^{+5.1}_{-4.3}(4.0\sigma)$	$10.2^{+5.0}_{-4.1}(3.4\sigma)$	$8.5^{+4.8}_{-3.8}(2.8\sigma)$
$K^*(892)^\pm K^\mp$	$1.6^{+2.8}_{-1.8}(0.9\sigma)$	$1.7^{+2.8}_{-1.8}(0.9\sigma)$	$1.9^{+2.8}_{-1.8}(1.0\sigma)$
$K^*_0(1430)^\pm\pi^\mp$	$16.2^{+8.1}_{-7.2}(2.6\sigma)$	$16.3^{+8.2}_{-7.2}(2.6\sigma)$	$16.5^{+8.2}_{-7.3}(2.6\sigma)$
$K^*_0(1430)^\pm K^\mp$	$0^{+2.3}$	$0^{+2.3}$	$0^{+2.3}$
$\rho(770)^0 K^0_S$	$6.9^{+5.1}_{-3.9}(2.3\sigma)$	$6.9^{+5.1}_{-3.9}(2.3\sigma)$	$7.0^{+5.1}_{-3.9}(2.3\sigma)$
$f_0(980)K^0_S$	$2.6^{+3.1}_{-2.1}(1.4\sigma)$	$2.6^{+3.1}_{-2.1}(1.4\sigma)$	$2.6^{+3.1}_{-2.1}(1.4\sigma)$
$K^0_S\pi^+\pi^-$ NR	$21.8^{+9.5}_{-8.3}(3.2\sigma)$	$21.8^{+9.6}_{-8.3}(3.2\sigma)$	$21.9^{+9.6}_{-8.3}(3.2\sigma)$
$K^0 K^\pm\pi^\mp$ NR	$0^{+3.7}$	$0^{+3.7}$	$0^{+3.7}$

Table 6.13: $K^0_S h^\pm\pi^\mp$ inclusive and Dalitz fit results with the one and two most signal-like events removed.

two charge conjugate states. The results for the signal and background components in these two fits are shown in Table 6.20. From these charge-separated fits, $\mathcal{A}_{+-}(B \to K^*(892)^\pm\pi^\mp)$ is determined to be $0.25^{+0.32}_{-0.31}$, which agrees well with the value from Table 6.17. We conclude that the negligible charge asymmetries in the background do not bias the charge asymmetry in $B \to K^*(892)^\pm\pi^\mp$, and we include the difference of $\delta\mathcal{A}_{+-}(B \to K^*(892)^\pm\pi^\mp) = 0.01$ between the two determinations in the systematic uncertainty.

Mode	No $K_0^*(1430)$	No NR	No $K_0^*(1430)$/NR
$K^*(892)^\pm(K_S^0\pi^\pm)\pi^\mp$	$12.4^{+5.2}_{-4.3}(4.2\sigma)$	$12.3^{+5.2}_{-4.3}(4.1\sigma)$	$14.7^{+5.3}_{-4.5}(5.3\sigma)$
$K^*(892)^\pm(K_S^0\pi^\pm)K^\mp$	$1.6^{+2.8}_{-1.8}(0.9\sigma)$	$1.6^{+2.8}_{-1.7}(0.9\sigma)$	$1.5^{+2.8}_{-1.7}(0.9\sigma)$
$K_0^*(1430)^\pm(K_S^0\pi^\pm)\pi^\mp$	—	$26.2^{+7.8}_{-6.9}(5.5\sigma)$	—
$K_0^*(1430)^\pm(K_S^0\pi^\pm)K^\mp$	—	$0^{+2.3}$	—
$\rho(770)^0K_S^0$	$6.8^{+5.0}_{-3.9}(2.2\sigma)$	$7.6^{+5.1}_{-4.0}(2.6\sigma)$	$8.1^{+5.2}_{-4.1}(2.8\sigma)$
$f_0(980)K_S^0$	$2.2^{+3.1}_{-2.0}(1.1\sigma)$	$3.4^{+3.1}_{-2.2}(2.1\sigma)$	$3.4^{+3.1}_{-2.2}(2.2\sigma)$
$K_S^0\pi^+\pi^-$ NR	$35.2^{+9.2}_{-8.3}(5.9\sigma)$	—	—
$K_S^0K^\pm\pi^\mp$ NR	$0^{+3.8}$	—	—
$K^*(892)^\pm(K^\pm\pi^0)\pi^\mp$	$7.1^{+5.7}_{-4.3}(2.1\sigma)$	$7.3^{+5.7}_{-4.3}(2.2\sigma)$	$7.4^{+5.7}_{-4.3}(2.2\sigma)$
$K^*(892)^\pm(K^\pm\pi^0)K^\mp$	$4.2^{+5.7}_{-4.4}(1.0\sigma)$	$4.3^{+5.8}_{-4.3}(1.0\sigma)$	$4.4^{+5.8}_{-4.3}(1.1\sigma)$
$K_0^*(1430)^\pm(K^\pm\pi^0)\pi^\mp$	—	$7.8^{+9.0}_{-8.0}(1.0\sigma)$	—
$K_0^*(1430)^\pm(K^\pm\pi^0)K^\mp$	—	$0^{+4.5}$	—
$K/\bar{K}^*(892)^0\pi^0$	$0^{+4.7}$	$0^{+3.8}$	$0^{+5.6}$
$K/\bar{K}_0^*(1430)^0\pi^0$	—	$18.5^{+8.2}_{-7.0}(3.4\sigma)$	—
$K^\pm\pi^\mp\pi^0$ NR	$22.2^{+11.4}_{-10.1}(2.4\sigma)$	—	—
$K^+K^-\pi^0$ NR	$6.8^{+10.4}_{-9.3}(0.8\sigma)$	—	—
$K/\bar{K}^*(892)^0\pi^\pm$	$6.6^{+3.7}_{-2.9}(3.3\sigma)$	$6.6^{+3.7}_{-2.9}(3.2\sigma)$	$6.6^{+3.7}_{-2.9}(3.3\sigma)$
$\bar{K}/K^*(892)^0K^\pm$	$0.8^{+2.5}_{-1.2}(0.5\sigma)$	$0.8^{+2.5}_{-1.4}(0.5\sigma)$	$0.8^{+2.5}_{-1.2}(0.5\sigma)$
$K/\bar{K}_0^*(1430)^0\pi^\pm$	—	$0.9^{+3.8}_{-2.8}(0.3\sigma)$	—
$\bar{K}/K_0^*(1430)^0K^\pm$	—	$0^{+1.9}$	—
$K^*(892)^\pm\pi^0$	$6.6^{+5.7}_{-4.6}(1.6\sigma)$	$6.4^{+5.7}_{-4.6}(1.5\sigma)$	$6.6^{+5.7}_{-4.6}(1.6\sigma)$
$K_0^*(1430)^\pm\pi^0$	—	$3.2^{+4.5}_{-2.8}(1.2\sigma)$	—
$\rho(770)^\pm K_S^0$	$10.6^{+6.8}_{-5.6}(2.2\sigma)$	$10.3^{+6.8}_{-5.6}(2.1\sigma)$	$10.6^{+6.8}_{-5.6}(2.2\sigma)$
$K_S^0\pi^\pm\pi^0$ NR	$0^{+3.7}$	—	—
$K_S^0K^\pm\pi^0$ NR	$0^{+1.6}$	—	—

Table 6.14: Dalitz fit results with yields for various broad components fixed to zero.

Mode	Yield	$\mathcal{A}_{+-}$
$K^*(892)^\pm\pi^\mp$	$11.5^{+5.0}_{-4.2}(3.9\sigma)$	0.19 ± 0.40
$K^*(892)^\pm K^\mp$	$2.4^{+2.8}_{-1.8}(1.5\sigma)$	$1.00^{+0.00}_{-0.62}$
$K_0^*(1430)^\pm\pi^\mp$	$18.4^{+7.4}_{-6.2}(4.5\sigma)$	$-1.00^{+0.34}_{-0.00}$
$K_0^*(1430)^\pm K^\mp$	$0^{+2.3}$	0
$\rho(770)^0 K_S^0$	$5.9^{+5.0}_{-3.8}(2.3\sigma)$	-0.35 ± 0.72
$f_0(980)K_S^0$	$2.8^{+2.8}_{-1.9}(1.8\sigma)$	$1.00^{+0.00}_{-0.71}$
$K_S^0\pi^+\pi^-$ NR	$19.4^{+8.6}_{-8.9}(3.7\sigma)$	$0.51^{+0.45}_{-0.43}$
$K_S^0 K^\pm\pi^\mp$ NR	$0^{+3.7}$	0
$b \to c$, $h = \pi$	458^{+45}_{-44}	
$b \to c$, $h = K$	$23.6^{+27.3}_{-23.6}$	
Continuum, $h = \pi$	$(6.37 \pm 0.09) \times 10^3$	
Continuum, $h = K$	4.98×10^3	

Table 6.15: Results of Dalitz fit with charge asymmetries for $K_S^0 h^\pm\pi^\mp$.

Mode	Yield	$\mathcal{A}_{+-}$
$K^*(892)^\pm\pi^\mp$	$7.3^{+5.7}_{-4.4}(2.3\sigma)$	$0.72^{+0.44}_{-0.69}$
$K^*(892)^\pm K^\mp$	$4.3^{+5.8}_{-4.5}(1.0\sigma)$	-0.10 ± 1.43
$K_0^*(1430)^\pm\pi^\mp$	$6.7^{+7.2}_{-6.1}(1.2\sigma)$	$1.00^{+0.00}_{-0.85}$
$K_0^*(1430)^\pm K^\mp$	$0^{+3.0}$	0
$K/\bar{K}^*(892)^0\pi^0$	$0^{+3.8}$	0
$K/\bar{K}_0^*(1430)^0\pi^0$	$16.1^{+8.1}_{-6.9}(2.9\sigma)$	$-0.06^{+0.47}_{-0.46}$
$K^\pm\pi^\mp\pi^0$ NR	$11.9^{+10.3}_{-8.6}(1.5\sigma)$	$-0.24^{+0.85}_{-0.62}$
$K^+K^-\pi^0$ NR	$6.9^{+10.2}_{-7.7}(1.1\sigma)$	$-1.00^{+1.45}_{-0.00}$
$b \to c$, $h = \pi$	915^{+77}_{-75}	
$b \to c$, $h = K$	512^{+64}_{-62}	
Continuum, $h = \pi$	$(1.72 \pm 0.01) \times 10^4$	
Continuum, $h = K$	9.91×10^3	

Table 6.16: Results of Dalitz fit with charge asymmetries for $K^\pm h^\mp\pi^0$.

Mode	Yield ($K^0_S h^\pm \pi^\mp$)	Yield ($K^\pm h^\mp \pi^0$)	$\mathcal{A}_{+-}$
$K^*(892)^\pm \pi^\mp$	$12.4^{+4.5}_{-3.9}(4.6\sigma)$	$5.9^{+2.2}_{-1.9}(4.6\sigma)$	$0.26^{+0.33}_{-0.34}$
$K^*(892)^\pm K^\mp$	$2.1^{+2.3}_{-1.6}(1.5\sigma)$	$4.0^{+2.2}_{-1.6}(1.5\sigma)$	$1.00^{+0.00}_{-0.74}$
$K^*_0(1430)^\pm \pi^\mp$	$13.9^{+7.1}_{-5.9}(3.6\sigma)$	$8.2^{+4.1}_{-3.7}(3.6\sigma)$	$-0.86^{+0.50}_{-1.54}$
$K^*_0(1430)^\pm K^\mp$	$0^{+1.5}$	$0^{+1.4}$	0
$\rho(770)^0 K^0_S$	$6.1^{+5.0}_{-3.8}(2.3\sigma)$		$-0.35^{+0.71}_{-0.65}$
$f_0(980) K^0_S$	$2.8^{+2.8}_{-1.9}(1.8\sigma)$		$1.00^{+0.00}_{-0.70}$
$K^0_S \pi^+ \pi^-$ NR	$21.0^{+9.3}_{-8.0}(3.7\sigma)$		$0.32^{+0.45}_{-0.42}$
$K^0_S K^\pm \pi^\mp$ NR	$0^{+4.7}$		0
$K/\bar{K}^*(892)^0 \pi^0$		$0^{+3.8}$	0
$K/\bar{K}^*_0(1430)^0 \pi^0$		$15.8^{+8.0}_{-6.9}(2.8\sigma)$	$-0.07^{+0.48}_{-0.47}$
$K^\pm \pi^\mp \pi^0$ NR		$14.3^{+10.6}_{-9.1}(1.7\sigma)$	$-0.02^{+0.71}_{-0.86}$
$K^+ K^- \pi^0$ NR		$4.9^{+8.8}_{-6.3}(0.9\sigma)$	$-1.00^{+0.88}_{-0.00}$
$b \to c$, $h = \pi$	458^{+45}_{-44}	916^{+77}_{-75}	
$b \to c$, $h = K$	$23.9^{+27.0}_{-24.8}$	512^{+64}_{-63}	
Continuum, $h = \pi$	$(6.37 \pm 0.09) \times 10^3$	$(1.72 \pm 0.01) \times 10^4$	
Continuum, $h = K$	4.98×10^3	9.91×10^3	

Table 6.17: Results of simultaneous $\mathcal{A}_{+-}$ fit of the $K^0_S h^\pm \pi^\mp$ and $K^\pm h^\mp \pi^0$ topologies.

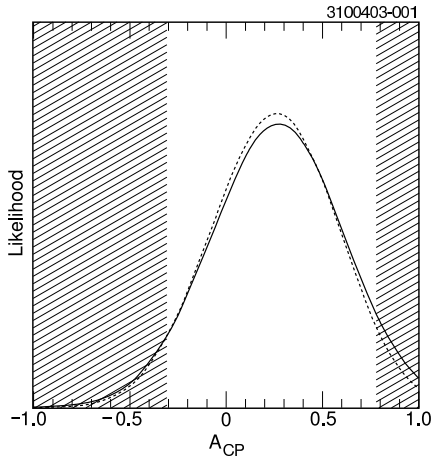

Figure 6.11: Likelihood as a function of $\mathcal{A}_{+-}(B \to K^*(892)^\pm \pi^\mp)$ for the simultaneous fit of the $K^0_S h^\pm \pi^\mp$ and $K^\pm h^\mp \pi^0$ topologies, before (dashed) and after (solid) including systematic uncertainties. The hatched regions each contain 5% of the integrated area and are excluded at the 90% confidence level.

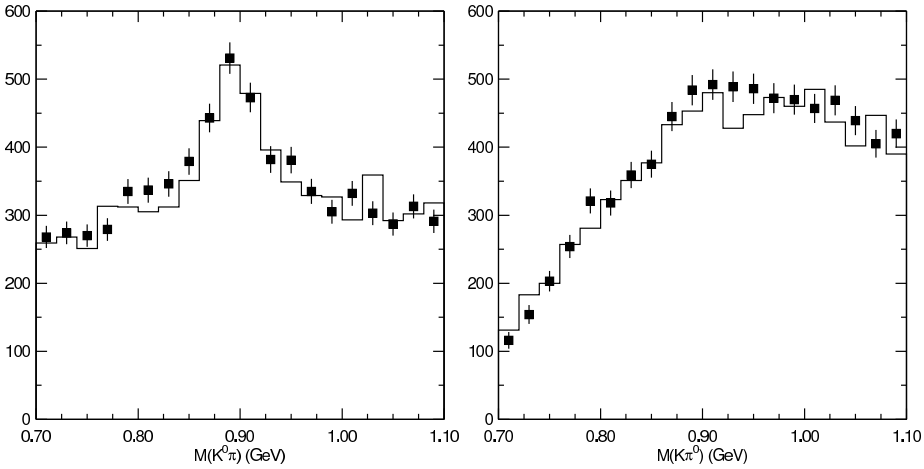

Figure 6.12: Invariant mass distributions of $K^*(892)^+$ (histogram) and $K^*(892)^-$ (points) candidates for the $K^0_S\pi^\pm$ (left) and $K^\pm\pi^0$ (right) decay modes.

Mode	Total Area	Area Asymmetry	Mean Asymmetry
$K^*(892)^\pm \to K^0_S\pi^\pm$	1798 ± 132	-0.039 ± 0.073	-0.001 ± 0.002
$K^*(892)^\pm \to K^\pm\pi^0$	477 ± 131	0.106 ± 0.273	0.003 ± 0.008

Table 6.18: Charge asymmetries in area and mean of the Breit-Wigner component of the $K^*(892)^\pm$ lineshape, measured in on- and off-resonance data.

Mode	$N_{\rm generated}$	$\epsilon_{\rm sel}$	$\epsilon_{\rm fit}$	$\epsilon_{\rm tot}$
$K^*(892)^+(K^0_S\pi^+)\pi^-$	29987	35.7 ± 0.3	69.6 ± 0.4	24.9 ± 0.2
$K^*(892)^-(K^0_S\pi^-)\pi^+$	15000	35.2 ± 0.4	68.2 ± 0.6	24.0 ± 0.3
$K^*(892)^+(K^+\pi^0)\pi^-$	32731	15.9 ± 0.2	87.4 ± 0.5	13.9 ± 0.2
$K^*(892)^-(K^-\pi^0)\pi^+$	15000	15.0 ± 0.3	89.7 ± 0.6	13.4 ± 0.3

Table 6.19: Selection, fit, and total efficiencies in percent for charge-separated states, not including branching fractions.

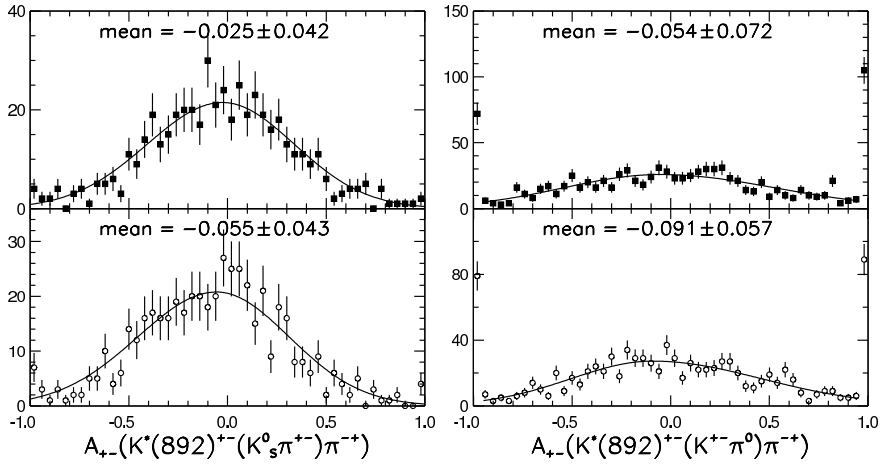

Figure 6.13: Distributions of $\mathcal{A}_{+-}(B \to K^*(892)^{\pm}\pi^{\mp})$ for ensembles of simulated experiments for the $K^0_S h^{\pm}\pi^{\mp}$ topology (left) and the $K^{\pm}h^{\mp}\pi^0$ topology (right), with signal MC for $B \to K^*(892)^{\pm}\pi^{\mp}$ only (top) and for all eight signal modes (bottom). The generated $\mathcal{A}_{+-}(B \to K^*(892)^{\pm}\pi^{\mp})$ values are 0.002 for $K^*(892)^{\pm} \to K^0_S\pi^{\pm}$ and 0.010 for $K^*(892)^{\pm} \to K^{\pm}\pi^0$.

Mode	Yield (h^+)	$\mathcal{B}(h^+)$	Yield (h^-)	$\mathcal{B}(h^-)$	$\mathcal{A}_{+-}$
	$K^0_S h^+\pi^-$ (6007 entries)		$K^0_S h^-\pi^+$ (5886 entries)		
$K^*(892)^\pm\pi^\mp$	$7.8^{+3.5}_{-2.9}(4.0\sigma)$	20^{+9}_{-7}	$4.5^{+3.0}_{-2.4}(2.3\sigma)$	12^{+8}_{-6}	$0.25^{+0.32}_{-0.31}$
$K^*(892)^\pm K^\mp$	$2.1^{+2.3}_{-1.6}(1.4\sigma)$	7^{+8}_{-5}	$0^{+0.9}$	0^{+3}	$0.86^{+0.34}_{-0.40}$
$K^*_0(1430)^\pm\pi^\mp$	$0.7^{+4.6}_{-9.5}(0.2\sigma)$	2^{+14}_{-29}	$13.1^{+5.6}_{-5.0}(3.0\sigma)$	39^{+17}_{-15}	$-0.72^{+0.40}_{-0.43}$
$K^*_0(1430)^\pm K^\mp$	$0.3^{+2.4}_{-5.1}(0.2\sigma)$	1^{+12}_{-24}	$0^{+0.8}$	0^{+8}	$0.40^{+0.72}_{-0.74}$
$\rho(770)^0 K^0/\bar{K}^0$	$2.0^{+3.8}_{-2.6}(0.8\sigma)$	4^{+7}_{-5}	$4.0^{+3.7}_{-2.6}(2.2\sigma)$	8^{+7}_{-5}	-0.20 ± 0.50
$f_0(980)K^0/\bar{K}^0$	$2.8^{+2.8}_{-1.9}(1.8\sigma)$	10^{+10}_{-7}	$0^{+1.2}$	0^{+4}	$0.91^{+0.19}_{-0.49}$
$K^0/\bar{K}^0\pi^+\pi^-$ NR	$14.3^{+6.6}_{-5.7}(3.1\sigma)$	28^{+13}_{-11}	$6.7^{+6.7}_{-5.1}(1.4\sigma)$	13^{+13}_{-10}	$0.32^{+0.32}_{-0.39}$
$\bar{K}^0/K^0 K^\pm\pi^\mp$ NR	$0^{+2.1}$	0^{+13}	$1.6^{+4.3}_{-4.0}(0.5\sigma)$	10^{+27}_{-25}	$-0.74^{+0.63}_{-0.41}$
$b \to c$, $h = \pi$	235^{+34}_{-32}		224^{+32}_{-30}		$0.02^{+0.10}_{-0.09}$
$b \to c$, $h = K$	9.9 ± 19.8		$11.7^{+18.6}_{-16.5}$		$0.05^{+0.53}_{-0.64}$
Cont., $h = \pi$	$(3.18 \pm 0.06) \times 10^3$		$(3.19 \pm 0.06) \times 10^3$		0.00 ± 0.01
Cont,, $h = K$	$(2.55 \pm 0.05) \times 10^3$		$(2.43 \pm 0.05) \times 10^3$		0.02 ± 0.01
	$K^- h^+\pi^0$ (14377 entries)		$K^+ h^-\pi^0$ (14212 entries)		
$K^*(892)^\pm\pi^\mp$	$3.7^{+1.7}_{-1.4}$	20^{+8}_{-6}	$2.2^{+1.8}_{-1.4}$	12^{+10}_{-7}	$0.25^{+0.32}_{-0.31}$
$K^*(892)^\pm K^\mp$	$3.2^{+1.8}_{-1.3}$	7^{+8}_{-5}	$0.9^{+0.9}_{-1.3}$	0^{+5}	$0.69^{+0.50}_{-0.54}$
$K^*_0(1430)^\pm\pi^\mp$	$0.4^{+2.7}_{-6.4}$	2^{+14}_{-29}	$7.7^{+3.3}_{-2.9}$	39^{+17}_{-15}	$-0.72^{+0.40}_{-0.43}$
$K^*_0(1430)^\pm K^\mp$	$0^{+2.2}$	3^{+11}_{-3}	$0^{+0.8}$	0^{+7}	$0.51^{+0.72}_{-0.60}$
$K/\bar{K}^*(892)^0\pi^0$	$0^{+2.7}$	0^{+5}	$0.2^{+5.7}_{-4.6}(0.1\sigma)$	0^{+11}	$-0.69^{+0.65}_{-0.49}$
$K/\bar{K}^*_0(1430)^0\pi^0$	$7.1^{+5.6}_{-4.4}(1.8\sigma)$	13^{+10}_{-8}	$8.8^{+6.1}_{-4.9}(2.2\sigma)$	16^{+11}_{-9}	$-0.12^{+0.44}_{-0.40}$
$K^\pm\pi^\mp\pi^0$ NR	$5.5^{+7.2}_{-6.1}(1.0\sigma)$	14^{+18}_{-15}	$7.7^{+7.4}_{-6.0}(1.4\sigma)$	19^{+18}_{-15}	$-0.14^{+0.55}_{-0.53}$
$K^+K^-\pi^0$ NR	$0^{+6.1}$	0^{+11}	$5.5^{+6.9}_{-6.2}(0.9\sigma)$	0^{+12}	$-0.13^{+0.89}_{-0.77}$
$b \to c$, $h = \pi$	538^{+56}_{-55}		380^{+52}_{-51}		0.17 ± 0.08
$b \to c$, $h = K$	272^{+46}_{-44}		243^{+45}_{-43}		$0.05^{+0.12}_{-0.11}$
Cont., $h = \pi$	$(8.67 \pm 0.10) \times 10^3$		$(8.52 \pm 0.10) \times 10^3$		0.01 ± 0.01
Cont., $h = K$	$(4.87 \pm 0.07) \times 10^3$		$(5.03 \pm 0.07) \times 10^3$		-0.02 ± 0.01

Table 6.20: Results of simultaneous fits of the $K^0_S h^\pm\pi^\mp$ and $K^\mp h^\pm\pi^0$ topologies, with charge states separated. Branching fractions are given in units of 10^{-6}.

Chapter 7 Systematic Uncertainties

In this chapter, we present the sources of systematic uncertainty in the three-body inclusive branching fractions, the exclusive branching fractions from the Dalitz fits, and the CP asymmetry in $B \to K^*(892)^{\pm}\pi^{\mp}$. Both additive and multiplicative uncertainties are considered for the branching fraction measurements, while the CP asymmetry only receives contributions from additive uncertainties.

7.1 Uncertainties on Inclusive Fit Results

Table 7.1 lists the systematic uncertainties assigned to the CP-averaged branching fractions for the three-body inclusive modes. The first section of the Table gives additive errors. The error arising from PDF parameter variation is taken to be $\frac{1}{\sqrt{12}}$ times the spread in yields from the extreme PDF variations discussed in Section 6.3.3. In the three $K\bar{K}\pi$ modes, the extreme PDF variations do not modify their zero yields, so we assign a conservative uncertainty equal to that of the corresponding $K\pi\pi$ mode.

In the $K^{\pm}h^{\mp}\pi^0$ topology, fitting the off-resonance data does not give zero yields, so we assign a one-sided uncertainty corresponding to the non-zero off-resonance yield scaled to the on-resonance luminosity.

The uncertainty due to fit variable correlations is estimated using toy MC, where all the PDFs are modeled by Gaussians because they are easily rotated into an arbitrary basis. We compare two ensembles of fits: one where the toy MC events are generated with uncorrelated variables, and another where the events are generated according to the correlation matrices observed in data and signal MC. The difference between the average signal yield in these two ensembles is consistently smaller than 1%, and we assign a conservative 1% systematic error to every mode for fit variable correlations.

The second section of Table 7.1 gives the multiplicative errors, which include errors on the efficiency, dominated by uncertainties in the accuracy of the MC reproduction of track, K^0_S, and π^0 reconstruction efficiencies. Based on high-statistics studies of $\tau^{\pm}$ decays and $\bar{D}^0/D^0 \to K^{\pm}\pi^{\mp}\pi^0$ decays, we assign correlated uncertainties of 2% per track, K^0_S or π^0. We also include 1% per track for the use of dE/dx information. Statistical uncertainties in the efficiency arise from finite MC statistics and from the binning used in determining the Dalitz-plot-dependent efficiency. The latter uncertainty also reflects the difference between the Dalitz-plot-dependent efficiency and that obtained by averaging the efficiencies of the exclusive modes in each topology. Thus, we have accounted for

the uncertainty in the efficiency of the π^0 momentum requirement from not knowing the true π^0 momentum distribution.

The final two sources, which are common to all modes, reflect our uncertainty in the numbers of charged and neutral B mesons produced. The uncertainty on the ratio of charged to neutral B mesons is taken from a recent CLEO measurement [120] of $f_{+-}/f_{00} = \Gamma(\Upsilon(4S) \to B^+B^-)/\Gamma(\Upsilon(4S) \to B^0\bar{B}^0) = 1.04 \pm 0.07 \pm 0.04$, which was made by comparing the rate for $B^0 \to J/\psi K^*(892)^0$ and its charge conjugate with that for $B^\pm \to J/\psi K^*(892)^\pm$. The total number of B mesons, $N_{B\bar{B}} = 9.66 \times 10^6$, is obtained from measurements of the luminosity, $\mathcal{L}$, and the $e^+e^- \to B\bar{B}$ cross section, σ. $\mathcal{L}$ is determined from detected yields of $e^+e^- \to e^+e^-$, $\mu^+\mu^-$, and $\gamma\gamma$ and from MC simulation of these processes combined with their calculated cross sections. The systematic error of 1.0% on $\mathcal{L}$ arises from the cuts (especially on the polar angle) made to select the above samples. The $e^+e^- \to \Upsilon(4S) \to B\bar{B}$ cross section is calculated from the differences in on- and off-resonance hadronic event yields and the known respective luminosities. Contributions to its systematic error include the time variation of σ within a dataset and different running conditions between on- and off-resonance. To span these uncertainties conservatively, we assign a systematic error to $N_{B\bar{B}} = \mathcal{L}\sigma$ of 2%.

The total systematic error for each mode is the quadrature sum of all the contributions. The branching fraction upper limits are inflated by one unit of the positive error, which gives conservative upper limits.

7.2 Uncertainties on Dalitz Fit Results

The systematic uncertainties on the CP-averaged branching fractions for the Dalitz fit modes are listed in Table 7.2. The uncertainties from PDF variation and from off-resonance signal yields are evaluated as for the inclusive fits (Section 7.1). The Dalitz PDF uncertainty is estimated by changing the binning of the two-dimensional histogram. The uncertainty due to the choice of components allowed to float in the fit is the full width of the larger of the two variations in the first two columns of Table 6.14. In some modes with zero yield, *e.g.*, $B \to K_0^*(1430)^\pm K^\mp$ and $B \to \bar{K}^0K^+\pi^-$ NR, applying systematic variations to the PDFs and fit components do not produce any change in signal yield. The procedure used to measure the error from neglecting interference is described in Section 7.2.1. Uncertainties common to all modes are those due to input variable correlations, the $\cos\theta_{\rm sph}$ requirement, f_{00}/f_{+-}, and $N_{B\bar{B}}$, amounting to a contribution of 8.6%. The $K_0^*(1430)$ modes also include a 10.8% error for the uncertainty in the branching fraction $\mathcal{B}(K_0^*(1430) \to K\pi) = (93 \pm 10)\%$ [5]. The common uncertainty of 8.6% and the $\mathcal{B}(K_0^*(1430) \to K\pi)$ uncertainty are not itemized in Table 7.2 (for lack of space) but are included in the total uncertainties.

For $B \to K^*(892)^\pm h^\mp$ and $B \to K_0^*(1430)^\pm h^\mp$, the combined branching fractions from Sec-

Source	$K^0\pi^+\pi^-$	$\bar{K}^0K^+\pi^-$	$K^+\pi^-\pi^0$	$K^+K^-\pi^0$	$K^0\pi^+\pi^0$	$\bar{K}^0K^+\pi^0$
Additive errors						
PDFs	±4.4	±4.4	±12.5	±12.5	±18.4	±18.4
Off-resonance	0	0	-28.5	0	0	0
Correlations	±1.0	±1.0	±1.0	±1.0	±1.0	±1.0
Multiplicative errors						
$\cos\theta_{\rm sph}$	±2.0	±2.0	±2.0	±2.0	±2.0	±2.0
Tracking	±8.0	±8.0	±4.0	±4.0	±6.0	±6.0
K^0_S finding	±2.0	±2.0	—	—	±2.0	±2.0
π^0 finding	—	—	±2.0	±2.0	±2.0	±2.0
dE/dx	±2.0	±2.0	±2.0	±2.0	±1.0	±1.0
MC statistics	±1.7	±1.9	±0.9	±1.7	±1.4	±3.2
ϵ vs. DP	±4.0	—	±7.4	—	±10.8	—
f_{00}/f_{+-}	±8.1	±8.1	±8.1	±8.1	±8.1	±8.1
$N_{B\bar{B}}$	±2.0	±2.0	±2.0	±2.0	±2.0	±2.0
Total	±13.6	±13.0	$^{+17.6}_{-33.5}$	±16.1	±24.0	±21.6

Table 7.1: Systematic uncertainties (%) on CP-averaged branching fractions for three-body inclusive modes. When a source does not apply to a given mode we give a "—" entry. Uncertainties that are found to be negligible are given a "0" entry.

tion 5.3.3 are equivalent to averages of the two $K^{*\pm}$ submodes, weighted by the squares of the individual significances ($\mathcal{S}^2$):

$$\bar{\mathcal{B}} = \frac{\mathcal{B}_A\mathcal{S}_A^2 + \mathcal{B}_B\mathcal{S}_B^2}{\mathcal{S}_A^2 + \mathcal{S}_B^2}. \tag{7.1}$$

Therefore, assuming uncorrelated uncertainties, the errors quoted for these four modes in Table 7.2 are averages over the two submodes:

$$\left(\frac{\sigma_{\bar{\mathcal{B}}}}{\bar{\mathcal{B}}}\right)_{\rm uncorr} = \frac{1}{\mathcal{S}_A^2 + \mathcal{S}_B^2}\sqrt{\left(\frac{\sigma_{\mathcal{B}_A}}{\mathcal{B}_A}\right)^2\mathcal{S}_A^4 + \left(\frac{\sigma_{\mathcal{B}_B}}{\mathcal{B}_B}\right)^2\mathcal{S}_B^4} \tag{7.2}$$

For MC modeling errors, which are correlated between the two submodes, the fractional error is:

$$\left(\frac{\sigma_{\bar{\mathcal{B}}}}{\bar{\mathcal{B}}}\right)_{\rm corr} = \frac{1}{\mathcal{S}_A^2 + \mathcal{S}_B^2}\sqrt{\left(\frac{\sigma_{\mathcal{B}_A}}{\mathcal{B}_A}\right)^2\mathcal{S}_A^4 + 2\frac{\sigma_{\mathcal{B}_A}\sigma_{\mathcal{B}_B}}{\mathcal{B}_A\mathcal{B}_B}\mathcal{S}_A^2\mathcal{S}_B^2 + \left(\frac{\sigma_{\mathcal{B}_B}}{\mathcal{B}_B}\right)^2\mathcal{S}_B^4}. \tag{7.3}$$

For $K_0^*(1430)^{\pm}K^{\mp}$, which has zero significance in both submodes, we weight the two contributions by the positive errors on the yields.

Mode	PDF	Bin	Comp	Off-res	Interf	Trk	K^0	π^0	$\frac{dE}{dx}$	MC	Tot
$K^*(892)^+\pi^-$	3.8	-4.4	3.5	0	5.2	8.0	2.0	—	2.0	1.0	
$K^*(892)^+K^-$	2.3	-25.5	1.2	0	0	8.0	2.0	—	2.0	2.0	
$K_0^*(1430)^+\pi^-$	3.1	-6.5	62.1	0	65.4	8.0	2.0	—	2.0	1.1	
$K_0^*(1430)^+K^-$	0	0	0	0	0	8.0	2.0	—	2.0	3.9	
$\rho(770)^0K^0$	7.9	-14.1	9.6	0	43.3	8.0	2.0	—	2.0	1.0	$^{+46.7}_{-48.7}$
$f_0(980)K^0$	4.9	$+8.5$	2.6	-27.2	63.9	8.0	2.0	—	2.0	1.1	$^{+65.8}_{-70.2}$
$K^0\pi^+\pi^-$ NR	4.5	$+13.8$	61.7	0	25.3	8.0	2.0	—	2.0	0.8	$^{+69.3}_{-67.9}$
$\bar{K}^0K^+\pi^-$ NR	0	0	0	0	0	8.0	2.0	—	2.0	3.0	12.5
$K^*(892)^+\pi^-$	11.5	-10.5	1.7	0	15.3	4.0	—	2.0	2.0	1.5	
$K^*(892)^+K^-$	10.3	-34.5	2.6	0	0	4.0	—	2.0	2.0	2.2	
$K_0^*(1430)^+\pi^-$	22.9	$+20.4$	179.9	0	109.3	4.0	—	2.0	2.0	1.6	
$K_0^*(1430)^+K^-$	0	0	0	0	0	4.0	—	2.0	2.0	2.5	
$K^*(892)^0\pi^0$	0	0	0	0	0	4.0	—	2.0	2.0	1.4	10.0
$K_0^*(1430)^0\pi^0$	8.3	-2.4	15.9	-103.5	60.7	4.0	—	2.0	2.0	1.8	$^{+65.0}_{-122.3}$
$K^+\pi^-\pi^0$ NR	8.4	$+3.6$	61.2	-4.7	24.0	4.0	—	2.0	2.0	1.4	$^{+67.1}_{-67.2}$
$K^+K^-\pi^0$ NR	23.3	-10.6	5.9	0	0	4.0	—	2.0	2.0	1.9	$^{+26.1}_{-28.1}$
$K^*(892)^+\pi^-$	3.9	-4.1	2.8	0	5.2	7.2	1.6	0.4	2.0	0.9	$^{+13.6}_{-14.2}$
$K^*(892)^+K^-$	5.8	-22.2	0.7	0	0	5.8	0.9	1.1	2.0	1.5	$^{+12.3}_{-25.4}$
$K_0^*(1430)^+\pi^-$	3.1	$^{+6.4}_{-0.4}$	61.1	-12.6	64.3	7.9	2.0	0	2.0	1.1	$^{+90.4}_{-91.1}$
$K_0^*(1430)^+K^-$	0	0	0	0	0	6.8	1.4	0.6	2.0	2.8	15.8
$K^*(892)^0\pi^+$	4.5	-0.7	0.6	-53.9	4.3	6.0	2.0	2.0	1.0	1.9	$^{+12.7}_{-55.4}$
$\bar{K}^*(892)^0K^+$	6.4	-23.7	0	0	0	6.0	2.0	2.0	1.0	3.0	$^{+13.0}_{-27.0}$
$K_0^*(1430)^0\pi^+$	84.9	$+59.7$	1.1	0	102.8	6.0	2.0	2.0	1.0	1.9	$^{+146.9}_{-134.2}$
$\bar{K}_0^*(1430)^0K^+$	194.0	0	0	0	0	6.0	2.0	2.0	1.0	2.9	194.6
$K^*(892)^+\pi^0$	43.5	5.4	3.3	0	8.3	6.0	2.0	2.0	1.0	1.2	46.1
$K_0^*(1430)^+\pi^0$	15.1	-11.3	0	0	34.6	6.0	2.0	2.0	1.0	1.3	$^{+40.8}_{-42.3}$
$\rho(770)^+K^0$	23.9	$+22.0$	2.3	0	2.8	6.0	2.0	2.0	1.0	1.6	$^{+34.5}_{-26.6}$
$K^0\pi^+\pi^0$ NR	0	0	0	0	0	6.0	2.0	2.0	1.0	1.3	11.0
$\bar{K}^0K^+\pi^0$ NR	0	0	0	0	0	6.0	2.0	2.0	1.0	3.3	11.4

Table 7.2: Systematic uncertainties (%) for $K_S^0h^\pm\pi^\mp$ (first section), $K^\pm h^\mp\pi^0$ (second section), and $K_S^0h^\pm\pi^0$ (last section) modes. The third section combines the first two sections. Totals include unitemized contributions of 8.6% for all modes (correlations, $\cos\theta_{\rm sph}$, f_{+-}/f_{00}, and $N_{B\bar{B}}$) as well as 10.8% for $K_0^*(1430)$ modes ($\mathcal{B}_{K\pi}$). Uncertainties are symmetric unless preceeded by + or −.

7.2.1 Interference

In the Dalitz fits, we neglect interference among the various two-body and NR complex amplitudes contributing to each topology. In reality, however, variations in the phases of these amplitudes can change the apparent yield for each mode. We employ a MC technique to estimate the size of the uncertainty introduced by these unknown phases.

For the decay of a particle D to an intermediate resonance R and a pseudoscalar C, where R subsequently decays to two pseudoscalars A and B, we approximate the resonant amplitudes with

relativistic Breit-Wigners. For the case where R is a scalar, the amplitude is given by

$$A = \frac{F_D F_R}{m_R^2 - m_{AB}^2 - i m_R \Gamma(q)}. \tag{7.4}$$

If R is a vector, the amplitude is

$$A = F_D F_R \frac{m_{AC}^2 - m_{BC}^2 + (m_D^2 - m_C^2)(m_B^2 - m_A^2)/m_R^2}{m_R^2 - m_{AB}^2 - i m_R \Gamma(q)}. \tag{7.5}$$

m_R is the nominal mass of the resonance, $\Gamma(q)$ is the mass-dependent width, and F_D and F_R are hadronic form factors. The mass-dependent width is given by the expression:

$$\Gamma(q) = \Gamma_0 \left[\frac{p_A(m_{AB})}{p_A(m_R)}\right]^{2J+1} \frac{m_R}{m_{AB}} F_R^2, \tag{7.6}$$

where Γ_0 is the width of the resonance at $m_{AB} = m_R$ and $p_A(x)$ is the momentum of A in the AB rest frame for $m_{AB} = x$. For the form factors, we use the Blatt-Weisskopf barrier penetration factors, which are unity for scalars. The form factors for vectors are given by

$$F_R = \sqrt{\frac{1 + r^2 p_A^2(m_R)}{1 + r^2 p_A^2(m_{AB})}} \tag{7.7}$$

$$F_D = \sqrt{\frac{1 + r^2 p_R^2(m_D)}{1 + r^2 p_{AB}^2(m_D)}}, \tag{7.8}$$

where the effective radius of the resonance, r, is taken to be 10 GeV^{-1} for the B meson and 1.5 GeV^{-1} for the intermediate resonance. The integrated rates are insensitive to the choices of r. For NR decays, $A_{NR} = 1$.

The total amplitude, $M_{\rm tot}$, is the sum of the resonant and NR contributions: $M_{\rm tot} = \sum_i M_i$, where $M_i = N_i a_i e^{i\delta_i} A_i$. The δ_i are the unknown strong phases, and the a_i^2 are the component fractions. The individual amplitudes are normalized to uniform integrated rates over the Dalitz plot (Φ): $1/N_i^2 = \int A_i^* A_i d\Phi$. The total rate at any given point in the Dalitz plot is $|M_{\rm tot}|^2 = M_{\rm tot}^* M_{\rm tot}$. The interference pattern in the Dalitz plot is determined by the constant strong phases δ_i and by the event-dependent strong phases $\arg A_i$ from the relativistic Breit-Wigners. Both contributions are simulated. In the MC, the a_i are fixed according to the measured branching fractions from the Dalitz fit, but the δ_i are randomly generated to probe the behavior of the decay rate under variation of the strong phases.

Focusing on a single resonance, i, we can separate the total amplitude into two pieces, with all non-i contributions considered to be background and labeled "bkg" below. The total rate can be expressed as $|M_{\rm tot}|^2 = |M_i|^2 + |M_{\rm bkg}|^2 + 2|M_i||M_{\rm bkg}|\cos(\delta_i - \delta_{\rm bkg})$. To estimate the yield for the i-th component, we first integrate $|M_{\rm tot}|^2$ in a $\pm 3\Gamma$ window around the resonance. For

the background estimate, we integrate $|M_{\rm bkg}|^2$ over the same window. We take the fitted yield of the i-th component to be the difference between these two integrated rates, which corresponds to $|M_i|^2 + 2|M_i||M_{\rm bkg}|\cos(\delta_i - \delta_{\rm bkg})$. Since the fitter neglects interference, the interference term must be absorbed into one of the yields. The yields of the non-i components are determined from other regions of the Dalitz plot, and this background is projected into the i-th resonance region. Therefore, it is most likely that the integrated interference term in the $\pm 3\Gamma$ region is assigned to the i-th component. For NR components, the region of integration consists of those portions of the Dalitz plot not included in any resonant signal region.

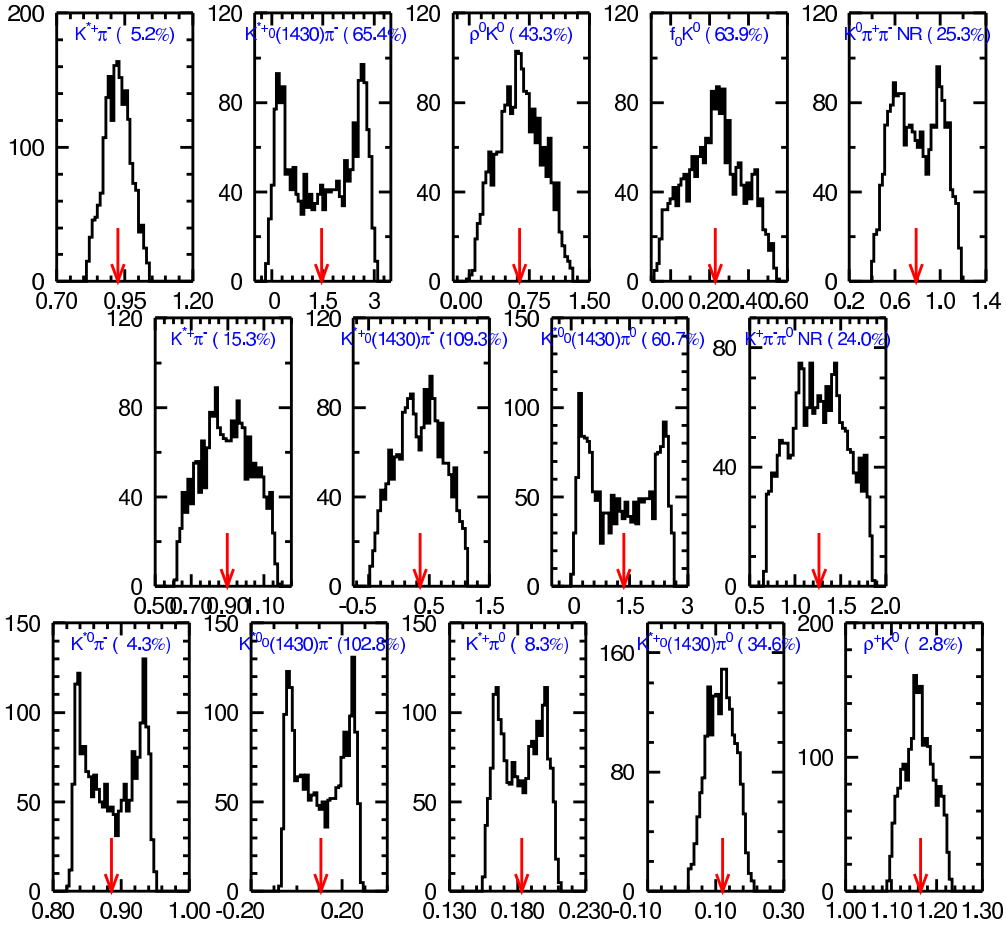

Figure 7.1: Integrated rates in the signal regions for modes with final states $K^0_S\pi^+\pi^-$ (top), $K^\pm\pi^\mp\pi^0$ (center), and $K^0_S\pi^\pm\pi^0$ (bottom), as seen by a fitter that ignores interference, under variation of the strong phases. The numbers in parentheses are the fractional r.m.s. widths of the distributions and are reproduced in Column 6 of Table 7.2. The result with non-interfering amplitudes is shown by the arrows.

Different choices for the strong phases result in the rate distributions shown in Figure 7.1. Only the modes with $K\pi\pi$ final states are shown; in each topology, only one $\bar{K}K\pi$ mode has a non-zero yield, so there are no interference effects for these modes. These plots show that neglecting

interference does not produce a significant bias, assuming a flat distribution for the unknown strong phases. However, there are strong phases in reality, so the widths of these distributions provide an indication of the induced error. The horizontal scales are arbitrarily normalized, and we assign systematic errors equal to the fractional widths of these distributions. These uncertainties are given in the sixth column of Table 7.2 and are included in the total uncertainties in the last column.

The presence of several broad resonances and of the NR component leads to large variations in most cases, thus precluding any meaningful branching fraction measurements. Because of the narrowness of the $K^*(892)^\pm$ and the large size of the $B \to K^*(892)^\pm\pi^\mp$ signals, the two systematic errors for this mode are well-controlled and do not degrade the overall precision appreciably.

7.3 Uncertainties on $\mathcal{A}_{CP}(B \to K^*(892)^\pm\pi^\mp)$

The sources of systematic uncertainty on the $B \to K^*(892)^\pm\pi^\mp$ branching fraction measurement do not all apply to the charge asymmetry measurement. Since $\mathcal{A}_{+-}$ is a ratio of branching fractions, the multiplicative errors cancel, assuming they act charge-symmetrically. Only the errors on the yield need to be considered. Of these, we evaluate directly the uncertainties from PDF variation (including Dalitz PDF binning), the choice of free components in the fit, and the neglect of interference in the fit. Table 7.3 gives a full list of the sources of systematic uncertainty and their contributions to $\mathcal{A}_{+-}(B \to K^*(892)^\pm\pi^\mp)$ in each $K^*(892)^\pm$ submode.

When uncertainties are measured separately for each topology, they are convoluted by treating the combined asymmetry as a weighted average of the asymmetries in each topology:

$$\bar{\mathcal{A}} = \frac{\mathcal{A}_A W_A + \mathcal{A}_B W_B}{W_A + W_B}, \tag{7.9}$$

where the weight factors W_A and W_B are the inverse squares of the average errors on each asymmetry. Using the results from Tables 6.15 and 6.16, we find weights of 2.00 and 1.00 for $K^*(892)^\pm(K^0_S\pi^\pm)\pi^\mp$ and $K^*(892)^\pm(K^\pm\pi^0)\pi^\mp$, respectively. If $\delta\mathcal{A}_A$ and $\delta\mathcal{A}_B$ are uncorrelated, then the uncertainty on the above average asymmetry is

$$\bar{\sigma}_{\rm uncorr} = \frac{\sqrt{\sigma_A^2 W_A^2 + \sigma_B^2 W_B^2}}{W_A + W_B}. \tag{7.10}$$

For cases where we assume 100% positive correlation between $\delta\mathcal{A}_A$ and $\delta\mathcal{A}_B$, the uncertainty on the average asymmetry is

$$\bar{\sigma}_{\rm corr} = \frac{\sqrt{\sigma_A^2 W_A^2 + 2\sigma_A\sigma_B W_A W_B + \sigma_B^2 W_B^2}}{W_A + W_B}. \tag{7.11}$$

The systematic uncertainties in dE/dx measurement and tracking at high and low momenta were discussed in Section 6.5. The uncertainties in the two momentum regions are assumed to be

	Source	$\sigma_{\mathcal{A}_{+-}}(K^0_S h^\pm \pi^\mp)$	$\sigma_{\mathcal{A}_{+-}}(K^\pm h^\mp \pi^0)$	$\sigma_{\mathcal{A}_{+-}}$
•	$\mathcal{A}_{+-}$ in high$-p$ tracking	± 0.002	± 0.002	± 0.006
	$\mathcal{A}_{+-}$ in low$-p$ tracking	± 0.005 $\Big\}\pm 0.003$	± 0.015 $\Big\}\pm 0.013$	
•	$\mathcal{A}_{+-}$ in dE/dx	± 0.010	± 0.010	± 0.010
•	$\mathcal{A}_{+-}$ in ϵ	± 0.017	± 0.019	± 0.018
	Other signal components	± 0.030	± 0.037	± 0.023
◇	$\mathcal{A}_{+-}$ in background			± 0.010
	PDF variation	± 0.009	± 0.043	± 0.016
	Dalitz PDF binning	$+0.017$	$+0.162$	$+0.055$
◇	Fitting method			± 0.060
◇	Choice of broad scalar			± 0.019
◇	$\mathcal{A}_{+-}$ of CP eigenstates			± 0.010
◇	$K^*_0(1430) \to K^*(1410)$			± 0.006
•	Interference	± 0.017	± 0.051	± 0.028
•	PDF correlations	± 0.012	± 0.017	± 0.014
	Total			$^{+0.097}_{-0.080}$

Table 7.3: Systematic uncertainties on the $\mathcal{A}_{+-}(B \to K^*(892)^\pm \pi^\mp)$ measurement. A bullet marks the uncertainties that are positively correlated between the two topologies. A diamond marks the uncertainties that are determined for the simultaneous fit directly.

perfectly correlated. Therefore, any asymmetry in the track yields is mitigated when considering pairs of oppositely charged tracks, such as those in $B \to K^*(892)^\pm \pi^\mp$. If the two tracks have equal asymmetries, then the cancellation is exact. Furthermore, if both track yield asymmetries are zero, then the uncertainty on the asymmetry of the pair is the difference between the individual asymmetries. This result is derived below. We denote the charge asymmetry in the high-momentum bachelor track by a and in the low-momentum $K^*(892)^\pm$ daughter track by b. Then, the yields in the two $B \to K^*(892)^\pm \pi^\mp$ charge states are

$$N(\bar{B}^0 \to K^*(892)^- \pi^+) \propto (1+a)(1-b) \tag{7.12}$$

$$N(B^0 \to K^*(892)^+ \pi^-) \propto (1-a)(1+b), \tag{7.13}$$

and the charge asymmetry is given by

$$\mathcal{A}_{+-}(B \to K^*(892)^\pm \pi^\mp) = \frac{a-b}{1-ab}. \tag{7.14}$$

Propagating the correlated errors on a and b, one finds the tracking uncertainty on $\mathcal{A}_{+-}(B \to$

$K^*(892)^{\pm}\pi^{\mp}$) to be

$$\sigma_{\mathcal{A}}^{\text{tracking}} = \frac{1}{(1-ab)^2}\sqrt{(1-b^2)^2\sigma_a^2 - 2(1-a^2)(1-b^2)\sigma_a\sigma_b + (1-a^2)^2\sigma_b^2}. \quad (7.15)$$

Thus, if $a = b = 0$, then $\sigma_{\mathcal{A}}^{\text{tracking}} = |\sigma_a - \sigma_b|$.

To determine the systematic uncertainty due to PDF uncertainties, we measure the change in $\mathcal{A}_{+-}(B \to K^*(892)^{\pm}\pi^{\mp})$ under extreme coherent variations in the m_B, ΔE, and $\mathcal{F}$ PDF parameters. The two topologies are not fitted simultaneously, and we assign uncertainties that are $\frac{1}{\sqrt{12}}$ times the spread in $\mathcal{A}_{+-}(B \to K^*(892)^{\pm}\pi^{\mp})$. We also vary the binning of the Dalitz plot PDFs for the NR, $b \to c$, and continuum components. Making the bin width in each dimension as much as four times smaller than in the standard fit, we find a one-sided uncertainty taken to be $\frac{2}{\sqrt{12}}$ of the spread in $\mathcal{A}_{+-}(B \to K^*(892)^{\pm}\pi^{\mp})$. The fitted asymmetries from these modified fits are given in Table 7.4.

PDF Variation	$\mathcal{A}_{+-}(K^*(892)^{\pm}(K_S^0\pi^{\pm})\pi^{\mp})$	$\mathcal{A}_{+-}(K^*(892)^{\pm}(K^{\pm}\pi^0)\pi^{\mp})$
None	0.19 ± 0.40	$0.72^{+0.44}_{-0.69}$
DP-averaged PDFs	0.15 ± 0.36	$0.63^{+0.49}_{-0.59}$
Extreme Down	0.17 ± 0.37	$0.71^{+0.77}_{-0.67}$
Extreme Up	$0.14^{+0.34}_{-0.35}$	$0.56^{+0.46}_{-0.52}$
Finer DP Binning	$0.22^{+0.40}_{-0.41}$	$1.00^{+0.00}_{-1.03}$

Table 7.4: Charge asymmetries from independent fits of the $K_S^0 h^{\pm}\pi^{\mp}$ and $K^{\pm}h^{\mp}\pi^0$ topologies with PDF variations.

The uncertainty due to the fitting method is assessed by comparing the weighted average of the charge asymmetries from the separate fits to each topology with the charge asymmetry from the simultaneous fit. The full width of this difference is included in the systematic uncertainty.

We also study the sensitivity of $\mathcal{A}_{+-}(B \to K^*(892)^{\pm}\pi^{\mp})$ to the number of free parameters in the fit by varying the mixture of broad scalar components allowed in the fit. Tables 7.5 and 7.6 show the results for the simultaneous fits with either the $K_0^*(1430)$ or the NR components removed. In addition, we repeat the standard fit with the charge asymmetries of the CP eigenstates fixed to zero, as shown in Table 7.7. None of these modifications affects $\mathcal{A}_{+-}(B \to K^*(892)^{\pm}\pi^{\mp})$ significantly, and we assign systematic uncertainties corresponding to the full widths of these variations.

As an additional test of the robustness of $\mathcal{A}_{+-}(B \to K^*(892)^{\pm}\pi^{\mp})$ against the precise nature of the broad resonances in the fit, we replace the scalars $K_0^*(1430)^{\pm}$ and $K_0^*(1430)^0$ with the vectors $K^*(1410)^{\pm}$ and $K^*(1410)^0$. The results of the simultaneous fit with this substitution are shown in Table 7.8. Virtually no change is seen in $\mathcal{A}_{+-}(B \to K^*(892)^{\pm}\pi^{\mp})$.

The effect of neglecting possible interference among the signal components is assessed with MC simulation, in a manner similar to that described in Section 7.2.1. For each signal component, we

Mode	Yield ($K^0_S h^\pm \pi^\mp$)	Yield ($K^\pm h^\mp \pi^0$)	$\mathcal{A}_{+-}$
$K^*(892)^\pm\pi^\mp$	$12.6^{+4.5}_{-3.9}(4.7\sigma)$	$6.0^{+2.2}_{-1.9}(4.7\sigma)$	$0.24^{+0.32}_{-0.33}$
$K^*(892)^\pm K^\mp$	$2.1^{+2.3}_{-1.6}(1.5\sigma)$	$4.1^{+2.2}_{-1.6}(1.5\sigma)$	$1.00^{+0.00}_{-0.74}$
$K^*_0(1430)^\pm\pi^\mp$	—	—	—
$K^*_0(1430)^\pm K^\mp$	—	—	—
$\rho(770)^0 K^0_S$	$6.2^{+5.0}_{-3.9}(2.2\sigma)$		$-0.37^{+0.70}_{-0.64}$
$f_0(980)K^0_S$	$2.8^{+2.8}_{-1.9}(1.8\sigma)$		$1.00^{+0.00}_{-0.70}$
$K^0_S\pi^+\pi^-$ NR	$34.9^{+9.2}_{-8.3}(5.9\sigma)$		$-0.17^{+0.25}_{-0.24}$
$K^0_S K^\pm\pi^\mp$ NR	$0^{+4.0}$		0
$K/\bar{K}^*(892)^0\pi^0$		$0^{+3.7}$	0
$K/\bar{K}^*_0(1430)^0\pi^0$		—	—
$K^\pm\pi^\mp\pi^0$ NR		$22.5^{+11.0}_{-9.9}(2.6\sigma)$	$0.01^{+0.47}_{-0.43}$
$K^+K^-\pi^0$ NR		$6.5^{+9.3}_{-6.0}(1.1\sigma)$	$-1.00^{+1.42}_{-0.00}$

Table 7.5: Results of the simultaneous $\mathcal{A}_{+-}$ fit of the $K^0_S h^\pm\pi^\mp$ and $K^\pm h^\mp\pi^0$ topologies with yields for $K^*_0(1430)$ components fixed to zero.

calculate two amplitudes, one for each charge of $h^\pm$, which differ only in normalization; the two amplitudes for each component share a common CP-conserving strong phase. We simulate interference between amplitudes with the same charge of $h^\pm$, but not between amplitudes of different charge states. The CP asymmetries are given by the differences in apparent yields of the two charge states of each component. We simulate the $K^0_S\pi^+\pi^-$ and $K^\pm\pi^\mp\pi^0$ final states separately, with amplitude normalizations fixed by the branching fractions in Table 6.9 and with CP asymmetries fixed to those in the simultaneous fit of Table 6.17. Figure 7.2 shows the distributions of $\mathcal{A}_{CP}(B\to K^*(892)^\pm\pi^\mp)$ in both topologies. The r.m.s. spreads of the distributions give systematic uncertainties of ± 0.017 for $K^*(892)^\pm\to K^0_S\pi^\pm$ and ± 0.051 for $K^*(892)^\pm\to K^\pm\pi^0$.

The final source of systematic uncertainty stems from our (partial) neglect of correlations among the input variables to the fit. Uncertainties on the yield from this source were determined in Section 7.1, and we use these to derive the corresponding asymmetry errors. To do so, we must account for the unknown charge asymmetry of the yield variations, which may differ from the charge asymmetry of the yield itself. The error on the yield, σ_S, is applicable to the sum of the two charge-conjugate yields, $S = S_+ + S_-$, which forms the denominator of $\mathcal{A}_{+-}\equiv(S_+ - S_-)/(S_+ + S_-)$. The numerator of $\mathcal{A}_{+-}$ is perfectly correlated or anti-correlated with the denominator if the yield variations affect only S_+ or S_-, but not both. The uncertainty on $\mathcal{A}_{+-}$ is

$$\sigma^2_{\mathcal{A}_{+-}} = \frac{4}{S^4}\left[S^2_+\sigma^2_- + S^2_-\sigma^2_+ - 2\rho S_+ S_-\sigma_+\sigma_-\right], \tag{7.16}$$

where $\sigma_\pm$ are the uncertainties on $S_\pm$, and ρ is the correlation coefficient between S_+ and S_-. If we

Mode	Yield ($K^0_S h^\pm \pi^\mp$)	Yield ($K^\pm h^\mp \pi^0$)	$\mathcal{A}_{+-}$
$K^*(892)^\pm\pi^\mp$	$13.3^{+4.6}_{-3.9}(5.1\sigma)$	$6.4^{+2.3}_{-2.0}(5.1\sigma)$	$0.26^{+0.31}_{-0.32}$
$K^*(892)^\pm K^\mp$	$2.0^{+2.3}_{-1.6}(1.4\sigma)$	$4.2^{+2.3}_{-1.7}(1.4\sigma)$	$1.00^{+0.00}_{-0.71}$
$K^*_0(1430)^\pm\pi^\mp$	$16.8^{+6.0}_{-5.3}(4.2\sigma)$	$9.9^{+4.9}_{-4.5}(4.2\sigma)$	$-0.50^{+0.34}_{-0.35}$
$K^*_0(1430)^\pm K^\mp$	$0.3^{+2.5}_{-1.5}(0.2\sigma)$	$0.3^{+2.4}_{-1.5}(0.2\sigma)$	0
$\rho(770)^0 K^0_S$	$6.4^{+5.1}_{-3.8}(2.3\sigma)$		$-0.17^{+0.66}_{-0.81}$
$f_0(980)K^0_S$	$3.4^{+2.8}_{-2.0}(2.6\sigma)$		$1.00^{+0.00}_{-0.67}$
$K^0_S\pi^+\pi^-$ NR	—		—
$K^0_S K^\pm\pi^\mp$ NR	—		—
$K/\bar{K}^*(892)^0\pi^0$		$0^{+3.7}$	0
$K/\bar{K}^*_0(1430)^0\pi^0$		$17.2^{+7.4}_{-6.2}(3.9\sigma)$	$-0.40^{+0.40}_{-0.37}$
$K^\pm\pi^\mp\pi^0$ NR		—	—
$K^+K^-\pi^0$ NR		—	—

Table 7.6: Results of the simultaneous $\mathcal{A}_{+-}$ fit of the $K^0_S h^\pm\pi^\mp$ and $K^\pm h^\mp\pi^0$ topologies with yields for NR components fixed to zero.

take $\rho = 0$, then $\sigma_S^2 = \sigma_+^2 + \sigma_-^2$. We define the asymmetry between σ_+ and σ_- to be

$$\alpha \equiv \frac{\sigma_+^2 - \sigma_-^2}{\sigma_+^2 + \sigma_-^2} = \frac{\sigma_+^2 - \sigma_-^2}{\sigma_S^2}. \tag{7.17}$$

The error on $\mathcal{A}_{+-}$ can then be expressed as

$$\sigma^2_{\mathcal{A}_{+-}} = \frac{4}{S^4}\left[\left(\frac{1+\mathcal{A}_{+-}}{2}S\right)^2\left(\frac{1+\alpha}{2}\sigma_S^2\right) + \left(\frac{1-\mathcal{A}_{+-}}{2}S\right)^2\left(\frac{1-\alpha}{2}\sigma_S^2\right)\right] \tag{7.18}$$

$$= \frac{\sigma_S^2}{S^2}[1 + \mathcal{A}_{+-}^2 + 2\alpha\mathcal{A}_{+-}]. \tag{7.19}$$

To be conservative, we maximize the systematic uncertainty by choosing $\alpha = \pm 1$, resulting in

$$\sigma_{\mathcal{A}_{+-}} = \frac{\sigma_S}{S}(1 + |\mathcal{A}_{+-}|). \tag{7.20}$$

The fractional errors on the yields, σ_S/S, are given in Table 7.2, and the values of $\mathcal{A}_{+-}$ are taken from the independent fits to each topology in Tables 6.15 and 6.16. We assume the yield uncertainties to be correlated between the two topologies.

The total systematic uncertainty on $\mathcal{A}_{+-}(B \to K^*(892)^\pm\pi^\mp)$, given in Table 7.3, is about one-fourth the size of the statistical uncertainty and is dominated by PDF uncertainties and variations in the fitting method. We model both the statistical and systematic uncertainties with bifurcated Gaussians and convolute them via MC simulation. The resultant likelihood function is shown in Figure 6.11, and we inflate the allowed region to $\mathcal{A}_{+-}(B \to K^*(892)^\pm\pi^\mp) \in [-0.31, 0.78]$ at the 90%

	Mode	Yield ($K^0_S h^\pm \pi^\mp$)	Yield ($K^\pm h^\mp \pi^0$)	$\mathcal{A}_{+-}$
	$K^*(892)^\pm \pi^\mp$	$12.3^{+4.5}_{-3.9}(4.6\sigma)$	$5.9^{+2.2}_{-1.9}(4.6\sigma)$	$0.27^{+0.33}_{-0.34}$
	$K^*(892)^\pm K^\mp$	$2.1^{+2.3}_{-1.6}(1.4\sigma)$	$4.0^{+2.2}_{-1.6}(1.4\sigma)$	$1.00^{+0.00}_{-0.71}$
	$K^*_0(1430)^\pm \pi^\mp$	$13.1^{+7.3}_{-6.0}(3.0\sigma)$	$7.7^{+3.9}_{-3.5}(3.0\sigma)$	$-0.75^{+0.48}_{-0.48}$
	$K^*_0(1430)^\pm K^\mp$	$0^{+1.5}$	$0^{+1.4}$	0
•	$\rho(770)^0 K^0_S$	$6.8^{+5.1}_{-3.9}(2.3\sigma)$		—
•	$f_0(980) K^0_S$	$2.6^{+3.1}_{-2.1}(1.4\sigma)$		—
•	$K^0_S \pi^+ \pi^-$ NR	$22.5^{+9.5}_{-8.3}(3.5\sigma)$		—
	$K^0_S K^\pm \pi^\mp$ NR	$0^{+4.6}$		0
	$K/\bar{K}^*(892)^0 \pi^0$		$0^{+3.8}$	0
	$K/\bar{K}^*_0(1430)^0 \pi^0$		$15.8^{+8.1}_{-6.8}(2.8\sigma)$	$-0.08^{+0.48}_{-0.47}$
	$K^\pm \pi^\mp \pi^0$ NR		$14.4^{+10.7}_{-9.1}(1.8\sigma)$	$-0.14^{+0.67}_{-0.58}$
•	$K^+ K^- \pi^0$ NR		$5.1^{+9.2}_{-8.2}(0.6\sigma)$	—

Table 7.7: Results of the simultaneous $\mathcal{A}_{+-}$ fit of $K^0_S h^\pm \pi^\mp$ and $K^\pm h^\mp \pi^0$ with $\mathcal{A}_{+-}$ for CP eigenstates (marked by bullets) fixed to zero.

confidence level.

Mode	Yield ($K^0_S h^\pm \pi^\mp$)	Yield ($K^\pm h^\mp \pi^0$)	$\mathcal{A}_{+-}$
$K^*(892)^\pm \pi^\mp$	$12.4^{+4.5}_{-3.9}(4.6\sigma)$	$6.0^{+2.2}_{-1.9}(4.6\sigma)$	$0.25^{+0.33}_{-0.34}$
$K^*(892)^\pm K^\mp$	$2.1^{+2.3}_{-1.6}(1.4\sigma)$	$4.0^{+2.2}_{-1.6}(1.4\sigma)$	$1.00^{+0.00}_{-0.74}$
$K^*(1410)^\pm \pi^\mp$	$7.2^{+6.3}_{-5.3}(1.5\sigma)$	$4.2^{+3.7}_{-3.1}(1.5\sigma)$	$-0.74^{+0.85}_{-1.25}$
$K^*(1410)^\pm K^\mp$	$0.4^{+2.6}_{-2.6}$	$0^{+1.4}$	0
$\rho(770)^0 K^0_S$	$5.8^{+5.0}_{-3.8}(2.1\sigma)$		$-0.33^{+0.73}_{-0.67}$
$f_0(980) K^0_S$	$2.8^{+2.8}_{-1.9}(1.8\sigma)$		$1.00^{+0.00}_{-0.69}$
$K^0_S \pi^+\pi^-$ NR	$28.8^{+9.8}_{-8.7}(4.5\sigma)$		$-0.03^{+0.33}_{-0.31}$
$K^0_S K^\pm \pi^\mp$ NR	$0^{+4.3}$		0
$K/\bar{K}^*(892)^0 \pi^0$		$0^{+3.4}$	0
$K/\bar{K}^*(1410)^0 \pi^0$		$16.0^{+7.3}_{-6.1}(3.7\sigma)$	$-0.43^{+0.42}_{-0.39}$
$K^\pm \pi^\mp \pi^0$ NR		$16.7^{+10.5}_{-9.2}(2.0\sigma)$	$0.05^{+0.60}_{-0.51}$
$K^+ K^- \pi^0$ NR		$5.4^{+8.9}_{-7.1}(0.9\sigma)$	$-1.00^{+0.54}_{-0.00}$

Table 7.8: Results of the simultaneous $\mathcal{A}_{+-}$ fit of the $K^0_S h^\pm \pi^\mp$ and $K^\pm h^\mp \pi^0$ topologies with $K^*_0(1430)$ resonances replaced by $K^*(1410)$.

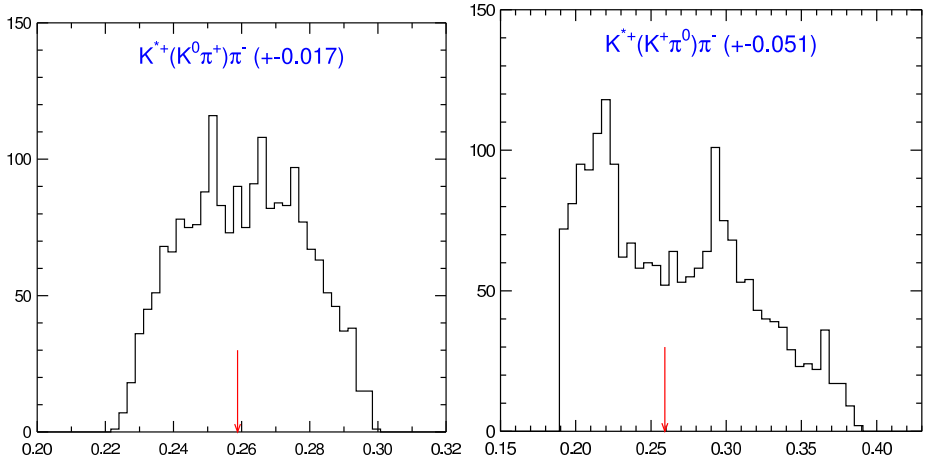

Figure 7.2: $\mathcal{A}_{+-}(B \to K^*(892)^\pm \pi^\mp)$ under variation of strong phases in the $K^0_S \pi^+\pi^-$ (left) and $K^\pm \pi^\mp \pi^0$ (right) final states, calculated from integrated rates in the signal regions, as seen by a fitter that ignores interference. The numbers in parentheses are the fractional r.m.s. widths of the distributions and are reproduced in Table 7.3. The result with non-interfering amplitudes is shown by the arrows.

Chapter 8 Summary and Discussion

In this chapter, we review the experimental results of the preceeding chapters. We also construct constraints on the CKM angle γ using our results on the decay $B \to K^*(892)^{\pm}\pi^{\mp}$. Although both experimental and theoretical uncertainties result in a wide allowed range for γ, our study suggests that if strong phases are small (as suggested by measurements of CP asymmetries in charmless hadronic B decays), then γ is larger than the value obtained from indirect fits. This possible discrepancy is supported by data from other $B \to PV$ modes. A tenfold improvement in the precision of the experimental inputs used in the study, along with an understanding of the strong phases in $B \to PV$ decays would constrain γ to 10° or better.

8.1 Summary of Results

We have searched for B decays to the three-body final states $K^0_S h^{\pm}\pi^{\mp}$, $K^{\pm}h^{\mp}\pi^0$, and $K^0_S h^{\pm}\pi^0$, both with and without distinguishing between NR production and intermediate resonances. We find significant yields for the two modes $B \to K^0_S\pi^+\pi^-$ and $B \to K^*(892)^{\pm}\pi^{\mp}$. The branching fractions for these decays are given in Table 8.1, along with upper limits at the 90% confidence level for modes without significant yields.

Table 8.1 also gives theoretical predictions [64, 83, 84, 85, 86, 87, 88] for models invoking SU(3) decomposition, naive factorization, QCD factorization, and perturbative-QCD factorization. The prediction for $\bar{K}^0/K^0\pi^+\pi^-$ NR is calculated under heavy meson chiral perturbation theory [100]. The measured branching fraction $\mathcal{B}(B \to K^*(892)^{\pm}\pi^{\mp})$ is higher than but consistent with most predictions. In all modes without significant signals, the branching fraction upper limits exceed the theoretical predictions.

We have also measured the CP asymmetry in $B \to K^*(892)^{\pm}\pi^{\mp}$ by performing a simultaneous maximum likelihood fit to the $B \to K^0_S h^{\pm}\pi^{\mp}$ and $B \to K^{\pm}h^{\mp}\pi^0$ topologies. We find $\mathcal{A}_{+-}(B \to K^*(892)^{\pm}\pi^{\mp}) = \mathcal{A}_{CP}(B \to K^*(892)^{\pm}\pi^{\mp}) = 0.26^{+0.33+0.10}_{-0.34-0.08}$ and a symmetric allowed interval at the 90% confidence level of $\mathcal{A}_{CP}(B \to K^*(892)^{\pm}\pi^{\mp}) \in [-0.31, 0.78]$, which includes systematic uncertainties.

8.2 Constraints on γ

In the flavor SU(3) decomposition of the amplitudes contributing to charmless $B \to PV$ decays, the transition $B \to K^*(892)^{\pm}\pi^{\mp}$ is dominated by two amplitudes, tree and penguin, pictured in

Mode	$\mathcal{B} \times 10^6$	SU(3)	NF	QCDF	PQCD
$K^0\pi^+\pi^-$	$50^{+10}_{-9} \pm 7$				
$K^+\pi^-\pi^0$	< 40				
$K^0\pi^+\pi^0$	< 66				
$\bar{K}^0K^+\pi^-$	< 21				
$K^+K^-\pi^0$	< 19				
$\bar{K}^0K^+\pi^0$	< 24				
$K^*(892)^+\pi^-$	$16^{+6}_{-5} \pm 2$	$[7, 17]$	$[6, 8]$	11	9.1
$K^*(892)^0\pi^0$	< 11	$[1, 2]$	$[2, 4]$	$[0.7, 0.9]$	2.8
$K^*(892)^0\pi^+$	< 105	$[5, 12]$	$[6, 12]$	10	10.0
$K^*(892)^+\pi^0$	< 34	$[4, 7]$	$[4, 7]$	$[2, 4]$	3.2
$K_0^*(1430)^+\pi^-$	< 68				
$K_0^*(1430)^0\pi^0$	< 41				
$K_0^*(1430)^0\pi^+$	< 136				
$K_0^*(1430)^+\pi^0$	< 31				
$\rho(770)^0K^0$	< 21	$[6, 14]$	$[0.5, 0.7]$	1.2	
$\rho(770)^+K^0$	< 52	$[5, 12]$	$[0.01, 0.03]$	$[0.6, 0.8]$	
$f_0(980)K^0$	< 24				
$K^*(892)^+K^-$	< 13			0.02	
$\bar{K}^*(892)^0K^+$	< 57		$[0.3, 0.7]$	$[0.2, 0.3]$	
$K_0^*(1430)^+K^-$	< 12				
$\bar{K}_0^*(1430)^0K^+$	< 153				
$K^0\pi^+\pi^-$ NR	< 59		0.5 (HMChPT)		
$K^+\pi^-\pi^0$ NR	< 26				
$K^0\pi^+\pi^0$ NR	< 20				
$\bar{K}^0K^+\pi^-$ NR	< 27				
$K^+K^-\pi^0$ NR	< 19				
$\bar{K}^0K^+\pi^0$ NR	< 22				

Table 8.1: Summary of measured branching fractions including systematic errors and theoretical predictions, both in units of 10^{-6}. Experimental measurements are averages over charge conjugate modes.

Figures 2.1a and 2.1c, which interfere with a weak phase given by the CKM angle $\gamma = \arg V_{ub}^*$ and with an unknown strong phase δ. Based on independent determinations of the magnitudes of these two amplitudes, we form an allowed range for $\cos\gamma\cos\delta$ up to a twofold ambiguity, using a toy MC to propagate experimental uncertainties. A second method of determining γ that adds information from $B \to \phi(1020)K$ decays is also discussed. We also make use of the CP asymmetry in $B \to K^*(892)^\pm\pi^\mp$ to probe γ and δ separately.

8.2.1 SU(3) Amplitude Decomposition

The SU(3) decomposition of amplitudes contributing to charmless hadronic B decays was discussed in Chapter 2. From Table 2.5, the amplitude for $B \to K^*(892)^\pm\pi^\mp$ is represented by $A(K^*(892)^+\pi^-) = -(p'_P + t'_P)$. The invariant amplitudes t' and p' carry the CKM matrix elements $V_{ub}V_{us}^*$ and $V_{tb}V_{ts}^*$, respectively, so their relative weak phase is $\pi - \gamma$. The amplitudes for the two

charge states are given by

$$A(K^*(892)^+\pi^-) = |p'_P| - |t'_P|e^{i\gamma}e^{i\delta} \quad (8.1)$$

$$A(K^*(892)^-\pi^+) = |p'_P| - |t'_P|e^{-i\gamma}e^{i\delta}, \quad (8.2)$$

and we can express the CP-averaged amplitude as follows:

$$\frac{1}{2}\left[|A(K^*(892)^+\pi^-)|^2 + |A(K^*(892)^-\pi^+)|^2\right] = |p'_P|^2 + |t'_P|^2 - 2|p'_P||t'_P|\cos\delta\cos\gamma. \quad (8.3)$$

We identify squared amplitudes, $|A|^2 = A^*A$, with branching fractions, $\mathcal{B}$, and we absorb all numerical factors, like G_F, m_B, phase space integrals, decay constants, form factors, and CKM matrix elements, into the definitions of the amplitudes. Nearly all the B branching fraction measurements in the literature are calculated assuming equal production of charged and neutral mesons. Therefore, before their branching fractions can be used to extract decay amplitudes, they must first be corrected for the ratio of B^+B^- to $B^0\bar{B}^0$ production rates, f_{+-}/f_{00}. The ratio of charged to neutral lifetimes, τ_+/τ_0, affects the apparent amplitudes through the total decay rate and is also taken into account. Since we are only concerned with ratios of branching fractions, we leave the $B^\pm$ branching fractions unaltered and scale the $B^0/\bar{B}^0$ branching fractions and their uncertainties by the product $\frac{f_{+-}}{f_{00}} \times \frac{\tau_+}{\tau_0}$.

Using only the CP-averaged branching fraction for $B \to K^*(892)^\pm\pi^\mp$, we cannot gain knowledge of the strong phase δ, and we are sensitive only to the product $\cos\gamma\cos\delta$, which is given by the following expression:

$$\cos\gamma\cos\delta = \frac{|p'_P|^2 + |t'_P|^2 - \mathcal{B}(K^*(892)^\pm\pi^\mp)\left(\frac{f_{+-}}{f_{00}} \times \frac{\tau_+}{\tau_0}\right)}{2|p'_P||t'_P|}. \quad (8.4)$$

8.2.2 Tree and Penguin Amplitudes

Numerical values of the tree and penguin amplitudes are derived from measurements of other charmless $B \to PV$ branching fractions [84]. The penguin amplitude is simply given by the decay $B^\pm \to K/\bar{K}^*(892)^0\pi^\pm$:

$$|p'_P| = |A(K^*(892)^0\pi^+)| = \sqrt{\frac{1}{2}[\mathcal{B}(K^*(892)^0\pi^+) + \mathcal{B}(\bar{K}^*(892)^0\pi^-)]}. \quad (8.5)$$

For the tree amplitude, we make use of $\Delta S = 0$ transitions and relate t_P to the $\Delta S = 1$ amplitude t'_P through ratios of CKM matrix elements and decay constants:

$$|t'_P| = \left|\frac{V_{us}}{V_{ud}}\right| \frac{f_{K^*}}{f_\rho}|t_P| = \left|\frac{V_{us}}{1 - \frac{1}{2}V_{us}^2}\right| \frac{f_{K^*}}{f_\rho}|t_P|. \quad (8.6)$$

The decay $B^0 \to \rho(770)^+\pi^-$ and its charge conjugate give the combination $|t_P + p_P|$, where $|p_P|$ is estimated to be around $0.2|t_P|$. Below, we present a method of subtracting the penguin contribution. However, we must first manipulate the branching fraction because what is measured experimentally is the sum of $B^0 \to \rho(770)^+\pi^-$, $B^0 \to \rho(770)^-\pi^+$, and their charge conjugates:

$$\mathcal{B}(\rho(770)^\pm\pi^\mp)\left(\frac{f_{+-}}{f_{00}} \times \frac{\tau_+}{\tau_0}\right) = |t_P + p_P|^2 + |t_V + p_V|^2. \tag{8.7}$$

To isolate $|t_P + p_P|$, we turn to the BABAR analysis of $B \to \pi^+\pi^-\pi^0$ [104]. Since the final state $\rho(770)^\pm\pi^\mp$ can be produced by both B^0 and $\bar{B}^0$ mesons, mixing-induced time-dependent CP asymmetries can arise from the interference of $B^0 \to \rho(770)^\pm\pi^\mp$ and $B^0 \to \bar{B}^0 \to \rho(770)^\pm\pi^\mp$, similar to the case of $B \to \psi K^0_S$. Measuring these asymmetries requires that the flavor of the $B \to \rho(770)^\pm\pi^\mp$ decay be tagged by the other B in the event. Therefore, this analysis can distinguish between $B^0 \to \rho(770)^+\pi^-$ and $B^0 \to \rho(770)^-\pi^+$, as well as the conjugate $\bar{B}^0$ decays.

The decay rate distributions for events with a B^0 or $\bar{B}^0$ tag are parametrized by the coefficients A, C, ΔC, S, and ΔS as follows:

$$f^{\rho^\pm\pi^\mp}_{B^0\ \mathrm{tag}} = (1 \pm A)\frac{e^{-|t|/\tau}}{4\tau}\left[1 + (S \pm \Delta S)\sin\Delta m t - (C \pm \Delta C)\cos\Delta m t\right] \tag{8.8}$$

$$f^{\rho^\pm\pi^\mp}_{\bar{B}^0\ \mathrm{tag}} = (1 \pm A)\frac{e^{-|t|/\tau}}{4\tau}\left[1 - (S \pm \Delta S)\sin\Delta m t + (C \pm \Delta C)\cos\Delta m t\right], \tag{8.9}$$

where t is the time interval between the decay of the $\rho(770)^\pm\pi^\mp$ candidate B and the decay of the tagging B. At $t = 0$, no mixing has occured, so the flavors of the two B mesons in the event are perfectly anticorrelated. Therefore, populations of each of the four charge combinations can be expressed in terms of A, C, and ΔC:

$$N(\bar{B}^0 \to \rho(770)^+\pi^-) \propto (1 + A)(1 - C - \Delta C) \tag{8.10}$$

$$N(B^0 \to \rho(770)^-\pi^+) \propto (1 - A)(1 + C - \Delta C) \tag{8.11}$$

$$N(\bar{B}^0 \to \rho(770)^-\pi^+) \propto (1 - A)(1 - C + \Delta C) \tag{8.12}$$

$$N(B^0 \to \rho(770)^+\pi^-) \propto (1 + A)(1 + C + \Delta C) \tag{8.13}$$

The time-integrated asymmetry between $B^0 \to \rho(770)^+\pi^-$ and $B^0 \to \rho(770)^-\pi^+$ (and between the corresponding charge conjugate decays) is denoted $\mathcal{A}_{PV}$ and is defined as follows:

$$\mathcal{A}_{PV} \equiv \frac{N(B^0 \to \rho^+\pi^-) + N(\bar{B}^0 \to \rho^-\pi^+) - N(B^0 \to \rho^-\pi^+) - N(\bar{B}^0 \to \rho^+\pi^-)}{N(B^0 \to \rho^+\pi^-) + N(\bar{B}^0 \to \rho^-\pi^+) + N(B^0 \to \rho^-\pi^+) + N(\bar{B}^0 \to \rho^+\pi^-)} \tag{8.14}$$

$$= AC + \Delta C. \tag{8.15}$$

We use $\mathcal{A}_{PV}$ along with $\mathcal{B}(\rho(770)^{\pm}\pi^{\mp})$ to obtain the desired branching fraction:

$$\mathcal{B}(\rho(770)^{\pm}\pi^{\mp})_P \equiv \frac{1}{2}[\mathcal{B}(B^0 \to \rho(770)^{+}\pi^{-}) + \mathcal{B}(B^0 \to \rho(770)^{-}\pi^{+}] \quad (8.16)$$

$$= \mathcal{B}(\rho(770)^{\pm}\pi^{\mp}) \left(\frac{f_{+-}}{f_{00}} \times \frac{\tau_{+}}{\tau_0}\right) \frac{1+\mathcal{A}_{PV}}{2}. \quad (8.17)$$

To extract $|t_P|$ from $\mathcal{B}(\rho(770)^{\pm}\pi^{\mp})_P$, we must estimate the magnitude and phase of the penguin amplitude p_P. The magnitude, $|p_P|$, can be obtained from $|p'_P|$ and from SU(3)-breaking factors:

$$|p_P| = \left|\frac{V_{td}}{V_{ts}}\right| \frac{f_\rho}{f_{K^*}} |p'_P|. \quad (8.18)$$

However, the phase of p_P is more difficult to ascertain. The relative weak phase between t_P and p_P is $\gamma + \beta$, and γ is unknown, *a priori*. Furthermore, there is an unknown strong phase, δ', between t_P and p_P. Since $\cos\gamma\cos\delta$ is not linear in $|t_P|$ and vice versa, we apply an iterative procedure to solve for both quantities simultaneously. We begin by neglecting p_P, which implies $|t_P| = \sqrt{\mathcal{B}(\rho(770)^{\pm}\pi^{\mp})_P}$, and determining $\cos\gamma\cos\delta$ from Equation 8.4. Then, we choose a value for $\cos\delta$ and use the resultant $\cos\gamma$ to solve for $|t_P|$ based on $\mathcal{B}(\rho(770)^{\pm}\pi^{\mp})_P$ and on an assumed value of $\cos\delta'$, this time without neglecting p_P. In turn, this value of $|t_P|$ is used to recalculate $\cos\gamma\cos\delta$. The cycle continues until the convergence criterion of $\Delta\cos\gamma\cos\delta < 0.01$ has been met. Convergence occurs in three iterations on average, and we apply this procedure to each trial of the toy MC.

For the CKM parameters $|V_{td}/V_{ts}|$ and β, we avoid using the results of the standard CKM fit [26], which relies on measurements involving B^0-$\bar{B}^0$ mixing. Rather, we determine these parameters in an internally consistent fashion using the world average $|V_{ub}/V_{cb}|$ [5] and the value of $\cos\gamma$ determined in each iteration of each toy MC trial. Using the relations $|V_{ub}/V_{cb}|^2 = \lambda^2(\rho^2+\eta^2)$ and $\rho = |V_{ub}|\cos\gamma/|V_{cb}|\lambda$, where ρ and η determine the apex of the Unitarity Triangle (Figure 2.3), we find

$$\left|\frac{V_{td}}{V_{ts}}\right| = |-\lambda(1-\rho-i\eta)| \quad (8.19)$$

$$= \lambda\sqrt{(1-\rho)^2+\eta^2} \quad (8.20)$$

$$= \lambda\sqrt{1 - \frac{2}{\lambda}\left|\frac{V_{ub}}{V_{cb}}\right|\cos\gamma + \frac{1}{\lambda^2}\left|\frac{V_{ub}}{V_{cb}}\right|^2} \quad (8.21)$$

and

$$\sin\beta = \left|\frac{V_{ts}}{V_{td}}\right|\left|\frac{V_{ub}}{V_{cb}}\right|\sin\gamma \quad (8.22)$$

$$\cos\beta = \lambda\left|\frac{V_{ts}}{V_{td}}\right|\left(1 - \frac{1}{\lambda}\left|\frac{V_{ub}}{V_{cb}}\right|\cos\gamma\right). \quad (8.23)$$

From the expression for the CP-averaged branching fraction,

$$\mathcal{B}(\rho(770)^{\pm}\pi^{\mp})_P = |p_P|^2 + |t_P|^2 + 2|p_P||t_P|\cos(\gamma+\beta)\cos\delta', \tag{8.24}$$

we solve for $|t_P|$ and apply Equation 8.6 to obtain

$$\begin{aligned} |t'_P| &= \left|\frac{V_{us}}{V_{ud}}\right|\left|\frac{V_{td}}{V_{ts}}\right||p'_P|\left\{-\cos(\gamma+\beta)\cos\delta' \pm \right. \\ &\qquad \left.\left[\cos^2(\gamma+\beta)\cos^2\delta' - 1 + \frac{\mathcal{B}(\rho(770)^{\pm}\pi^{\mp})_P}{|p_P|^2}\right]^{1/2}\right\} \qquad (8.25) \\ &= \left|\frac{V_{us}^2}{V_{ud}}\right||p'_P|y\left\{1 \pm \left[1 - \frac{1}{y^2}\left(1 - \frac{2}{|V_{us}|}\left|\frac{V_{ub}}{V_{cb}}\right|\cos\gamma + \frac{1}{|V_{us}|^2}\left|\frac{V_{ub}}{V_{cb}}\right|^2\right) + \right.\right. \\ &\qquad \left.\left.\left(\frac{f_{K^*}}{f_\rho}\right)^2\frac{\mathcal{B}(\rho(770)^{\pm}\pi^{\mp})_P}{|V_{us}|^2|p'_P|^2y^2}\right]^{1/2}\right\}, \qquad (8.26) \end{aligned}$$

where

$$y \equiv \left(\frac{1}{|V_{us}|}\left|\frac{V_{ub}}{V_{cb}}\right| - \cos\gamma\right)\cos\delta'. \tag{8.27}$$

To simplify matters, we assume that $\delta' = \delta$, *i.e.*, that the tree-penguin relative strong phase in $\Delta S = 0$ transitions is the same as in $|\Delta S = 1|$ transitions. In Section 8.2.6, we verify that the simulated value of $\cos\gamma\cos\delta$ is insensitive to the choice of δ' used to calculate $|t'_P|$. In the future, precise measurements of the CP asymmetry in both $B \to K^*(892)^{\pm}\pi^{\mp}$ and the $B \to \rho(770)^{\pm}\pi^{\mp}$ system will determine δ and δ', thus eliminating this source of theoretical uncertainty.

8.2.3 *CP* Asymmetries and the Strong Phase

The CP asymmetry in $B \to K^*(892)^{\pm}\pi^{\mp}$ provides an additional piece of information that allows us to disentangle the phases δ and γ. While the CP-averaged branching fraction for $B \to K^*(892)^{\pm}\pi^{\mp}$ is sensitive to $\cos\gamma\cos\delta$, the rate difference between $\bar{B}^0 \to K^*(892)^-\pi^+$ and $B^0 \to K^*(892)^+\pi^-$ decays is proportional to $\sin\gamma\sin\delta$. Beginning with the two conjugate amplitudes, from Equations 8.1 and 8.2, we express the observable branching fractions to the two charge states as functions of the two phases:

$$|A(K^*(892)^+\pi^-)|^2 = |p'_P|^2 + |t'_P|^2 - 2|p'_P||t'_P|\cos(\gamma+\delta) \tag{8.28}$$

$$|A(K^*(892)^-\pi^+)|^2 = |p'_P|^2 + |t'_P|^2 - 2|p'_P||t'_P|\cos(\gamma-\delta), \tag{8.29}$$

which implies

$$\cos(\gamma+\delta) = \frac{|p'_P|^2+|t'_P|^2-|A(K^*(892)^+\pi^-)|^2}{2|p'_P||t'_P|} \quad (8.30)$$

$$\cos(\gamma-\delta) = \frac{|p'_P|^2+|t'_P|^2-|A(K^*(892)^-\pi^+)|^2}{2|p'_P||t'_P|}. \quad (8.31)$$

Solving for γ and δ, we obtain

$$\gamma = \frac{1}{2}\left[\cos^{-1}\frac{|p'_P|^2+|t'_P|^2-|A(K^*(892)^+\pi^-)|^2}{2|p'_P||t'_P|} + \cos^{-1}\frac{|p'_P|^2+|t'_P|^2-|A(K^*(892)^-\pi^+)|^2}{2|p'_P||t'_P|}\right] \quad (8.32)$$

$$\delta = \frac{1}{2}\left[\cos^{-1}\frac{|p'_P|^2+|t'_P|^2-|A(K^*(892)^+\pi^-)|^2}{2|p'_P||t'_P|} - \cos^{-1}\frac{|p'_P|^2+|t'_P|^2-|A(K^*(892)^-\pi^+)|^2}{2|p'_P||t'_P|}\right], \quad (8.33)$$

which can be determined from experimental measurements.

8.2.4 Additional Information from $B \to \phi(1020)K$

The possibility of determining γ from the decays $B \to K^*(892)^\pm\pi^\mp$ and $B \to \phi(1020)K^\pm$ was first noticed by Gronau and Rosner [121]. The concrete formulation of this method was subsequently put forth by Gronau [58, 122].

The SU(3) decomposition of the $B \to \phi(1020)K^\pm$ amplitude is $A(\phi(1020)K^+) = p'_P + s'_P = p'_P - \frac{1}{3}P'^P_{EW}$ to $\mathcal{O}(\lambda)$. The weak phase of P'^P_{EW} is the same as that of p'_P, and its strong phase is expected to be the same as in t'_P because of the similarity of their flavor topologies. The magnitude of P'^P_{EW} has been calculated under the factorization *ansatz* [121, 123, 124] to be half that of p'_P. In the toy MC, we vary $|P'^P_{EW}/p'_P|$ according to an *ad hoc*, uniform distribution between $\frac{1}{3}$ and $\frac{2}{3}$, which is a conservative range corresponding to values for m_t of 130 GeV and 190 GeV, respectively. Thus, the CP-averaged ratio of the $B \to K^*(892)^+\pi^-$ and $B \to \phi(1020)K^+$ amplitudes gives a measure of γ:

$$R \equiv \frac{|A(K^*(892)^+\pi^-)|^2+|A(K^*(892)^-\pi^+)|^2}{|A(\phi(1020)K^+)|^2+|A(\phi(1020)K^-)|^2} = \frac{1+r^2-2r\cos\delta\cos\gamma}{1+\left|\frac{P'^P_{EW}}{3p'_P}\right|^2-2\cos\delta\left|\frac{P'^P_{EW}}{3p'_P}\right|} \quad (8.34)$$

or

$$\cos\gamma = \frac{1}{2r\cos\delta}\left[1+r^2-R\left(1+\left|\frac{P'^P_{EW}}{3p'_P}\right|^2-2\cos\delta\left|\frac{P'^P_{EW}}{3p'_P}\right|\right)\right], \quad (8.35)$$

where $r \equiv |t'_P/p'_P|$ is determined from $\mathcal{B}(B^0 \to \rho(770)^-\pi^+)$ and $\mathcal{B}(B^\pm \to K/\bar{K}^*(892)^0\pi^\pm)$, as described in Section 8.2.2. With this method, we must make some assumptions about the size of δ. It is believed, based on perturbative [125] and statistical [126] calculations, that $0° < \delta < 90°$. The limits on $\cos\gamma$ are presented as a function of δ over this range. Again, we choose $\delta' = \delta$, but the iterative procedure involves Equation 8.35 instead of Equation 8.4.

For greater statistical power, we combine the branching fractions for $B^\pm \to \phi(1020)K^\pm$ and

$B^0 \to \phi(1020)K^0/\bar{K}^0$ since they receive the same dominant p'_P and P'^P_{EW} contributions, differing only in the spectator quark. Thus, R is expressed as

$$R = \frac{\mathcal{B}(K^*(892)^{\pm}\pi^{\mp})\left(\frac{f_{+-}}{f_{00}} \times \frac{\tau_+}{\tau_0}\right)}{\left[\sigma^2_{\phi K^0}\mathcal{B}(\phi(1020)K^{\pm}) + \sigma^2_{\phi K^{\pm}}\mathcal{B}(\phi(1020)K^0/\bar{K}^0)\left(\frac{f_{+-}}{f_{00}} \times \frac{\tau_+}{\tau_0}\right)\right]/(\sigma^2_{\phi K^0} + \sigma^2_{\phi K^{\pm}})}, \tag{8.36}$$

where $\sigma_{\phi K^{\pm}}$ and $\sigma_{\phi K^0}$ refer to the average of the positive and negative errors on the $\mathcal{B}(\phi(1020)K^{\pm})$ and $\mathcal{B}(\phi(1020)K^0/\bar{K}^0)$ measurements, respectively.

8.2.5 Experimental Inputs

To evaluate the above expressions for $\cos\gamma\cos\delta$, γ, and δ (using $B \to K^*(892)^{\pm}\pi^{\mp}$ and its CP asymmetry), as well as $\cos\gamma$ (using both $B \to K^*(892)^{\pm}\pi^{\mp}$ and $B \to \phi(1020)K$ with assumptions about δ), we propagate the errors on the experimental measurements using a toy MC with the following inputs: $\frac{f_{+-}}{f_{00}} \times \frac{\tau_+}{\tau_0}$, f_{K^*}/f_ρ, $|V_{us}|$, $|V_{ub}|$, $|V_{cb}|$, $\mathcal{A}_{PV}$, $\mathcal{A}_{CP}(B \to K^*(892)^{\pm}\pi^{\mp})$, and the branching fractions for $B \to \rho(770)^{\pm}\pi^{\mp}$, $K/\bar{K}^*(892)^0\pi^{\pm}$, $K^*(892)^{\pm}\pi^{\mp}$, $\phi(1020)K^{\pm}$, and $\phi K^0/\bar{K}^0$. The values of these parameters and the resolution functions used in the simulation are summarized in Table 8.2. The inputs that contribute the largest uncertainties to γ are the $B \to K^*(892)^{\pm}\pi^{\mp}$ branching fraction and CP asymmetry measured in this thesis.

Parameter	Value	References	Resolution Function
$\frac{f_{+-}}{f_{00}} \times \frac{\tau_+}{\tau_0}$	1.11 ± 0.07	[120, 127]	Gaussian
f_{K^*}/f_ρ	1.04 ± 0.02	[84]	Gaussian
$\lvert V_{us}\rvert$	0.2196 ± 0.0023	[5]	Gaussian
$\lvert V_{ub}\rvert$	$(3.78 \pm 0.37) \times 10^{-3}$	[5]	Gaussian
$\lvert V_{cb}\rvert$	$(4.07 \pm 0.10) \times 10^{-2}$	[5]	Gaussian
$\mathcal{A}_{PV}$	$0.281 \pm 0.190 \pm 0.084$	[104]	Gaussian
$\mathcal{B}(B \to \rho(770)^{\pm}\pi^{\mp})$	$(25.4 \pm 4.2) \times 10^{-6}$	[128, 131, 134]	Gaussian
$\mathcal{B}(B \to K/\bar{K}^*(892)^0\pi^{\pm})$	$(12.4 \pm 2.5) \times 10^{-6}$	[128, 132, 135]	Gaussian
$\mathcal{B}(B \to K^*(892)^{\pm}\pi^{\mp})$	$(16.4^{+4.2}_{-4.0}) \times 10^{-6}$	[129, 136, 137]	Bifurcated Gaussian
$\mathcal{B}(B \to \phi(1020)K^{\pm})$	$(8.2 \pm 1.1) \times 10^{-6}$	[130, 133, 138]	Gaussian
$\mathcal{B}(B \to \phi(1020)K^0/\bar{K}^0)$	$(8.7 \pm 1.6) \times 10^{-6}$	[130, 133, 138]	Gaussian
$\mathcal{A}_{CP}(B \to K^*(892)^{\pm}\pi^{\mp})$	$0.26^{+0.33+0.10}_{-0.34-0.08}$	[105]	Bifurcated Gaussian
$\lvert P'^P_{EW}/p'_P\rvert$	$\left[\frac{1}{3}, \frac{2}{3}\right]$	[123, 124]	Uniform

Table 8.2: Input parameters to the toy MC used to constrain γ. References [129] and [105] are based on the results in this thesis.

The product $\frac{f_{+-}}{f_{00}} \times \frac{\tau_+}{\tau_0}$ is taken from recent CLEO measurements [120, 127]. The ratio f_{K^*}/f_ρ is derived from τ decay measurements and standard kinematic factors [84]. For $|V_{us}|$, $|V_{ub}|$, and $|V_{cb}|$,

we use the current world averages [5].

The value of $\mathcal{A}_{PV}$ is calculated from the BABAR measurements: $A = -0.22 \pm 0.08 \pm 0.07$, $C = 0.45^{+0.18}_{-0.19} \pm 0.09$, $\Delta C = 0.38^{+0.19}_{-0.20} \pm 0.11$. The statistical uncertainties on A, C, and ΔC are propagated using the correlation matrix [104],

	A	C	ΔC
A	1	-0.118	-0.104
C	-0.118	1	0.239
ΔC	-0.104	0.239	1

Because the correlation matrix for the systematic uncertainties on A, C, and ΔC is not reported, we assign, *ad hoc*, a relative systematic uncertainty to $\mathcal{A}_{PV}$ of 30%, which is a typical value among the measurements in the BABAR study. Hence, we arrive at the value $\mathcal{A}_{PV} = 0.281 \pm 0.190 \pm 0.084$, which results in a 24% error on $|t'_P|^2$, compared to a 20% error on $|p'_P|^2$ and a 25% error on $\mathcal{B}(K^*(892)^\pm\pi^\mp)\left(\frac{f_{+-}}{f_{00}} \times \frac{\tau_+}{\tau_0}\right)$. The correlation between $\mathcal{A}_{PV}$ and $\mathcal{B}(\rho(770)^\pm\pi^\mp)$ is negligible, since the tagging requirement reduces the sample size in the time-dependent measurement to one-fourth of that used in the BABAR branching fraction measurement, which is furthermore combined with the results of two other experiments.

For the five branching fractions, we combine all the measurements that have been publicly presented. For $B \to \rho(770)^\pm\pi^\mp$, we include the CLEO measurement [128] despite its low statistical significance (3.6σ) because it has been used in previous phenomenological studies. Table 8.3 lists the measurements and their weighted averages, which are calculated with statistical and systematic errors added in quadrature and assuming bifurcated Gaussian resolution functions on the individual measurements. Where possible or appropriate, the contribution from f_{+-}/f_{00} to the systematic error has been removed, since it is included coherently in the MC. We neglect all other correlations among the systematic errors. The CLEO measurements of $\mathcal{B}(K^*(892)^\pm\pi^\mp)$ and $\mathcal{A}_{CP}(K^*(892)^\pm\pi^\mp)$ are taken from recent publications [105, 129] based on the work presented in this thesis.

Mode	CLEO	BABAR	Belle	Average
$\rho(770)^\pm\pi^\mp$	$27.6^{+8.4}_{-7.4}\pm4.2$	$28.9 \pm 5.4 \pm 4.3$	$20.8^{+6.0+2.8}_{-6.3-3.1}$	25.4 ± 4.2
$K/\bar{K}^*(892)^0\pi^\pm$	$7.6^{+3.5}_{-3.0}\pm1.6$	$15.5 \pm 1.8^{+1.5}_{-3.2}$	$19.3^{+4.2+4.1}_{-3.9-7.1}$	12.4 ± 2.5
$K^*(892)^\pm(K^0_S\pi^\pm)\pi^\mp$	$\Big\}16^{+6}_{-5}\pm2$		$20.3^{+7.5}_{-6.6} \pm 4.4$	$\Big\}16.4^{+4.2}_{-4.0}$
$K^*(892)^\pm(K^\pm\pi^0)\pi^\mp$			$13.0^{+3.9+2.0+6.9}_{-3.6-1.8-6.1}$	
$\phi(1020)K^\pm$	$5.5^{+2.1}_{-1.8}\pm0.6$	$7.7^{+1.6}_{-1.4}\pm0.8$	$10.7 \pm 1.0^{+0.9}_{-1.6}$	8.2 ± 1.1
$\phi(1020)K^0/\bar{K}^0$	$5.4^{+3.7}_{-2.7}\pm0.7$	$8.1^{+3.1}_{-2.5}\pm0.8$	$10.0^{+1.9+0.9}_{-1.7-1.3}$	8.7 ± 1.6

Table 8.3: Branching fraction measurements used to constrain γ, given in units of 10^{-6} and averaged over charge conjugate states.

We determine $A(K^*(892)^+\pi^-)$ and $A(K^*(892)^-\pi^+)$ from the measurements of the CP-averaged

$\mathcal{B}(B \to K^*(892)^{\pm}\pi^{\mp})$ and $\mathcal{A}_{CP}(B \to K^*(892)^{\pm}\pi^{\mp})$. To do so, we must account for the correlation between the CLEO branching fraction and CP asymmetry measurements, since they are based on the same dataset. However, the two charge conjugate branching fractions, denoted $\mathcal{B}_+ \equiv \mathcal{B}(\bar{B}^0 \to K^*(892)^-\pi^+)$ and $\mathcal{B}_- \equiv \mathcal{B}(B^0 \to K^*(892)^+\pi^-)$ are essentially independent, so we simulate them directly using

$$\mathcal{B}_+ = \mathcal{B}(1+\mathcal{A}) \tag{8.37}$$

$$\mathcal{B}_- = \mathcal{B}(1-\mathcal{A}), \tag{8.38}$$

where $\mathcal{B} \equiv \mathcal{B}(B \to K^*(892)^{\pm}\pi^{\mp})$ and $\mathcal{A} \equiv \mathcal{A}_{CP}(B \to K^*(892)^{\pm}\pi^{\mp})$ have been smeared by their systematic uncertainties, which are assumed to be uncorrelated. The statistical uncertainties on $\mathcal{B}_+$ and $\mathcal{B}_-$ are derived from those on $\mathcal{B}$ and $\mathcal{A}$, as shown below. First, we express $\mathcal{B}$ and $\mathcal{A}$ in terms of $\mathcal{B}_+$ and $\mathcal{B}_-$:

$$\mathcal{B} = \frac{\mathcal{B}_+ + \mathcal{B}_-}{2} \tag{8.39}$$

$$\mathcal{A} = \frac{\mathcal{B}_+ - \mathcal{B}_-}{\mathcal{B}_+ + \mathcal{B}_-} = \frac{\mathcal{B}_+ - \mathcal{B}_-}{2\mathcal{B}}. \tag{8.40}$$

Then, we find the uncertainties on $\mathcal{B}$ and $\mathcal{A}$ in terms of the uncertainties on $\mathcal{B}_{\pm}$, denoted by $\sigma_{\pm}$:

$$\sigma_{\mathcal{B}}^2 = \frac{\sigma_+^2 + \sigma_-^2}{4} \tag{8.41}$$

$$\sigma_{\mathcal{A}}^2 = \frac{\mathcal{B}_-^2\sigma_+^2 + \mathcal{B}_+^2\sigma_-^2}{4\mathcal{B}^4}. \tag{8.42}$$

Solving this system of equations, we obtain σ_+ and σ_-:

$$\sigma_+^2 = \frac{1}{\mathcal{A}}[(1+\mathcal{A})^2\sigma_{\mathcal{B}}^2 - \mathcal{B}^2\sigma_{\mathcal{A}}^2] \tag{8.43}$$

$$\sigma_-^2 = \frac{1}{\mathcal{A}}[\mathcal{B}^2\sigma_{\mathcal{A}}^2 - (1-\mathcal{A})^2\sigma_{\mathcal{B}}^2]. \tag{8.44}$$

Here, we use the fixed peak values of $\mathcal{B}$ and $\mathcal{A}$, not the generated values for each trial. These uncertainties are then applied to the generated values of $\mathcal{B}_+$ and $\mathcal{B}_-$.

We apply $\mathcal{A}_{CP}$ determined from CLEO data to Belle's CP-averaged measurements, denoted $\mathcal{B}_a$, to obtain branching fractions for each charge state. We combine these results with the CLEO measurements, $\mathcal{B}_+$ and $\mathcal{B}_-$, using the relative weights determined below. We define the average branching fractions for each charge state, denoted $\bar{\mathcal{B}}_+$ and $\bar{\mathcal{B}}_-$ as follows:

$$\bar{\mathcal{B}}_+ = \frac{1}{\alpha+\beta}\left[\alpha\mathcal{B}_+ + \beta\mathcal{B}_a\frac{\mathcal{B}_+}{\mathcal{B}}\right] \tag{8.45}$$

$$\bar{\mathcal{B}}_- = \frac{1}{\bar{\alpha}+\bar{\beta}}\left[\bar{\alpha}\mathcal{B}_- + \bar{\beta}\mathcal{B}_a\frac{\mathcal{B}_-}{\mathcal{B}}\right]. \tag{8.46}$$

We choose the weights α, β, $\bar{\alpha}$, and $\bar{\beta}$ to give the smallest error on the combined branching fractions. Since the two measurements to be averaged in each case are highly correlated, the optimal weights are not simply inverses of the variances of the individual measurements. We begin by propagating the errors on the individual branching fractions:

$$\sigma^2_{\bar{\mathcal{B}}_+} = \frac{1}{(\alpha+\beta)^2}\left[\sigma_+^2\left(\alpha + \frac{\beta\mathcal{B}_a\mathcal{B}_-}{2\mathcal{B}^2}\right)^2 + \sigma_-^2\frac{\beta^2\mathcal{B}_a^2\mathcal{B}_+^2}{4\mathcal{B}^4} + \sigma_a^2\frac{\beta^2\mathcal{B}_+^2}{\mathcal{B}^2}\right] \tag{8.47}$$

$$\sigma^2_{\bar{\mathcal{B}}_-} = \frac{1}{(\bar{\alpha}+\bar{\beta})^2}\left[\sigma_+^2\frac{\bar{\beta}^2\mathcal{B}_a^2\mathcal{B}_-^2}{4\mathcal{B}^4} + \sigma_-^2\left(\bar{\alpha} + \frac{\bar{\beta}\mathcal{B}_a\mathcal{B}_+}{2\mathcal{B}^2}\right)^2 + \sigma_a^2\frac{\bar{\beta}^2\mathcal{B}_-^2}{\mathcal{B}^2}\right], \tag{8.48}$$

where σ_a is the uncertainty on $\mathcal{B}_a$, and σ_-, σ_+, and σ_a are averages of the upper and lower errors on the branching fractions. Differentiating these expressions with respect to α, β, $\bar{\alpha}$, and $\bar{\beta}$, and equating them to zero, we find

$$\alpha = \sigma_+^2\mathcal{B}_a\mathcal{B}_-(\mathcal{B}_a\mathcal{B}_- - 2\mathcal{B}^2) + \sigma_-^2\mathcal{B}_a^2\mathcal{B}_+^2 + 4\sigma_a^2\mathcal{B}^2\mathcal{B}_+^2 \tag{8.49}$$

$$\beta = 2\sigma_+^2\mathcal{B}^2(2\mathcal{B}^2 - \mathcal{B}_a\mathcal{B}_-) \tag{8.50}$$

$$\bar{\alpha} = \sigma_+^2\mathcal{B}_a^2\mathcal{B}_-^2 + \sigma_-^2\mathcal{B}_a\mathcal{B}_+(\mathcal{B}_a\mathcal{B}_+ - 2\mathcal{B}^2) + 4\sigma_a^2\mathcal{B}^2\mathcal{B}_-^2 \tag{8.51}$$

$$\bar{\beta} = 2\sigma_-^2\mathcal{B}^2(2\mathcal{B}^2 - \mathcal{B}_a\mathcal{B}_+). \tag{8.52}$$

In determining these weights, we have neglected the correlation between $\mathcal{B}_+$ and $\mathcal{B}_-$ arising from the common systematic errors, which are a factor of 4–5 smaller than the statistical errors.

8.2.6 Results of Simulation

Figure 8.1 shows the simulated distribution of $\cos\gamma\cos\delta$ using $B \to K^*(892)^{\pm}\pi^{\mp}$ from 50000 MC trials. In solving for $|t'_P|$, we used the value $\delta' = 0°$. Fitting this distribution to a bifurcated Gaussian yields the measurement $\cos\gamma\cos\delta = -0.63 \pm 0.59$. For $\cos\gamma\cos\delta < 0$, the tree and penguin amplitudes t'_P and p'_P interfere constructively. Based on the smallness of direct CP asymmetries $B \to K\pi$, one can infer a strong phase between tree and penguin amplitudes in these decays of $8° \pm 10°$ [28]. If the strong phase in $B \to PV$ decays is as small as in $B \to PP$ decays, then our analysis favors $\cos\gamma < 0$. In particular, for $\delta = 0°$, the peak value corresponds to $\gamma|_{\delta=0°} = 129°$. The variation of $\cos\gamma\cos\delta$ is roughly linear in the value of $\cos\delta'$ used to solve for $|t'_P|$, with a slope of $\frac{d\cos\gamma\cos\delta}{d\cos\delta'} = 0.084$. So, when we use $\delta' = 80°$, the simulation gives $\cos\gamma\cos\delta = -0.70^{+0.65}_{-0.69}$, which results in a change in $\gamma|_{\delta=0°}$ of 5°.

Also shown in Figure 8.1 is the distribution of $\cos\gamma$ at $\delta = 0°$ using $B \to K^*(892)^{\pm}\pi^{\mp}$ and $B \to \phi(1020)K$. With this method, we obtain $\cos\gamma|_{\delta=0°} = -0.46^{+0.51}_{-0.50}$.

If we forgo the iterative procedure to account for the penguin amplitude in $B^0 \to \rho(770)^+\pi^-$ and take $|t_P| = \sqrt{\mathcal{B}(\rho(770)^\pm\pi^\mp)_P}$, then we find $\cos\gamma\cos\delta = -0.58^{+0.63}_{-0.95}$ using $B \to K^*(892)^\pm\pi^\mp$ alone and $\cos\gamma|_{\delta=0^\circ} = -0.38^{+0.53}_{-0.77}$ using both $B \to K^*(892)^\pm\pi^\mp$ and $B \to \phi K$, as shown in Figure 8.1. The effect of the iterative procedure is to sharpen both of the simulated distributions, reducing the low-side uncertainty to about the same size as the high-side uncertainty.

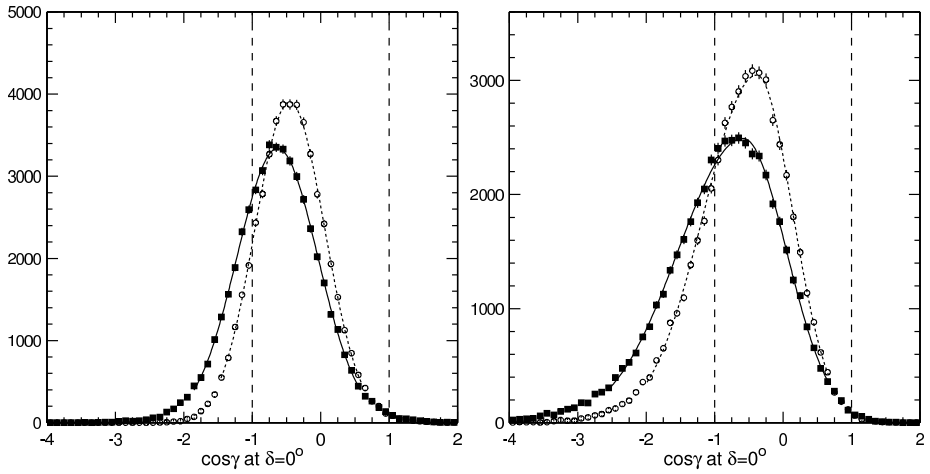

Figure 8.1: Distribution of $\cos\gamma\cos\delta$ using $B \to K^*(892)^\pm\pi^\mp$ (solid squares) and $\cos\gamma$ at $\delta = 0^\circ$ using $B \to K^*(892)^\pm\pi^\mp$ and $B \to \phi(1020)K$ (open circles), with (left) and without (right) accounting for p_P in $B \to \rho(770)^\pm\pi^\mp$ iteratively. Overlaid on the histograms are the fits to bifurcated Gaussians. The vertical lines demarcate the physical region.

We define an upper bound on $\cos\gamma\cos\delta$ or $\cos\gamma$ at a given confidence level to be the value that lies above no more than that fraction of the distribution, without being restricted to the physical region. The 90%, 95%, and 99% confidence level (C.L.) upper limits on $\cos\gamma\cos\delta$ from the method with $B \to K^*(892)^\pm\pi^\mp$ alone are 0.13, 0.36, and 0.85, respectively, which, for $\delta = 0^\circ$ correspond to lower limits on γ of 83°, 69°, and 32°. Using $B \to K^*(892)^\pm\pi^\mp$ and $B \to \phi(1020)K$, we find 90%, 95%, and 99% C.L. lower limits on γ of 78°, 66°, and 35°, respectively, again for $\delta = 0^\circ$.

Figure 8.2 shows the $\cos\gamma$ distributions determined from $B \to K^*(892)^\pm\pi^\mp$ and $B \to \phi(1020)K$ at various fixed values of δ, as well as the variations of the peak values and the 90%, 95%, and 99% C.L. upper limits with δ. The first two limits become more stringent with increasing δ. So, restricting the range of δ to a window around 0° weakens these two limits but strengthens the last one. Incorporating the $B \to \phi(1020)K$ decays in the measurement of γ results in greater precision than using $B \to K^*(892)^\pm\pi^\mp$ alone, but the theoretical uncertainties incurred are also larger, not least in the assumed value of δ. The validity of this method rests on the applicability of flavor SU(3) in relating the penguin amplitudes in $B \to \phi(1020)K$ to those in $B \to K^*(892)^\pm\pi^\mp$, as well as on the factorization calculation of the magnitude of P'^P_{EW}.

Figure 8.3 shows the simulated distributions, using $\mathcal{A}_{CP}(B \to K^*(892)^\pm\pi^\mp)$, of $\cos(\gamma+\delta)$ and

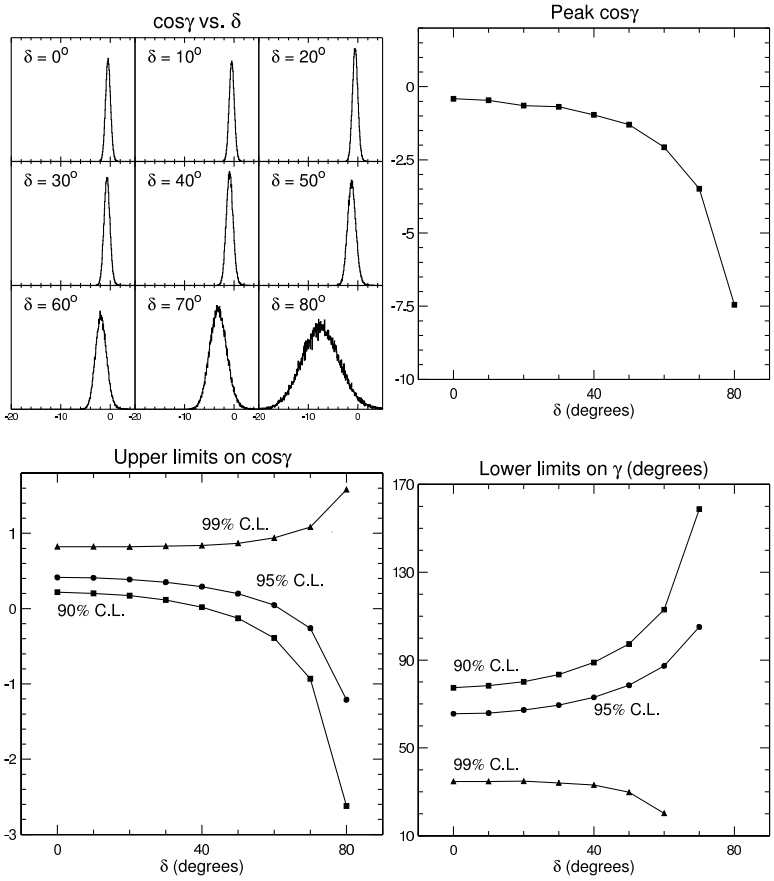

Figure 8.2: Distributions of $\cos\gamma$ at various values of δ (top left), peak values of $\cos\gamma$ (top right), upper limits on $\cos\gamma$ (bottom left), and lower limits on γ in degrees (bottom right) versus δ, with $B \to \phi(1020)K$ included in the determination.

$\cos(\gamma-\delta)$, which are measured to be $0.01^{+0.88}_{-0.93}$ and $-1.20^{+1.01}_{-1.02}$, respectively. The peak value of $\gamma+\delta$ is 89°, whereas the peak value of $\gamma-\delta$ is unphysical. The fraction of trials where both $\cos(\gamma+\delta)$ and $\cos(\gamma-\delta)$ attain physical values is 28.6%. Considering only these trials, the distributions of the weak and strong phases imply $\gamma = (106^{+23}_{-25})^\circ$ and $\delta = (-13^{+27}_{-24})^\circ$, as shown in Figure 8.3. The correlation coefficient between γ and δ is 3×10^{-4}. To calculate $|t'_P|$, we imposed $\delta' = 0^\circ$ (which is consistent with $(-13^{+27}_{-24})^\circ$), even for those trials that gave a physical value for δ because the peak value given above cannot be considered representative of the entire allowed region. The variations of $\cos(\gamma+\delta)$ and $\cos(\gamma-\delta)$ with $\cos\delta'$ are given by $\frac{d\cos(\gamma+\delta)}{d\cos\delta'} = 0.005$ and $\frac{d\cos(\gamma-\delta)}{d\cos\delta'} = 0.117$. The values of γ and δ both change by less than 1° between $\delta' = 0^\circ$ and $\delta' = 80^\circ$.

If we omit the Belle measurements of $\mathcal{B}(B \to K^*(892)^\pm\pi^\mp)$ and use only the results of this thesis (published in References [105] and [129]), then, for $\delta' = 0^\circ$, we find $\cos(\gamma+\delta) = -0.04^{+1.00}_{-0.97}$, $\cos(\gamma-\delta) = -1.28^{+1.21}_{-1.13}$, $\gamma = (103^{+25}_{-28})^\circ$, and $\delta = (-10^{+26}_{-25})^\circ$, with 25.4% of the trials in the physical region. The precision of the current experimental measurements does not yet permit a meaningful

extraction of these phases.

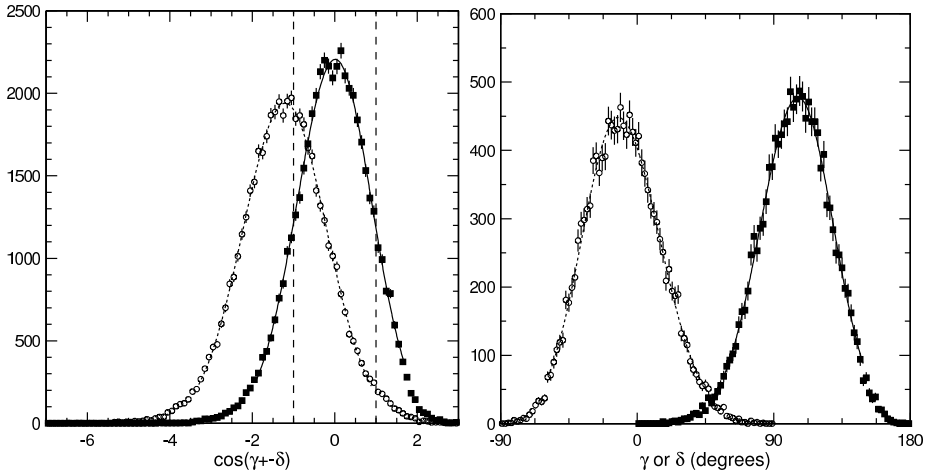

Figure 8.3: Distributions of $\cos(\gamma+\delta)$ (left, solid squares) and $\cos(\gamma-\delta)$ (left, open circles), as well as γ (right, solid squares) and δ (right, open circles) using the 22.4% of trials with physical values of both $\cos(\gamma+\delta)$ and $\cos(\gamma-\delta)$. The vertical lines demarcate the physical region.

Using the above simulation, we also determine the ratio of tree to penguin amplitudes in $|\Delta S|=1$ decays to be $r = 0.32^{+0.07}_{-0.05}$. The inverse ratio for $\Delta S = 0$ decays is $|p_P/t_P| = \frac{1}{r}|V_{us}V_{td}/V_{ud}V_{ts}| = 0.19^{+0.02}_{-0.03}$. In addition, we find the experimental averages of $B \to K^*(892)^{\pm}\pi^{\mp}$ branching fractions for the two charge states to be $\bar{\mathcal{B}}_+ = (20.8^{+7.8}_{-7.1}) \times 10^{-6}$ and $\bar{\mathcal{B}}_- = (12.1^{+6.6}_{-6.1}) \times 10^{-6}$ with a correlation coefficient -0.33 arising from the use of the CP-averaged Belle measurement. The simulated distributions of these quantities are shown in Figure 8.4.

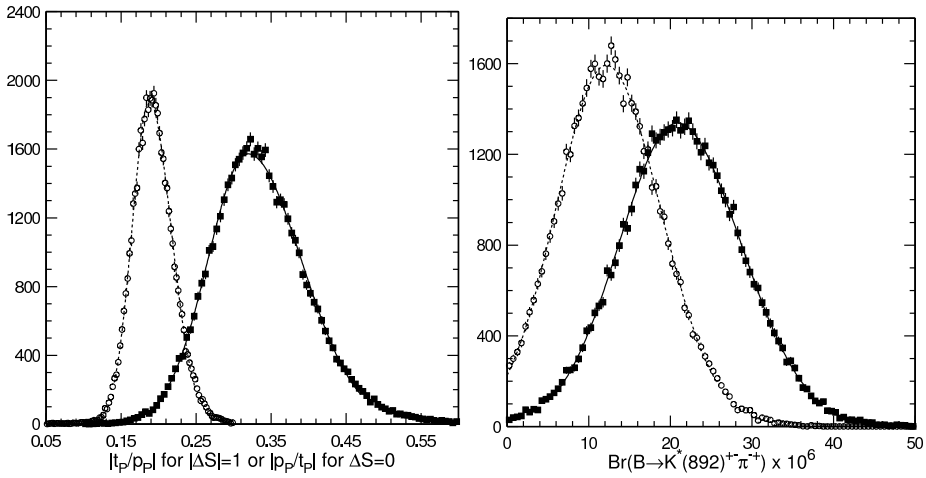

Figure 8.4: Distributions of $|t'_P/p'_P|$ (left, solid squares), $|p_P/t_P|$ (left, open circles), $\bar{\mathcal{B}}_+$ (right, solid squares) and $\bar{\mathcal{B}}_-$ (right, open circles).

An alternative method of constraining γ [26], mentioned in Chapter 2, involves fits to current values of $|V_{ub}/V_{cb}|$, Δm_{B_d}, $\Delta m_{B_d}/\Delta m_{B_s}$, and ϵ, which delineate an allowed interval at the 95% confidence level of $[34°, 82°]$. On the other hand, a global fit to the $B \to K\pi$ and $\pi\pi$ branching fractions in the QCD factorization framework [28, 139] favors values of γ near 90°. An analysis of both branching fractions and CP asymmetries in $B \to K\pi$ and $\pi^+\pi^-$ employing isospin and SU(3) flavor symmetries [140] also finds evidence for $\cos\gamma < 0$, which agrees with indications from our analysis. A discrepancy between the constraints on γ derived from charmless hadronic B decays and from B^0-$\bar{B}^0$ mixing might arise from New Physics contributions affecting either B^0-$\bar{B}^0$ mixing or the $b \to s$ or $b \to d$ penguins. The latter possibility would lead to a difference between the mixing phases measured in $B \to J/\psi K^0_S$ and in $B \to \phi(1020)K^0_S$.

8.2.7 Resolution of $\cos\gamma$

In the method using $B \to K^*(892)^{\pm}\pi^{\mp}$ alone, the width of the $\cos\gamma\cos\delta$ distribution is dominated by experimental uncertainties on the $B \to \rho(770)^{\pm}\pi^{\mp}$, $K/\bar{K}^*(892)^0\pi^{\pm}$, and $K^*(892)^{\pm}\pi^{\mp}$ branching fractions and on $\mathcal{A}_{PV}$. The first three entries of Table 8.4 show the effect of improved precision in these four measurements on the determination of $\cos\gamma\cos\delta$. The central values of the branching fractions and $\mathcal{A}_{PV}$ are kept constant while their uncertainties are reduced to a fraction of their original values, given by $\frac{\sigma'}{\sigma}(\mathcal{B}, \mathcal{A}_{PV})$. The improvement in the resolution of $\cos\gamma\cos\delta$ is commensurate with the size of the errors on the branching fractions and $\mathcal{A}_{PV}$ until $\frac{\sigma'}{\sigma}(\mathcal{B}, \mathcal{A}_{PV})$ reaches 10%. At this point, the resolution of $\cos\gamma\cos\delta$ begins to be dominated by the uncertainty on $\frac{f_{+-}}{f_{00}} \times \frac{\tau_+}{\tau_0}$. Only by lowering $\frac{\sigma'}{\sigma}\left(\frac{f_{+-}}{f_{00}} \times \frac{\tau_+}{\tau_0}\right)$ can we reduce the width of $\cos\gamma\cos\delta$ further. The distributions of $\cos\gamma\cos\delta$ with various combinations of $\frac{\sigma'}{\sigma}(\mathcal{B}, \mathcal{A}_{PV})$ and $\frac{\sigma'}{\sigma}\left(\frac{f_{+-}}{f_{00}} \times \frac{\tau_+}{\tau_0}\right)$ are shown in Figure 8.5. In order to constrain γ to within $\mathcal{O}(10°)$, the combined statistical and systematic errors on the measurements mentioned above must be reduced by an order of magnitude, and the strong phase δ must be reliably estimated.

$\frac{\sigma'}{\sigma}(\mathcal{B}, \mathcal{A}_{PV})$	$\frac{\sigma'}{\sigma}\left(\frac{f_{+-}}{f_{00}} \times \frac{\tau_+}{\tau_0}\right)$	$\sigma^{+/-}_{\cos\gamma\cos\delta}$	$\sigma^{+/-}_{\gamma}$
100%	100%	0.59/0.59	28°/31°
50%	100%	0.31/0.32	22°/17°
10%	100%	0.12/0.12	9°/7°
10%	50%	0.08/0.08	6°/5°
10%	10%	0.06/0.06	5°/4°

Table 8.4: Effect of uncertainties in branching fraction and $\frac{f_{+-}}{f_{00}} \times \frac{\tau_+}{\tau_0}$ measurements on $\cos\gamma\cos\delta$ resolution, using $B \to K^*(892)^{\pm}\pi^{\mp}$ alone. σ^+ and σ^- refer to upper and lower widths of a bifurcated Gaussian resolution function. The values in the last column are evaluated at $\delta = 0°$.

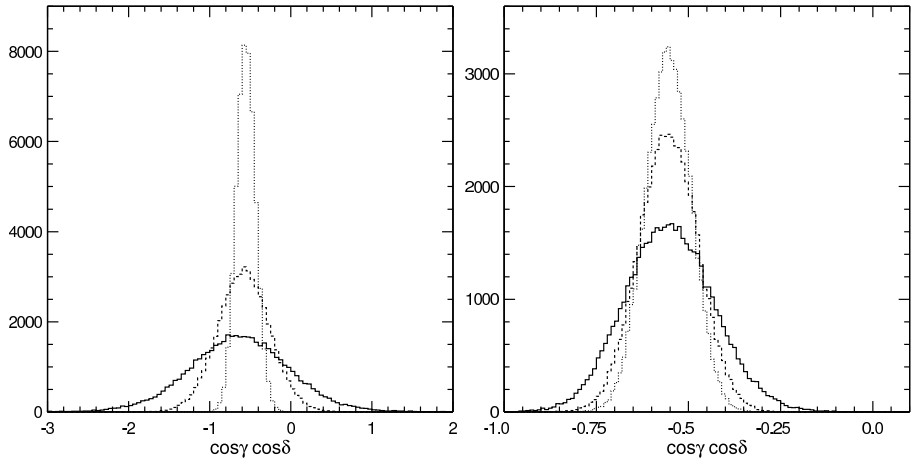

Figure 8.5: Distributions of $\cos\gamma\cos\delta$ using $B \to K^*(892)^{\pm}\pi^{\mp}$ alone. Histograms on the left are generated with $\frac{\sigma'}{\sigma}(\mathcal{B}, \mathcal{A}_{PV}) = 100\%$, 50%, and 10% (solid, dashed, and dotted, respectively) and $\frac{\sigma'}{\sigma}\left(\frac{f_{+-}}{f_{00}} \times \frac{\tau_+}{\tau_0}\right)$ fixed to 100%. Histograms on the right are generated with $\frac{\sigma'}{\sigma}\left(\frac{f_{+-}}{f_{00}} \times \frac{\tau_+}{\tau_0}\right) = 100\%$, 50%, and 10% (solid, dashed, and dotted, respectively) and $\frac{\sigma'}{\sigma}(\mathcal{B}, \mathcal{A}_{PV})$ fixed to 10%. The dotted histogram on the left is identical to the solid histogram on the right.

In the method using both $B \to K^*(892)^{\pm}\pi^{\mp}$ and $B \to \phi(1020)K$, experimental uncertainties on branching fractions and $\mathcal{A}_{PV}$ also dominate the resolution of $\cos\gamma$. However, when these uncertainties have been reduced to 10% of their original values, the theoretical uncertainty on the size of $|P'^{IP}_{EW}/p'_P|$ becomes the dominant contribution, as illustrated in Table 8.6. Figure 8.6 displays the distributions of $\cos\gamma$ at $\delta = 0°$ with varying $\frac{\sigma'}{\sigma}(\mathcal{B}, \mathcal{A}_{PV})$ and with different allowed ranges of $|P'^{IP}_{EW}/p'_P|$. Clearly, if this method is to yield a precise measurement of γ, then the theoretical uncertainties on $|P'^{IP}_{EW}/p'_P|$ as well as on δ must be controlled.

$\frac{\sigma'}{\sigma}(\mathcal{B}, \mathcal{A}_{PV})$	$\lvert P'^{IP}_{EW}/p'_P\rvert$	$\sigma^{+/-}_{\cos\gamma}$	$\sigma^{+/-}_{\gamma}$
100%	[0.33, 0.67]	0.51/0.50	29°/27°
50%	[0.33, 0.67]	0.29/0.30	20°/16°
10%	[0.33, 0.67]	0.18/0.21	15°/9°
10%	[0.40, 0.60]	0.13/0.13	8°/7°
10%	[0.45, 0.55]	0.10/0.09	6°/6°

Table 8.5: Effect of uncertainties in branching fraction measurements and $|P'^{IP}_{EW}/p'_P|$ on $\cos\gamma$ resolution, evaluated at $\delta = 0°$, using $B \to K^*(892)^{\pm}\pi^{\mp}$ and $B \to \phi(1020)K$. σ^+ and σ^- refer to upper and lower widths of a bifurcated Gaussian resolution function.

In the determination of γ and δ using $\mathcal{A}_{CP}(K^*(892)^{\pm}\pi^{\mp})$, reducing the total uncertainties on the branching fractions, $\mathcal{A}_{PV}$, and $\mathcal{A}_{CP}(K^*(892)^{\pm}\pi^{\mp})$ by an order of magnitude would constrain both γ and δ to within less than 10°, as shown in Table 8.6. However, if experimental measurements

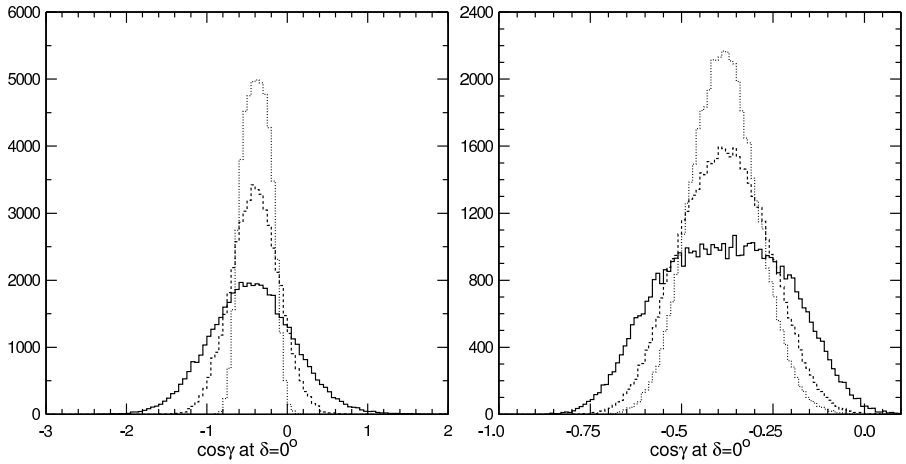

Figure 8.6: Distributions of $\cos\gamma$ at $\delta = 0°$ using $B \to K^*(892)^{\pm}\pi^{\mp}$ and $B \to \phi(1020)K$. Histograms on the left are generated with $\frac{\sigma'}{\sigma}(\mathcal{B}, \mathcal{A}_{PV}) = 100\%$, 50%, and 10% (solid, dashed, and dotted, respectively) and $|P'^{P}_{EW}/p'_P| \in [0.33, 0.67]$. Histograms on the right are generated with $|P'^{P}_{EW}/p'_P| \in [0.33, 0.67]$, $[0.40, 0.60]$, and $[0.45, 0.55]$ (solid, dashed, and dotted, respectively) and $\frac{\sigma'}{\sigma}(\mathcal{B}, \mathcal{A}_{PV})$ fixed to 10%. The dotted histogram on the left is identical to the solid histogram on the right.

remain at their present values, then unphysical values of $\cos(\gamma - \delta)$ would be strongly favored, and this inconsistency would force reexamination of SU(3) breaking or previously neglected amplitudes as well as indicate the possible presence of New Physics.

$\frac{\sigma'}{\sigma}(\mathcal{B}, \mathcal{A}_{PV}, \mathcal{A}_{CP})$	$\sigma^{+/-}_{\cos(\gamma+\delta)}$	$\sigma^{+/-}_{\cos(\gamma-\delta)}$	$\sigma^{+/-}_{\gamma}$	$\sigma^{+/-}_{\delta}$	f_{physical}
100%	0.88/0.93	1.01/1.00	23°/25°	27°/24°	0.286
50%	0.47/0.47	0.51/0.55	16°/17°	19°/17°	0.356
10%	0.13/0.13	0.16/0.16	6°/8°	6°/6°	0.190

Table 8.6: Effect of uncertainties in branching fraction and $\mathcal{A}_{CP}(K^*(892)^{\pm}\pi^{\mp})$ measurements on γ and δ resolution. f_{physical} refers to the fraction of MC trials with both $\cos(\gamma + \delta)$ and $\cos(\gamma - \delta)$ in the physical region. σ^+ and σ^- refer to upper and lower widths of a bifurcated Gaussian resolution function.

8.3 Tests of SU(3) Symmetry

As discussed in Section 2.5, SU(3) invariance leads to a series of relations among CP-violating rate differences in charmless hadronic $B \to PV$ decays. The relations in Equations 2.29 and 2.30 can be evaluated using currently available CP-averaged branching fraction measurements and the BABAR time-dependent study of $B \to \pi^+\pi^-\pi^0$ and $K^{\pm}\pi^{\mp}\pi^0$ [104], as well as the CP asymmetry in $B \to K^*(892)^{\pm}\pi^{\mp}$ presented above. The degree to which these relations are satisfied gives an

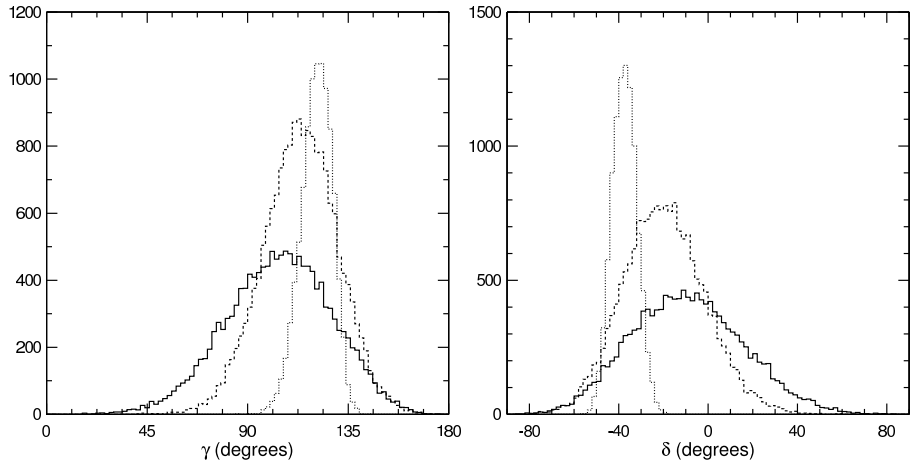

Figure 8.7: Distributions of γ and δ using $\mathcal{A}_{CP}(K^*(892)^{\pm}\pi^{\mp})$. Histograms are generated with $\frac{\sigma'}{\sigma}(\mathcal{B}, \mathcal{A}_{PV}, \mathcal{A}_{CP}) = 100\%$, 50%, and 10% (solid, dashed, and dotted, respectively).

indication of the validity of the SU(3) assumption.

In the following discussion, we neglect the form factor ratios, as they are expected to be close to unity. The decay constant ratios are given by $f_\pi/f_K \approx 0.82$ and $f_\rho/f_{K^*} \approx 0.96$. We neglect the 1%–3% uncertainties on these ratios, as they are far smaller than the branching fraction uncertainties. Since, experimentally, $\Delta(\bar{B}^0 \to \rho(770)^+\pi^-)$ and $\Delta(\bar{B}^0 \to \rho(770)^-\pi^+)$ are negatively correlated, their statistical uncertainty is reduced by considering the sum of Equations 2.29 and 2.30, given in Equation 2.31.

The rate differences $\Delta(\bar{B}^0 \to \rho(770)^+\pi^-)$, $\Delta(\bar{B}^0 \to \rho(770)^-\pi^+)$, and $\Delta(\bar{B}^0 \to \rho(770)^+K^-)$ are given by the BABAR study described in Section 8.2.2. Based on Equations 8.10–8.13, we can express the two $\rho(770)^{\pm}\pi^{\mp}$ rate differences as

$$-\Delta(\bar{B}^0 \to \rho(770)^+\pi^-) = (C + A\Delta C - A) \cdot \mathcal{B}(B \to \rho(770)^{\pm}\pi^{\mp}) \quad (8.53)$$

$$-\Delta(\bar{B}^0 \to \rho(770)^-\pi^+) = (C + A\Delta C + A) \cdot \mathcal{B}(B \to \rho(770)^{\pm}\pi^{\mp}). \quad (8.54)$$

Evaluating these rate differences using the measurements and correlation matrix given in Section 8.2.5, we obtain

$$-\Delta(\bar{B}^0 \to \rho(770)^+\pi^-) = (0.59 \pm 0.19 \pm 0.18) \cdot (25.4 \pm 4.2) \times 10^{-6} \quad (8.55)$$

$$= (13.2^{+8.0}_{-6.0}) \times 10^{-6} \quad (8.56)$$

$$-\Delta(\bar{B}^0 \to \rho(770)^-\pi^+) = (0.15 \pm 0.20 \pm 0.04) \cdot (25.4 \pm 4.2) \times 10^{-6} \quad (8.57)$$

$$= (3.2^{+5.6}_{-5.0}) \times 10^{-6}, \quad (8.58)$$

where we have assigned a systematic error of 30% to the asymmetries. In both cases, the rate difference consists of a product of two Gaussian-distributed variables, which is distributed as a bifurcated Gaussian. We employ MC simulation to multiply the two Gaussian distribution functions. For the rate difference relation in Equation 2.31, we sum the two $\bar{B}^0 \to \rho(770)^{\pm}\pi^{\mp}$ rate differences given above:

$$-\Delta(\bar{B}^0 \to \rho^+\pi^-) - \Delta(\bar{B}^0 \to \rho^-\pi^+) = 2(C + A\Delta C) \cdot \mathcal{B}(B \to \rho(770)^{\pm}\pi^{\mp}) \quad (8.59)$$

$$= 2(0.37 \pm 0.18 \pm 0.11) \cdot (25.4 \pm 4.2) \times 10^{-6} \quad (8.60)$$

$$= (16.4^{+12.3}_{-9.7}) \times 10^{-6}. \quad (8.61)$$

The BABAR study also includes a measurement of the CP asymmetry in $B \to \rho(770)^{\pm}K^{\mp}$, $\mathcal{A}_{\rho K} = 0.19 \pm 0.14 \pm 0.11$. To obtain the rate difference, we combine this quantity with the branching fraction corresponding to the 3.5σ yield for $B \to \rho(770)^{\pm}K^{\mp}$ found in [128], $\mathcal{B}(B \to \rho(770)^{\pm}K^{\mp}) = (16.0^{+7.6}_{-6.4} \pm 2.8) \times 10^{-6}$:

$$\Delta(\bar{B}^0 \to \rho(770)^+K^-) = 2A_{\rho K} \cdot \mathcal{B}(B \to \rho(770)^{\pm}K^{\mp}) \quad (8.62)$$

$$= 2(0.19 \pm 0.14 \pm 0.11) \cdot (16.0^{+7.6}_{-6.4} \pm 2.8) \times 10^{-6}. \quad (8.63)$$

The correlation coefficients between $\mathcal{A}_{\rho K}$ and the other three asymmetry parameters, A, C, and ΔC, are 0.034, -0.013, and -0.011, respectively. We neglect these correlations and treat $\mathcal{A}_{\rho K}$ as an independent variable. The quantity $\Delta(\bar{B}^0 \to \rho(770)^+K^-)$ is a product of a Gaussian-distributed variable with a bifurcated-Gaussian-distributed variable. The resultant distribution is not well described by a bifurcated Gaussian. Nonetheless, we represent $\Delta(\bar{B}^0 \to \rho(770)^+K^-)$ by the admittedly poor fit in Figure 8.8 and assign it a value of $(3.1^{+9.1}_{-4.7}) \times 10^{-6}$.

The rate difference for $B \to K^*(892)^{\pm}\pi^{\mp}$ is obtained from the MC simulation described in Section 8.2. The distribution of $\Delta(\bar{B}^0 \to K^*(892)^-\pi^+)$ is shown in Figure 8.8, and its value is found to be $(9.2^{+10.4}_{-11.3}) \times 10^{-6}$.

With these rate differences in hand, we evaluate Equations 2.29–2.31 as shown in Table 8.7. When $\Delta(\bar{B}^0 \to \rho(770)^+K^-)$ and $\Delta(\bar{B}^0 \to K^*(892)^-\pi^+)$ are summed in the right-hand side of Equation 2.31, the non-Gaussian nature of the $\Delta(\bar{B}^0 \to \rho(770)^+K^-)$ distribution is masked by the large uncertainty in $\Delta(\bar{B}^0 \to K^*(892)^-\pi^+)$, and the full expression is well modeled by a bifurcated Gaussian. In none of the three Equations do we find a significant departure from the SU(3) prediction, and we conclude that SU(3) symmetry holds at the current level of experimental precision, thus confirming the validity of the constraints on $\cos\gamma$ constructed in the SU(3) framework.

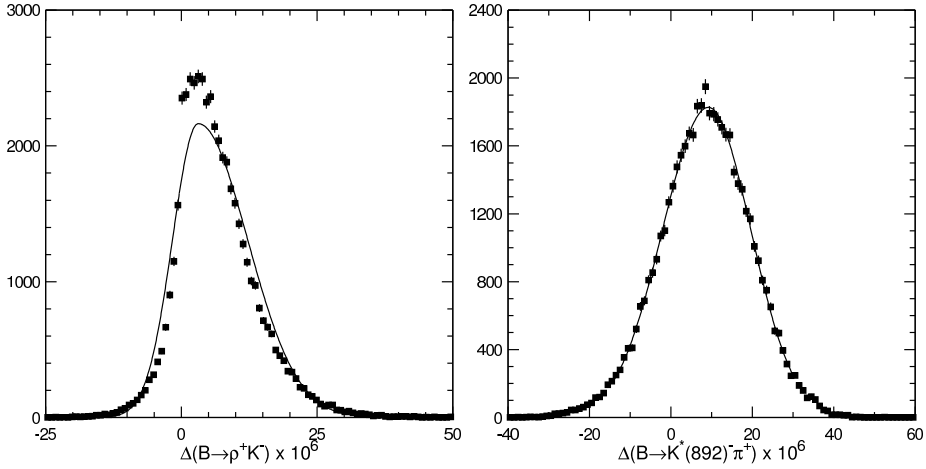

Figure 8.8: CP-violating rate differences $\Delta(\bar{B}^0 \to \rho(770)^+K^-)$ (left) and $\Delta(\bar{B}^0 \to K^*(892)^-\pi^+)$ (right).

Equation	Left-hand side $\times 10^6$	Right-hand side $\times 10^6$
2.29	$13.2^{+8.0}_{-6.0}$	$(0.82)^2(3.1^{+9.1}_{-4.7}) = 2.1^{+6.1}_{-3.2}$
2.30	$3.2^{+5.6}_{-5.0}$	$(0.96)^2(9.2^{+10.4}_{-11.3}) = 8.5^{+9.6}_{-10.4}$
2.31	$16.4^{+12.3}_{-9.7}$	$(0.82)^2(3.1^{+9.1}_{-4.7}) + (0.96)^2(9.2^{+10.4}_{-11.3}) = 12.0^{+11.3}_{-11.0}$

Table 8.7: Evaluation of SU(3) rate difference relations.

Appendix A Search for a Scalar Bottom Quark

A.1 Motivation

Recent years have seen renewed interest in the possibility of a light scalar bottom quark [142, 143], the supersymmetric partner of the conventional bottom quark. At the LEPC meeting on July 20, 2000, the ALEPH Collaboration presented results [144] on a bottom squark search conducted "as a result of a communication from CDF." ALEPH searched for $e^+e^- \to \tilde{b}\bar{\tilde{b}}$, with $\tilde{b}$ decaying $\tilde{b} \to c\ell^-\tilde{\nu}$. They assumed that the $\tilde{\nu}$ is massless and that the bottom squark has mass $m_{\tilde{b}} \approx 4$ GeV, lifetime $\tau_{\tilde{b}} \approx 1$ ps, and branching fractions $\mathcal{B}(\tilde{b} \to c\mu^-\tilde{\nu}) = \mathcal{B}(\tilde{b} \to ce^-\tilde{\nu}) = 50\%$. They measured the rate for hadronic events containing pairs of oppositely charged leptons and a B tag and found an excess over that expected from Standard Model processes, with a probability of occurring as a fluctuation of $\mathcal{O}(10^{-3})$. A subsequent re-evaluation of their lepton identification yielded no excess [145].

Nevertheless, a $\tilde{b}$ with the properties given above is allowed in a small region of MSSM parameter space [146] and is furthermore accessible to CLEO. In addition, the production cross section of scalar quarks in e^+e^- annihilations, well above threshold, is one-fourth that of spin-$\frac{1}{2}$ quarks of the same charge, with an angular distribution of $\sin^2\theta$ rather than $1 + \cos^2\theta$. Thus, $\tilde{b}\bar{\tilde{b}}$ production would contribute $\frac{1}{12}$ unit to R, the ratio of hadronic cross section to $\mu^+\mu^-$ cross section, and such an increase cannot be ruled out by existing measurements [147]. Indirect evidence from the measured B semileptonic branching fraction disfavors the existence of a light $\tilde{b}$ [148]. Throughout this Appendix, sums over charge-conjugate decays are implied.

If $\tilde{b}$ is the lightest supersymmetric particle (LSP) and if R-parity is conserved, then $\tilde{b}$ would be stable. If, instead, a scalar neutrino $\tilde{\nu}$ is the LSP, then $\tilde{b}$ will decay $\tilde{b} \to c\ell^-\tilde{\nu}$ and/or $\tilde{b} \to u\ell^-\tilde{\nu}$. If R-parity is violated, $\tilde{b}$ will decay $\tilde{b} \to c\ell^-$ and/or $\tilde{b} \to u\ell^-$. We have searched for a light $\tilde{b}$ that decays $\tilde{b} \to c\ell^-\tilde{\nu}$ and/or $\tilde{b} \to c\ell^-$. Such a particle would dress itself as a supersymmetric $\tilde{B}$ meson. The dressed decays would be $\tilde{B} \to DX\ell^-\tilde{\nu}$ and $\tilde{B} \to DX\ell^-$, where X represents possible additional conventional hadrons.

The decays we search for, characterized by leptons and charmed mesons, have much in common with conventional B decays. We perform a direct search, avoiding the B background by using 4.52 fb^{-1} of off-resonance data at $\sqrt{s} = 10.52$ GeV. Analysis of an additional 2.24 fb^{-1} collected on the $\Upsilon(4S)$ resonance provides a sample of B mesons, which can mimic the behavior of $\tilde{B}$ mesons, thus allowing us to verify our experimental technique.

For scalar quark production near threshold, the naive behavior of the cross section is $\sigma(e^+e^- \to \tilde{b}\bar{\tilde{b}}) \sim \beta^3$. However, strong interaction effects could increase $\sigma(e^+e^- \to \tilde{b}\bar{\tilde{b}})$ above the naive ex-

pectations, as occurs in $c\bar{c}$ and $b\bar{b}$ production. Ignoring these effects, one finds the threshold factor, β^3, to be 0.42 for $m_{\tilde{b}} = 3.5$ GeV, 0.27 for $m_{\tilde{b}} = 4.0$ GeV, and 0.14 for $m_{\tilde{b}} = 4.5$ GeV, where we have used $E_{\tilde{b}} = E_{\rm beam} = 5.26$ GeV. Thus, for charge $-\frac{1}{3}$ squarks, the cross sections are $\frac{1}{12}\sigma(e^+e^- \to \mu^+\mu^-) = 65$ pb multiplied by the threshold factor: 27 pb, 18 pb, 9 pb, for $m_{\tilde{b}} = 3.5, 4.0,$ and 4.5 GeV, respectively. For comparison, the cross section for $c\bar{c}$ production, $\frac{4}{3}\sigma(e^+e^- \to \mu^+\mu^-)$, is 1.0 nb. Our off-resonance data sample would contain 81 thousand $\tilde{b}\bar{\tilde{b}}$ pairs with $m_{\tilde{b}} = 4.0$, if they were to exist. It also contains 4.52×10^6 $c\bar{c}$ pairs.

A.2 Experimental Signatures

For the decay mode given, $\tilde{b} \to c\ell^-\tilde{\nu}$, each $\tilde{b}\bar{\tilde{b}}$ event will contain two charmed mesons *and* two charged leptons (μ or e). The charmed mesons may decay semileptonically, giving events with three or four leptons. Or, they may decay hadronically, giving events with two leptons and one or two reconstructable D mesons.

The probable background, *i.e.*, the source of leptons and charmed mesons in continuum data, is $e^+e^- \to c\bar{c}$. This final state can give events with two leptons and no reconstructable D mesons (both D mesons decaying semileptonically), events with one lepton and one reconstructable D meson (one D decaying semileptonically, the other hadronically), and events with no leptons and two reconstructable D mesons (both decaying hadronically). Given this background behavior, we can form a simple experimental signature for $e^+e^- \to \tilde{b}\bar{\tilde{b}}$ events, consisting of a reconstructed D in the presence of a pair of oppositely-charged leptons. We consider charged and neutral D and D^* mesons.

There are mechanisms by which $e^+e^- \to c\bar{c}$ events can give our $D^{(*)}\ell^+\ell^-$ signature. For example, with one real lepton and one fake lepton, $c\bar{c}$ events can give a reconstructed D plus two (apparent) leptons. Also, in principle, a $c\bar{c}$ pair can be popped from the vacuum: $e^+e^+ \to c\bar{c}c\bar{c}$. Another possible background is the two-photon process $e^+e^- \to e^+e^-c\bar{c}$. Other sources of leptons include kaons that decay in flight, photon conversions, and π^0 Dalitz decays.

If the R-parity-violating decay $\tilde{b} \to c\ell^-$ were to occur, then some fraction of the time it would appear as the dressed decay $\tilde{B} \to D\ell^-$ or $\tilde{B} \to D^*\ell^-$. While the $D^{(*)}\ell^+\ell^-$ signature discussed above is also sensitive to these decays, we gain greater statistical power by examining the $D\ell^-$ and $D^*\ell^-$ invariant mass distributions in $D^{(*)}\ell^+\ell^-$ events for evidence of a peak indicating such two-body decays.

A.3 Analysis Details

Hadronic events are selected according to the criteria given in Section 4.1. Events are rejected if they contain fewer than five reconstructed tracks. Charged tracks and π^0 candidates forming $D^{(*)}\ell^+\ell^-$ triplets must satisfy the same requirements as those for B candidates, given in Section 4.1. Muon candidates must penetrate the steel absorber to a depth of at least five nuclear interaction lengths, which effectively places a lower bound on the muon momentum of 1.2 GeV. Electrons are identified by a likelihood that includes the fraction of the particle's energy deposited in the calorimeter and the spatial distribution of the deposited energy. To reduce contamination from low-momentum hadrons, the electron momentum is required to be greater than 1.0 GeV. For electrons that are combined with another lepton satisfying the above criteria, the momentum requirement is lowered to 600 MeV. Electron pairs from photon conversions are rejected by requiring the dielectron invariant mass to be greater than 200 MeV. We rely on the detector simulation to estimate the remaining contribution of hadrons to the lepton sample.

Figure A.1 shows the event-generator-level lepton and D momentum spectrum for $\tilde{B} \to D\ell^-\tilde{\nu}$ MC. To maximize detection efficiency, no requirements are placed on the momentum of the D candidate. D mesons are reconstructed in the modes $D^0 \to K^-\pi^+$ and $D^+ \to K^-\pi^+\pi^+$, where a sum over charge conjugate modes is implied. The daughters of the D candidates must undergo ionization energy loss consistent with the particle hypothesis at the level of three standard deviations ($\left|\sigma^{K/\pi}_{dE/dx}\right| < 3$). We reconstruct D^* mesons in the modes $D^{*0} \to D^0\pi^0$, $D^{*+} \to D^0\pi^+$, and $D^{*+} \to D^+\pi^0$. When used in the D^* modes, D candidates must have invariant masses less than 15 MeV (about 2.5 standard deviations) from the known mass. The mass resolutions are typically 6.5–7.0 MeV for m_D and 0.5–1.0 MeV for $m_{D^*} - m_D$, the D^*-D mass difference.

We determine the efficiency for detecting a supersymmetric $\tilde{B}$ meson using MC simulation. A range of values for the $\tilde{B}$ mass, $m_{\tilde{B}}$, from 3.5 to 4.5 GeV, has been explored. Also, the sneutrino mass, $m_{\tilde{\nu}}$, was varied within the kinematically allowed range. In the process $e^+e^- \to \tilde{b}\bar{\tilde{b}}$, followed by hadronization, the supersymmetric $\tilde{B}$ mesons have energies $E_{\tilde{B}}$ distributed from $m_{\tilde{B}}$ to $E_{\rm beam}$ according to some unknown fragmentation function, which we approximate by a delta function $\delta(E_{\tilde{B}} - E_0)$, with E_0 given a value between $m_{\tilde{B}}$ and $E_{\rm beam}$. We simulate both $\tilde{B}$ mesons and their daughters, as well as the additional hadrons that result from fragmentation. We determine the dependence of efficiency on $m_{\tilde{B}}$, $m_{\tilde{\nu}}$, and E_0. To simulate the decay $\tilde{B} \to D\ell^-X$, we have taken X to be a single pion and used three-body phase space for the decay. For $\tilde{b} \to c\ell^-\tilde{\nu}$, we have used $D\ell^-\tilde{\nu}$ three-body phase space. In choosing a naive phase space model, we neglect the theoretical uncertainty in the decay distribution [149] and facilitate comparison with other models.

These variations affect the $\tilde{B}$ meson detection efficiency primarily through the lepton momentum spectrum. Figure A.2 contains representative graphs of the efficiency variations for the $D^0\ell^+\ell^-$ and

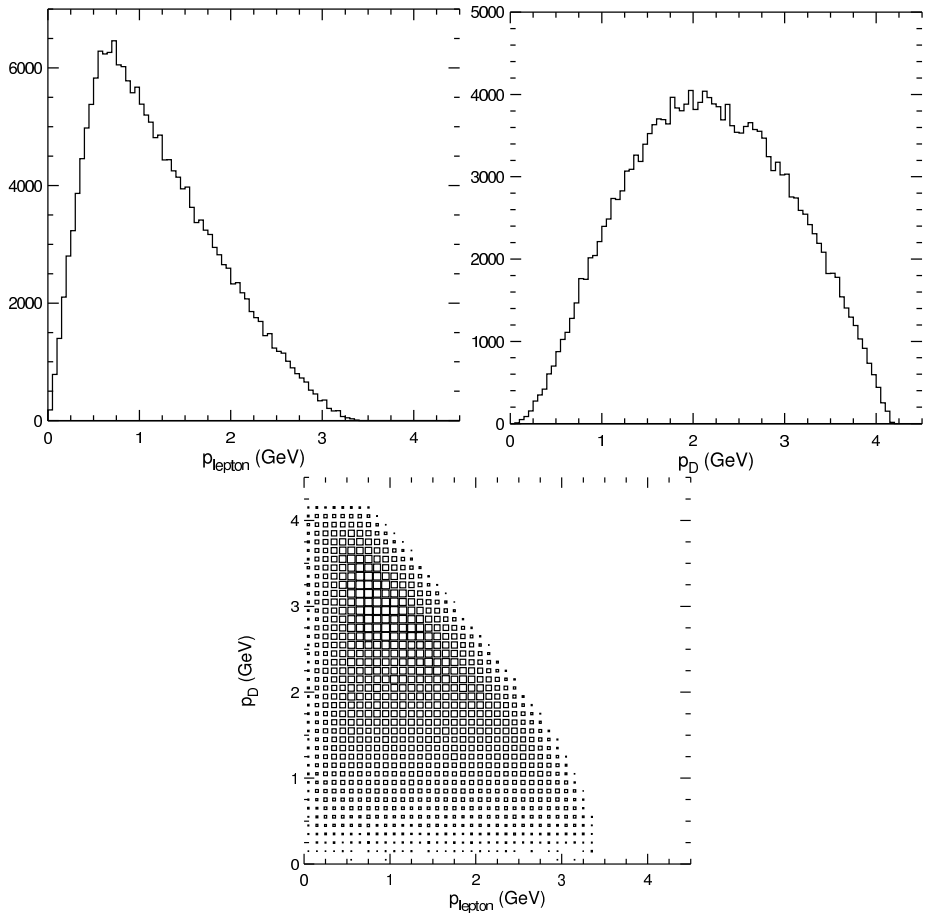

Figure A.1: Generator-level lepton and D meson momentum spectra in $\tilde{B} \to D\ell^-\tilde{\nu}$ decays.

$D^+\ell^+\ell^-$ signatures. The efficiency exhibits weak dependence on $m_{\tilde{B}}$, but lower values of E_0 tend to soften the lepton momentum spectrum, resulting in reduced efficiency. For the smallest value of E_0 we considered (3.7 GeV), the efficiencies are one-fourth of those with $E_0 = E_{\rm beam}$. For all modes, the variation of the efficiency with $m_{\tilde{\nu}}$ is roughly linear between $m_{\tilde{\nu}} = 0$ GeV and $m_{\tilde{\nu}}^{\rm max} \equiv 0.6 m_{\tilde{B}} - 0.8$ GeV, where the efficiency vanishes.

The detection efficiency is also affected by the additional particles produced in fragmentation. From MC studies, we have determined that for each fragmentation particle, the relative decrease in efficiency is approximately 3% and depends on the momentum and species of the fragmentation particles. By considering MC simulation of $e^+e^- \to c\bar{c}$, we estimate roughly two fragmentation particles per GeV of fragmentation energy. The detection efficiency has been corrected accordingly.

To search for the R-parity-violating decay, $\tilde{b} \to c\ell^-$, we apply the same candidate selection critera as described above, with the additional requirements that the invariant mass of the D candidate fall within 15 MeV (about 2.5σ) of the known mass and that $m_{D^*} - m_D$ lie below 145 MeV for

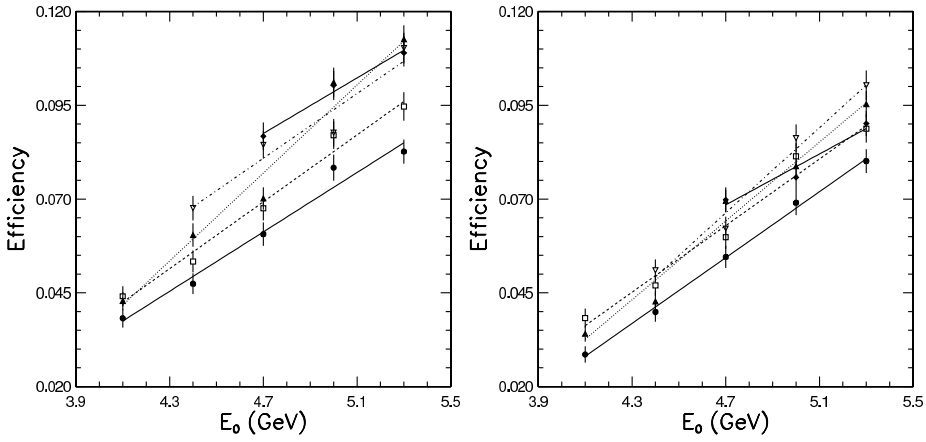

Figure A.2: Signal efficiencies (not including D branching fractions) as a function of $m_{\tilde{B}}$ and E_0 for $D^0\ell^+\ell^-$ (left) and $D^+\ell^+\ell^-$ (right). The five curves, from top to bottom at $E_0 = 4.7$ GeV, are for $m_{\tilde{B}} = 4.50$ GeV, 4.25 GeV, 4.00 GeV, 3.75 GeV, and 3.50 GeV.

$D^{*0} \to D^0\pi^0$, 147 MeV for $D^{*+} \to D^0\pi^+$, and 144 MeV for $D^{*+} \to D^+\pi^0$. By generating signal MC at various values of $m_{\tilde{B}}$ and E_0 as described above, we parametrize both the signal efficiency and the $m_{D^{(*)}\ell^-}$ resolution. We have assumed the natural width of the $\tilde{B}$ to be small compared to the detector resolution. Typical signal efficiencies are 1.5 times larger than for the R-parity-conserving decay because of the stiffer leptons, and the $m_{D^{(*)}\ell^-}$ resolutions are typically around 10 MeV.

A.4 Results

Figure A.3 shows the $K^-\pi^+$ and $K^-\pi^+\pi^+$ invariant mass distributions of D^0 and D^+ candidates, respectively, associated with two oppositely charged leptons. Also shown are the normalizing distributions for D candidates paired with a single lepton of either charge. The analogous distributions for the D^* modes, showing the D^*-D mass difference, are given in Figure A.4. The $D^{(*)}$-dilepton distributions reveal a striking absence of signal. The $D^{(*)}$ yields are extracted from a fit of each histogram to a Gaussian distribution over a linear background for the D modes and a quadratic background for the D^* modes. The means and widths of the Gaussians for the $D^{(*)}$-dilepton fit are fixed to values determined from the normalizing distributions. Table A.1 lists the yields observed in data as well as the expected yields determined from continuum MC. No significant excess is observed in any mode. Also given in Table A.1 is a representative set of detection efficiencies and the resultant 95% confidence level upper limits on the cross section, assuming $m_{\tilde{B}} = 4.0$ GeV, $m_{\tilde{\nu}} = 0$ GeV, and $E_0 = E_{\rm beam}$.

In the normalizing distributions there is good agreement between the data and simulated continuum events. In addition, by analyzing data taken on the $\Upsilon(4S)$ resonance, we observe the closely

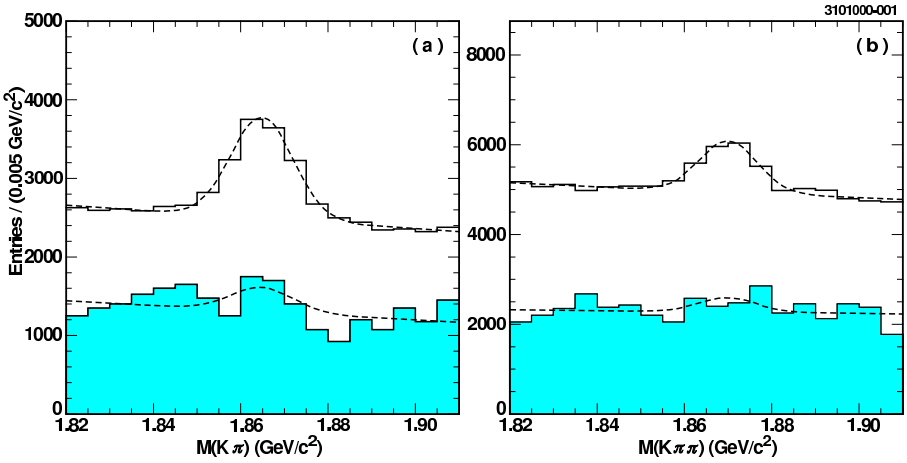

Figure A.3: Invariant mass distributions for (a) $D^0 \to K^-\pi^+$ and (b) $D^+ \to K^-\pi^+\pi^+$ candidates paired with a single lepton of either charge (open histogram) or with two oppositely charged leptons (shaded histogram). The two D-dilepton distributions have been scaled by a factor of 25 to facilitate comparison with the normalizing distributions. The fits of each distribution to a Gaussian and a linear background are shown in the dashed curves.

related semileptonic B decay with yields that agree well with predictions from the detector simulation.

We give the upper limit on the product of the $\tilde{B}\bar{\tilde{B}}$ production cross section and the $\tilde{B} \to D^{(*)}\ell\{\pi, \tilde{\nu}\}$ branching fraction as a function of $m_{\tilde{B}}$ and E_0, assuming $m_{\tilde{\nu}} = 0$ GeV. The upper limits for a finite $m_{\tilde{\nu}}$ would be those for $m_{\tilde{\nu}} = 0$ GeV, but scaled by the factor $(1 - m_{\tilde{\nu}}/m_{\tilde{\nu}}^{\max})^{-1}$. Upper limits have been inflated to account for uncertainties in the detector simulation and in the D and D^* branching fractions, which amount to systematic errors of 20%. We also assign an error of 10% to the expected Standard Model yields due to uncertainties in the simulation of both fake and real leptons. Also, we include a systematic error per fragmentation particle of $\pm 2.5\%$ for the D modes and $\pm 5\%$ for the D^* modes to allow for the uncertainty in the efficiency correction. The total systematic uncertainties are small compared to the statistical errors on the background-subtracted yields.

Figure A.6 shows the 95% confidence level upper limit on the product of $\sigma(e^+e^- \to \tilde{B}\bar{\tilde{B}})$ and $\mathcal{B}(\tilde{B} \to D^{(*)}\ell\{\pi, \tilde{\nu}\})$ as a function of $m_{\tilde{B}}$ and E_0, assuming $m_{\tilde{\nu}} = 0$ GeV. The strong rise of the upper limits with decreasing $E_0/E_{\rm beam}$ reflects the softening of the lepton spectrum. Because of the β^3 dependence of the cross section near threshold, the cross section at $\sqrt{s} = 10.52$ GeV is heavily dependent on the assumed $m_{\tilde{B}}$. These predicted cross sections are shown as the thick curves in Figure A.6. For both the D-dilepton and D^*-dilepton signatures, the upper limits in nearly all of the kinematically allowed $m_{\tilde{B}}$-E_0 parameter space with $m_{\tilde{\nu}} = 0$ GeV fall below the predicted $\tilde{b}\bar{\tilde{b}}$ production cross section. Below $m_{\tilde{B}} = 3.9$ GeV, the D^*-dilepton efficiency vanishes, so we exclude

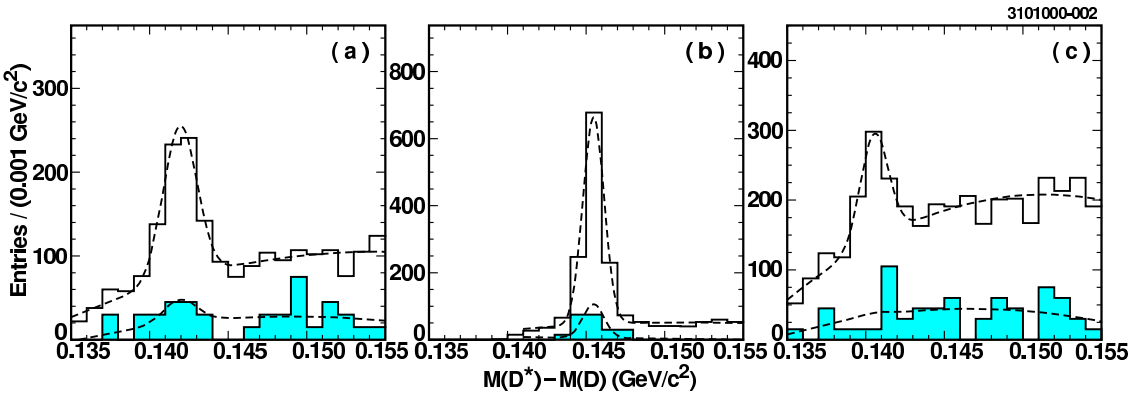

Figure A.4: Distributions of the D^*-D mass difference for (a) $D^{*0} \to D^0\pi^0$, (b) $D^{*+} \to D^0\pi^+$, and (c) $D^{*+} \to D^+\pi^0$ candidates paired with a single lepton of either charge (open histogram) or with two oppositely charged leptons (shaded histogram). The three D^*-dilepton distributions have been scaled by a factor of 15 to facilitate comparison with the normalizing distributions. The fits of each distribution to a Gaussian and a quadratic background are shown in the dashed curves.

a $\tilde{B}$ that decays $\tilde{B} \to D^*\ell\{\pi, \tilde{\nu}\}$ only in the mass range 3.9–4.5 GeV. No portion of the parameter space is excluded if $m_{\tilde{\nu}}$ is greater than 1.2 GeV and 1.3 GeV for the D-dilepton and D^*-dilepton signatures, respectively.

We search for R-parity-violating decays of $\tilde{B}$ in the $m_{D^{(*)}\ell^-}$ distributions shown in Figure A.5. We find no evidence of a peak. Fitting the distributions to a polynomial background plus a Gaussian width given by our experimental resolution, and stepping the Gaussian mean over the mass range, we obtain upper limits on the product of the $\tilde{b}\bar{\tilde{b}}$ production cross section and the $\tilde{B} \to D^{(*)}\ell^-$ decay branching fraction, as a function of $m_{\tilde{B}}$. These upper limits, which include 15% systematic errors on the yields, are shown in Figure A.6. For $\tilde{B} \to D\ell^-$, the upper limit is less than 0.3 pb for all masses except near 4.36 GeV, where it is 1.0 pb. For $\tilde{B} \to D^*\ell^-$ the upper limit is weaker, typically 3 pb for masses around 4 GeV, dropping to 0.3 pb for masses near 4.5 GeV.

In conclusion, we have searched for associated $\tilde{B}\bar{\tilde{B}}$ production in e^+e^- collisions with center-of-mass energy below the $B\bar{B}$ production threshold. Considering D-dilepton and D^*-dilepton combinations, we find no evidence of a light scalar bottom quark produced at $\sqrt{s} = 10.52$ GeV. Upper limits on the $\tilde{B}\bar{\tilde{B}}$ production cross section depend on the assumed mass and energy of the $\tilde{B}$ meson, as well as the mass of the sneutrino. For $m_{\tilde{\nu}}$ less than $\mathcal{O}(1$ GeV), the existence of a light scalar bottom quark with mass between 3.5 GeV and 4.5 GeV has been excluded at the 95% confidence level. A light scalar quark decaying 100% of the time $\tilde{b} \to c\ell\tilde{\nu}$ and/or $\tilde{b} \to c\ell$ would have escaped our notice only if its decay matrix element results in a lepton spectrum much softer than three-body phase space (*e.g.*, if $m_{\tilde{\nu}}$ approaches 1.2 GeV). This study was published in Physical Review D Rapid Communications [150].

Mode	Yield	Expected Yield	$\epsilon_{\rm sig}$ (%)	$\sigma(e^+e^- \to \tilde{b}\tilde{\bar{b}})\times$ $\mathcal{B}(\tilde{B} \to D^{(*)}\ell\{\pi,\tilde{\nu}\})$
$D^0\ell^+\ell^-$	47.6 ± 20.0	$33.7 \pm 14.7 \pm 3.4$	0.44 ± 0.02	
$D^+\ell^+\ell^-$	37.4 ± 25.1	$58.3 \pm 21.3 \pm 5.8$	0.86 ± 0.04	
$D\ell^+\ell^-$				< 2.7 pb at 95% C.L.
$D^{*0}\ell^+\ell^-$	4.9 ± 3.4	$4.2 \pm 2.6 \pm 0.4$	0.08 ± 0.01	
$D^{*+}(D^0\pi^+)\ell^+\ell^-$	11.3 ± 3.8	$4.0 \pm 2.0 \pm 0.4$	0.12 ± 0.01	
$D^{*+}(D^+\pi^0)\ell^+\ell^-$	0.2 ± 3.6	$3.6 \pm 2.3 \pm 0.4$	0.09 ± 0.01	
$D^*\ell^+\ell^-$				< 3.7 pb at 95% C.L.

Table A.1: Fitted D and D^* yields for the $D^{(*)}$-dilepton signature. The expected yields due to Standard Model processes are obtained from an analysis of simulated continuum events and include a systematic error of 10% due to uncertainties in the modeling of both fake and real leptons. The representative signal efficiencies given include the $D^{(*)}$ branching fractions and assume $m_{\tilde{B}} = 4.0$ GeV, $E_0 = E_{\rm beam}$, and $m_{\tilde{\nu}} = 0$ GeV. The corresponding 95% confidence level upper limits on the product of the $e^+e^- \to \tilde{b}\tilde{\bar{b}}$ production cross section and the $\tilde{B} \to D^{(*)}\ell\{\pi,\tilde{\nu}\}$ branching fraction are calculated from the excess in the measured yield over the expected yield. These upper limits include systematic errors of 20% on the reconstruction efficiency.

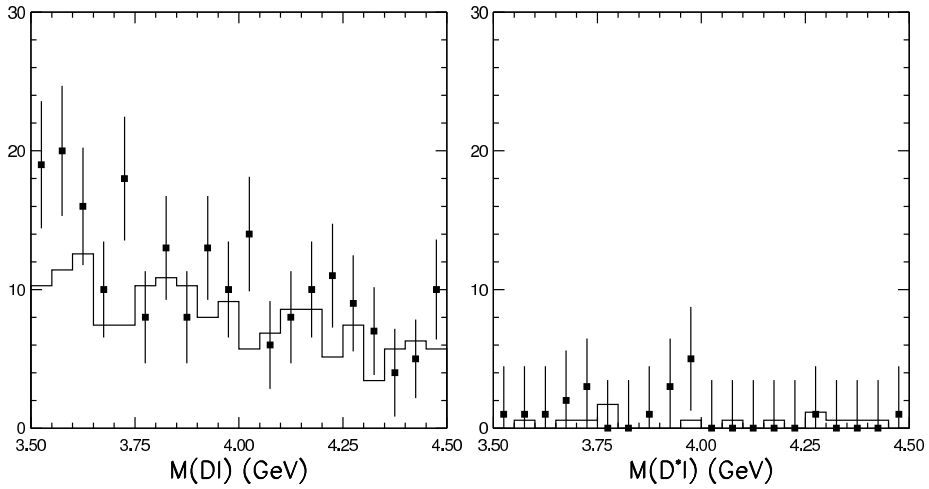

Figure A.5: Distributions of $D\ell^-$ (left) and $D^*\ell^-$ (right) invariant mass in data (points) and simulated continuum events (histogram).

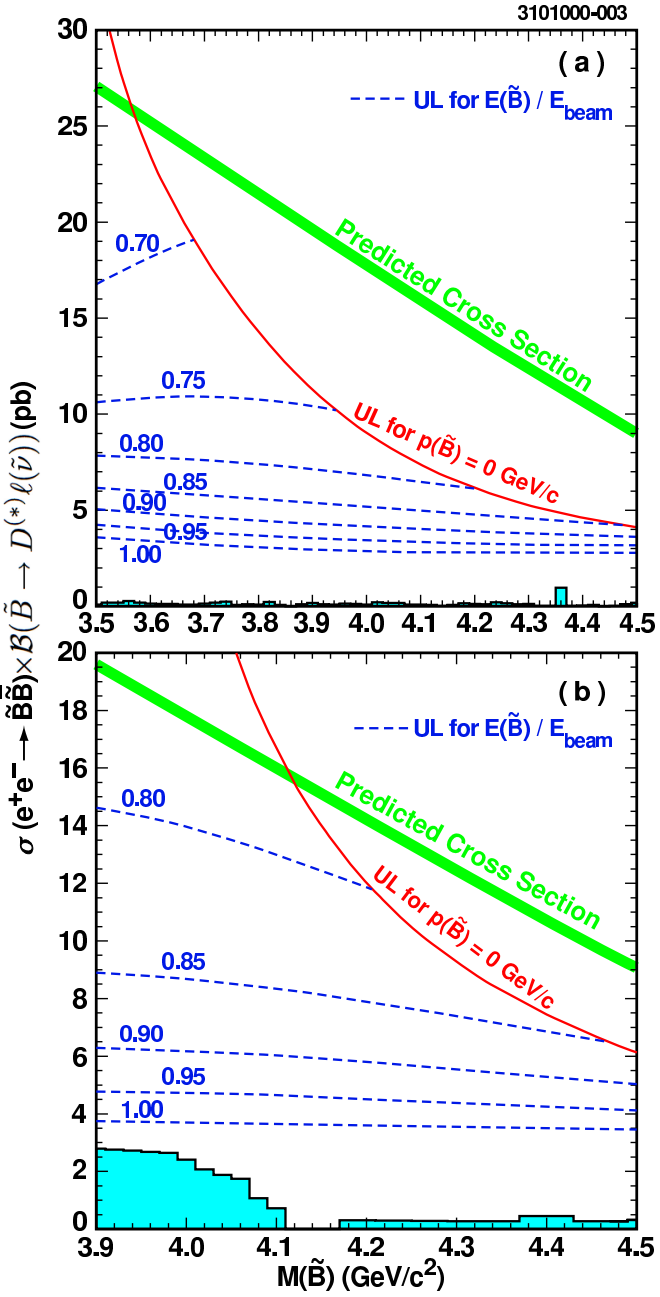

Figure A.6: Upper limits at the 95% confidence level on the product of the $e^+e^- \to \tilde{B}\bar{\tilde{B}}$ production cross section and the $\tilde{B} \to D^{(*)}\ell^-\{\pi, \tilde{\nu}\}$ branching fraction. The energy of the $\tilde{B}$ meson, $E_{\tilde{B}}$, is expected to lie between the energy corresponding to its rest mass, $m_{\tilde{B}}$, and the beam energy, $E_{\rm beam}$. The upper limits for the (a) D-dilepton and (b) D^*-dilepton signatures are given for the full kinematic range of $E_{\tilde{B}}/E_{\rm beam}$ as a function of $m_{\tilde{B}}$, assuming $m_{\tilde{\nu}} = 0$ GeV. The thick curves show the theoretically predicted cross sections, derived from the cross section for pointlike fermions and scaled by $\beta^3 = \left(1 - \frac{m^2_{\tilde{B}}}{E^2_{\rm beam}}\right)^{3/2}$. For finite $m_{\tilde{\nu}}$, the upper limits are increased by a factor $\left(1 - \frac{m_{\tilde{\nu}}}{0.6 m_{\tilde{B}} - 0.8\ \rm GeV}\right)^{-1}$. The shaded histograms represent the largest upper limits, for each given $m_{\tilde{B}}$, on an R-parity-violating $\tilde{B}$ that decays $\tilde{B} \to D^{(*)}\ell$.

Bibliography

[1] W. Pauli, Letter to the Tübingen Congress, 1930. See `http://www.pp.rhul.ac.uk/~ptd/TEACHING/PH2510/pauli-letter.html` and `http://www.ethbib.ethz.ch/exhibit/pauli/neutrino.html`.

[2] M. Gell-Mann, Phys. Lett. **8**, 214 (1964).

[3] J. H. Christenson, J. W. Cronin, V. L. Fitch and R. Turlay, Phys. Rev. Lett. **13**, 138 (1964).

[4] For a more detailed discussion of the Standard Model, see, for instance, J. L. Rosner, arXiv:hep-ph/0108195, or F. Halzen and D. Martin, *Quarks and Leptons*, John Wiley and Sons, New York, 1984.

[5] K. Hagiwara *et al.* [Particle Data Group Collaboration], Phys. Rev. D **66**, 010001 (2002).

[6] M. Goldhaber, Proc. Nat. Acad. Sci. **99**, 33 (2002) [arXiv:hep-ph/0201208].

[7] P. Langacker, arXiv:hep-ph/0304186.

[8] N. Arkani-Hamed, A. G. Cohen and H. Georgi, Phys. Lett. B **513**, 232 (2001) [arXiv:hep-ph/0105239].

[9] N. Isgur and M. B. Wise, Phys. Lett. B **232**, 113 (1989).

[10] N. Isgur and M. B. Wise, Phys. Lett. B **237**, 527 (1990).

[11] C. S. Wu, E. Ambler, R. W. Hayward, D. D. Hoppes and R. P. Hudson, Phys. Rev. **105**, 1413 (1957).

[12] M. Kobayashi and T. Maskawa, Prog. Theor. Phys. **49**, 652 (1973).

[13] N. Cabibbo, Phys. Rev. Lett. **10**, 531 (1963).

[14] B. Aubert *et al.* [BABAR Collaboration], Phys. Rev. Lett. **89**, 201802 (2002) [arXiv:hep-ex/0207042].

[15] K. Abe *et al.* [Belle Collaboration], Phys. Rev. D **66**, 071102 (2002) [arXiv:hep-ex/0208025].

[16] A. D. Sakharov, Pisma Zh. Eksp. Teor. Fiz. **5**, 32 (1967) [JETP Lett. **5**, 24 (1967 SOPUA,34,392-393.1991 UFNAA,161,61-64.1991)].

[17] M. Dine, R. G. Leigh, P. Y. Huet, A. D. Linde and D. A. Linde, Phys. Rev. D **46**, 550 (1992) [arXiv:hep-ph/9203203].

[18] M. B. Gavela, P. Hernandez, J. Orloff, O. Pene and C. Quimbay, Nucl. Phys. B **430**, 382 (1994) [arXiv:hep-ph/9406289].

[19] G. 't Hooft, Phys. Rev. Lett. **37**, 8 (1976).

[20] R. Jackiw and C. Rebbi, Phys. Rev. Lett. **37**, 172 (1976).

[21] C. G. Callan, R. F. Dashen and D. J. Gross, Phys. Lett. B **63**, 334 (1976).

[22] V. Baluni, Phys. Rev. D **19**, 2227 (1979).

[23] L. Wolfenstein, Phys. Rev. Lett. **51**, 1945 (1983).

[24] C. Jarlskog, Phys. Rev. Lett. **55**, 1039 (1985).

[25] C. Jarlskog, Z. Phys. C **29**, 491 (1985).

[26] A. Höcker, H. Lacker, S. Laplace and F. Le Diberder, Eur. Phys. J. C **21**, 225 (2001) [arXiv:hep-ph/0104062]. For most recent fit results, see `http://www.slac.stanford.edu/~laplace/ckmfitter/ckm_wellcome.html`.

[27] M. Beneke, G. Buchalla, M. Neubert and C. T. Sachrajda, Nucl. Phys. B **606**, 245 (2001) [arXiv:hep-ph/0104110].

[28] M. Neubert, arXiv:hep-ph/0207327.

[29] M. Gronau and D. London, Phys. Rev. Lett. **65**, 3381 (1990).

[30] H. J. Lipkin, Y. Nir, H. R. Quinn and A. Snyder, Phys. Rev. D **44**, 1454 (1991).

[31] A. E. Snyder and H. R. Quinn, Phys. Rev. D **48**, 2139 (1993).

[32] Y. Grossman and H. R. Quinn, Phys. Rev. D **56**, 7259 (1997) [arXiv:hep-ph/9705356].

[33] A. Deandrea, R. Gatto, M. Ladisa, G. Nardulli and P. Santorelli, Phys. Rev. D **62**, 036001 (2000) [arXiv:hep-ph/0002038].

[34] A. Deandrea and A. D. Polosa, Phys. Rev. Lett. **86**, 216 (2001) [arXiv:hep-ph/0008084].

[35] N. G. Deshpande, G. Eilam, X. G. He and J. Trampetic, Phys. Rev. D **52**, 5354 (1995) [arXiv:hep-ph/9503273].

[36] R. Enomoto, Y. Okada and Y. Shimizu, Phys. Lett. B **433**, 109 (1998) [arXiv:hep-ph/9712202].

[37] A. Deandrea, R. Gatto, M. Ladisa, G. Nardulli and P. Santorelli, Phys. Rev. D **62**, 114011 (2000) [arXiv:hep-ph/0007059].

[38] R. E. Blanco, C. Gobel and R. Mendez-Galain, Phys. Rev. Lett. **86**, 2720 (2001) [arXiv:hep-ph/0007105].

[39] N. G. Deshpande, N. Sinha and R. Sinha, arXiv:hep-ph/0207257.

[40] I. Dunietz, Phys. Lett. B **427**, 179 (1998) [arXiv:hep-ph/9712401].

[41] D. London, N. Sinha and R. Sinha, Phys. Rev. Lett. **85**, 1807 (2000) [arXiv:hep-ph/0005248].

[42] M. Diehl and G. Hiller, Phys. Lett. B **517**, 125 (2001) [arXiv:hep-ph/0105213].

[43] M. Gronau and D. London., Phys. Lett. B **253**, 483 (1991).

[44] M. Gronau and D. Wyler, Phys. Lett. B **265**, 172 (1991).

[45] B. Kayser and D. London, Phys. Rev. D **61**, 116013 (2000) [arXiv:hep-ph/9909561].

[46] D. Atwood and A. Soni, arXiv:hep-ph/0206045.

[47] M. Gronau, Phys. Rev. D **58**, 037301 (1998) [arXiv:hep-ph/9802315].

[48] Y. Grossman, Z. Ligeti and A. Soffer, arXiv:hep-ph/0210433.

[49] M. Gronau, O. F. Hernandez, D. London and J. L. Rosner, Phys. Rev. D **50**, 4529 (1994) [arXiv:hep-ph/9404283].

[50] A. S. Dighe, M. Gronau and J. L. Rosner, Phys. Rev. D **57**, 1783 (1998) [arXiv:hep-ph/9709223].

[51] M. Ciuchini, E. Franco, G. Martinelli and L. Silvestrini, Nucl. Phys. B **501**, 271 (1997) [arXiv:hep-ph/9703353].

[52] M. Ciuchini, R. Contino, E. Franco, G. Martinelli and L. Silvestrini, Nucl. Phys. B **512**, 3 (1998) [Erratum-ibid. B **531**, 656 (1998)] [arXiv:hep-ph/9708222].

[53] M. Gronau, O. F. Hernandez, D. London and J. L. Rosner, Phys. Rev. D **52**, 6374 (1995) [arXiv:hep-ph/9504327].

[54] M. Gronau, O. F. Hernandez, D. London and J. L. Rosner, Phys. Rev. D **52**, 6356 (1995) [arXiv:hep-ph/9504326].

[55] R. Fleischer and T. Mannel, Phys. Rev. D **57**, 2752 (1998) [arXiv:hep-ph/9704423].

[56] M. Neubert and J. L. Rosner, Phys. Lett. B **441**, 403 (1998) [arXiv:hep-ph/9808493].

[57] M. Neubert and J. L. Rosner, Phys. Rev. Lett. **81**, 5076 (1998) [arXiv:hep-ph/9809311].

[58] M. Gronau, Phys. Rev. D **62**, 014031 (2000).

[59] G. Paz, arXiv:hep-ph/0206312.

[60] K. G. Wilson, Phys. Rev. **179** (1969) 1499.

[61] C. Davies, arXiv:hep-ph/0205181 and references therein.

[62] M. Bauer, B. Stech and M. Wirbel, Z. Phys. C **34**, 103 (1987).

[63] L. L. Chau, H. Y. Cheng, W. K. Sze, H. Yao and B. Tseng, Phys. Rev. D **43**, 2176 (1991) [Erratum-ibid. D **58**, 019902 (1998)].

[64] A. Ali, G. Kramer and C. D. Lu, Phys. Rev. D **58**, 094009 (1998) [arXiv:hep-ph/9804363] and references therein.

[65] H. Y. Cheng and B. Tseng, Phys. Rev. D **58**, 094005 (1998) [arXiv:hep-ph/9803457].

[66] M. A. Shifman, A. I. Vainshtein and V. I. Zakharov, Nucl. Phys. B **147**, 385 (1979).

[67] M. A. Shifman, A. I. Vainshtein and V. I. Zakharov, Nucl. Phys. B **147**, 448 (1979).

[68] P. Colangelo and A. Khodjamirian, arXiv:hep-ph/0010175.

[69] J. D. Bjorken, Nucl. Phys. Proc. Suppl. **11**, 325 (1989).

[70] C. H. Chang and H. n. Li, Phys. Rev. D **55**, 5577 (1997) [arXiv:hep-ph/9607214].

[71] T. W. Yeh and H. n. Li, Phys. Rev. D **56**, 1615 (1997) [arXiv:hep-ph/9701233].

[72] M. Beneke, G. Buchalla, M. Neubert and C. T. Sachrajda, Nucl. Phys. B **591**, 313 (2000) [arXiv:hep-ph/0006124].

[73] A. Khodjamirian, Nucl. Phys. B **605**, 558 (2001) [arXiv:hep-ph/0012271].

[74] C. W. Bauer, S. Fleming and M. E. Luke, Phys. Rev. D **63**, 014006 (2001) [arXiv:hep-ph/0005275].

[75] C. W. Bauer, S. Fleming, D. Pirjol and I. W. Stewart, Phys. Rev. D **63**, 114020 (2001) [arXiv:hep-ph/0011336].

[76] C. W. Bauer and I. W. Stewart, Phys. Lett. B **516**, 134 (2001) [arXiv:hep-ph/0107001].

[77] C. W. Bauer, D. Pirjol and I. W. Stewart, Phys. Rev. D **65**, 054022 (2002) [arXiv:hep-ph/0109045].

[78] M. Ciuchini, E. Franco, G. Martinelli, M. Pierini and L. Silvestrini, Phys. Lett. B **515**, 33 (2001) [arXiv:hep-ph/0104126].

[79] S. Gardner, arXiv:hep-ph/0209080.

[80] Y. Y. Keum, H. n. Li and A. I. Sanda, Phys. Lett. B **504**, 6 (2001) [arXiv:hep-ph/0004004].

[81] Y. Y. Keum, H. N. Li and A. I. Sanda, Phys. Rev. D **63**, 054008 (2001) [arXiv:hep-ph/0004173].

[82] Y. Y. Keum and H. n. Li, Phys. Rev. D **63**, 074006 (2001) [arXiv:hep-ph/0006001].

[83] J. L. Rosner, Nucl. Instrum. Meth. A **462**, 44 (2001) [arXiv:hep-ph/0011183].

[84] C. W. Chiang and J. L. Rosner, Phys. Rev. D **65**, 074035 (2002) [arXiv:hep-ph/0112285].

[85] D. S. Du, H. J. Gong, J. F. Sun, D. S. Yang and G. H. Zhu, Phys. Rev. D **65**, 094025 (2002) [Erratum-ibid. D **66**, 079904 (2002)] [arXiv:hep-ph/0201253].

[86] D. S. Du, J. F. Sun, D. S. Yang and G. H. Zhu, arXiv:hep-ph/0209233.

[87] Y. Y. Keum and A. I. Sanda, arXiv:hep-ph/0209014.

[88] Y. Y. Keum, arXiv:hep-ph/0210127.

[89] B. Aubert *et al.* [BABAR Collaboration], Phys. Rev. Lett. **89**, 281802 (2002) [arXiv:hep-ex/0207055].

[90] B. Aubert *et al.* [BABAR Collaboration], arXiv:hep-ex/0207063.

[91] B. Aubert *et al.* [BABAR Collaboration], arXiv:hep-ex/0207065.

[92] K. Abe *et al.* [BELLE Collaboration], Phys. Rev. Lett. **87**, 101801 (2001) [arXiv:hep-ex/0104030].

[93] B. C. Casey *et al.* [Belle Collaboration], Phys. Rev. D **66**, 092002 (2002) [arXiv:hep-ex/0207090].

[94] D. Cronin-Hennessy *et al.* [CLEO Collaboration], Phys. Rev. Lett. **85**, 515 (2000).

[95] S. Chen *et al.* [CLEO Collaboration], Phys. Rev. Lett. **85**, 525 (2000) [arXiv:hep-ex/0001009].

[96] D. M. Asner *et al.* [CLEO Collaboration], Phys. Rev. D **65**, 031103 (2002) [arXiv:hep-ex/0103040].

[97] B. Bajc, S. Fajfer, R. J. Oakes, T. N. Pham and S. Prelovsek, Phys. Lett. B **447**, 313 (1999) [arXiv:hep-ph/9809262].

[98] S. Fajfer, R. J. Oakes and T. N. Pham, Phys. Rev. D **60**, 054029 (1999) [arXiv:hep-ph/9812313].

[99] S. Fajfer, R. J. Oakes and T. N. Pham, Phys. Lett. B **539**, 67 (2002) [arXiv:hep-ph/0203072].

[100] H. Y. Cheng and K. C. Yang, Phys. Rev. D **66**, 054015 (2002) [arXiv:hep-ph/0205133].

[101] C. H. Chen and H. n. Li, arXiv:hep-ph/0209043.

[102] X. G. He, Eur. Phys. J. C **9**, 443 (1999) [arXiv:hep-ph/9810397].

[103] N. G. Deshpande, X. G. He and J. Q. Shi, Phys. Rev. D **62**, 034018 (2000) [arXiv:hep-ph/0002260].

[104] B. Aubert *et al.* [BABAR Collaboration], arXiv:hep-ex/0207068.

[105] B. I. Eisenstein *et al.* [CLEO Collaboration], arXiv:hep-ex/0304036.

[106] J. J. Aubert *et al.*, Phys. Rev. Lett. **33**, 1404 (1974).

[107] J. E. Augustin *et al.*, Phys. Rev. Lett. **33**, 1406 (1974).

[108] S. W. Herb *et al.*, Phys. Rev. Lett. **39**, 252 (1977).

[109] Y. Kubota *et al.* [CLEO Collaboration], Nucl. Instrum. Meth. A **320**, 66 (1992).

[110] R. E. Kalman, J. Basic Eng. **82**, 34 (1961); R. E. Kalman and R. S. Bucy, J. Basic Eng. **83**, 95 (1961); P. Billoir, Nucl. Instrum. Meth. A **225**, 352 (1984); P. Billoir, R. Frühwirth and M. Regler, Nucl. Instrum. Meth. A **241**, 115 (1985); R. Frühwirth, Nucl. Instrum. Meth. A **262**, 444 (1987).

[111] G. Brandenburg *et al.* [CLEO Collaboration], Phys. Rev. D **61**, 072002 (2000) [arXiv:hep-ex/9907057].

[112] R. Brun *et al.*, CERN DD/EE/84-1.

[113] C. Bebek *et al.*, Nucl. Instrum. Meth. A **302**, 261 (1991).

[114] C. J. Bebek *et al.*, Nucl. Instrum. Meth. A **338**, 447 (1994).

[115] T. S. Hill, Nucl. Instrum. Meth. A **418**, 32 (1998).

[116] D. Peterson, Nucl. Instrum. Meth. A **409**, 204 (1998).

[117] H. Albrecht *et al.* [ARGUS Collaboration], Phys. Lett. B **241**, 278 (1990); H. Albrecht *et al.* [ARGUS Collaboration], Phys. Lett. B **254**, 288 (1991).

[118] G. C. Fox and S. Wolfram, Phys. Rev. Lett. **41**, 1581 (1978).

[119] T. E. Coan *et al.* [CLEO Collaboration], Phys. Rev. Lett. **84**, 5283 (2000) [arXiv:hep-ex/9912057].

[120] J. P. Alexander *et al.* [CLEO Collaboration], Phys. Rev. Lett. **86**, 2737 (2001) [arXiv:hep-ex/0006002].

[121] M. Gronau and J. L. Rosner, Phys. Rev. D **61**, 073008 (2000) [arXiv:hep-ph/9909478].

[122] M. Gronau, arXiv:hep-ph/0001317.

[123] R. Fleischer, Z. Phys. C **62**, 81 (1994).

[124] N. G. Deshpande and X. G. He, Phys. Lett. B **336**, 471 (1994) [arXiv:hep-ph/9403266].

[125] M. Beneke, G. Buchalla, M. Neubert and C. T. Sachrajda, Phys. Rev. Lett. **83**, 1914 (1999) [arXiv:hep-ph/9905312]; H. n. Li, arXiv:hep-ph/9903323; H. Y. Cheng and K. C. Yang, Phys. Rev. D **62**, 054029 (2000) [arXiv:hep-ph/9910291]; M. Bander, D. Silverman and A. Soni, Phys. Rev. Lett. **43**, 242 (1979).

[126] M. Suzuki and L. Wolfenstein, Phys. Rev. D **60**, 074019 (1999) [arXiv:hep-ph/9903477].

[127] S. B. Athar *et al.* [CLEO Collaboration], Phys. Rev. D **66**, 052003 (2002) [arXiv:hep-ex/0202033].

[128] C. P. Jessop *et al.* [CLEO Collaboration], Phys. Rev. Lett. **85**, 2881 (2000) [arXiv:hep-ex/0006008].

[129] E. Eckhart *et al.* [CLEO Collaboration], Phys. Rev. Lett. **89**, 251801 (2002) [arXiv:hep-ex/0206024].

[130] R. A. Briere *et al.* [CLEO Collaboration], Phys. Rev. Lett. **86**, 3718 (2001) [arXiv:hep-ex/0101032].

[131] C. Dallapiccola [BABAR Collaboration], AIP Conf. Proc. **618**, 192 (2002).

[132] B. Aubert *et al.* [BABAR Collaboration], arXiv:hep-ex/0303022.

[133] B. Aubert *et al.* [BABAR Collaboration], arXiv:hep-ex/0303029.

[134] A. Gordon *et al.* [Belle Collaboration], Phys. Lett. B **542**, 183 (2002) [arXiv:hep-ex/0207007].

[135] K. Abe *et al.* [Belle Collaboration], Phys. Rev. D **65**, 092005 (2002) [arXiv:hep-ex/0201007].

[136] T. J. Gershon [Belle Collaboration], arXiv:hep-ex/0205033; H. C. Huang [BELLE Collaboration], arXiv:hep-ex/0205062.

[137] P. Chang (for the Belle Collaboration), talk presented at the XXXI International Conference on High Energy Physics, Amsterdam, Netherlands, 24–31 July 2002.

[138] K. F. Chen (for the Belle Collaboration), talk presented at the XXXI International Conference on High Energy Physics, Amsterdam, Netherlands, 24–31 July 2002.

[139] M. Beneke, arXiv:hep-ph/0207228.

[140] R. Fleischer and J. Matias, Phys. Rev. D **66**, 054009 (2002) [arXiv:hep-ph/0204101].

[141] V. Chernyak, Phys. Lett. B **509**, 273 (2001) [arXiv:hep-ph/0102217].

[142] S. Pacetti and Y. Srivastava, arXiv:hep-ph/0007318.

[143] A. Dedes and H. K. Dreiner, JHEP **0106**, 006 (2001) [arXiv:hep-ph/0009001].

[144] G. Taylor, Representing the ALEPH Collaboration, LEPC Presentation, 20 July 2000, `http://alephwww.cern.ch`.

[145] D. Schlatter, Representing the ALEPH Collaboration, LEPC Presentation, 5 September 2000, `http://alephwww.cern.ch`; M. Pepe-Altarelli, Representing the LEP Collaborations, IVth Rencontres du Vietnam, Hanoi, Vietnam, 19-25 July 2000.

[146] M. Carena, S. Heinemeyer, C. E. Wagner and G. Weiglein, Phys. Rev. Lett. **86**, 4463 (2001) [arXiv:hep-ph/0008023].

[147] R. Ammar *et al.* [CLEO Collaboration], Phys. Rev. D **57**, 1350 (1998) [arXiv:hep-ex/9707018]; E. Rice *et al.*, Phys. Rev. Lett. **48**, 906 (1982); A. Osterheld *et al.*, SLAC-PUB-4160; Z. Jakubowski *et al.* [Crystal Ball Collaboration], Z. Phys. C **40**, 49 (1988); H. Albrecht *et al.*, Phys. Lett. B **116**, 383 (1982); B. Niczyporuk *et al.* [LENA Collaboration], Z. Phys. C **15**, 299 (1982); J. Siegrist *et al.*, And Inclusive Momentum Distributions," Phys. Rev. D **26**, 969 (1982); P. A. Rapidis *et al.*, Phys. Rev. Lett. **39**, 526 (1977) [Erratum-ibid. **39**, 974 (1977)]; P. A. Rapidis, thesis, SLAC-Report-220 (1979); A. E. Blinov *et al.*, Z. Phys. C **70**, 31 (1996); A. Bäcker, thesis Gesamthochschule Siegen, DESY F33-77/03 (1977); C. Gerke, thesis, Hamburg Univ. (1979); C. Berger *et al.* [PLUTO Collaboration], Phys. Lett. B **81**, 410 (1979); W. Lackas, thesis, RWTH Aachen, DESY Pluto-81/11 (1981).

[148] U. Nierste and T. Plehn, Phys. Lett. B **493**, 104 (2000) [arXiv:hep-ph/0008321].

[149] M. Neubert, private communication.

[150] V. Savinov *et al.* [CLEO Collaboration], Phys. Rev. D **63**, 051101 (2001) [arXiv:hep-ex/0010047].